The Spatial Distribution of Quasars

Caroline Rachel Goldschmidt

Presented for the Degree of Doctor of Philosophy

at the University of Edinburgh

1993

This thesis is my own composition, except where specifically indicated in the text.

June, 1993

Abstract

This thesis is concerned with the cosmological evolution of quasars. I describe the construction of the Edinburgh Multicolour Survey from COSMOS scans of UK Schmidt photographic plates, taken in $UBVRI$ wavebands at high galactic latitude in a contiguous area of 0.1 steradians (13 UK Schmidt fields). Two plates are taken close together in time in each waveband in each field so that spurious detections can be eliminated, and the errors on the measured magnitudes reduced. The raw COSMOS datasets were calibrated using photoelectric and CCD sequences in each waveband in each field. Systematic errors in the calibration due to "field effects" (variations in image size across each plate) are minimised by using the colours of the stars on each plate. Differences between the plates in each waveband are minimised. Differences in each waveband between fields are minimised by using the spatial distribution of stars in the survey, and requiring it to be uniform across the whole survey area. The calibration of the "worst" (as judged by the level of field effects) is tied in with that of the "best" plates. The final dataset is uniformly and accurately calibrated across the entire survey area. The systematic error in the COSMOS-measured magnitudes at $B = 15 - 16$ is $0.01m$. The rms error at $B = 17 - 18$ (where most of the quasars are) is $0.09m$.

The Edinburgh Multicolour Survey was used to select a sample of bright UVX candidates. I then describe how follow-up spectroscopy was carried out to determine the nature of the candidates, and in the case of the quasars, to measure their redshifts. I compare the surface density of quasars found in this way to that measured by previous surveys, in particular the Palomar-Green Survey (Schmidt & Green 1983). Until now, the Palomar-Green Survey was the principal source of bright, optically selected quasars and, as such, has been used to determine the nature of quasar evolution. However I show in Chapter 4 that the Palomar-Green Survey is significantly incomplete, by a factor 3, when compared to the Edinburgh Survey, and that the slope of the differential log(number)-magnitude relation is 0.73 ± 0.07, substantially less than previous determinations. I then use the Edinburgh Survey, together with the fainter, larger AAT survey (Boyle *et al.* 1990) to calculate the luminosity function in redshift slices. I compare this luminosity function with the accepted model; Pure Luminosity Evolution (Boyle 1991), in two ways; by comparing the model and observed cumulative distributions in absolute magnitude, and by fitting a function to the observed differential luminosity function. I show that Pure Luminosity Evolution is not a good description of the data, and it appears that the luminous part of the luminosity function changes shape as a function of redshift, such that the most luminous quasars evolve the least. I discuss the implications of this result, in particular with respect to hierarchical galaxy formation models and with respect to quasar lifetimes. When Pure Luminosity Evolution was the best-fit model and there was no need for density evolution, workers favoured long lifetimes. I argue that there is no justification for that, and that nothing can be known about quasar lifetimes by studying the luminosity function. I discuss possible future work.

Acknowledgements

I am enormously indebted to Lance Miller, who has been my supervisor for the past three years. He has endeavoured to teach me how to do good astronomy and tried not to laugh at my computer programs. I am grateful to the United Kingdom Schmidt Telescope Unit, for providing the photographic plate material that this thesis is based on, and to the COSMOS unit, for measuring the plates. I acknowledge the S.E.R.C. for a studentship, and the D.S.S. for supporting me for the past few months. I thank the department of astronomy for their support, in particular Peter Brand and Liz Gibson. I am also grateful for allocations of observing time at the INT, the UKST and ESO.

I have learnt much from many people over the past few years, in particular I have enjoyed discussions with Phil Blanco, Karl Glazebrook, Bob Nichol, Brian Boyle, Erica Ellingson, Mike Hawkins, John Peacock, Alan Heavens, Ann Savage, Tom Broadhurst, Fabio La Franca, Stefano Cristiani, Andy Taylor, Bob Mann, Phil James, Tom Shanks, Fred Watson, Stuart Lumsden, Chris Collins, Kathy Romer, and Peter Brand. I am grateful to Paul Hewett for providing me with a machine-readable copy of the Large Bright Quasar Survey. I have enjoyed collaborating with Fabio and Stefano, and hope that this will continue. Various people read various bits of this thesis; Lance read all of it, Phil James read most of it, and Bob Mann and Andy Taylor read Chapter 1. Thanks, chaps.

The past few months have not been much fun, but many people helped me through it. In particular Suzie, a fellow sufferer, was "always there", Lance was sympathetic, Andy T. provided much support and whisky, and Kathy sent helpful e-mails. Other bods who have enlivened my life in various ways since I have been at ROE include oldies Rijdat, Philbo, Karlopod, Big Boy Bobb, Schmeve, Keef, Chrispy, Penny, Cuddly Ant, and Stuart. Suzie and I have eaten many a happy (and drunken) dinner together. Phil J. and Karl had to feed my cat on occasion and yet never complained. Andy C. was the soul of sweetness and light whilst he was writing up and never banged my head on a table. I have been privileged to share an office with Ruth, who was strangely Ruth-like, Dave, who knew lots about Monty Python, Hugh, who made lots of phone calls and of course, the orange. Other people who have probably suffered whilst I was writing up include Bob M. ("phwooaarr what a huuuuge introduction"), Doddsie (and his trendy shoes), Phil J. (groovy hairstyle and nasty tee-shirts), Phil P. (just nasty tee-shirts), and the firsties. Outside the observatory, Gail, Chris, Nick, Claire and of course Neepy the cat were "the flatmates".

I owe so much to my family for all their love and support, in particular my parents, to whom this thesis is dedicated. Paul, my husband, has helped me with his love, support, and good humour. Without him I could not have done this.

Contents

Chapter 1

Introduction

1.1 Outline

In this chapter I describe some of the fundamental results in modern cosmology. This framework is used throughout the thesis to determine the evolutionary properties of quasars. I summarise methods of selecting complete samples of quasars at optical wavelengths, and previous attempts at modelling the cosmological evolution of these samples. I then outline the aims of this thesis and describe how it relates to previous work.

1.2 The Foundations of Modern Cosmology

Modern cosmology is based on the Cosmological Principle and together with general relativity (GR) can be used to determine the large-scale spatial and temporal properties of the universe. The Cosmological Principle (CP) derives from the Copernican Principle that the earth is not at a unique vantage point, and from the observation that the universe is isotropic on large scales. Evidence for isotropy comes from measurements of the Cosmic Microwave Background (CMB), which show that temperature variations in the early universe were a factor 10^{-5} less than the measured temperature of the CMB (Smoot *et*

al. 1992), and from measurements of the spatial distribution of radio galaxies (Webster, 1976) which show a variation of $\leq 3\%$ in the number density of these objects on scales of ≈ 100 Mpc. If the universe is isotropic everywhere, then it must also be homogeneous, i.e. the physical properties must be the same everywhere.

Two other observations which make up the cornerstone of cosmology are;

1) The sky is dark at night (Olbers' paradox), showing that the universe cannot be both infinitely old and static, or isotropic on the largest scales, if it were, every single line-of-sight would rest on a star and the night sky would be as bright as the surface of a star.

2) In 1929 Hubble measured the recessional velocities of, and distances to galaxies, and showed that their velocities were proportional to their distances, i.e. the universe is not static, but expanding. When Einstein initially used GR to model the dynamics of the universe, he did not consider the idea of an expanding universe and concluded that the only stable solution to his field equations was a static, positively curved space-time. In order to prevent this universe from collapsing in on itself due to its own gravity, Einstein added in the Cosmological Constant Λ; which is equivalent to a negative density. However, Friedmann reworked the Einstein field equations, showing that another stable solution is an expanding universe with no need for Λ, and ruled out the static model.

If the CP is a true assumption then there can exist fundamental observers on hypersurfaces surrounding each point of space-time. These observers can all measure the same physical properties and can all observe the universe as being isotropic. The line metric of these hypersurfaces is the Friedmann-Robertson-Walker (FRW) metric (see Weinberg 1972 for a complete derivation);

$$ds^2 = dt^2 - \frac{R^2(t)}{c^2}\left[\frac{dr^2}{1-kr^2} + r^2\left(d\theta^2 + \sin^2\theta d\phi^2\right)\right], \tag{1.1}$$

where dt is the proper time, r, θ, and ϕ describe the local coordinate system, r being the comoving distance (i.e. the proper distance at the present epoch), and $R(t)$ is a scale factor describing the expansion of the universe with time. The curvature of space is described by the factor k. If $k = -1$ then space is negatively curved and has no boundaries, if

$k = 0$ then space is flat, and if $k = 1$ then space is positively curved and finite but has no boundaries. We show below how this curvature is related to the density of matter in the universe.

1.2.1 Redshift and the Expansion of the Universe

Consider the FRW metric for a photon propagating along a radial trajectory, emitted at time t_e and observed at time t_o; $ds^2 = 0$ for a photon, and because the path is radial $d\theta = d\phi = 0$. Therefore its trajectory is determined from equation 1.1 which becomes

$$dt = \frac{-R(t)}{c} dr. \tag{1.2}$$

If we integrate this over the time interval between emission and observation; $t_o - t_e$ we get

$$\int_{t_e}^{t_o} \frac{cdt}{R(t)} = -\int_r^0 dr. \tag{1.3}$$

If we consider the wavelength of the photon, emitted over a period of time Δt_e and observed over Δt_o, then the above equation becomes

$$\int_{t_e+\Delta t_e}^{t_o+\Delta t_o} \frac{cdt}{R(t)} = \int_{t_e}^{t_o} \frac{cdt}{R(t)}. \tag{1.4}$$

This implies

$$\Delta t_o = \frac{\Delta t_e}{R(t_e)}. \tag{1.5}$$

Since $R(t_e)$ is always less than 1 (it is the scale size at an earlier epoch relative to the present epoch), this shows that time intervals are dilated by the expansion of the universe. The wavelength of the photon λ_e is proportional to the interval t_e and therefore

$$\lambda_o = \frac{\lambda_e}{R(t_e)}. \tag{1.6}$$

Redshift is defined to be

$$z = \frac{\lambda_o - \lambda_e}{\lambda_e}. \tag{1.7}$$

We can see that redshift is a measure of the relative sizes of the universe at the time of emission and observation;

$$1 + z = \frac{R(t_o)}{R(t_e)}. \tag{1.8}$$

This is the fundamental meaning of cosmological redshift, and although a few astronomers disagree with it, (*e.g.* see Field *et al.* 1973, "The Redshift Controversy") most agree that an object's redshift is a direct measure of the relative size of the universe at the epoch of emission. It is this interpretation that will be used throughout this thesis and allows us to use redshifts to determine the cosmological evolution of quasars.

The CP predicts that the universe is homogeneous. Therefore the only allowed distortion in the velocity field is purely radial, i.e. shear terms are forbidden. If we consider the proper distance $x = rR(t)$ to a particle and its velocity v;

$$v = \frac{dx}{dt} = r\dot{R}(t) \tag{1.9}$$

and therefore

$$v = \frac{\dot{R}(t)}{R(t)}x. \tag{1.10}$$

At the present epoch we can write this as

$$v = \frac{\dot{R}(0)}{R(0)}x = H_0 x, \tag{1.11}$$

where H_0 is a measure of the rate of expansion and is called Hubble's constant. H_0 was originally measured by Hubble (1929) to be $\sim$ 500 kms^{-1} Mpc^{-1}. However this figure has been drastically revised since then and is now thought to be between 50 and 100 $\mathrm{kms}^{-1}\mathrm{Mpc}^{-1}$. See Rowan-Robinson (1986) for a review of the problems associated with measuring distances in the universe and the determination of H_0.

So far we have not attempted to explain exactly how the function $R(t)$, which describes the expansion of the universe with respect to time, is related to the mass-energy content of the universe. General relativity shows that the curvature of space-time is directly related to the total density of energy-mass in the universe. The Friedmann equations (a simplified form of the GR field equations) describe the relation between curvature and energy density;

$$\frac{d^2R}{dt^2} = \frac{-4\pi GR}{3}\left(\rho + \frac{3p}{c^2}\right) + \frac{1}{3}\Lambda R^2 \tag{1.12}$$

and

$$\dot{R}^2 = \frac{8\pi G\rho}{3R} - kc^2 + \frac{1}{3}\Lambda R^2 \tag{1.13}$$

where $\rho + 3p/c^2$ is the relativistic energy density, k is the constant of curvature and Λ is the Cosmological Constant as discussed earlier. We will assume that $\Lambda = 0$ from now on. Remembering that R_0, by definition, is equal to unity (since $R(t)$ is the scale size of the universe relative to the present epoch) the above equation becomes

$$\dot{R}_0^2 = \frac{8\pi G\rho_0}{3R_0} - kc^2 = \frac{8\pi G\rho_0}{3} - kc^2 \tag{1.14}$$

Therefore, since H_0 is defined as $H_0 = \dot{R}_0/R_0 = \dot{R}_0$

$$H_0^2 = \frac{8\pi G\rho_0}{3} - kc^2 \tag{1.15}$$

If we define a critical density ρ_c such that the universe is neither open or closed and therefore the curvature k is zero, then

$$H_0^2 = \frac{8\pi G\rho_c}{3} \tag{1.16}$$

and therefore

$$\frac{\rho_0}{\rho_c} \equiv \Omega_0 = \frac{8\pi G\rho_0}{3H_0^2} \tag{1.17}$$

We can rewrite equation 1.15 in terms of Ω_0;

$$k = \frac{\Omega_0 - 1}{c^2/H_0^2} \tag{1.18}$$

This last equation shows the one-to-one correspondence between the curvature of space and the density of the universe in the absence of a Cosmological Constant. How is the rate of expansion $\dot{R}$ related to Ω_0? From equation 1.14 we can see that

$$\dot{R}^2 = \frac{H_0^2\Omega_0}{R} - kc^2 = H_0^2\left(\frac{\Omega_0}{R} + 1 - \Omega_0\right) \tag{1.19}$$

If $\Omega_0 = 1$ then $\dot{R}$ tends to zero as R tends to infinity; space is flat and the universe will asymptotically approach a limit of zero rate of expansion, without ever actually stopping expanding and recollapsing. This is known as the Einstein-de Sitter model. If $\Omega_0 < 1$ then k is negative, $\dot{R} > 0$ and the universe will expand for ever. If $\Omega_0 > 1$ then k is positive, $\dot{R} < 0$ and the rate of expansion will decrease until it reverses and the universe recollapses. We can see that the future of the universe depends on Ω_0.

We can write Ω_0 in terms of a dimensionless parameter q_0 related to R_0, $\dot{R}_0$ and $\ddot{R}_0$ where q_0 is defined as;

$$q_0 = -\frac{\ddot{R}_0 R_0}{\dot{R}_0^2} \tag{1.20}$$

Now

$$-\ddot{R}_0 R_0 = \frac{4\pi G\rho_0 R_0^2}{3} \tag{1.21}$$

and therefore, since $H_0^2 R_0^2 = \dot{R}_0^2$,

$$q_0 = \frac{4\pi G\rho_0}{3H_0^2} = \Omega_0/2 \tag{1.22}$$

This shows the relation between density (as expressed by Ω_0) and deceleration (as measured by q_0).

1.2.2 The Standard Model

The energy density of photons, and hence the corresponding temperature, was higher in the past than now by a factor $(1+z)^4$. However the density of matter varies with redshift as $(1+z)^3$. Therefore, we can see that the universe was hotter in the past, and there existed an epoch earlier than which the universe was radiation-dominated. The Standard Model asserts that the universe started as a singularity, and has been expanding and cooling since then. If ϵ_0 is the energy density of radiation in the current epoch, and ρ_0 is the density of matter in the current epoch, then

$$\frac{\epsilon(z)}{\rho(z)c^2} = \frac{\epsilon_0}{\rho_0 c^2}(1+z). \tag{1.23}$$

The ratio of radiation to mass-energy is $\epsilon_0/\rho_0 \sim 10^{-3}$ and so for $z \geq 1000$ the universe was radiation-dominated.

Coincidently, $z \sim 1000$ is also the epoch of "recombination", at which the universe became cool enough for protons and electrons to combine and form neutral hydrogen. Prior to this, free electrons and photons were highly coupled by Thomson and Compton scattering; the mean free path of the photons was very short and the universe was effectively opaque. As the universe expanded and cooled, hydrogen formed and there were no longer enough free electrons to scatter the photons. This is known as the epoch of last scattering. As the universe continued expanding and cooling to the present day the effective temperature of these photons dropped, but their distribution remained the same. In 1965 Penzias & Wilson detected these remnant photons at microwave wavelengths and showed it to have a Planckian spectrum described by a temperature of $T = 2.735K$ and have the same peak intensity to within 0.1% on all scales anywhere on the sky. This radiation was interpreted by Dicke *et al.* (1965) to be the relic of the hot big bang; its remarkable isotropy is the clearest evidence so far discovered of the isotropy of the universe. The blackbody nature of the radiation indicated that radiation and matter had once been in thermal equilibrium.

Long before the CMB was actually discovered Gamow (1946) showed that if the universe had been hotter and denser in the past then light elements such as deuterium, lithium and helium could be formed in the early universe. A crucial test, therefore, of the Standard

Model was whether, given the initial conditions, it could predict the observed abundances of these light elements. For instance, the predicted abundance of ^{4}He relative to hydrogen is $\sim 25\%$, and this is close to what is measured. Detailed simulations of conditions in the early universe by Wagoner (1973) accurately predict the relative abundances of light elements provided that $0.015 \leq \Omega_b h^2 \leq 0.026$ where h represents the dependency on H_0. (See Kolb & Turner 1990, for a review of the theory and observations on primordial nucleosynthesis.)

1.3 Quasars: Cosmological Probes into the Early Universe

The extraordinarily high luminosities of quasars enables them to be detected out to much larger distances than ordinary galaxies, so they can be used to constrain models of the early universe. Quasars have been detected out to $z = 4.89$ (Schmidt *et al.* 1991), which for $\Omega = 1$ and $H_0 = 50$, corresponds to $\approx 90\%$ of the age of the universe. Therefore accurate determinations of the quasar space density and its cosmological evolution put powerful constraints on the formation and evolution of objects in the universe. Conversely, the fact that quasars are observed at such high redshifts requires a relativistic cosmological model (as described above) as a framework in which to place the results.

In this thesis I use the standard definition of a quasar to be a very luminous galactic nucleus, ($M_B \leq -23$) which emits energy at all wavelengths from radio to x-ray, with very broad (1000's of km/s) and narrow (100's of km/s) emission lines. The magnitude cutoff is somewhat arbitrary, and arises from the observational selection criteria. Objects which fulfill all the above criteria but are fainter than $M_B = -23$ are known as Seyfert I galaxies. It is thought that quasars are a sub-set of a class of objects known as active galactic nuclei (AGN's); these galaxies all emit non-thermal radiation.

1.3.1 The Discovery of Quasars

Quasars were first discovered in 1963 when radio astronomers developed the technique of lunar occultation to give radio positions on the sky with accuracies comparable to optical positions. This enabled unambiguous identifications of the radio source 3C 273

(and others) (Schmidt 1963, Hazard *et al.* 1963) and follow-up spectroscopy showed that these apparently stellar objects were associated with large redshifts ($z = 0.158$ for 3C 273).

There was considerable controversy for some years as to whether the redshifts were cosmological; *i.e.* whether they obeyed Hubble's law. The strongest arguments advanced in favour of the cosmological interpretation used the fact that radio properties of quasars and radio galaxies were similar (the continuity argument) and the steepness of the log(N)-log(S) plot (steeper than that for a non-evolving population in a Euclidean universe) showing substantial evolution as a function of redshift.

Radio-selected samples of quasars were compiled and it was shown by Schmidt in 1968 using the $< V/V_{max} >$ test that quasars underwent strong positive evolution, in that they were either more luminous or more common in the past compared to today. This test uses the flux of the object, the flux limit of the survey and the redshift of the object to calculate the maximum redshift at which the object could be located and still be included within the survey. This maximum redshift is then used to calculate the corresponding volume surveyed to find that object, and then the ratio of the actual volume to the object to the maximum volume is calculated. For a uniformly distributed sample of objects it can be seen that the expected value of V/V_{max} is 0.5, and therefore a higher value indicates that the majority of objects within the sample are located near the volume limit of the sample and therefore the sample is evolving.

1.3.2 Optical Selection Techniques

In carrying out systematic radio surveys it was soon realised (by *e.g.* Sandage & Veron, 1965) that nearly all very blue objects near the centre of the radio position were quasars, and one could choose known quasars by virtue of their "blueness" or ultra-violet excess (UVX), and select nearly all known quasars. Furthermore, when selecting quasar candidates using this method, only a few of the resulting quasars were radio-loud. Veron (1983) measured the colours of quasars with $z \leq 2.2$ selected using a variety of techniques and showed that $\sim 95\%$ of the quasars were UVX, proving the efficacy of UVX selection. Above $z = 2.2$ the method breaks down, as the Lyα emission line is redshifted into the B

band, and the Lyα forest is in the U band. The combination of these phenomena means that the quasar is no longer UVX. This method is straightforward to implement; one applies a colour criterion to the sample of stellar objects being considered and observes all candidates bluer than a certain limit. It is also efficient in that a high fraction of blue objects selected in this way are quasars; $\sim 50\%$ at $B \sim 18$. This was shown by Shanks *et al.* (1983) who studied the clustering properties of a sample of faint stellar UVX objects, and showing them to be significantly clustered, implying that a large fraction of the sample were at cosmological distances.

Other systematic techniques of finding quasars have been developed such as scanning objective prism plates, using the shape of the continuum plus the presence of strong emission lines to detect quasar candidates (*e.g.* Clowes 1986). This method is most reliable in narrow redshift bands such as $1.8 \leq z \leq 2.5$ where Lyman-α is redshifted into the B band, but with careful detection algorithms can be used over a wide range of redshifts (e.g. for the Large Bright Quasar Survey (LBQS hereafter), Morris *et al.*, 1991 and refs therein). It has the advantage of not relying solely on the UVX properties and can therefore select quasars out to much higher redshifts than UVX selection alone. The drawback of this method is that the objects are selected on the relative strength of their emission lines compared to the underlying continuum, thus it is difficult to quantify the flux limit of the sample. However if the sample is to be used to determine the luminosity function (LF hereafter), it is vitally important that this flux limit is well determined, as the lg(N)-lg(S) relation, and hence the LF is very steep.

Quasars have been shown to be variable at optical wavelengths with observed periods of the order of a few years. Thus searching for variable stellar objects using a baseline of ~ 10 years is an efficient selection method with no obvious redshift-dependent selection effects (Hawkins 1986). It is interesting to note that the cause of the variability on these timescales has not been determined, with some workers claiming it to be intrinsic to the quasar (e.g Cristiani *et al* 1990) and others claiming it to be due to microlensing (e.g Hawkins, private communication). When combined with a UVX search, variability is capable of selecting practically all known quasars with $z \leq 2.2$ and much more efficiently than by using UVX selection alone ($80 - 90\%$ of candidates are quasars).

The UVX method can be extended by using more colour information; this is known as multi-colour selection. Due to the shape of the quasar spectrum when compared to the standard black-body spectrum, quasars are redder in V and R bands than hot blue stars. Thus by selecting candidates which are blue in U–B and red in B–R one can discriminate against hot blue O and B stars. La Franca *et al.* (1992) calculated the completeness of this method as a function of redshift by applying a multicolour selection to 200 radio-selected quasars for which they had acquired UBV photometry. They then re-selected $\sim 90\%$ of them as UVX objects, with the fraction selected as UVX varying with redshift. the minimum ($\sim 80\%$) occurred at $0.6 \leq z \leq 0.9$, due to the presence of MgII in the B band, rendering the quasar less UVX.

1.4 Previous Quasar Surveys

Quasar Surveys at $z \leq 2.2$

The main motivation behind many of these surveys was to get adequate information on the distribution of quasars in absolute magnitude-redshift parameter space, so that when parametrizing the evolution, not too many assumptions about the form of the LF and its evolution need be made. Obviously no one individual survey can equally well sample both the most and least luminous parts of the parameter space without using a prohibitively large amount of follow-up observing time, and thus surveyors tend to choose between large-area coverage of the sky to relatively bright flux limits and small-area, deep surveys.

The Braccesi survey (Braccesi *et al.* 1970) chose 175 UVX objects in 36 degs^2 down to a flux limit of $B = 19.5$. Follow-up spectroscopy was carried out to produce the AB sample (22 quasars to $B = 18.25$, Marshall *et al.*, 1983) and the BF sample (35 quasars to $B = 19.8$, Marshall *et al.*, 1984). These samples were used by Schmidt & Green (1983) in their pioneering analysis of quasar evolution, along with the Palomar-Green (PG) Survey (Green *et al.* 1986) and the Curtis-Schmidt survey (Osmer & Smith, 1977) which was the first survey to concentrate on redshifts ≥ 2.2. The PG survey consisted of double exposure Palomar Schmidt plates in U and B bands covering $\sim 10,000$degs^2 and aimed to select all UVX objects brighter than B ≤ 16.2. This made it ideal for empirically determining the

quasar LF at low redshift but the bright magnitude limit meant that it could not be used to determine the form of the evolution of the LF. Schmidt & Green used a $< V'/V'_{max} >$ analysis, in which the volumes searched are multiplied by an assumed density evolution model which is then adjusted to give $< V'/V'_{max} >= 0.5$, the expected value in the absence of evolution. This method does not necessarily give a unique fit, but it does maximise the information available in the sample. Schmidt & Green found that evolution seemed to be a function of luminosity in which the most luminous quasars at z $\sim$ 2 evolved faster than less luminous ones and they fit a luminosity-dependent density evolution model.

Density evolution was the "paradigm" until Mathez (1976) showed that the data equally well fit a pure luminosity evolution model, and Longair & Scheuer (1970) showed that for a featureless luminosity function pure luminosity evolution and pure density evolution are indistinguishable. If the LF is a power law then there is no way of knowing how the LFs at different redshifts relate to one another, i.e. whether they shift vertically (density evolution) or horizontally (luminosity evolution). The only way to resolve the problem would be to discover a "feature" in the log(N)-log(S) relation and trace the corresponding feature in the luminosity function as a function of redshift. Thus the faint survey by Koo & Kron (1982) which showed that the number-count relation for quasars fainter than B $\geq$ 19 did not continue rising steeply as for brighter quasars but became flatter, was used to rule out pure density evolution (Marshall *et al.* 1983) which predicted a featureless number count relation. However the Koo-Kron faint survey consisted of only $\sim$ 40 quasars with confirmed redshifts and thus was not large enough by itself to determine accurately the shape of the LF and its evolution.

There was clearly a need for a large sample of faint quasars to confirm the Koo-Kron result and also to determine uniquely the LF and its evolution. With the advent of multi-fibre and multi-slit instruments enabling observers to gather data simultaneously on many objects, it became possible to construct large samples of faint objects without using prohibitively large amounts of telescope time. The AAT survey (Boyle *et al.*, 1988 hereafter BSP, Boyle *et al.*, 1990) was the first quasar survey to make use of multi-fibre instruments, specifically FOCAP on the Anglo-Australian Telescope. This survey consists of data from 34 $\times$ 0.35degs^2 areas, selected from Schmidt plates scanned and measured by COSMOS and calibrated using photoelectric, CCD and electronographic sequences.

The accuracy in the final data set varied as a function of magnitude and was $\sim$ 0.15 mags at B $\sim$ 21. Candidates were selected on their U–B colours, (the cut-off varied from area to area) and then observed with FOCAP. This survey was a follow-up to an earlier smaller single-slit survey at brighter magnitudes (B $\leq$ 19) (Boyle *et al.* 1985) and thus the FOCAP areas were centred on known quasars. The final sample consisted of 420 quasars down to B $\sim$ 21 (the completeness limits varied from field to field).

This sample was used to confirm the presence of the break in the n(m) relation. BSP calculated the LF in four redshift bins out to z = 2.2 using this, as well as other brighter surveys in order to sample the luminous end of the LF. The break showed up in each redshift bin and appeared to move to higher luminosities as redshift increased. The shape and normalisation of the LF appeared to stay constant as a function of redshift. BSP fit a variety of models to the LF and its evolution using the maximum likelihood formulation of Marshall *et al.* (1984) and concluded that the best fit model was Pure Luminosity Evolution (PLE) in which the shape of the LF was parametrised by two power-laws crossing over at higher luminosities at higher redshifts;

$$\phi(\mathrm{M},\mathrm{z}) = \frac{\phi^*}{\left[10^{0.4(\alpha+1)(\mathrm{M}-\mathrm{M}^*(z))} + 10^{0.4(\beta+1)(\mathrm{M}-\mathrm{M}^*(z))}\right]} \tag{1.24}$$

where α, β are the indices of the LF and M^* evolves with respect to (1+z);

$$\mathrm{M}^*(z) = \mathrm{M}_0^* - 2.5k\log_{10}(1+z) \tag{1.25}$$

PLE can be interpreted as either representing the *actual* evolution of individual objects in which a single population of quasars formed at one epoch and have been growing dimmer ever since, or as the *statistical* evolution of the properties of successive populations of objects, in which each generation of objects is dimmer than the previous one. The latter implies a conspiracy between birth and death rates, in order to conserve the total numbers of objects. It also predicts an increase in the numbers of very faint quasars as redshift decreases due to large numbers of quasars "piling up" at the faint end of the low redshift LF, which was not seen, although this could be due to incompleteness in the AAT survey. As a result, workers have tended to favour the long-lived hypothesis.

Boyle, Jones & Shanks (1991) have constructed a faint survey consisting of 66 quasars out to $B = 22$, and Zitelli *et al.* (1992) have completed a similar survey of 54 quasars to $B = 22$. Both surveys used multicolour techniques to select candidates, and Zitelli *et al.* also used grism and variability searches. Because of this, both surveys are complete up to $z = 2.9$. Boyle (1991) used these surveys together with other brighter ones to remodel the luminosity function and its evolution. The best-fit LF was still a two power-law model, evolving solely in terms of luminosity, but now because of the extra constraints at higher redshift, there is a redshift cutoff in the model beyond which the LF does not evolve. The evolution is modelled similarly to the 1988 BSP model;

$$M_B(z) = M_B(0) - 2.5\log_{10}(1+z) \tag{1.26}$$

for $z \leq z_{max} = 1.9$ and

$$M_B(z) = M_B(z_{max}) \tag{1.27}$$

for $z > 1.9$.

The majority of surveys discussed above used the UVX method to select quasars; an exception is the Large Bright Quasar Survey (LBQS) (Morris *et al.* 1991 and references therein) which used automatically scanned objective prism plates covering $\sim$ 450degs^2 down to B = 18.85 and claims to be complete out to z = 3.4. Objective prism surveys have proved unpopular in the past, as they produce obvious incompleteness at certain redshifts where no strong emission lines are present in the waveband used for prism plates. LBQS claim to circumvent this problem by using the shape of the continuum as well as the presence of lines. Very strong lines will, however, be saturated and thus not appear on the plates, and so they estimate that this survey is not complete at B $\leq$ 16.5.

The final LBQS sample consists of 1052 AGNs. Recently, Hewett *et al.* (1993) have used this sample to calculate the LF out to z = 2.2 and compare it to PLE. They find a deficit of quasars at the faint end, and an excess at the luminous end of each LF in each redshift bin, and find that the slope of the LF for luminous quasars decreases as redshift decreases, thus ruling out PLE as the best-fit model to the evolution.

Hawkins & Veron (1993) have used the observed variability of quasars to select a sample from a sequence of Schmidt plates spanning a baseline of 10 years. This sample consists of 48 quasars in an area of 2degs^2 out to $z \approx 3$. LFs were constructed in three redshift bins in the range $0.7 \leq z \leq 2.2$ and compared to the AAT survey. Contrary to the findings of BSP, the LF in all bins was a featureless power-law, and the variability-selected sample showed a higher space density than the AAT sample at the faintest luminosities sampled in each bin. Hawkins & Veron suggest that this could be due to incompleteness in the AAT sample, and point out that although the UVX method is an efficient method of selecting quasars, care must be taken to calibrate the data accurately if the final sample is to be complete.

Quasar Surveys at $z \geq 2.2$

Historically, because of the relative ease of selecting quasars with $z \leq 2.2$, there has been a division between our knowledge of the space density of quasars with $z \leq 2.2$, and of higher redshift quasars. At very high ($z \geq 3.4$) redshifts, there has been considerable controversy, with some workers claiming a constant space density and no evidence of a turnover, and other workers claiming a strong decrease in the space density.

The Curtis-Schmidt survey (Osmer & Smith 1977) used objective-prism data to detect quasars in the range $1.8 \leq z \leq 3.4$ on the basis of their Lyα emission. This survey found 13 quasars with $z \geq 2.2$, demonstrating for the first time that there was no sharp cutoff in the space density of quasars above $z \sim 2.2$, as had been previously thought, but rather the space density seems to be constant in the range $1.8 \leq z \leq 3.25$. The expectation was that the selection technique being used, namely selecting candidates off either direct or objective prism plates using IIIa-J emulsion with its red cutoff, was responsible for no quasars being selected with $z \geq 3.4$. However even when IIIa-F emulsion (which has a redder response) was used, and which could in principle select quasars out to $z = 4.7$, none were found by 1982 (Osmer 1982), leading workers to believe that they really had found the true cutoff in quasar activity.

However Hazard & McMahon (1985) found two bright quasars with $z = 3.4$ and $z = 3.7$ from visual inspection of objective prism plates, and follow-up work by Hazard *et al.*

(1986) showed that the apparent cutoff in space density at high redshift was in reality more of a gradual decline. However, this work was carried out by eyeball searches, making the results hard to assess, i.e. the flux limit of the search was not well quantified, and so the results were not very useful for trying to quantify the rate of evolution at high redshifts.

At this time other workers were developing the multi-colour technique of systematically searching for high-redshift objects. The basic idea is that information from Schmidt plates in the bands $UBVRI$ is used to calculate the colours of objects and then the distance of objects to the main-sequence stellar locus is calculated in 4D colour space. Objects with extreme red colours such as high-redshift quasars will therefore stand out a long way from the locus and be selected. This method was used with great success by Warren *et al.* (1989) to find 53 quasars with $z \geq 3.0$. Warren *et al.* showed that the space density of quasars stays constant out to $z \sim 4.5$. Mitchell *et al.* (1990) used the Edinburgh survey and the multicolour technique to search for bright high redshift quasars, and found three in the range $3.4 \leq z \leq 4.1$ with $M_B \sim -28$. They used this to show that the space density of quasars in this redshift range agrees with that at $z \sim 2$, showing a strong decrease in the rate of evolution between $2.2 \leq z \leq 4.1$.

Schmidt, Schneider & Gunn (1991, and references therein) used a completely different method to search for high redshift quasars. They carried out a transit grism survey using a large-area CCD (the 4-shooter CCD camera, which gives continuous read-out) with narrow-band filters to search for objects with Lyα or CIV emission lines, thus they are sensitive to quasars in the range $2 \leq z \leq 4.7$. They only detect objects with emission lines greater than a certain equivalent width (50$\mathring{A}$ in the case of Lyα), which has led to accusations of incompleteness (e.g. Irwin *et al.*, 1991). This survey has has 141 quasars. Preliminary analysis (Schmidt *et al.*, 1991) shows that the space density of quasars with $2 \leq z \leq 3$ is roughly constant, but for $3 \leq z \leq 4.7$ it declines steeply.

The findings of Schmidt *et al.* are in conflict with those of Warren *et al.* (1989) who find a higher space density. However the picture is complicated by the small numbers of objects in each survey, and the necessity to bin over wide ranges in redshift. If the luminosity function flattens at $z \sim 4$ then the space density of faint quasars will decline faster than

that of more luminous quasars, thus reconciling Schmidt *et al.*'s results with those at higher luminosity. Alternatively, the discrepancy between the surveys could be due to Schmidt *et al.* selecting by the presence of emission lines. This could cause increasing incompleteness with redshift in the case of Lyα, because absorption due to intervening clouds (the Lyα "forest") will mean that the equivalent width will decrease with increasing redshift. Schmidt *et al.* argue that this is not important as Lyα always has such a large equivalent width.

The accurate measurement of the space density of very high-redshift quasars is important not just for the determination of the correct form of quasar evolution, but also because it can put interesting constraints on galaxy formation in general. Efstathiou & Rees (1988) estimated the mass of an object needed to host a luminous quasar at $z \sim 4$ in a Cold Dark Matter universe, and concluded that this model could just explain the observed density of high redshift quasars provided that the individual lifetimes were much shorter than the Hubble time, otherwise the mass of the black hole needed to fuel the quasar will be far too big to have formed so early on in the history of the universe.

To summarize, until the Hawkins & Veron and the LBQS samples were published, PLE seemed to be a good fit to the data out to the highest redshifts sampled, although with a much reduced rate of evolution for quasars with $z \geq 2$. Now, however, the picture looks much less clear-cut, and it seems that the LF changes shape as a function of redshift for $z \leq 2$. The Hawkins & Veron result makes the picture look even more pessimistic; if this result is correct then the LF is a featureless power-law and we have no way of distinguishing between different evolutionary models.

1.5 Thesis Aims

As described above, the accepted model to quasar evolution is Pure Luminosity Evolution (PLE). This model was fitted using a number of samples, but only one of them (the Palomar-Green survey; Schmidt & Green 1983) attempted to measure the space density of very luminous quasars, and this survey is thought to be very incomplete (e.g. Wampler & Ponz 1985). If this is so, then this could have repercussions for the PLE model.

In this thesis I describe recent work on the Edinburgh Multicolour Survey and how it has been used to select a complete sample of bright quasars and determine their space density as a function of cosmological epoch. I describe the calibration of the dataset in chapter 2, and the selection and spectral observations of the UVX candidates in chapter 3. I then compare the surface density of bright quasars as measured by the Edinburgh and the Palomar-Green surveys in chapter 4. In chapter 5 I use a variety of statistical methods to compare the PLE model with the Edinburgh and the AAT surveys (Boyle *et al.* 1990). Finally I discuss the implications of the observed space density and its evolution for theories of galaxy formation, quasar lifetimes and unification schemes. I make suggestions for future work.

Chapter 2

The Construction of the Edinburgh Survey

2.1 Introduction

In this chapter I summarise the process of acquiring photographic plates used in the Edinburgh Survey from the U.K. Schmidt telescope and measuring these plates automatically on the COSMOS measuring machine. I briefly discuss previous work on the calibration of the resulting dataset, using photoelectric and CCD photometry and morphological analysis. I then describe in more detail the work carried out within each field, to reduce the existing systematic errors in the measured magnitudes, and also in the survey area as a whole, to reduce the magnitude offsets between the fields, to ensure that the fields are consistently and uniformly zero-pointed. The main aim is to produce a dataset that is sufficiently accurately calibrated such that it can be used to select a complete sample of bright quasar candidates.

2.1.1 Acquisition of plate material from the U.K. Schmidt Telescope.

The Edinburgh survey is constructed from 130 photographic plates taken in 5 wavebands U, B_J, V, R, I covering ~ 0.1 steradians (330 degs^2) of sky. The plates were taken on the U.K. Schmidt telescope (U.K.S.T.) at the Anglo-Australian Observatory from 1985 to 1988 before the start of this thesis. The region of the sky chosen is equatorial so that it can be easily accessed for follow-up work by telescopes in both hemispheres, and is at high galactic latitude $b \geq 50°$, so that galactic extinction is always less than $E_{B-V} = 0.03$ magnitudes (Burstein & Heiles, 1982).

The Schmidt telescope design is unique in that it has a large field-of-view ($\approx 6.4° \times 6.4°$ in the case of the U.K.S.T.) and, as such, has been of crucial importance in the construction of all-sky databases. The large field-of-view is achieved by use of a spherical mirror with an achromatic corrector lens at the aperture of the telescope, meaning that images in the whole field-of-view are free from aberration. Thin glass plates are loaded into the curved focal plane of the telescope, and exposed for variable times, depending on which filter is being used. Standard Schmidt field centres are 5° apart on the sky, so that there is considerable overlap between fields. See Mitchell (1989, PSM hereafter) for a complete list of all Schmidt plates used in this survey.

Field effects

Field effects are principally caused by two phenomena;

a) Differential atmospheric refraction, and

b) Variations in sensitivity of the photographic emulsion across each Schmidt plate.

The former occurs because different parts of each Schmidt field are at different zenith distances and therefore undergo differing amounts of atmospheric refraction. The effect of this is to compress the apparent size of the field. This is further complicated by the fact that each exposure takes a finite length of time and so the hour angle and hence the zenith distance vary during the exposure. Also, the field will rotate about the polar axis, i.e the parallactic angle varies during the exposure. The combined effect means that images on the plate will be trailed, the effect becoming more pronounced the further away from the

plate centre the image is. (See Wallace & Tritton, 1979, for a detailed description of the effects of differential atmospheric refraction on images on Schmidt plates.) The effect is also wavelength dependent, because at shorter wavelengths the effect of atmospheric refraction increases, and also because the corrector lens is not truly achromatic over the whole wavelength range covered by the Edinburgh survey.

Variations in sensitivity of the photographic emulsion across the plate mean that parts of the plate will detect fainter images than other parts of the plate, and thus the true flux limit of the survey will be unknown although, again, this can be compensated for by dividing by the local sky background.

It can be seen therefore that if the aim of the survey is to detect a complete sample of point-like objects, as is the case here, then it is paramount importance to try to minimise the field effects. Accordingly much of this chapter is concerned with the detection and reduction of field effects in the Edinburgh survey.

2.1.2 The COSMOS automatic plate measuring machine

COSMOS is an automatic flying-spot micro-densitometer measuring machine which gives information on the relative intensity and morphology of objects on photographic plates, as well as astrometry.

The plates are loaded into the machine and scanned by a light spot of varying size produced by a cathode ray tube. The intensity of the transmitted light is measured by a photomultiplier and compared to a reference beam which has not been passed through the plate, to find the relative transmission. The spot is moved in the x direction whilst the plate is moved in the y direction. Scanning is carried out in "lanes" until the whole measurable area ($5.35^\circ \times 5.35^\circ$) has been scanned. What happens next with this information depends on which of the two modes of measurement have been chosen. In mapping mode (MM), the transmission values of all the pixels are recorded for future analysis. This requires enormous amounts of storage space, and in practice is not needed for the majority of astronomical applications. In image analysis mode (IAM) the sky background of the plate is first determined by a low-resolution scan, and then the plate is scanned

again. This time a threshold intensity value is applied so that only pixels with intensities brighter than some threshold are stored. If stored pixels are found to be connected then they are joined up into single objects and the total intensity value for this object is stored. The threshold value is defined as a percentage of the sky (and was usually set at about 7% for this work) and there is also an area threshold, in that only objects larger than a certain number of pixels (in this case, 3) are recorded. All the information about the intensity and morphology of each object is then obtained from this database. Astrometry is carried out by calculating a transformation between measured x and y coordinates to known R.A. and declination coordinates of standard stars from the S.A.O. (Smithsonian Astrophysical Observatory Star Catalogue, 1966). The positional accuracy is 0.3 arcsecs (MacGillivray & Stobie, 1984).

Image classification using COSMOS

The main morphological requirement for the quasar survey is that we not only wish to exclude genuine galaxies, but also blended images, which would have peculiar colours and contaminate the candidate lists. Amongst the parameters that COSMOS produces for each object are IMAJAX and IMINAX, the intensity-weighted major and minor axes. The ellipticity of each object can therefore be defined as the ratio of these parameters (the axial ratio parameter; b/a, b is the minor and a is the major axis), and this can be used to discriminate between stellar and extended objects. For stars, the ratio should ideally be unity, however this is not true for faint stellar images , i.e. the mean value of b/a decreases as intensity decreases. This is because of random noise, meaning that pixels are erroneously detected and therefore make a comparatively larger contribution to the measured intensity of an image as the signal-to-noise decreases. Therefore a more useful measure of ellipticity is one which is divided by the noise at a given area;

$$\sigma_A = \frac{\overline{b/a} - b/a}{1 - \overline{b/a}} \tag{2.1}$$

where $\overline{b/a}$ is the mean axial ratio at any given area, and $1 - \overline{b/a}$ is a measure of the noise. Typically a value of $\sigma_A = 1.5$ was chosen, from PSM's work (1989) showing that this excluded most extended images.

Other COSMOS parameters used in image classification were AREA; the total area of an object (i.e. the number of pixels in that image above the threshold value) and IMAX; the maximum intensity of an object. For a given total intensity a galaxy will have a larger AREA and a smaller IMAX value than a star. Again, the effectiveness of these parameters varies with magnitude, AREA is useful at bright magnitudes and less effective at faint magnitudes because of random noise. IMAX is more useful at faint magnitudes than AREA, because it is a measure of the *peak* intensity of the image, and therefore, for a given overall intensity, will have a higher signal-to-noise ratio than AREA. The magnitude ranges over which each parameter is effective can be estimated simply by plotting each parameter versus magnitude for the whole dataset.

2.1.3 Previous work on the Edinburgh survey

Previous work on the Edinburgh survey was carried out by P. Mitchell from 1985 to 1989, what follows is a brief summary of what he achieved and the status of the survey when I took over from him in 1989.

The two plates taken in each waveband were paired up, in that only the objects in common with both plates were stored. It was found necessary to derive a coordinate transformation between the plates; this was done using the 40,000 brightest images on the plates, and then applying half the transformation to each plate. In practice, the transformation required was always linear. This process of pairing the plates in each waveband eliminated any spurious detections that might occur on single plates, and which would contaminate the candidate lists, and also reduced the error on the measured magnitudes.

The main problem, when transforming machine measured COSMOS magnitudes to a standard system is that the relationship between COSMOS magnitudes and "true" magnitudes is non-linear and dependent on many factors. For instance at bright magnitudes the COSMOS measurement is "saturated" and so the true intensity of the object is underestimated. This is because the light spot in COSMOS gets partially scattered by the photographic plate and some of this scattered light will always be detected, and therefore the intensity of the image will be underestimated. Because of the complicated nature of this relationship, and its dependence on image structure (i.e. it will be worse for point-like

images than for extended images) it had to be determined separately for each plate.

The n(m) relation for the datasets was smoothed by forcing it to onto the Bahcall-Soneira (1980) model of the galaxy. This model was used to predict stellar number counts at the galactic coordinates of this survey. This smoothed n(m) relation was used to calculate "pseudo" magnitudes for the calibrating data and then a spline fit was used to transform the COSMOS data onto these pseudo magnitudes. This step ensured that the final transformation applied to the COSMOS data was of a much lower order and therefore much better behaved in regions with no data and at fainter magnitudes than otherwise.

The datasets were then externally calibrated using photoelectric and CCD sequences. The photoelectric sequences included standard stars and so provided an absolute calibration; the only way of determining the zero point of the COSMOS-true relation. The CCD sequences were not always taken in photometric conditions and did not always include standard stars; they also went much deeper than the photoelectric sequences. They could not be used to determine the zero point but were used to determine the *shape* of the COSMOS-true relation over a wide range of magnitudes. A low order polynomial (typically third order) was fitted to the relation between the COSMOS and the calibrating data.

Morphological analysis was carried out using the axial ratio, IMAX and AREA parameters as described above. This analysis was not only used to carry out star-galaxy separation but also to judge the level of field effects in the data. The datasets in each waveband were combined by transforming the coordinates onto those in the R band dataset.

The combined dataset was then further analysed for evidence of field effects by looking at the position of the stellar locus in colour space (e.g. $B-R$,$R-I$) as a function of position on the plate relative to the position of the locus in the central 2 degs^2 of the plate. This assumed that two wavebands R and B were free of any such systematic error, and so any shift could be applied to the third band. Star-galaxy separation was then carried out using the morphological analysis, and the resulting dataset of stellar images was deemed suitable from which to select quasar candidates.

PSM (1989) measured the accuracy of the final dataset by comparing the COSMOS mag-

nitudes on each of the two plates in each wavebands, after allowing for any systematic offsets, i.e. he calculated the rms scatter as a function of magnitude between the two plates. He concluded that the rms scatter in the mean was always less than 0.05 magnitudes for all the data brighter than two magnitudes brighter than the plate limit. However this underestimates the true error because it ignores any systematic errors such as offsets between the two plates in each waveband due to intrinsic differences in the quality of the plate material, and also offsets *between* fields, due to the plate material and also the quality and quantity of the calibrating data in each field. The remainder of this chapter is concerned with measuring and reducing offsets between plates within each field, measuring and reducing residual field effects in a more general way than that outlined above, and also reducing offsets between fields, so that the entire survey is zero-pointed consistently.

2.2 Inter-field corrections

2.2.1 Straightening the n(m) relation

The process outlined above of calibrating each field using photoelectric and CCD sequences was re-analysed. In particular, PSM's method of using the Bahcall-Soneira model of the galaxy (1980) to force the COSMOS n(m) relation to be smooth was changed to the less stringent requirement that the n(m) relation simply be a low-order polynomial. This was because of fears that being over-reliant on this particular model of the galaxy would introduce systematic errors in the calibrated dataset (See Chapter 4 for a discussion of this problem with respect to the Palomar-Green survey). A low order polynomial was fitted to the COSMOS n(m) relation up to the magnitude of the faintest calibrating star. Then the polynomial was linearly extrapolated beyond this point to the plate limit.

2.2.2 Magnitude offsets between plates in the R band

Because the R plates suffered relatively little, compared to the other wavebands, from field effects and went relatively deep; on average the plate limit in the R band was $R \approx 20$, (the I plates suffered least but the average plate limit was only $I \approx 18$) it was decided

to transform the COSMOS magnitude scales on each of the R plates in each field such that the offset between them would be zero. Once the R plates had been transformed and corrected for the low-level field effects (see next section) they would be suitable for use as a "template", to minimise field effects in other wavebands, using information on colours.

In each field the relative quality of the R plates was judged by considering the log(n)–m relation on each plate; plates which are better calibrated will show a straighter relation over a wider range of magnitudes than worse calibrated plates. The level of field effects was also considered by looking at the output from the morphological analysis program, but as mentioned above, this waveband does not suffer badly from field effects apart from a few pathological plates.

The offset between each pair of R plates was then calculated as a function of magnitude in bins of $0.01m$ using the central 2° of each plate. The offset-magnitude relation was then smoothed using a Gaussian filter (of width ~ 0.5 magnitudes on average) to ensure that the resulting n(m) relation for the corrected plates did not have any sharp features introduced as a result of this method. If there were fewer than 10 objects in each bin at bright magnitudes then the offset was extrapolated from the brightest bin with 10 or more objects in it to brighter magnitudes.

See Figure 2.1 for a diagram of the smoothed offset-magnitude relation in field 862 before and after correction. Then, using the information on the relative quality of the plates, this offset was either applied to the worst plate, or if the plates had been judged to be of similar quality, half the offset was applied to each plate. In fact, the plates were mostly judged to be of similar quality. The offset between the plates was then re-measured after the correction had been applied over the whole area of each field, not just the central 2° and always found to be less than $0.05m$ at any magnitude, for instance in field 862, the offset between the corrected plates is always less than $0.01m$.

2.2.3 Minimising field effects on the R plates

(The work described in this section was carried out by Dr. L. Miller)

The objects on each R plate were binned in bins of unit magnitude and in 12×12 bins

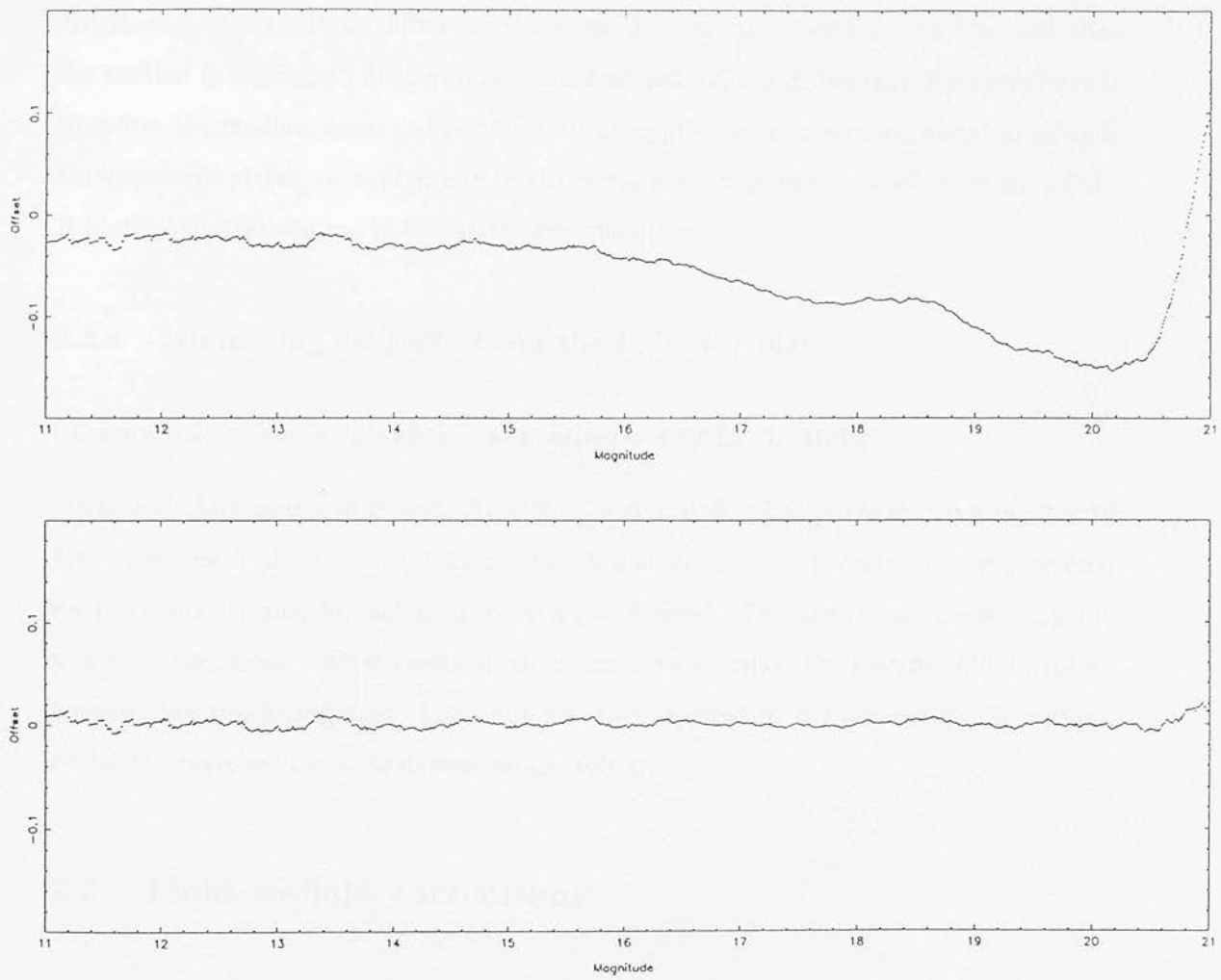

Figure 2.1: The magnitude offset between the two R plates in field 862 before (top) and after (bottom) correction. As can be seen, before the correction was applied, the offset reached a maximum of $0.15m$ at $R = 20$, and nowhere was it zero. After the correction was applied, the maximum offset was $0.01m$.

as a function of position on the plate. Cumulative distributions were constructed of the distribution of magnitude differences between the two plates within each bin, and then the median value of each distribution was calculated. The shift between the two plates is therefore the median value and so this shift as applied as a correction, either sharing it between both plates, or applying it to the worse plate depending on whether one of the R plates had been chosen to be better than the other.

2.2.4 Minimising field effects on the U, B_J, V, I plates

(The work described in this section was carried out by Dr. L. Miller)

Normalised histograms of $U-R$, B_J-R, $V-R$ and $R-I$ were constructed in 12×12 bins across each plate, and in $0.25m$ bins. A histogram in each colour was constructed for the central region in each field, covering ~ 4 degs^2. The histogram in each x, y bin was cross-correlated with the central one in order to calculate the best-fit shift in colour between the two histograms. This shift was then applied to the non-central histogram, i.e. to the waveband used to determine the colour.

2.3 Field-to-field corrections

As explained above, the relation between COSMOS and true magnitudes is unique for each Schmidt plate, due to differences in the quality of the calibrating data, the uniformity of the photographic emulsion across the plate, and the severity of field effects. Because of this and because each plate is independently calibrated (i.e. without using overlap regions with other fields, as has been done in other surveys, e.g. the APM galaxy survey, Maddox *et al.* 1990) there exist magnitude offsets between fields. The presence of these offsets means that the sample of quasars selected from each field is complete to a different limiting magnitude, and that some fields are better calibrated than others. This can be seen in the varying quality of the rms errors from field to field; if we look at the "spread" in the stellar locus due to rms errors in each field then we can see marked differences between fields. (See Figure 2.2.)

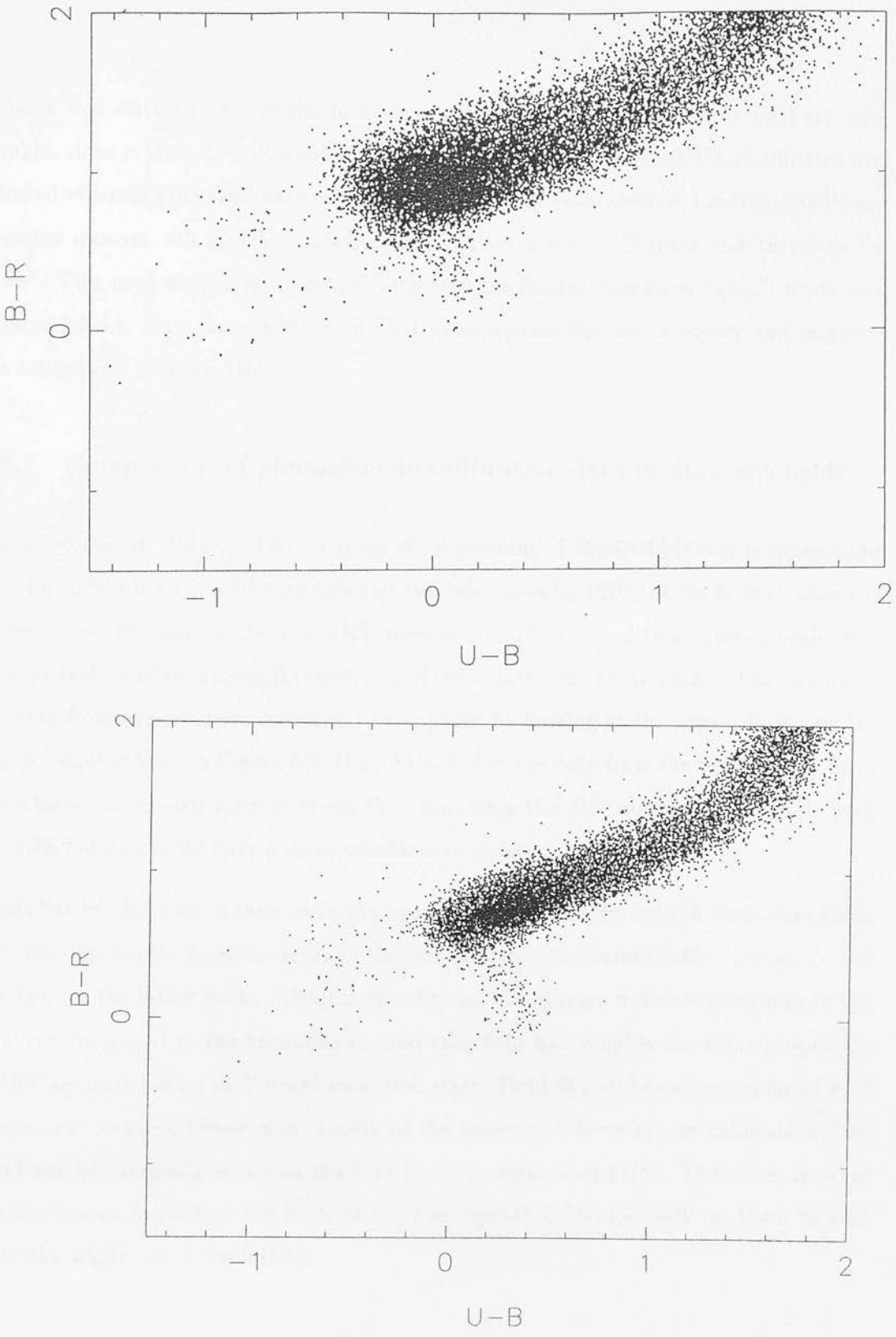

Figure 2.2: Stellar loci in colour space for fields 789 (top) and 862 (bottom). Note the difference in the spread of the loci, due to differences in the rms errors from field to field.

A large rms scatter in the stellar locus will affect the completeness of the final selected sample, since a bluer $U - B$ limit will have to be chosen when the UVX candidates are selected otherwise the candidate list will be swamped by stars scattered in from the locus. Genuine quasars will also be scattered redder than the $U - B$ limit and therefore be "lost". This next section is concerned with how the information from "good" fields was maximised, i.e. how these fields were used to zero-point the whole survey and improve the calibration in other fields.

2.3.1 Comparison of photoelectric calibration data in different fields

The photoelectric data used to tie down the zero-point of the COSMOS-true magnitude transformation in each field were taken at two telescopes by PSM; at the 60 inch Steward telescope in 1986 and at the 1 m JKT telescope in 1988. Conditions during both runs were variable, and only a small proportion of the nights were photometric. The quality of the data from the two telescopes can be compared by looking at the spread in the stellar loci in colour space, see Figure 2.3. It is obvious that the data from the Steward run have much larger associated random errors than that from the JKT run, therefore fields with more JKT data should have a more reliable zero point.

Fields 861-867 have more than twice the amount of photoelectric data in them than fields 789-794, so again the random errors on the zero points in the former fields should be much less than in the latter fields. About twice the number of stars were observed during the JKT run compared to the Steward run, and each field had roughly the same proportion of JKT-measured stars to Steward-measured stars. Field 861 still has large residual field effects, due to the intrinsic poor quality of the plates and therefore its calibration data could not be extrapolated across the field to tie in with other fields. Therefore, in what follows, it was decided to use fields 862-867 as "good" fields, i.e. rely on them to zero point the whole survey uniformly.

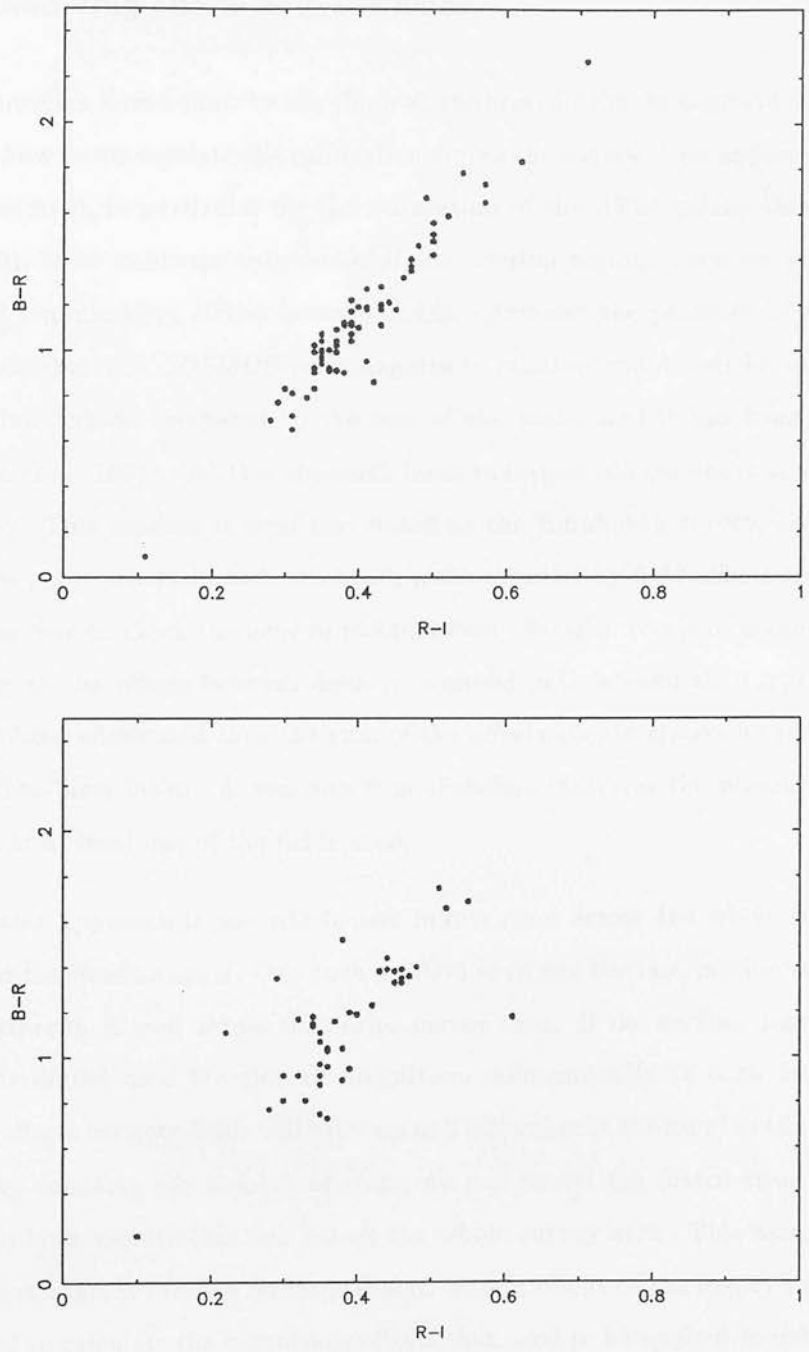

Figure 2.3: Stellar loci plotted in colour space for JKT data (top) and Steward data (bottom). Note the larger spread in the locus for the Steward data, due to the larger rms errors in the data set.

2.3.2 Minimising offsets between fields

The main problem here is how to use the well-calibrated fields to improve the rest of the survey, i.e. how to extrapolate the calibration across the survey. One approach that other workers have used, in particular for the calibration of the APM galaxy survey (Maddox *et al.* 1990), is to calibrate only some of the overlap regions between fields, thereby automatically minimising offsets between fields. However the presence of residual field effects means that the COSMOS-true magnitude relation could well be quite different in the overlap regions compared to the rest of the plate, and it has been argued (e.g. Hale-Sutton *et al.* 1991) that this approach leads to large-scale gradients across the whole APM survey. This method is even less suited to the Edinburgh survey, because we are interested in point sources which are much more affected by field effects than extended images. It is easy to check the level of residual field effects in terms of magnitude offsets, by summing all the offsets between fields in a closed path around the survey. If all field effects have been eliminated then the sum of the offsets should always be zero, no matter what path has been taken. A non-zero sum therefore indicates the presence of residual field effects in at least one of the fields used.

A much better approach is one which uses information across the whole survey region, and not just the overlap areas. One such method is to use the information on the surface density of stars measured across the entire survey area. If the surface density of stellar images is measured as a function of magnitude independently in each field, then any magnitude offsets between fields will show up as a difference in the number of stars counted. Therefore by counting the number of stars, we can model the distribution of stars and force this to be a smooth function across the whole survey area. This assumes that the distribution of stars is random on large scales. The gradient of the $\log(n)$–m relation can then be used to calculate the magnitude offsets that need to be applied to individual fields in order to achieve this.

Star-galaxy separation was carried out on the field-corrected catalogues and the objects in the resulting stellar indices were binned as a function of position in the survey (each field was divided up into 5×5 bins, i.e. roughly 1 degree square), and as a function of magnitude (in bins of unit magnitude) in each waveband. In order to be useful, this needed to be

done over a wide range of magnitudes, ideally the range of magnitudes covered should have extended to the brightest magnitudes where the photoelectric data were taken, i.e. $12 \leq m \leq 14$ in order to get a direct measure on the accuracy of the zero points as determined by these data. However at these magnitudes, there are such few objects in each field that the Poisson errors on the stellar densities and hence the associated errors in the magnitude offsets become comparable to, or larger than the actual offsets themselves. For instance, in field 789, in the magnitude range $12 \leq B_J \leq 13$ there are only 320 stellar objects in the whole field. The 99% Poisson confidence limit on this number is 54, and the slope of the log(n)–m relation in this waveband is 0.23, therefore the associated error in the corresponding magnitude offset is $0.29m$, of the same order of size (if not larger) than the expected correction. Therefore I decided to use the magnitude range $15 \leq m \leq 20$ to calculate the offsets, and I discuss later how the calculated correction was extrapolated smoothly to brighter magnitudes. The slope to the differential log(number)-magnitude relation was calculated in each waveband in each field by assuming the following;

$$\frac{d\log(n)}{dm} = \alpha m + k \tag{2.2}$$

where k is a constant, and α is the gradient.

In each magnitude slice, a low-order 2-dimensional polynomial was fitted to the stellar number counts as a function of R.A. and dec. Because of the shape of the survey it was found necessary to fit to a higher order in the R.A. direction than in the dec. direction. A variety of polynomials of different orders were fitted to the data using a NAG routine (F04ATF) to solve for the polynomial coefficients in the following equation;

$$\log(n) = \sum_{i=0}^{n}\sum_{j=0}^{m} a_{ij}x^i y^j \tag{2.3}$$

where log(n) is the log of the number of stars in each bin, x and y are the spatial coordinates (corresponding to R.A. and dec. respectively) and $n > m$. This was solved using least-squares by inverting the following matrix, where the double summation signs mean that the data are being summed over all fields in the survey, and the single summation signs mean that the data are being summed for individual fields, i.e. to solve for the zero point term in that field, where $a_{00i=1-13}$ are the zero point terms for each of the 13 fields.

$N_{i=1-13}$ is simply the number of data points used in each bin i.e. 25. The matrix below represents equation 2.3 where $n = 2, m = 1$. The equation was solved in each magnitude bin in each waveband.

$$\begin{pmatrix} \sum\sum x^4y^2 & \sum\sum x^4y & \sum\sum x^3y^2 & \sum\sum x^3y & \sum\sum x^2y^2 & \sum_{i=1} x^2y & \sum_{i=2} x^2y & \cdots \\ \sum\sum x^4y & \sum\sum x^4 & \sum\sum x^3y & \sum\sum x^3 & \sum\sum x^2y & \sum_{i=1} x^2 & \sum_{i=2} x^2 & \cdots \\ \sum\sum x^3y^2 & \sum\sum x^3y & \sum\sum x^2y^2 & \sum\sum x^2y & \sum\sum xy^2 & \sum_{i=1} xy & \sum_{i=2} xy & \cdots \\ \sum\sum x^3y & \sum\sum x^3 & \sum\sum x^2y & \sum\sum x^2 & \sum\sum xy & \sum_{i=1} x & \sum_{i=2} x & \cdots \\ \sum\sum x^2y^2 & \sum\sum x^2y & \sum\sum xy^2 & \sum\sum xy & \sum\sum xy^2 & \sum_{i=1} y & \sum_{i=2} y & \cdots \\ \sum_{i=1} x^2y & \sum_{i=1} x^2 & \sum_{i=1} xy & \sum_{i=1} x & \sum_{i=1} y & N_{i=1} & - & - \\ \sum_{i=2} x^2y & \sum_{i=2} x^2 & \sum_{i=2} xy & \sum_{i=2} x & \sum_{i=2} y & - & N_{i=2} & - \\ \vdots & \vdots & \vdots & \vdots & \vdots & - & - & \ddots \end{pmatrix} \times \begin{pmatrix} a_{21} \\ a_{20} \\ a_{11} \\ a_{10} \\ a_{01} \\ a_{00i=1} \\ a_{00i=2} \\ \vdots \end{pmatrix}$$

$$= \begin{pmatrix} \sum\sum \log(n)x^2y \\ \sum\sum \log(n)x^2 \\ \sum\sum \log(n)xy \\ \sum\sum \log(n)x \\ \sum\sum \log(n)y \\ \sum_{i=1} \log(n) \\ \sum_{i=2} \log(n) \\ \vdots \end{pmatrix}$$

The goodness-of-fit of the model was tested externally by looking at the average difference between the model and the data over the whole survey and also internally by looking at the variance in the calculated zero points a_{00}. Ideally all the zero points should be identical and any true variation in the stellar number counts from field to field should be described by the higher order terms in the polynomial. Any evidence of a correlation with zero point term and position of field in the survey indicates that the wrong order polynomial is being used. Below are the averaged rms deviations over the whole range of magnitudes used ($15 \leq B_J \leq 20$) for the B_J band for each polynomial fit to the data; this was considered to be the most important waveband to test, since it is the one from which quasar candidates are actually selected so significant errors in the calibration of this band would result in significant errors in the surface density of quasars detected by this survey.

On the basis of the rms scatter in the zero points and also the differences between the

model and the data, it was decided to use the polynomial $\log(n) = \sum_{i=1}^{2} \sum_{j=0}^{1} a_{ij} x^i y^j$ to correct the catalogues. The corrections were calculated in the following way; the average zero point and the average gradient of the $log(n)$–m relation in each waveband were calculated using the "best" fields as defined above. For each field, the difference between its zero point and the average zero point was calculated and converted into a magnitude offset;

$$\Delta m_i = \frac{a_{00i} - \overline{a_{00}}}{\overline{\alpha}} \tag{2.4}$$

where Δm_i is the magnitude offset for field i, aa_{00i} is its zero point, $\overline{a_{00}}$ is the average zero point, and $\overline{\alpha}$ is the gradient of the $\log(n) - m$ relation in the appropriate waveband in the fields used to find the best fit zero points. Δm_i is calculated in bins of unit magnitude and so it needs to be smoothed somehow, otherwise the correction applied will be "quantised" in bins of unit magnitude and the number-magnitude distribution will be similarly distorted.

It was decided to fit a low-order polynomial to the Δm – magnitude relation, and to use this polynomial only in the magnitude range $15 \leq m \leq 20$, i.e. where it was directly constrained by the data. This was because of fears that it might be unreliable in regions where no offset data existed. The offset calculated in the bin $15 \leq m \leq 16$ was extrapolated to brighter magnitudes, and then in order to ensure a smooth transition between this extrapolation and the polynomial, the whole relation over all magnitudes was smoothed with a gaussian filter of width 2 magnitudes.

A formal goodness-of-fit test was not carried out to see if the polynomial fit to the Δm – magnitude relation was a good description of the data, as the scatter on the data was large and a quick test by eye ensured that the polynomial looked reasonable.

See Figure 2.4 for a typical example of how the smoothed polynomial compares to the actual data.

After the catalogues had been corrected using this method, they were checked in the following ways;

1. By calculating the magnitude difference between the corrected COSMOS magnitudes

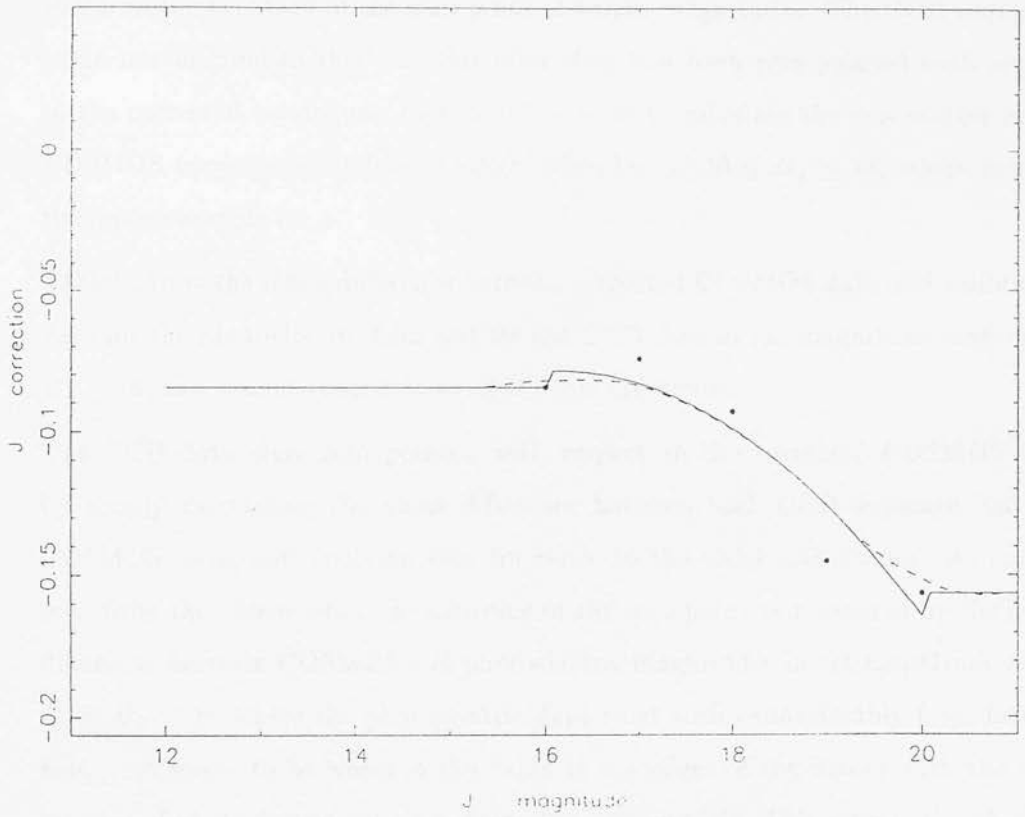

Figure 2.4: Magnitude corrections as a function of B_J magnitude for field 792. The points are the data, the solid line is the polynomial fit to the data, and the dashed line is the Gaussian smoothing of the polynomial and represents the final correction made to the data.

and the photoelectric magnitudes for the calibration stars, this enabled an *absolute* check on the accuracy of the zero point at bright magnitudes. The CCD sequences could not be used in this way, but after they had been zero-pointed with respect to the corrected catalogues, they could be used to calculate the rms scatter in the COSMOS magnitudes at fainter magnitudes, i.e. at $16 \leq B_J \leq 18$, where most of the quasar sample is.

Table1 shows the mean difference between corrected COSMOS data and calibrating data for the photoelectric data and for the CCD data in the magnitude range $16 \leq B_J \leq 18$, and also the rms scatter about this difference.

The CCD data were zero pointed with respect to the corrected COSMOS data by simply calculating the mean difference between each CCD sequence and the COSMOS data, and applying this difference to the CCD magnitudes. As can be seen from the above table, the accuracy of the zero point as measured by the mean difference between COSMOS and photoelectric magnitudes in the magnitude range $12 \leq B_J \leq 14$ where the photoelectric data exist varies considerably from field to field, and seems to be worst in the fields at the edges of the survey with the least amount of photoelectric data, i.e. fields 789, 790 and 794. This reflects the absolute accuracy of the calibrated COSMOS magnitudes with respect to *external* calibration. For the CCD data, the mean difference between the COSMOS data and the CCD data is nearly always consistent with zero, as one would expect because the CCD data have been zero-pointed with respect to the COSMOS data.

The rms scatter for both magnitude ranges is fairly constant from field to field and consists of the combined scatter on both the COSMOS data and the calibrating data, although the scatter on the COSMOS data probably dominates. This scatter reflects the *internal* error and shows that it is of the order of $0.13m$ for data in the brighter magnitude range and of the order of $0.09m$ for data in the range $16 \leq B_J \leq 18$. This possibly reflects COSMOS's poorer performance at bright magnitudes as discussed above. See Appendix A for diagrams showing COSMOS data versus calibration data in each field.

2. We can look at the position of the stellar loci in colour space from field to field and this shows that the positions are more consistent than before the field-to-field

Field	Mean difference for pe. data	RMS error for pe. data	Mean difference for CCD data	RMS error for CCD data
789	-0.43 ± 0.06	0.14	0.04 ± 0.06	0.14
790	-0.24 ± 0.14	0.34	0.07 ± 0.05	0.13
791	-0.02 ± 0.07	0.13	-0.03 ± 0.01	0.04
792	0.03 ± 0.02	0.04	0.02 ± 0.09	0.12
793	-0.09 ± 0.06	0.16	-0.08 ± 0.05	0.06
794	0.03 ± 0.31	0.53	0.03 ± 0.05	0.05
861	0.04 ± 0.04	0.14	0.00 ± 0.06	0.18
862	0.00 ± 0.03	0.09	-0.05 ± 0.01	0.04
863	0.02 ± 0.03	0.11	-0.02 ± 0.03	0.09
864	-0.02 ± 0.03	0.10	-0.01 ± 0.03	0.09
865	0.06 ± 0.02	0.08	0.00 ± 0.01	0.04
866	0.16 ± 0.02	0.11	0.05 ± 0.06	0.09
867	0.33 ± 0.02	0.09	0.01 ± 0.01	0.04

Table 2.1: This table shows both the absolute and relative errors for the final calibrated datasets in each field. The second column shows the absolute difference between the COSMOS data and the photoelectric data. The third column shows the rms scatter for the COSMOS data used to define the absolute difference. The fourth and fifth columns show the absolute difference between the COSMOS data and the CCD data (which is nearly always consistent with zero, as explained in the text) and the rms scatter of the COSMOS data used to define this difference.

corrections were applied. For the uncorrected catalogues, the positions of the loci often differed by up to $0.5m$ from field to field, representing the offsets between the fields. By comparing the measured position of the stellar locus in each field in $U-B, B-R$ colour space with theoretical colours derived by Johnson (1966), we can get a rough idea of the error on the absolute accuracy of the COSMOS data at faint magnitudes. For instance A0 stars, by definition, have colours equal to zero. If we look at the stellar loci in all the fields (Figures 2.5 to 2.11) we can see that in most cases the beginning of the horizontal branch (which is dominated by A0 stars) has colours consistent with zero, indicating that there is no significant error in the absolute calibration of the colours. The exception to this is field 790 which appears to have too blue colours.

3. To make sure that the correction applied to each field was indeed smooth, the number - magnitude distribution was inspected for each field to see if any sharp features had been introduced as a result of this method. See Figures 2.12 to 2.15 for differential $\log(n)$–m distributions in the B_J band for each field. As can be seen, up to the plate limit, the distributions are always smooth.

To summarise, the mean difference between the corrected COSMOS data and the photoelectric data at bright magnitudes for the whole survey showing the absolute accuracy of the calibration with reference to an external standard is $-0.01 \pm 0.19m$. The mean rms scatter at bright magnitudes for the whole survey is $0.13m$ and at faint magnitudes is $0.09m$, showing the internal accuracy of the COSMOS data, i.e. the scatter about the relationship between COSMOS and "true" magnitudes. This shows that the absolute accuracy of the calibration in the survey as a whole is good, with no systematic offsets, although some individual fields do still have residual offsets. These offsets seem to decrease at fainter magnitudes, as measured by the position of the horizontal branch in colour space. This is possibly due to COSMOS's better performance at fainter magnitudes. The internal accuracy is excellent, particularly at faint magnitudes, where the majority of the quasars are. These internal errors can be compared to those derived for other surveys, e.g. the AAT survey (Boyle et al., 1990) and are smaller than those quoted there (typically $0.2-0.3m$).

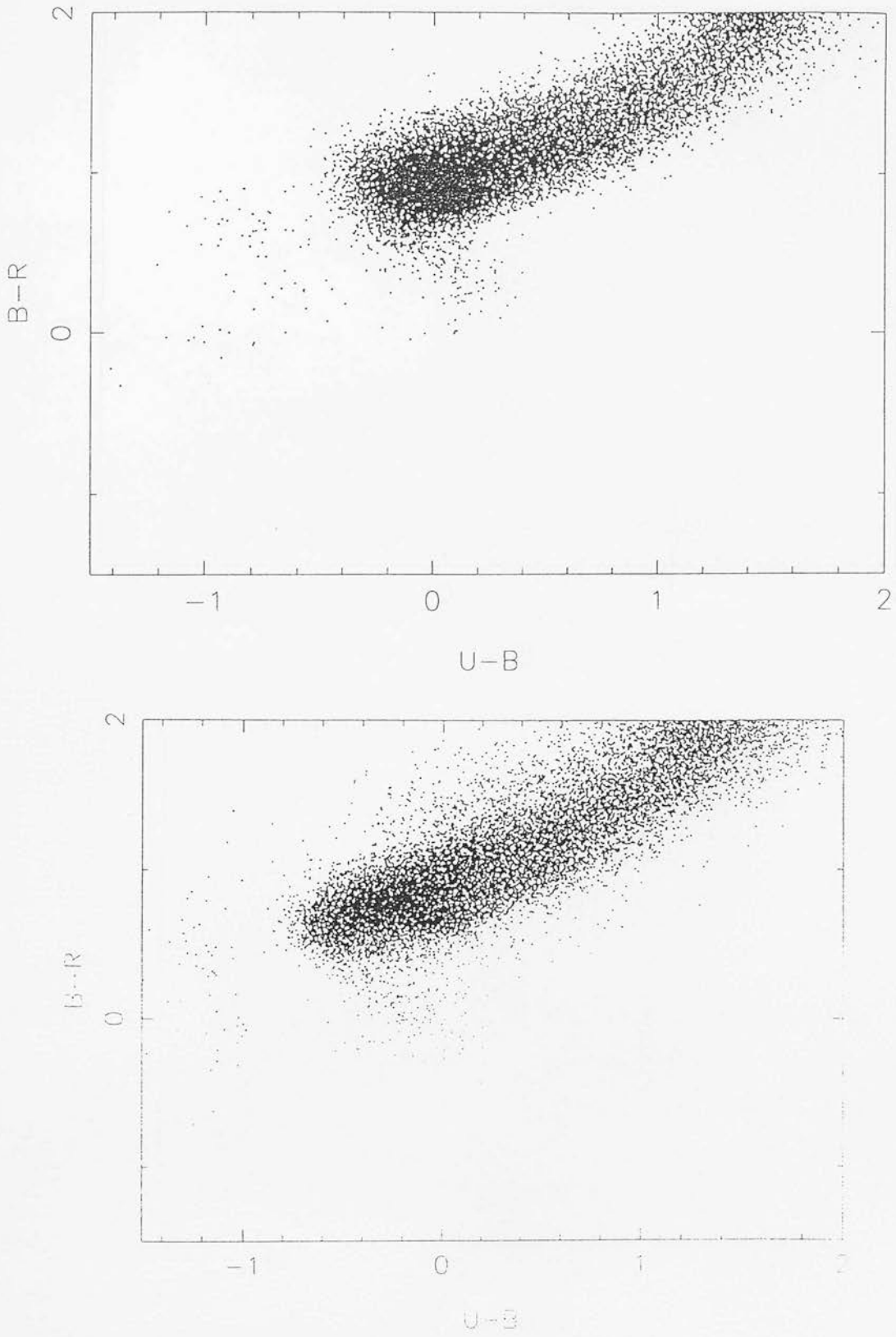

Figure 2.5: Stellar loci for fields 789 (top) and 790 (bottom)

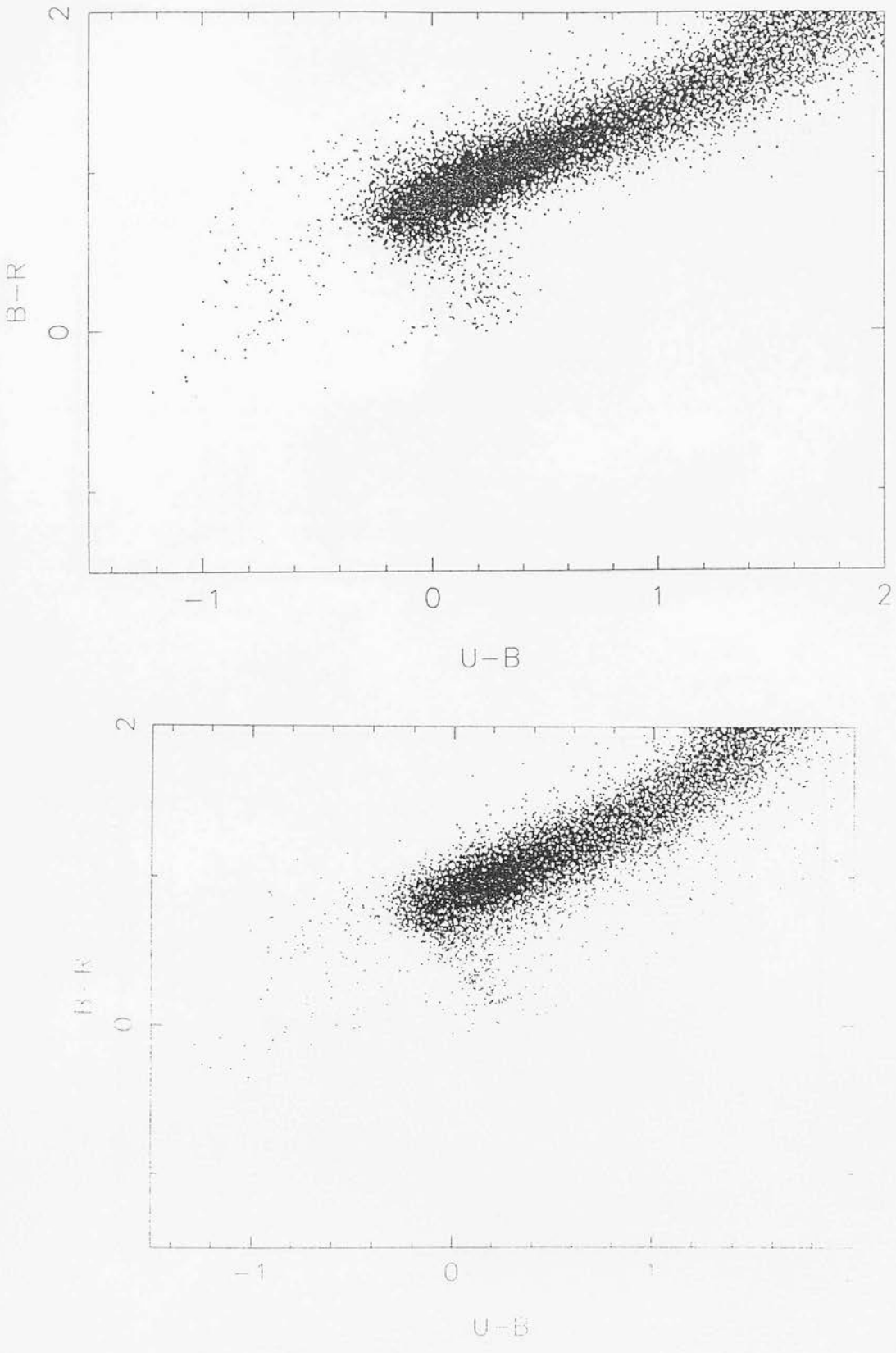

Figure 2.6: Stellar loci for fields 791 (top) and 792 (bottom)

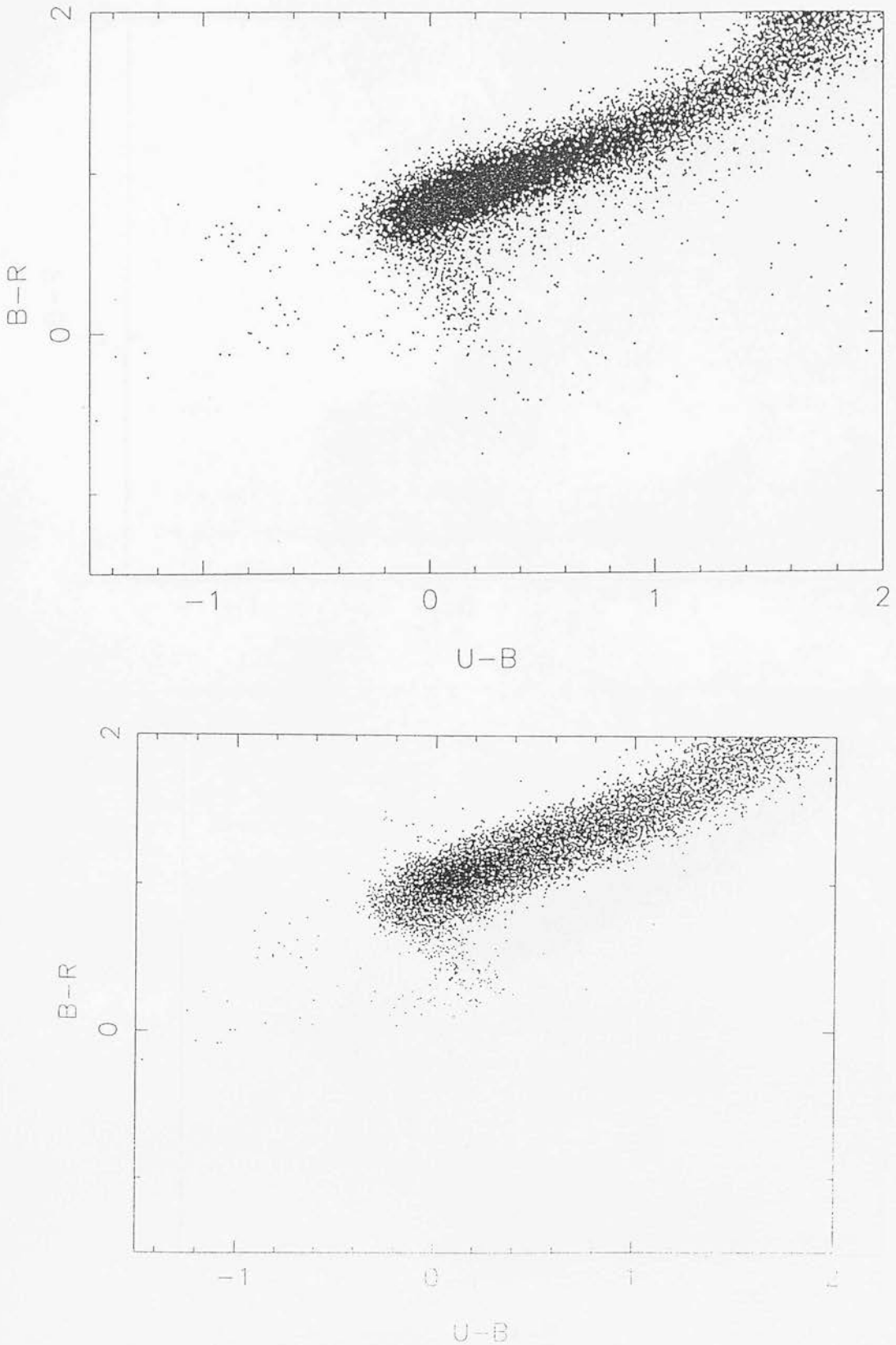

Figure 2.7: Stellar loci for fields 793 (top) and 794 (bottom)

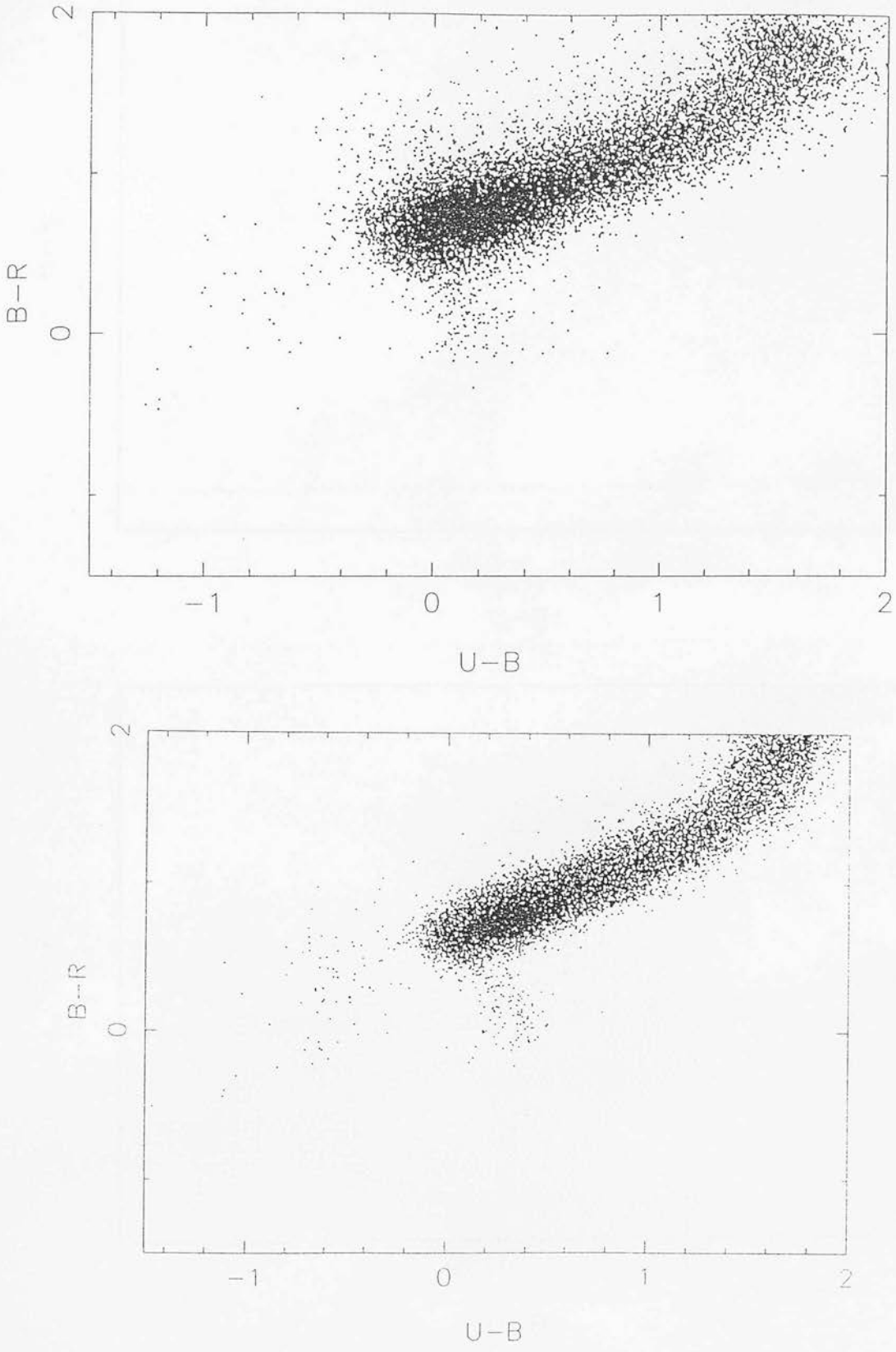

Figure 2.8: Stellar loci for fields 861 (top) and 862 (bottom)

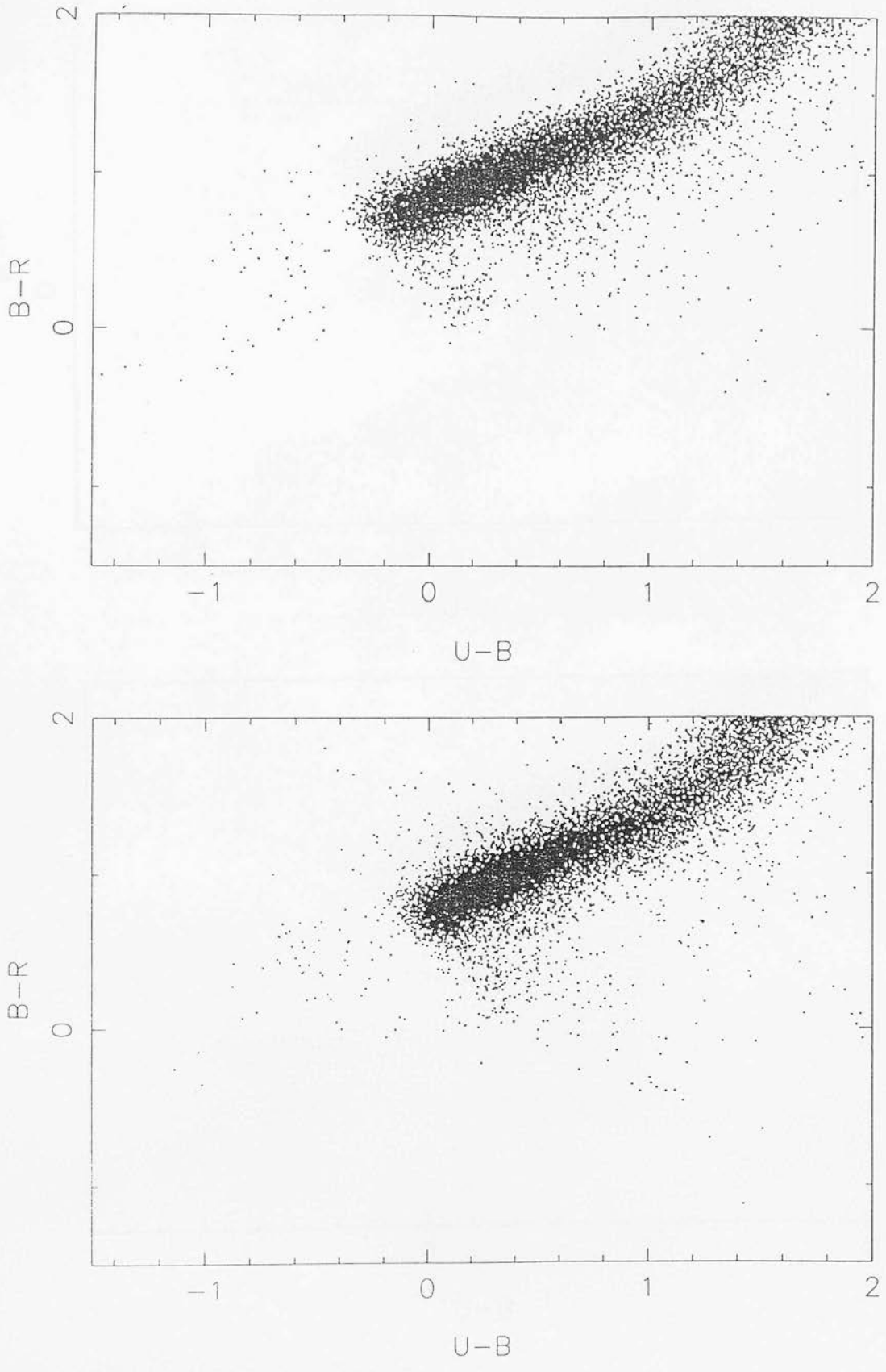

Figure 2.9: Stellar loci for fields 863 (top) and 864 (bottom)

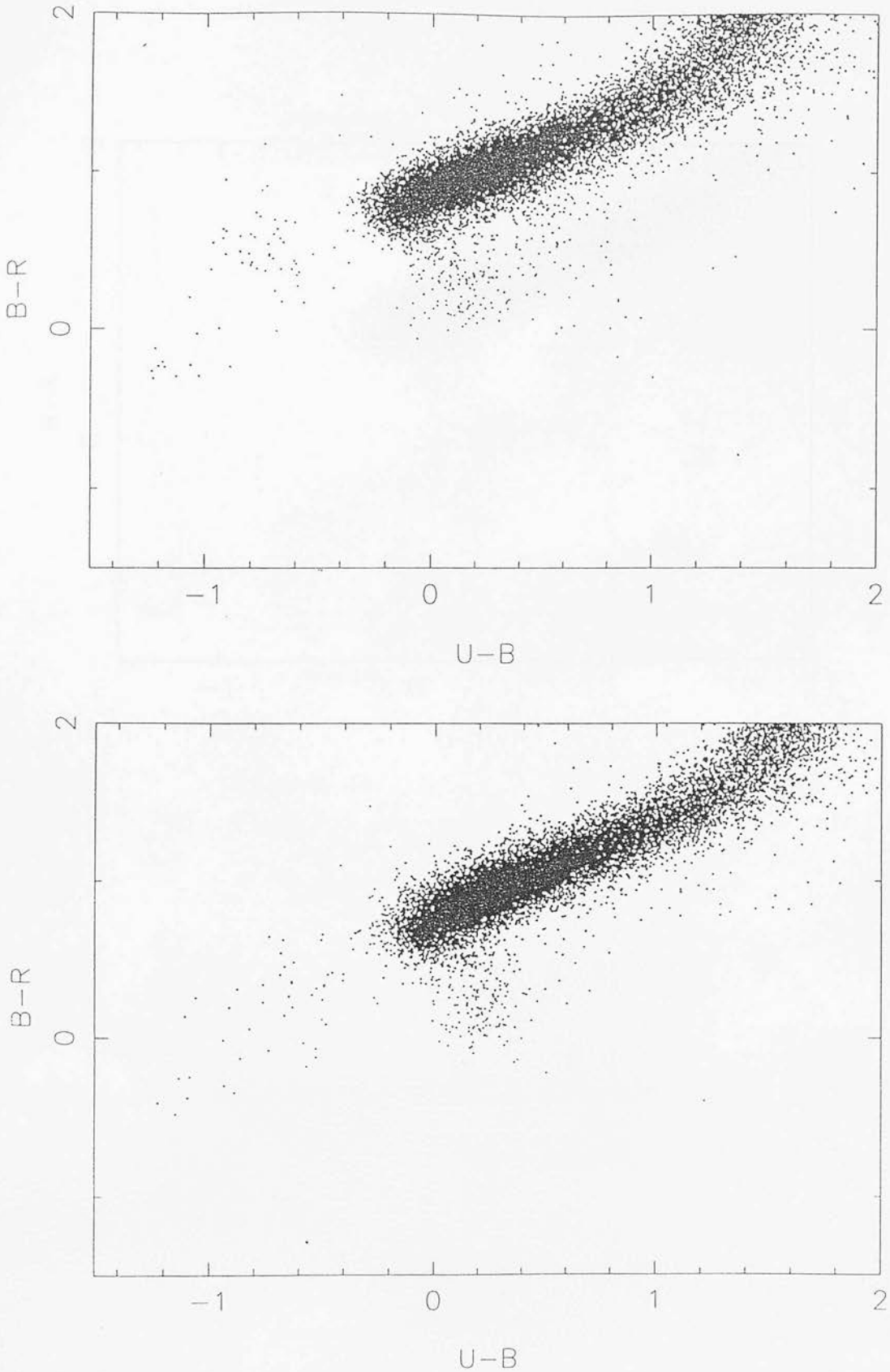

Figure 2.10: Stellar loci for fields 865 (top) and 866 (bottom)

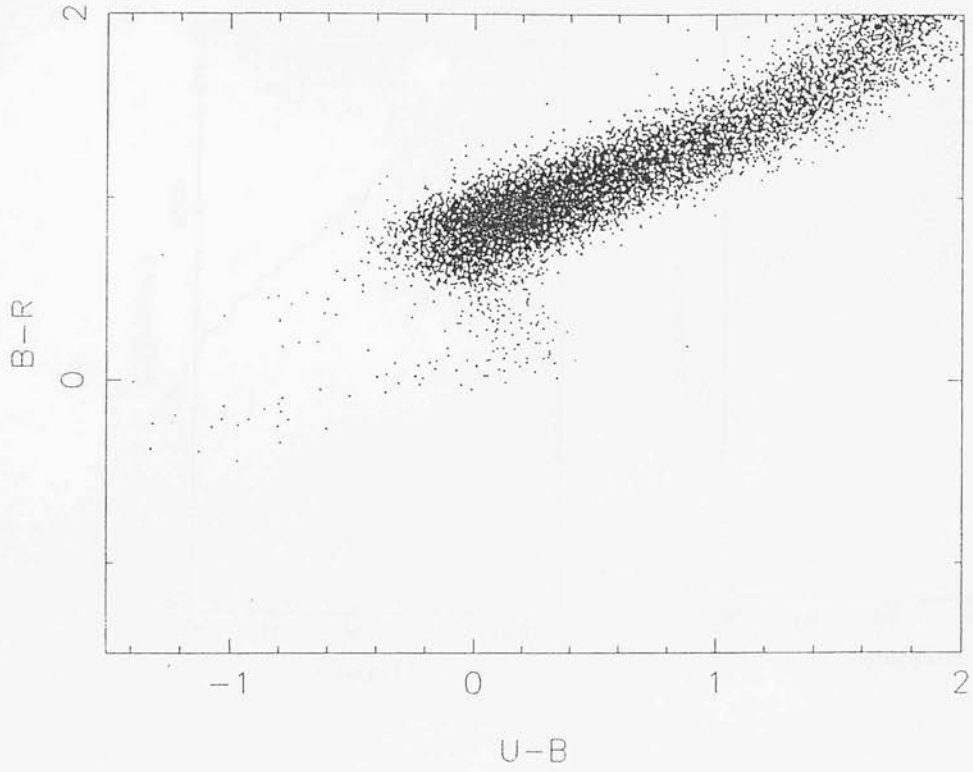

Figure 2.11: Stellar loci for field 867

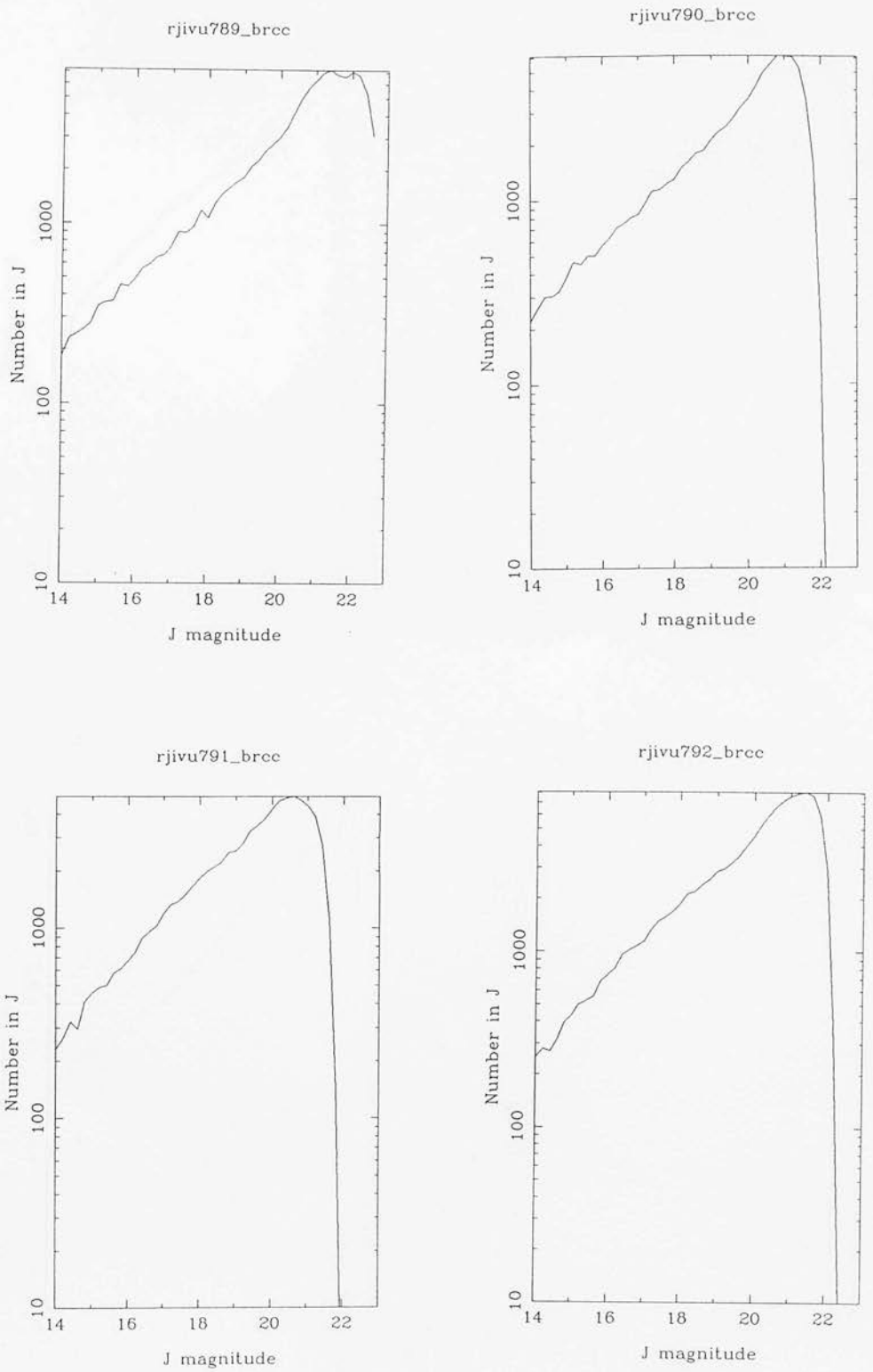

Figure 2.12: Differential log(n)–m relations for calibrated COSMOS data in the B_J band for 789 (top left), 790 (top right), 791 (bottom left) and 792 (bottom right).

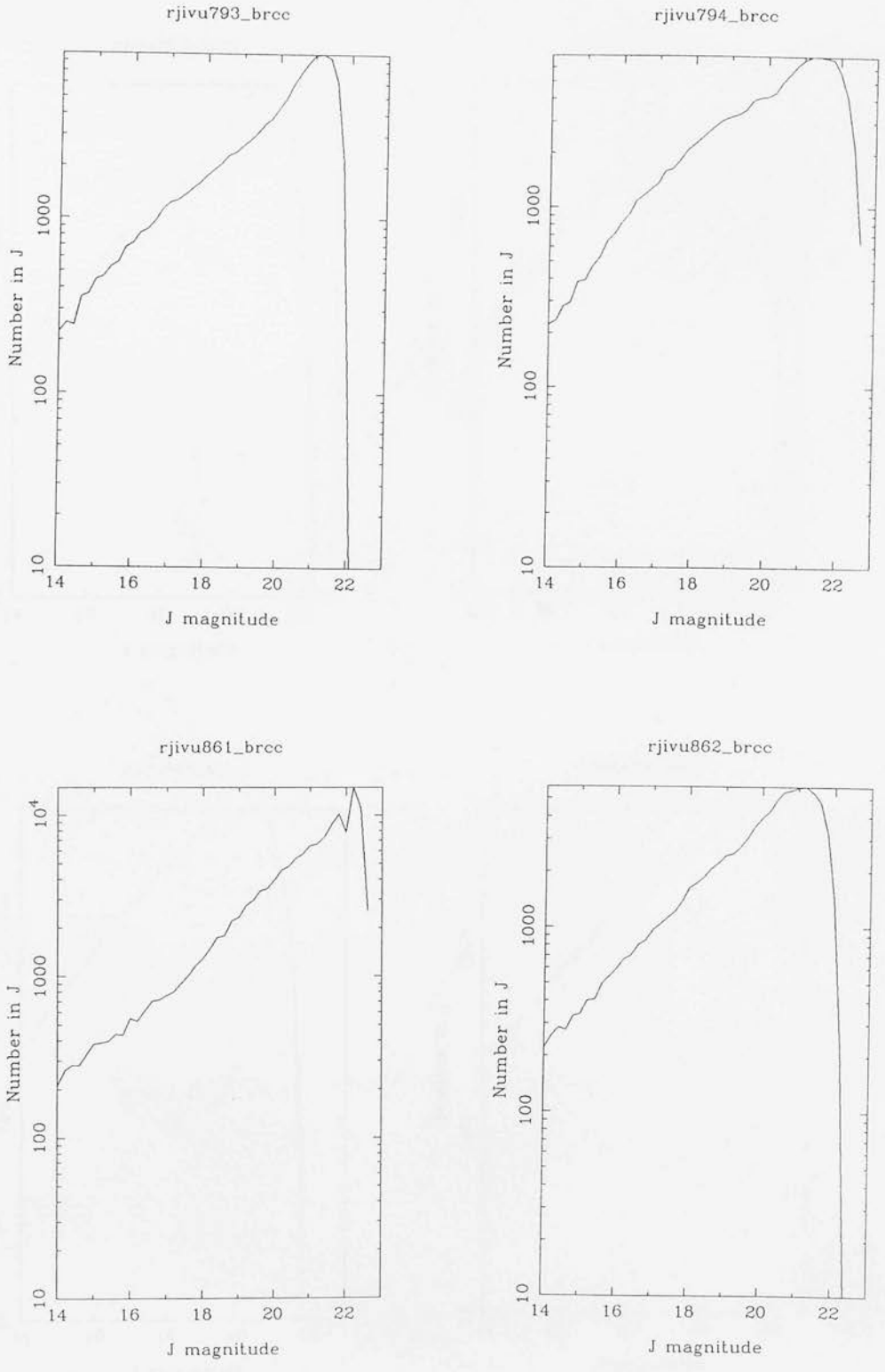

Figure 2.13: Differential log(n)–m relations for calibrated COSMOS data in the B_J band for 793 (top left), 794 (top right), 861 (bottom left) and 862 (bottom right).

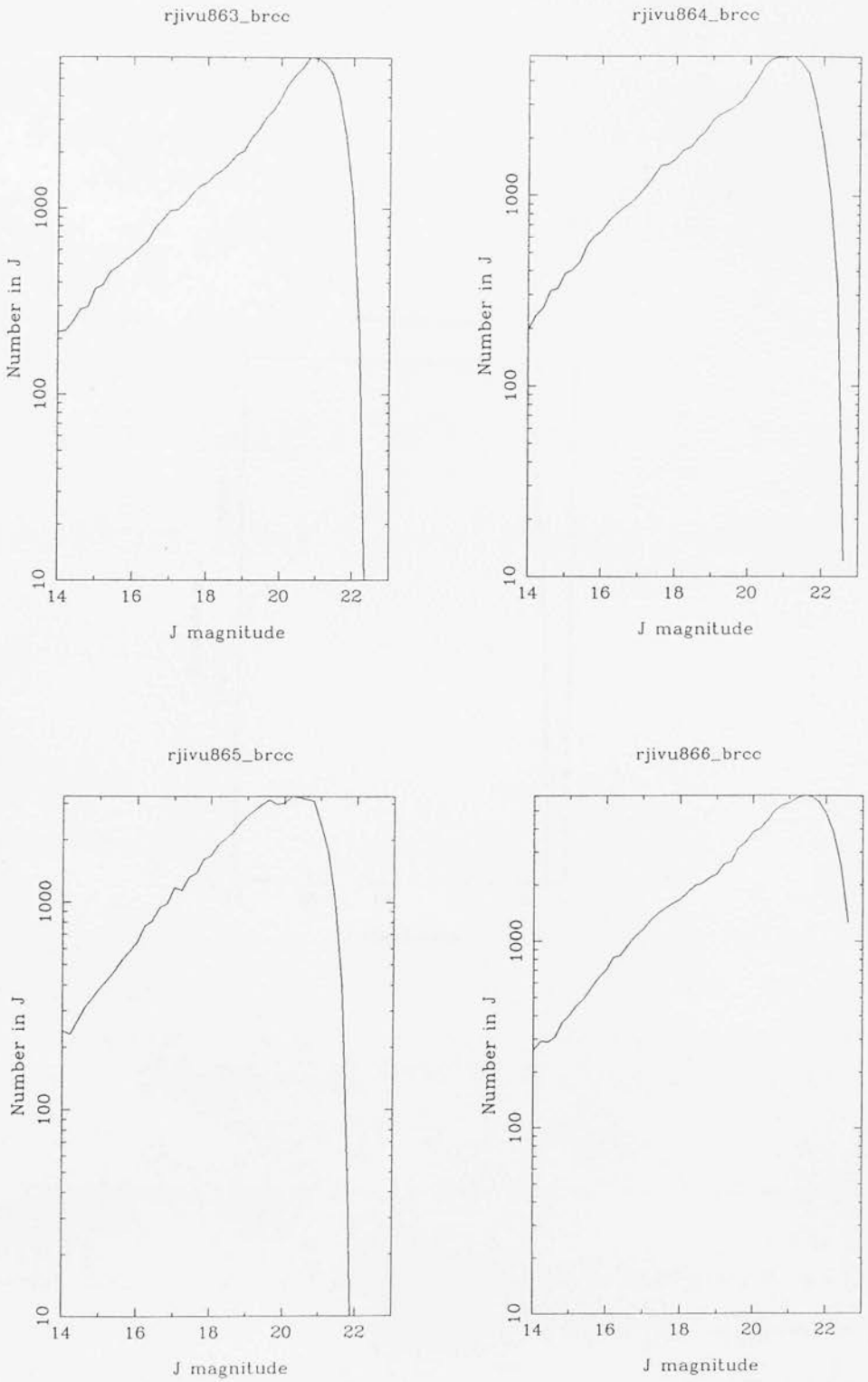

Figure 2.14: Differential log(n)–m relations for calibrated COSMOS data in the B_J band for 863 (top left), 864 (top right), 865 (bottom left) and 866 (bottom right).

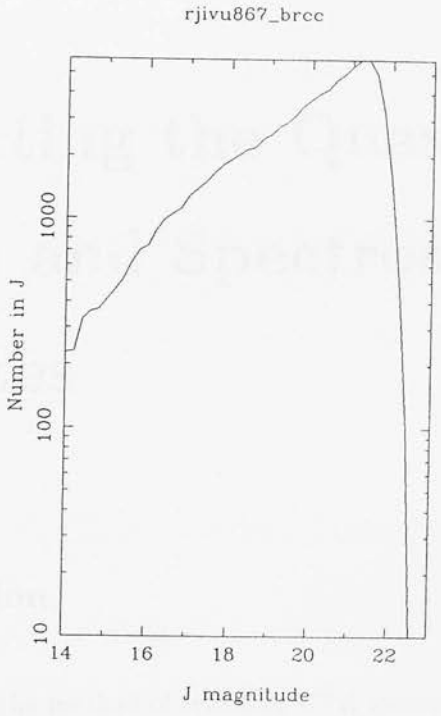

Figure 2.15: Differential log(n)–m relation for calibrated COSMOS data in the B_J band for 867.

Chapter 3

Constructing the Quasar Survey: Selection and Spectroscopy of the Candidates

3.1 Introduction

This chapter discusses the method of selecting UVX quasar candidates using broad band photometry from the Edinburgh survey and then describes the acquisition and reduction of spectra for these objects from various different telescopes, the overall aim being to select a complete sample of bright UVX quasars.

3.1.1 The observed spectral energy distribution from UVX quasars

The spectral energy distribution (S.E.D.) of a quasar can be approximated by a single power law from x-ray through optical to infra-red wavelengths with additional features superposed at different wavelengths (see Lawrence 1987, for a review of S.E.D.s of AGNs). For example, for quasars with $z \leq 2.2$ the flux observed in the observer's rest frame at ultra-violet to optical wavelengths can be described by a power law with excess emission ("the blue bump") superposed at near ultra-violet wavelengths. This excess may be due

to thermal black-body emission from the accretion disk (e.g. Malkan & Sargent, 1982). The combined effect of the power-law and the thermal emission shows up as a blue excess in the observed spectrum, and thus the quasar will be bluer than most objects with purely thermal energy distributions, e.g. main-sequence stars. Thus, when broad band photometry is carried out in the U and B bands, UVX quasars have bluer $U-B$ colours than main-sequence stars. For quasars with $z > 2.2$ this blue bump together with the Lyman-α line (which has a large equivalent width) is redshifted to higher wavelengths. In addition, the absorption due to the intervening Lyman-α forest bluewards of this line means that the flux is depleted at ultra-violet wavelengths. The combination of these phenomena mean that these quasars will not have much measured flux in the U band and will no longer be UVX. Thus this method of selecting quasars has a sharp redshift cutoff at $z = 2.2$, and providing that not too blue a $U-B$ limit has been chosen for the selection of candidates, is capable of selecting $\approx 95\%$ of all known quasars with $z \leq 2.2$ (Veron 1983).

3.2 Selection of UVX Quasar Candidates

One of the main advantages of multi-colour selection of quasar candidates is its simplicity. In the case of UVX candidate selection, two (out of the five) wavebands were used; U and B. The main criterion is requiring the candidates to be blue in $U-B$ with respect to the main sequence stellar locus. An additional criterion was also sometimes used here; that of requiring that candidates also be red in $B-R$. The difference between quasars' power-law and blue stars' thermal black-body energy distributions means that even when the two classes of objects have similar $U-B$ colours this extra requirement discriminates against blue stars. This criterion was sometimes relaxed, as in the case of the FLAIR observations, to show that the extra objects selected as a result really were blue stars and not quasars.

3.2.1 Morphological selection

A morphological selection was carried out before any colour criteria were applied; principally to discriminate against spurious blended and extended objects which might have spuriously peculiar colours and therefore dominate the candidate lists. If the quasar's host galaxy is detected this will mean that the quasar will appear extended and be discriminated against on morphological grounds. This means that very low-redshift quasars will be discriminated against and thus there is a redshift limit below which the sample will be incomplete. In the past, workers have set this limit to be $z = 0.3 - 0.4$, however this depends on the ratio of the quasar luminosity to that of the host galaxy and therefore is probably higher for faint UVX surveys than for ones detecting only bright quasars (such as this survey). The limit also depends on the quality and depth of the plate material used to choose the candidates. Following previous workers we have chosen a limit of $z = 0.3$. However the only way of properly determining this is to compare the space density of low redshift quasars selected without using morphological or UVX criteria, such as an x-ray selected sample.

The morphological selection was only carried out in the U band. Three COSMOS image analysis parameters were used in the morphological selection; the area (AREA), maximum intensity (IMAX) and axial ratio of each image. Because a fraction of all objects in the survey were thrown out as result of this selection, the effective area searched for quasars decreased proportionately. Table 3.2.1 shows the number of objects included by the morphological criterion in each field as a percentage of the total number of objects, and the magnitude limits within which that field is complete.

3.2.2 Colour selection

The prime consideration when selecting quasar candidates is that of completeness; one must be confident that no "interesting" candidates are being missed out by the colour criteria. The opposing consideration is that of requiring that the candidates be observed in a finite amount of observing time; by setting the colour limits too far into the stellar locus one may be sure of completeness but then the ratio of detected quasars to stars

Field	$U - B_J$ limit	B_J Limit	No. objects %
789	-0.5	18.0	85.0%
790	-0.8	17.5	88.6%
791	-0.3	17.7	89.9%
792	-0.3	18.1	88.4%
793	-0.3	17.5	88.9%
794	-0.4	18.0	90.6%
861	-0.3	18.1	90.3%
862	-0.3	18.0	88.2%
863	-0.35	18.1	87.5%
864	-0.15	18.0	89.9%
865	-0.3	18.1	93.2%
866	-0.3	18.2	89.3%
867	-0.4	18.3	89.4%

Table 3.1: This table shows the $U - B_J$ selection cutoff applied to each field, the limiting magnitude of completeness and the percentage of objects left after morphological selection had been applied.

decreases rapidly. Also, if the *internal* calibration of the plate material is accurate then the main-sequence stellar locus, the horizontal-branch turn-off, and the clump of UVX quasars should all be clearly defined in colour space (See Figures2.5 to 2.11 in Chapter 2). This is a simple check on the accuracy of the calibration (regardless of any field-to-field zero-point offsets) and thus for a well-calibrated field it should be straightforward to define the colour criteria. The $U-B$ limits in each field were chosen by looking at the position of the stellar locus in U, B, R colour space. Table 3.2.1 shows the nominal limits chosen in each field. As can be seen, the average $U-B$ limit chosen is -0.3, considerably redder than the average $U-B$ colours of known UVX quasars, apart from field 790, whose zero point is obviously wrong. Looking at the average $U-B$ colours for the quasars in each field we get

$$(U-B_{lim}) - \left(U-B_{QSO}\right) \geq 0.2m \tag{3.1}$$

where $U-B_{lim}$ is the $U-B$ cutoff applied in each field, below which all objects were selected as candidates, and $U-B_{QSO}$ is the average $U-B$ quasar colour in each field. Therefore the quasars are significantly bluer than the $U-B$ limits chosen. An additional criterion of $B-R \geq 0$ was applied to select candidates for the observing runs at the INT.

3.3 Spectroscopic Observations and Reduction

Spectroscopic observations were carried out on the 2.5m Isaac Newton Telescope (INT), the 2.2m and 1.52m telscopes at ESO-La Silla, and the 1.2m U.K. Schmidt telescope. The following section describes how the data were taken and reduced at each telescope.

3.3.1 Observations at the 2.5m Isaac Newton Telescope

Six nights of observations were carried out on the INT with Dr. L. Miller over a period of two years, using two spectrographs; the Faint Object Spectrograph (FOS, which has a GEC CCD detector) and the Intermediate Dispersion Spectrograph (IDS) (the latter setup was only used for one night and so much of the following is only concerned with

FOS). FOS is ideally suited to spectral identification as it covers a very large wavelength range; 4000 Åto 10500 Å, and thus maximises the observable number of spectral features in each object. The light is dispersed by a transmission grating and a cross-dispersing prism. The advantage is that since there is no collimator the minimal number of surfaces increases the throughput; the disadvantage is that the curvature is difficult to remove completely and thus there are residual sky features in the reduced spectra.

The first observing run using FOS and the IDS took place from 1st to 5th March, 1990. The weather was not photometric and much time was lost due to low-lying fog. Accurate wavelength calibration for UVX candidates is important to positively identify them, and in the case of quasars, to measure the redshifts. We took Copper-Argon arcs throughout each night in order to wavelength-calibrate and detect any small changes in wavelength as a function of time, but the instrument was extremely stable, particularly as we were using a very low dispersion grating and one arc was usually sufficient to calibrate the data for each night. We verified this by cross-correlating arcs taken at different times throughout the night, the shifts between arcs taken at the beginning and end of the night were always considerably less than one pixel. Flat fields were also taken, using a tungsten lamp. Data taken with the IDS were reduced using standard FIGARO routines. First, the bias-subtracted flat fields were collapsed in the cross-dispersion direction to create a one-dimensional spectrum. Then each row of the two-dimensional flat field data was divided by this spectrum to remove the spectral variation of the light-source. This also removes all instrumental variations in the dispersion direction, leaving only variations in the cross-dispersion spatial direction. The resulting data were normalised, suitable for use as a flat field. The object data were bias-subtracted to remove the offset "bias" charge, then divided by the normalised flat field, sky-subtracted and then extracted by adding the weighted data in the cross-dispersion direction. The data were weighted by a Gaussian function fit to the instrumental profile. This is in order to maximise the signal/noise ratio in the extracted data. The resulting one-dimensional spectra were wavelength-calibrated using the reduced arc spectra, by copying the pixel-wavelength information from the arc spectrum into each object spectrum and then re-binning the data so that the relation between pixel number and wavelength was now linear.

Data taken with FOS were also reduced using FIGARO, but the process was somewhat

more tortuous because of the curvature of the spectra. Because the cross-disperser is a prism, the curvature varies with wavelength. In order to straighten the spectra, the FIGARO routine SDIST was used, this software interactively fits a polynomial to the curvature of a template, e.g. a bright star, and then inverts the polynomial to derive the correction. This assumes that the curvature occurs only in the cross-dispersion direction, i.e. the data in the dispersion direction is undistorted. Since the instrument is so stable this correction only needs to be derived once per night and in fact, hardly varied throughout each observing run. The arc frames were straightened and then a low-order polynomial was fit to the wavelength-pixel relation. The rms scatter to this fit was usually 2 Åand always less than 4 Å. The flat-field frames were straightened in the same way, and then collapsed in the cross-dispersion direction as described above to remove the spectral response of the flat field lamp. The straightened data were then flat-fielded, sky-subtracted, extracted by fitting a Gaussian profile to the instrumental profile in the cross-dispersion direction and then wavelength-calibrated. The accuracy of the wavelength calibration was quantified by looking at the measured wavelengths of known spectral features such as sky emission lines and the Balmer absorption sequence in the white dwarfs detected in the survey. The measured wavelengths never deviated by more than $\approx$ 4 Åfrom the true values, although the very low dispersion of the spectra (11 Åper pixel in the 1st order) makes this difficult to quantify exactly. This error translates into an error of ≤ 0.001 in redshift.

The wavelength-calibrated spectra were then flux-calibrated. This was primarily to remove the instrumental response in the dispersion direction (which makes each spectrum looked "humped") so that the two spectral orders could be merged together into one sensible-looking spectrum for each object. Observations of one standard star were taken each night and then divided by flux-calibrated observations of these stars in order to calculate the instrumental response as a function of wavelength. Because the observations were taken in variable non-photometric conditions, the resulting spectra do not represent absolute fluxes, but the *shapes* of the spectra should be approximately correct.

3.3.2 Observations at the 1.2m U.K. Schmidt

Spectroscopic data were obtained at the 1.2m UKST using the multi-fibre instrument FLAIR during two observing runs in 1991 and 1992. FLAIR consists of a standard Schmidt plateholder with attached optical fibres which can then be positioned along a slit such that the output falls onto a grating and is then detected by a CCD. The data observed in 1991 were on average half a magnitude brighter than that observed in 1992 and thus were more straightforward to reduce. However the principles involved in both sets of data reduction are the same and are as follows. The main advantage with FLAIR (and multi-fibre instruments in general) is that it allows the simultaneous acquisition of data for many objects. FLAIR is unique amongst multi-fibre instruments in that it is situated on the Schmidt telescope and thus utilizes the Schmidt's large field-of-view; $\approx$ 28degs^2. This makes it ideal for surveys of bright objects with low surface density, such as bright quasars and galaxies. The main disadvantage is that as the combined signal from the source and the sky travels down each fibre towards the spectrograph it gets "scrambled" and thus one cannot simply subtract the surrounding sky from the source in the resulting spectrum. The solution is to use some of the fibres in each field to measure the sky alone and then subtract the average of these sky spectra from each object spectrum.

However each fibre has a different response which is the product of the individual fibre's transmission function with the vignetting function of the telescope, and this must be measured and taken into account before subtracting the signal measured in one fibre from that in another fibre. The relative transmissions for each fibre are measured by taking observations of a spatially uniform source, such as the twilight sky or the unfocussed interior of the illuminated telescope dome. For the brighter candidates it was enough to consider simply the total transmission for each fibre, but for the fainter ones (measured during the 1992 run) the transmission for each fibre was modelled as a function of wavelength. This was necessary because the diameter of each fibre was 6.7arcsecs and the wavelength range used was large; $\approx$ 3600 Å- $\approx$ 7000 Å. The sky brightness was therefore $\approx$ 20 mags per arcsec^2, or $\approx$ 16 mags in total in each fibre. The magnitude of the faintest objects was $\approx$ 18 mags, in this wavelength range, therefore the object flux was $\approx$ 20% of the sky flux. This assumes that the seeing is good, and also that the object is centred on the fibre, i.e.

all the object flux is measured by the fibre. If, as was frequently the case, the seeing was *not* good (it was typically 4-5 arcsecs) and the objects were imperfectly centred on the fibres (because of inaccuracies in the positioning of the fibres) then the ratio of object to sky flux dropped dramatically. Because the object flux was so low compared to the sky flux the raw data was completely sky-dominated and this sky had to be subtracted accurately, i.e. keeping the noise down to less than 10%, to stop the signal-to-noise in the final sky-subtracted spectrum from decreasing too much.

The accuracy of the vignetting function was limited by the significant amount of scattered light detected by the CCD. If there is a uniform component of scattered light detected by the chip then the variance in the fibre responses will be underestimated and hence the fibre-to-fibre variations will not be entirely removed. This scattered light was inadvertently measured during the first night of the second run because one of the fibres broke and thus the corresponding part of the CCD was unexposed. However there was still an appreciable level of light detected in this part of the CCD, presumably due to scattered light in the instrument, and this contributed approximately $5 - 10\%$ of the overall amount of light detected per pixel. However in order to subtract this light, one must decide how much of this light is "uniform" and covers the whole chip and how much is simply due to leakage from adjacent spectra. As the scattered light was only measured over a small part of the chip there was not enough information to calculate and hence subtract the scattered light component from the whole array. It has been suggested (e.g. Wyse & Gilmore, 1992) that parts of the chip should not be exposed for the express purpose of measuring this component of scattered light. It was decided to ignore the scattered light contribution.

The data for each night were obtained as follows:

During the day, the fibres were glued onto the positions of the chosen candidates in the field to be observed that night. This is done using a "mask"; a glass copy of the J survey Schmidt plate for that particular field and special position-finding software written by F. Watson.

Five "fiducial" fibres and one "guide probe" fibre are glued onto the positions of bright stars in the field; the guide probe is placed on a star near the centre of the field. This is in order to acquire the field with sufficient accuracy. The mask with the fibres glued onto it

is then put into the plate holder which is loaded into the telescope. When the field is being acquired the light transmitted by the fiducial fibres is measured in real-time by a CCD camera, so that when the field is successfully acquired all of these fibres transmit light. In practice this means that the central bright star is first acquired and then the plate holder is rotated until the other fiducial fibres are transmitting light as well. Theoretically, only three fiducial stars are needed to acquire the field.

Bias frames were taken at the start of each night in order to be examined later for any evidence of possible structure.

Exposures of Mercury-Cadmium and Neon arc lamps were taken in order to provide wavelength calibration. Short integrations (about $30 - 180$ seconds) were taken of the twilight sky or of the inside of the dome, in order to calculate the fibre responses. The twilight sky was deemed preferable as it has the same spectral response as the dark sky. The field is acquired as described above. Since long integrations are taken it is essential that the telescope is automatically guiding using a bright guide star and so after the field is acquired the guiding telescope is used to acquire a bright guiding star. Integrations were started on the field. It was estimated that $\approx 6 - 8$ hours of data were needed for each field. The data were binned on the CCD such that the output from 2 resolution elements from the grating fell onto one CCD pixel. This reduced the resolution in the final output, but increased the signal-noise ratio in the data because the read-out noise was reduced. There are two conflicting criteria for deciding how long each integration should last; read-out noise and cosmic ray events. Read-out noise is constant as a function of time, so ideally each exposure should be as long as possible. Cosmic ray events increase as the integration time increases and therefore each exposure time should be as short as possible. It was decided on the basis of past experience that 50 minutes is the optimal exposure time. After this period of time, about 0.5% of the information on the chip was lost due to cosmic ray events; this was considered to be acceptable. Integration on the field was stopped towards the end of each night as the zenith distance of the field became too large. More bias frames and arcs were taken and then the plate holder was taken off the telescope, the fibres were un-glued, and fibring-up was started for the next night's observations.

Data from each night were reduced as follows:

The bias frames were examined for any signs of structure. None was ever found and so the bias strip for each exposure was used to calculate the bias level for that individual exposure; this bias level was then subtracted. This is more accurate than calculating the bias from the bias frames taken at the beginning and end of each night, because the bias level varied slightly throughout the night.

Cosmic ray events were removed automatically, by coadding the set of bias-subtracted frames corresponding to each set of field, dome and arc exposures. This was done using software written by K. Glazebrook; the software "stacked" the set of frames and then calculated the median value for each pixel. The cosmic rays were removed by flagging the data for each pixel which deviated by more than a user-specified amount from the median for that pixel and then re-calculated the median for the pixel, using only the unflagged data. This is much quicker and more accurate than laboriously removing the cosmic rays interactively.

The coadded twilight sky frame was then used to calculate the position of each spectrum on the chip. The twilight data for each fibre were then extracted into 1-dimensional spectra, by simply summing up all the rows that the light from each fibre occupied on the chip. In principle, it is better to optimally extract the spectra by fitting the instrumental profile to the cross-section of each spectrum (as was done for data from the INT) but in practice each spectrum only occupied about 3 rows on the chip and so this was not feasible.

The 1-dimensional spectra were added together to calculate the average twilight sky spectrum. This average spectrum was then divided into each twilight spectrum and the residual was then fitted with a low-order polynomial. The resulting spectrum was the vignetting function for that particular fibre. By dividing by the average twilight spectrum, each vignetting function was normalised to take into account transmission differences between fibres. The fits to the vignetting functions were checked by dividing them into the "raw" twilight spectra, looking at the distribution in the flux values in these spectra and comparing it to that for the uncorrected spectra. If the vignetting functions had removed all the variations from the spectra then the distribution for the corrected spectra should be

much narrower than that for the uncorrected spectra, and this was indeed the case. The spread in the distribution for the uncorrected spectra was $\approx 20\%$ of the mean flux, for the corrected spectra it was $\approx 5\%$. In principle, this should have meant that the calculated vignetting functions were accurate enough to remove most of the variations between fibres. However, on the object frames, the presence of scattered light, much of it non-uniform, meant that the vignetting functions could not completely remove the variations.

The spectra corresponding to each fibre in the coadded object frame were then extracted and divided by their corresponding vignetting functions. Then the linear shifts between spectra had to be removed. These shifts occur because the fibres are not lined up perfectly along the slit. The shifts were removed by first calculating the size of the shift in pixels by cross-correlating between each arc spectrum and the central arc spectrum. Arc spectra were used to calculate the shifts because they had strong features across the whole wavelength range being sampled. The shift was then applied to the corresponding *object* spectrum. Then the object spectra were wavelength-calibrated by copying the pixel-wavelength information from the calibrated arc spectrum into each object spectrum. The wavelength calibration was checked by looking at the wavelengths of the sky lines in a random sample of spectra taken from across the whole frame. The measured wavelengths of these lines never differed by more than $1 - 2$ Åfrom the standard values.

The spectra were then sky-subtracted. The mean of the sky fibres was calculated and then this average sky spectrum had to be scaled to each object spectrum because not all the fibre-to-fibre variations had been removed by the vignetting functions. This was done by using the total counts measured in the OII 5007 Åline in each spectrum. This still did not scale the sky spectrum perfectly, suggesting that the scattered light component varied with wavelength.

3.3.3 Observations at the 1.52m and 2.2m at ESO, Chile

Data for $\sim$ 30 candidates with $15 \leq B \leq 17$ were taken at these telescopes in April, 1991. Dr. F. La Franca was co-observer and also reduced the data. The instrument used on both telescopes was a Boller and Chivens spectrograph. This instrument uses a collimator to deflect the incoming light onto a grating, the light is then focussed using a

Schmidt camera onto the detector (usually a CCD). Figures 3.12 to 3.14 show the spectra of extra-galactic objects found during this run.

3.4 Identifying objects and measuring redshifts

Once the reduced spectra had been wavelength calibrated, they were then identified. This was done by interactively examining each spectrum for emission or absorption features. For instance, many objects observed were white dwarfs, which can be easily identified as such because of their strong Balmer absorption features. F and G type stars also, to a lesser extent, show Balmer absorption lines, enabling them to be positively identified if the signal-to-noise is high enough. Figure 3.15 shows spectra of typical stars found.

An object was identified as being a quasar if it exhibited very broad (i.e. resolved) emission lines (or, very rarely, very broad absorption features). The redshift was then calculated by "guessing" the identification of one detected line and seeing if this correctly predicted the observed wavelengths of other detected features.

Objects were classified as Narrow Emission Line Galaxies (NELGs) if they had strong narrow unresolved emission lines and almost no continuum. A good example of this type of galaxy is object 1421-073 ($z = 0.301$) whose spectrum is illustrated in figure 3.5. On the same page is a spectrum of object 1423-053 ($z = 0.291$). The latter object was classified as a quasar as it has much broader Hβ than the former and a much higher continuum level. Objects classified as NELGs were not included in the final quasar sample used for analysis in chapters 4 and 5 as it is not at all clear how these objects are related to the AGN phenomenon.

3.4.1 Reliability of redshift measurements

Quality flags were assigned to each quasar to give an indication on the reliability of both the identification of the object as a quasar, and the reliability of its redshift. I used three independent criteria in assigning quality flags;

a) the number of observed emission lines,

b) the signal-to-noise ratio of the data, and

c) the ambiguity of the measured redshift (i.e. if there were more than one possible redshift interpretation).

A quality flag of 1 indicates certainty; the object is definitely a quasar and has an unambiguous redshift. Objects which were independently detected in both the Edinburgh and LBQS surveys and had the same measured redshifts in both surveys were all assigned quality flags of 1. A quality flag of 2 indicates that the object is definitely a quasar and that the redshift assigned is the most probable one. A quality flag of 3 indicates that the object is possibly a quasar but the signal-to-noise is poor, and therefore there is some doubt over its ID. Table C1 in Appendix C shows the candidates observed on all runs described above, along with their identifications, and in the case of quasars, redshifts. As can be seen from the quality flags assigned to the quasars, there are 13 quasars in all with quality flags of 3; 6 of those quasars are part of the complete sample used in the analysis in the following chapters. The effect of these quasars upon the analysis is discussed in Chapter 5.

We were fortunate in that the LBQS covered four fields in the Edinburgh survey region and thus many candidates that were chosen in the Edinburgh survey and yet did not have positive IDs were identified as quasars in the LBQS. In particular, field 864 which had many unidentified candidates benefitted from having been observed as part of the LBQS. The notes to table C1 show which quasars had redshifts determined by the Edinburgh survey alone, which ones were identified by both surveys, and which were identified solely by the LBQS.

Some spectra had low signal-to-noise and thus even though they showed evidence of emission lines, there was doubt as to whether the redshift assigned was the correct one. The majority of these objects were fainter than the flux limit in their particular field, and so for the purposes of the analysis in the following chapters, whether or not the redshifts are in error is not important. However these objects should be re-observed in the future in an attempt to identify them properly for future analysis. These objects include 1358-044 ($z = 0.200$, $B_J = 18.04$), 1253-032 ($z = 2.238$, $B_J = 17.49$), 1335-042 ($z = 0.272$, $B_J = 18.35$), 1331-001 ($z = 0.859$, $B_J = 18.31$) and 1416-051 ($z = 0.960$, $B_J = 18.50$). One of these objects is brighter than the flux limit of its field. Many of these objects

seem to have emission lines that cannot be identified if the object's assigned redshift is correct. Poorly subtracted sky emission lines could leave residuals in the final reduced spectra; the sodium emission line at 5898 Åis probably responsible for strong features still present in 1253-032 and 1335-042 as many other spectra show a residual feature at this wavelength. The presence of sodium emission in the sky implies the presence of clouds reflecting emission from street-lights, and therefore implies that the weather conditions were less than perfect.

It can be seen from table C1 that the 1992 observing run using FLAIR to observe candidates with $18.0 \leq B_J \leq 18.5$ suffered a low success rate, in that comparatively few objects could be positively identified. The success rate did not seem to depend on the objects' magnitudes, as one might naively expect. There are two factors which could be responsible for this;

1) Scattered light from adjacent objects on the CCD as discussed above.

2) Incorrect positioning of fibres. This could be due to human error; the positioning software relies on the observer to tell it where each object is on the mask. Also, the masks are J survey plates which are always taken on the meridian, whereas the observations using FLAIR were sometimes taken at high hour angles. Therefore the initial positioning of the fibres will be affected by differential atmospheric refraction. This effect could be seen during the observing run by looking at the light detected by each fiducial fibre in real time; very rarely were all these fibres detecting the fiducial stars. This implies that as the telescope tracks the field across the sky during the night and the hour angle varies, the apparent position of the objects on the plane of the sky varies, meaning that some of them will fall outside the area covered by the fibres at any one time.

The success rate during this run did seem to be a strong function of seeing, in that fields observed on nights with good seeing (e.g. 792, 864 and 865) had a higher success rate than other fields.

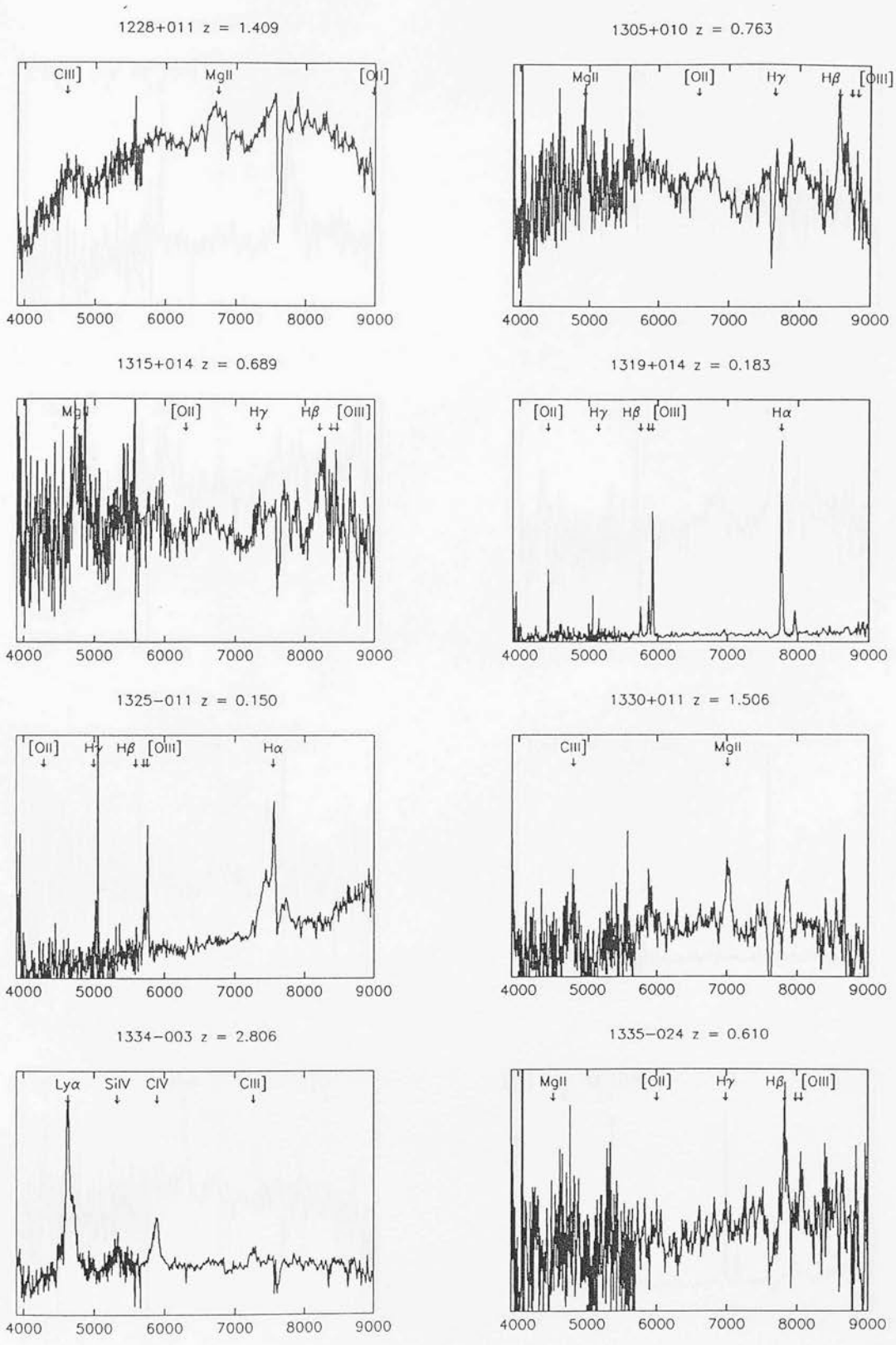

Figure 3.1: Extra-galactic objects observed during the INT runs.

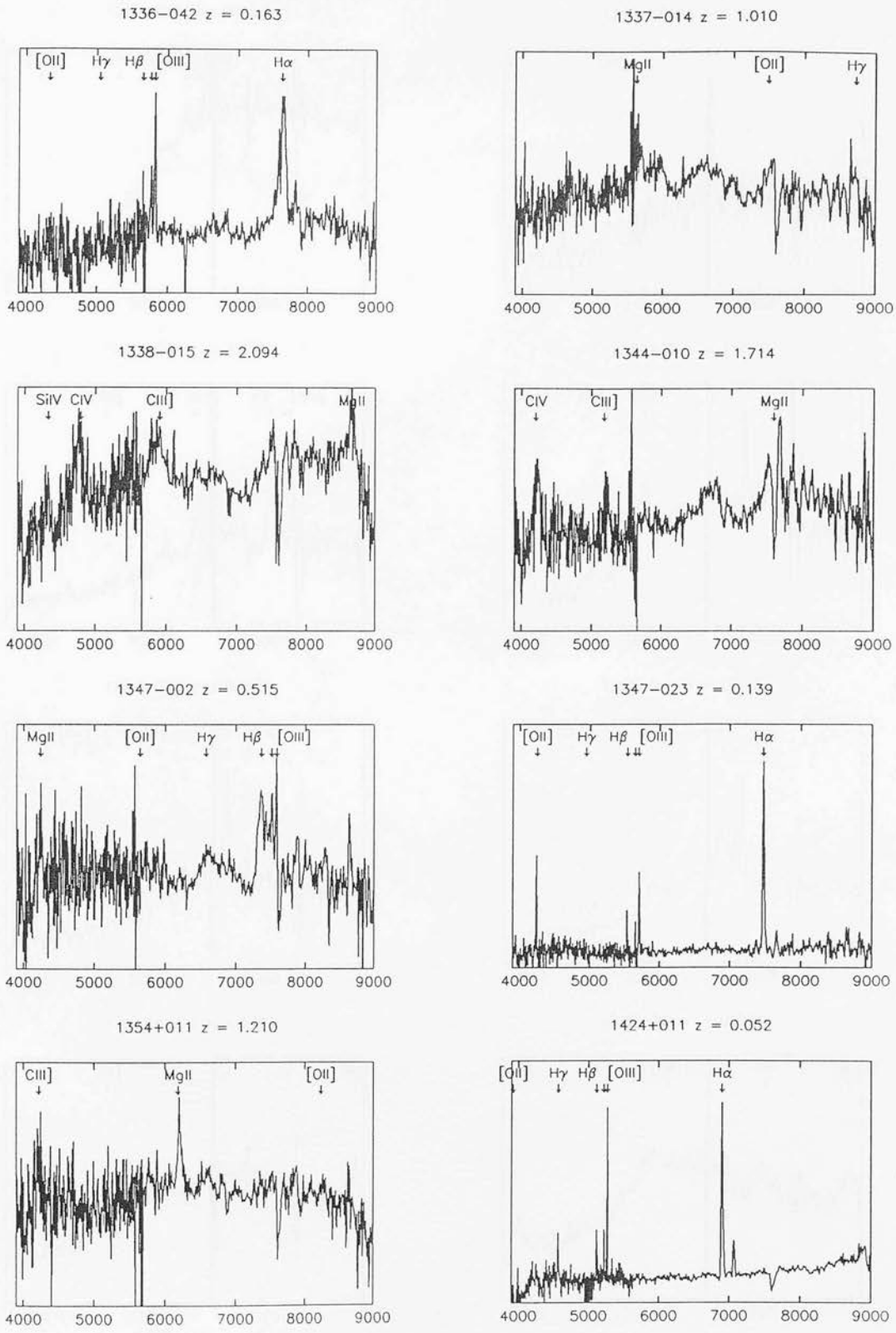

Figure 3.2: Extra-galactic objects observed during the INT runs.

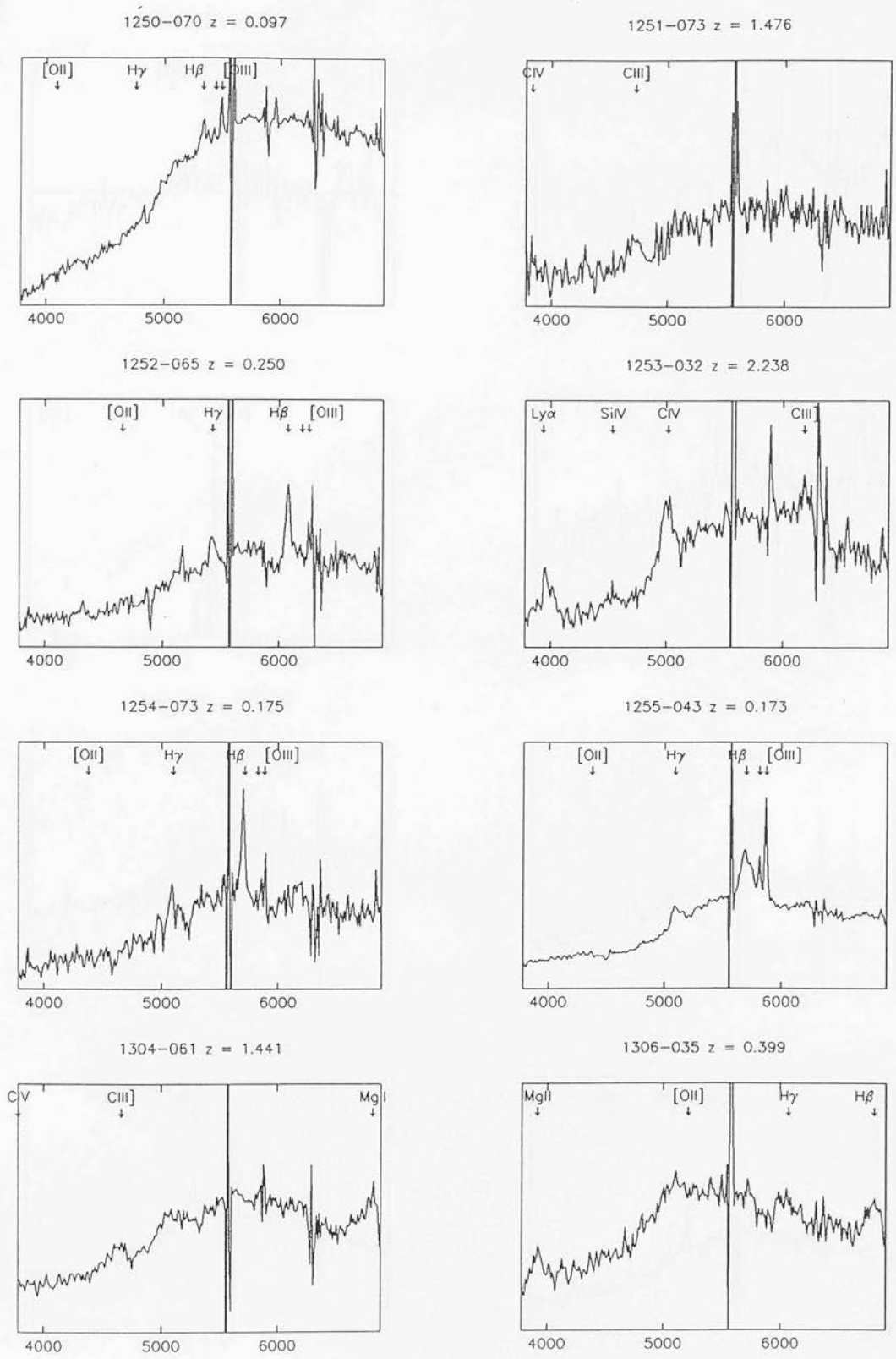

Figure 3.3: Extra-galactic objects observed during the 1991 FLAIR run.

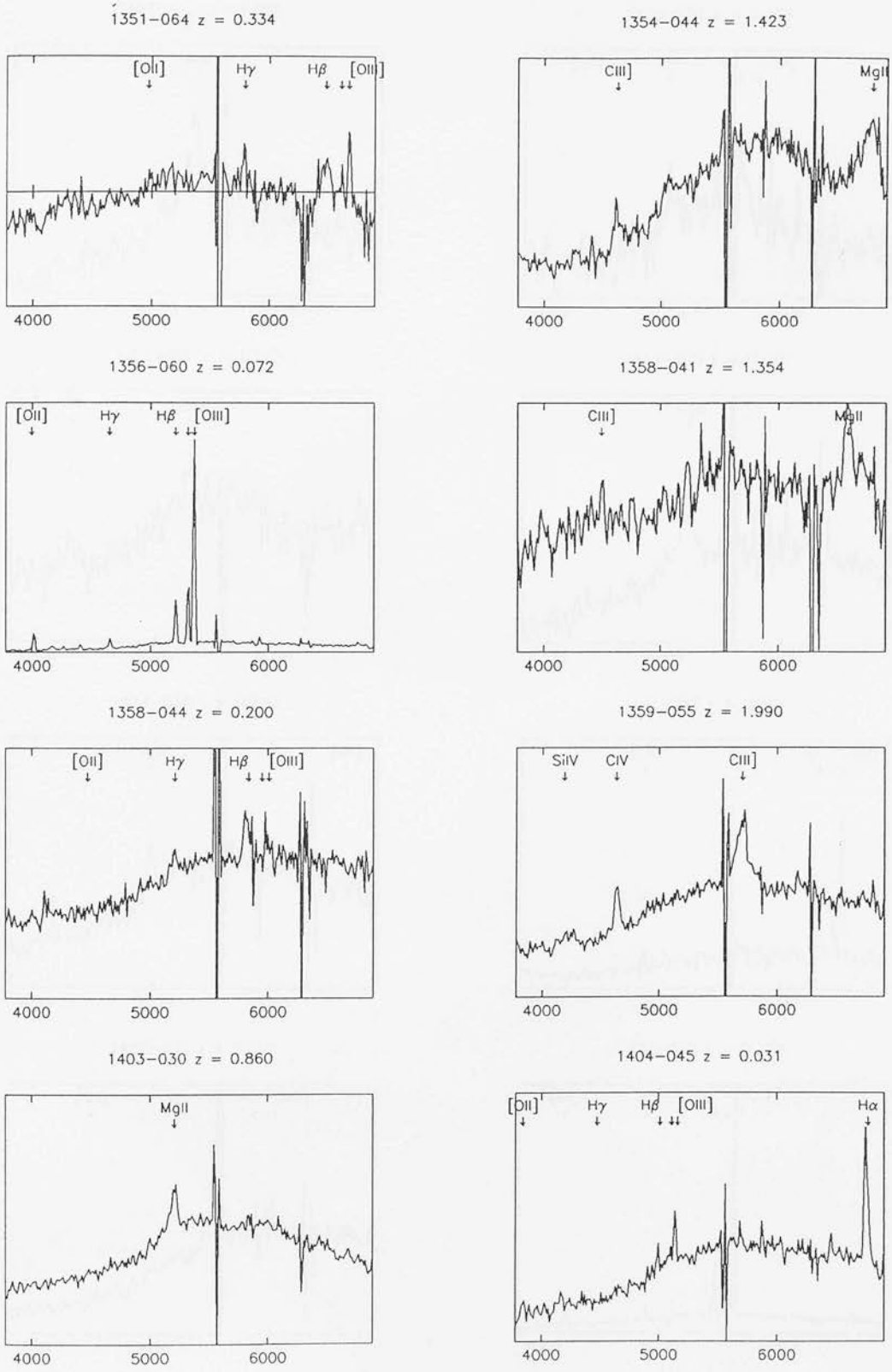

Figure 3.4: Extra-galactic objects observed during the 1991 FLAIR run.

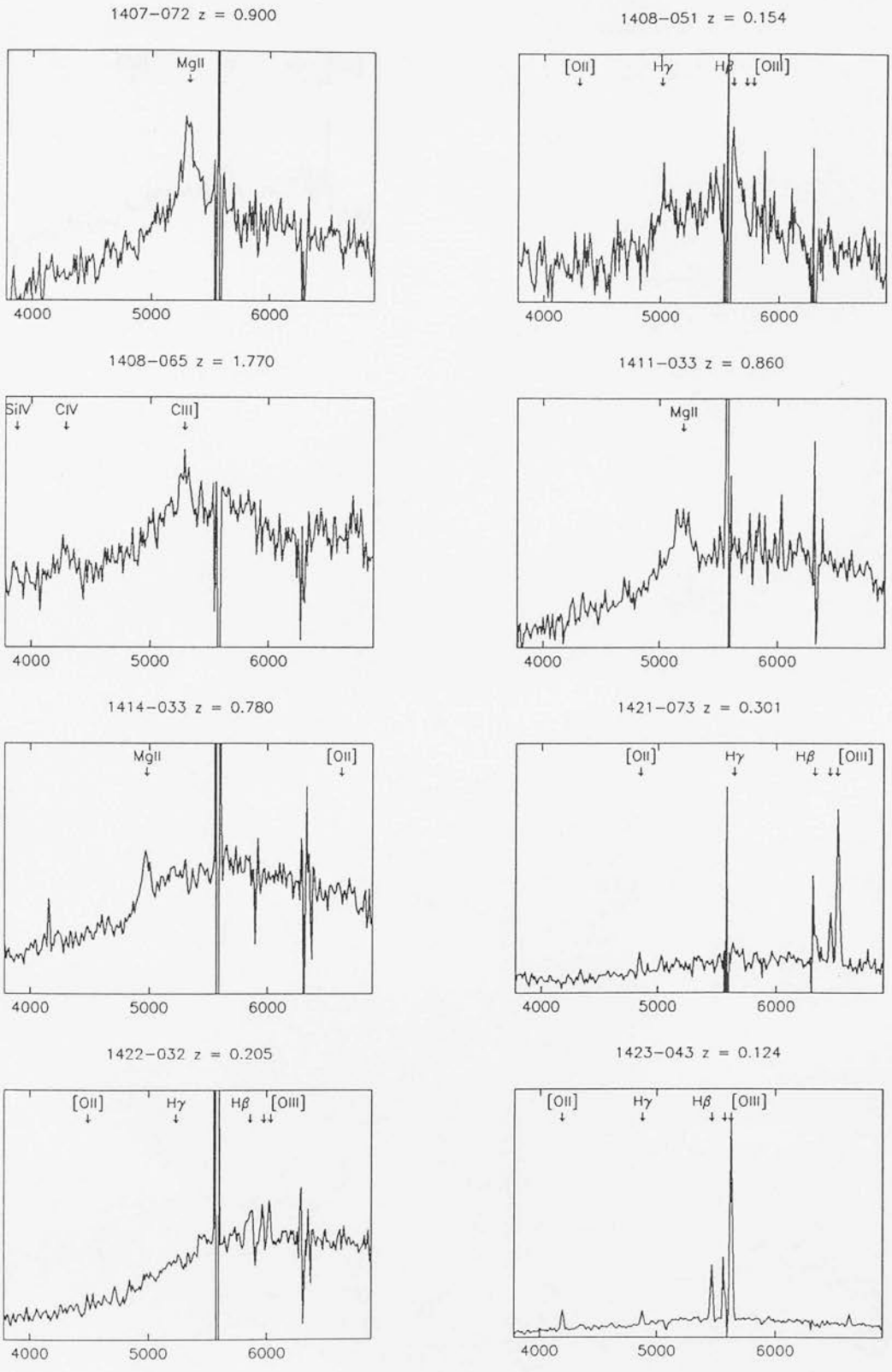

Figure 3.5: Extra-galactic objects observed during the 1991 FLAIR run.

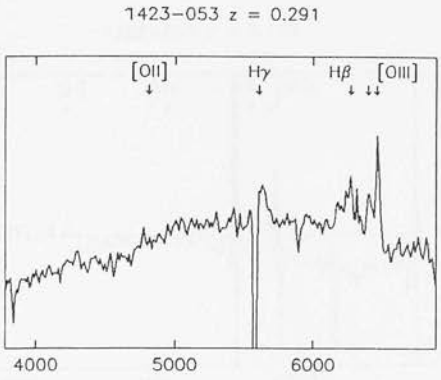

Figure 3.6: Extra-galactic objects observed during the 1991 FLAIR run.

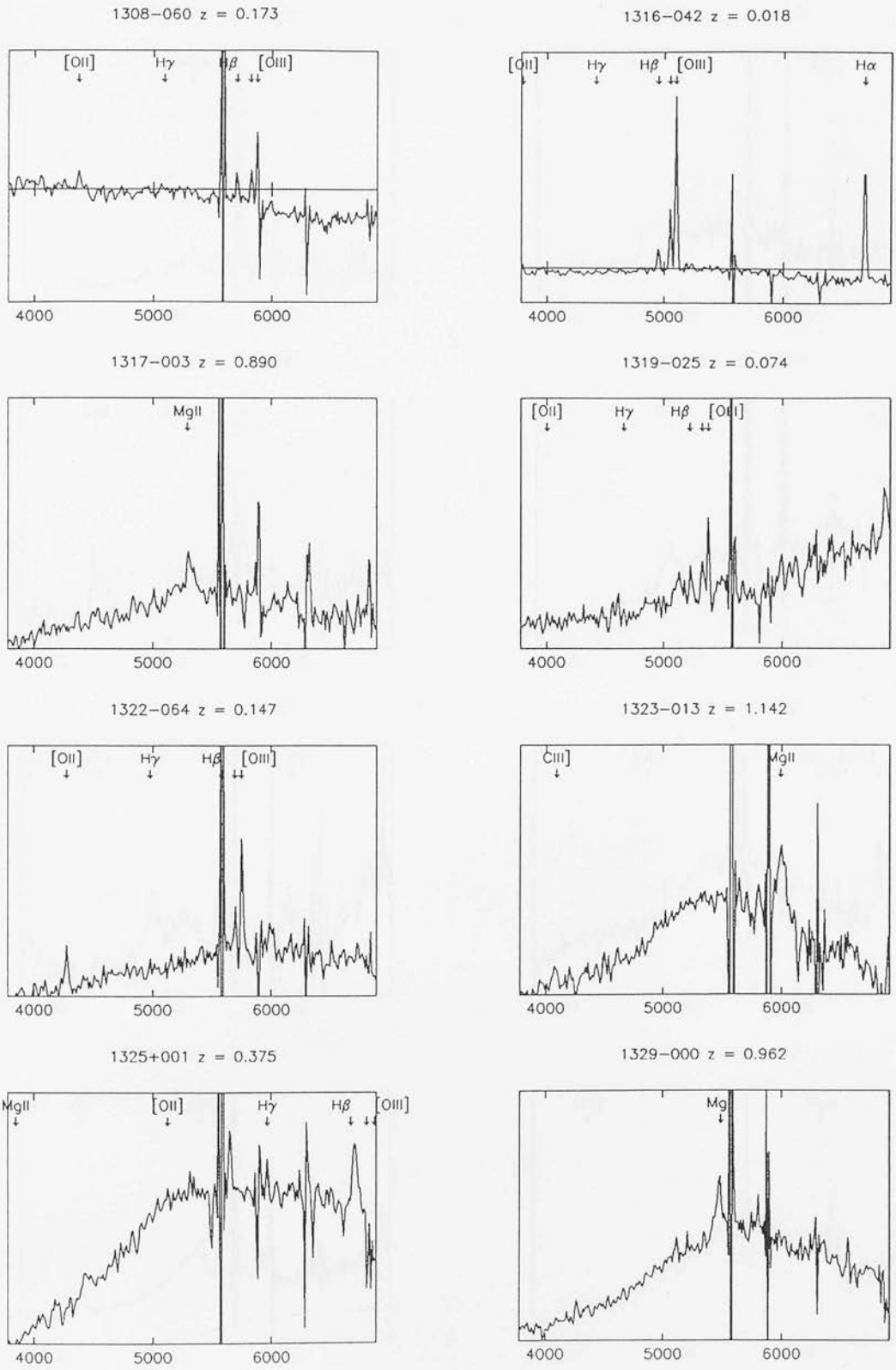

Figure 3.7: Extra-galactic objects observed during the 1992 FLAIR run.

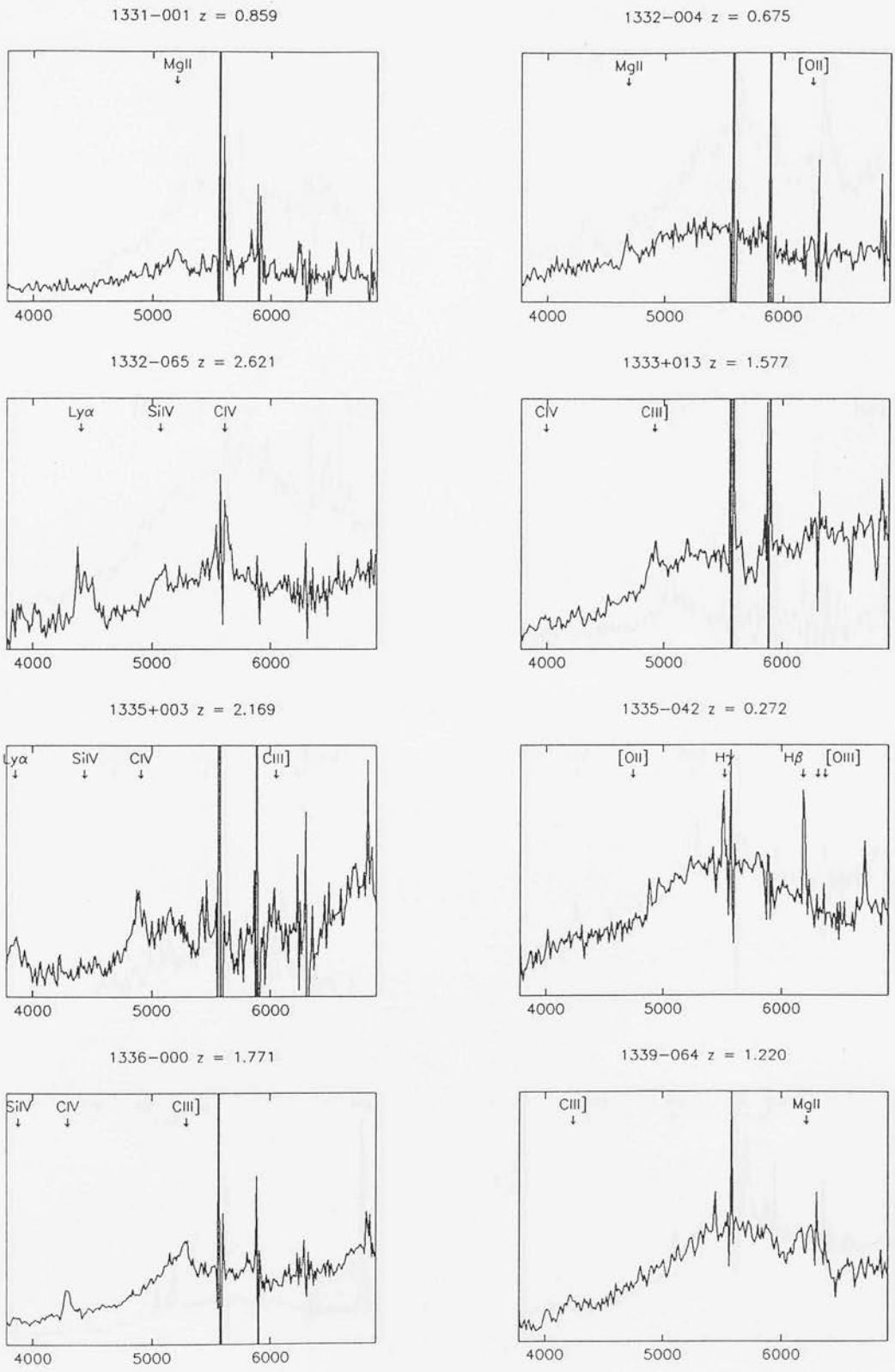

Figure 3.8: Extra-galactic objects observed during the 1992 FLAIR run.

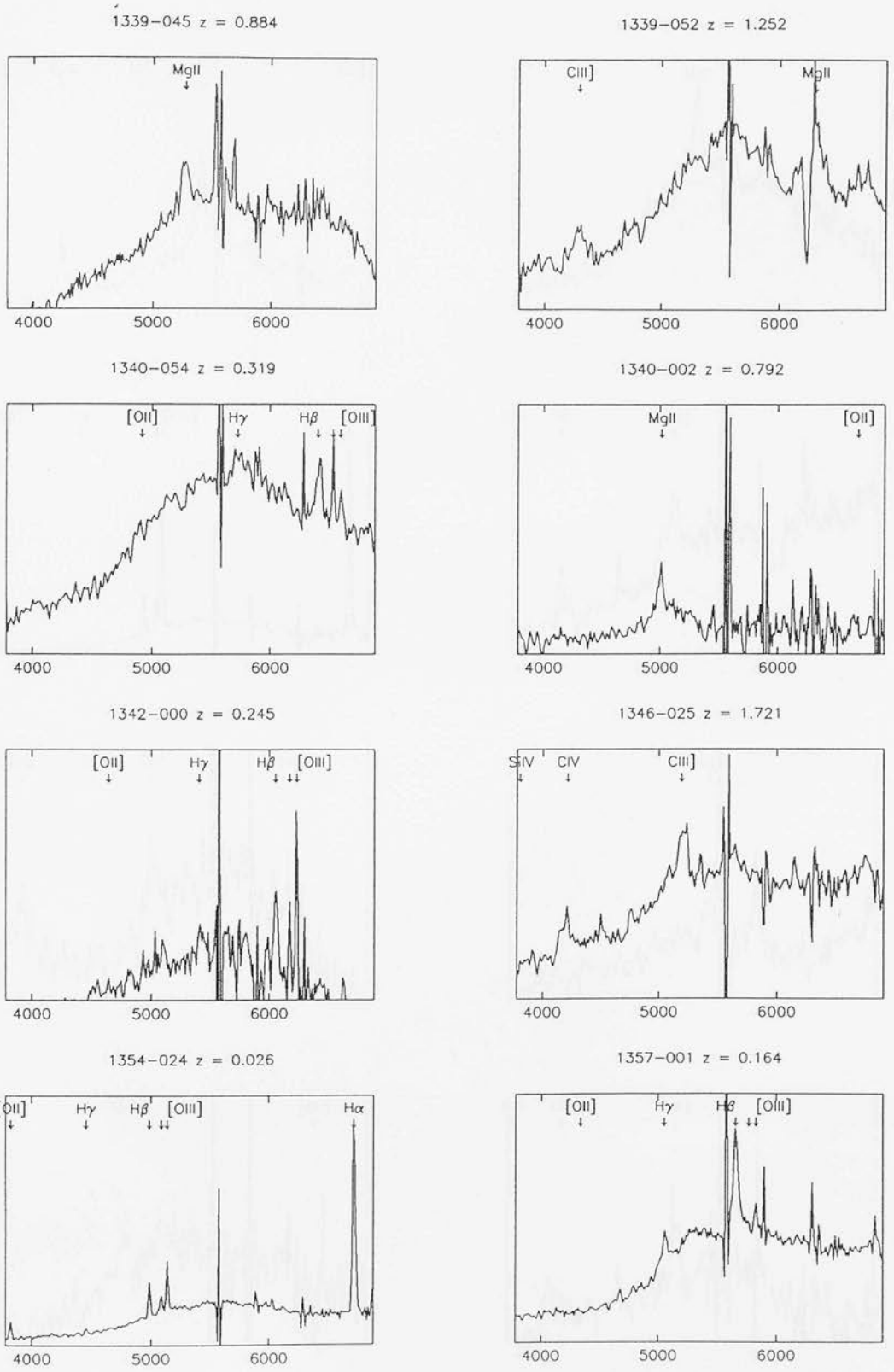

Figure 3.9: Extra-galactic objects observed during the 1992 FLAIR run.

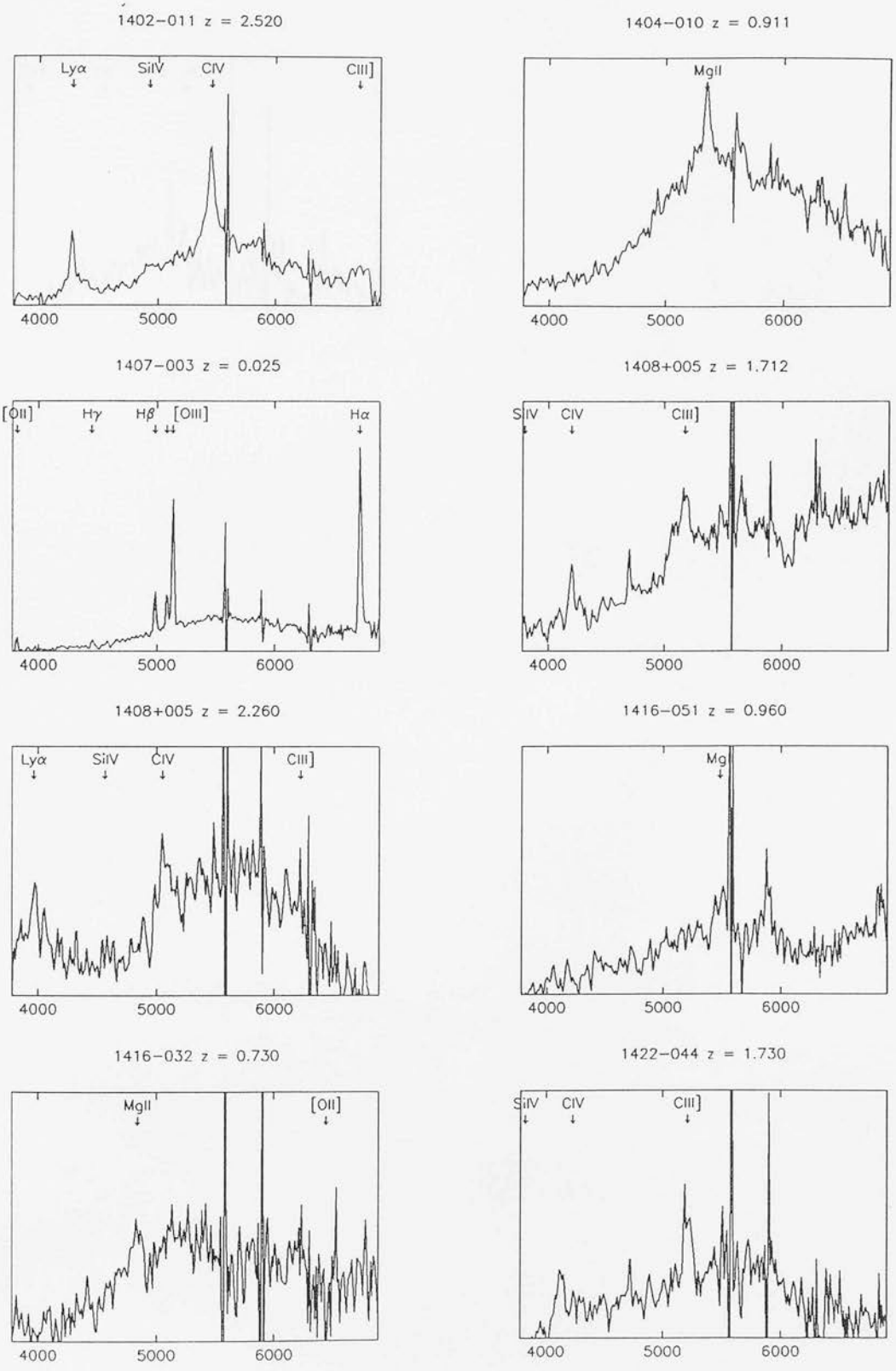

Figure 3.10: Extra-galactic objects observed during the 1992 FLAIR run.

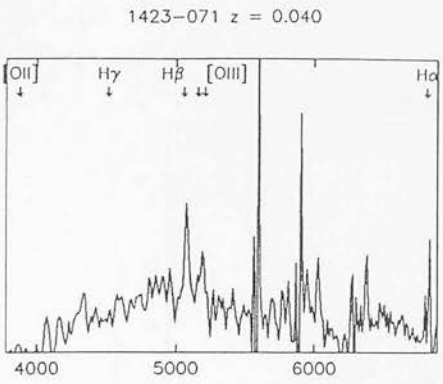

Figure 3.11: Extra-galactic objects observed during the 1992 FLAIR run.

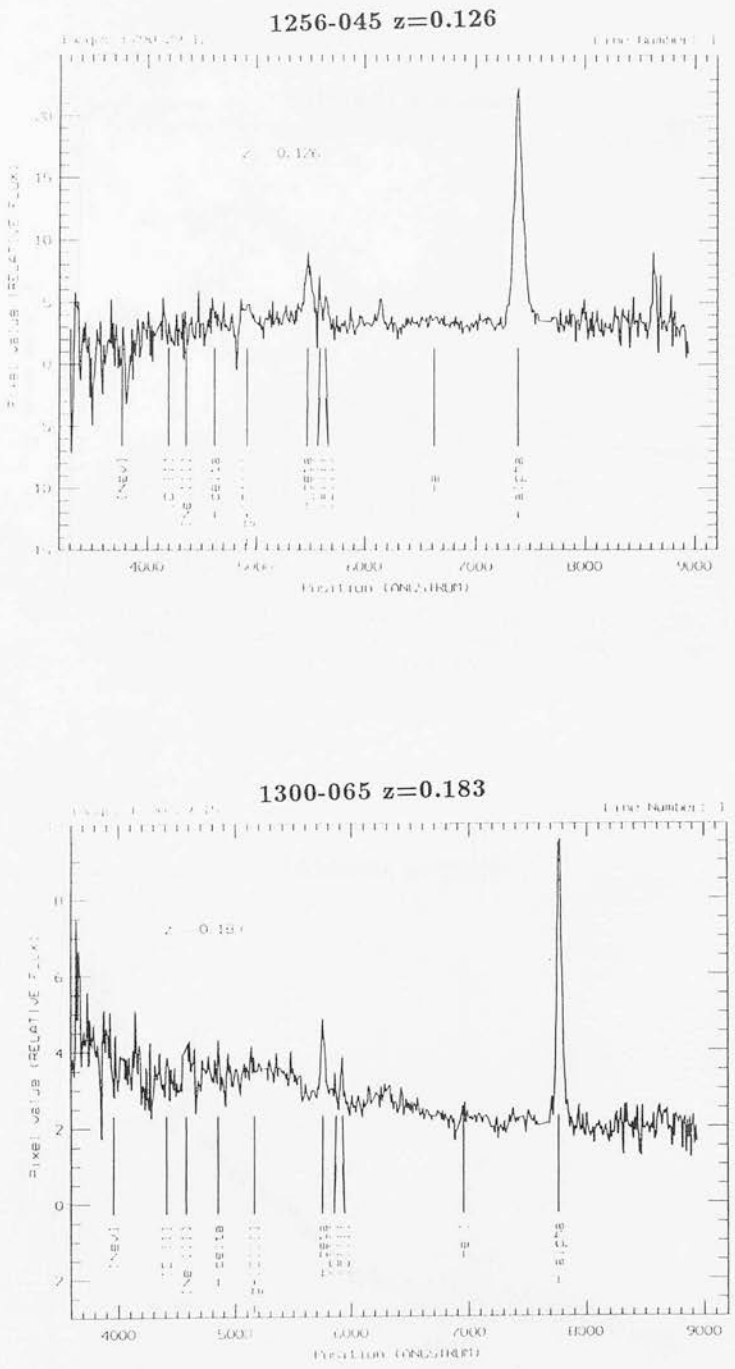

Figure 3.12: Extra-galactic objects observed during the 1991 ESO run.

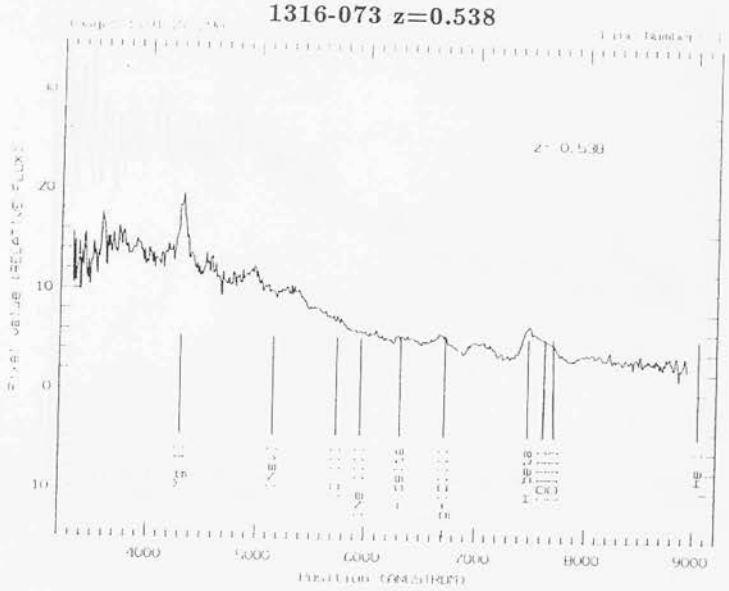

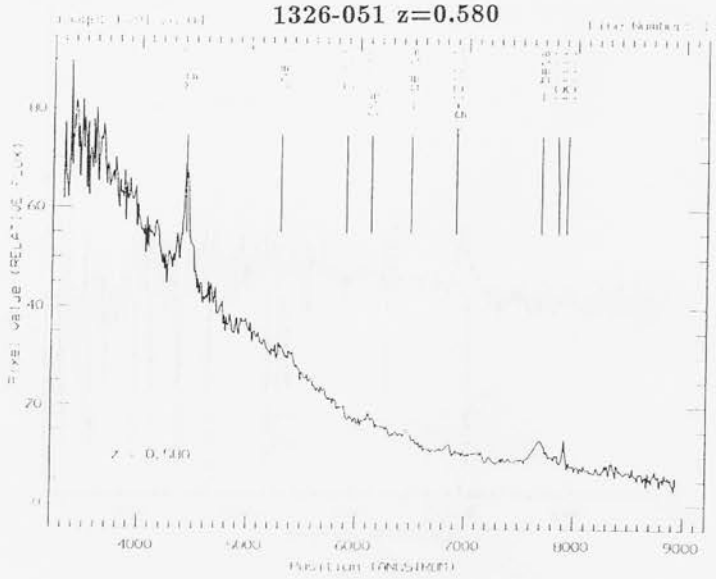

Figure 3.13: Extra-galactic objects observed during the 1991 ESO run.

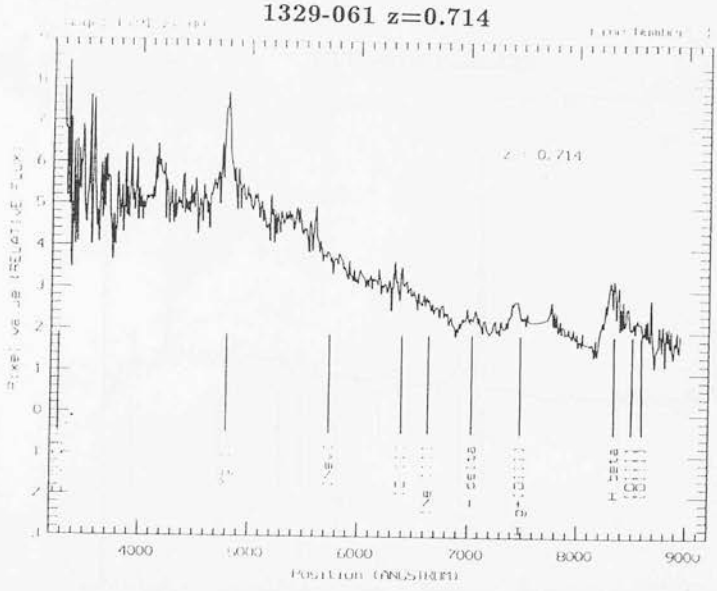

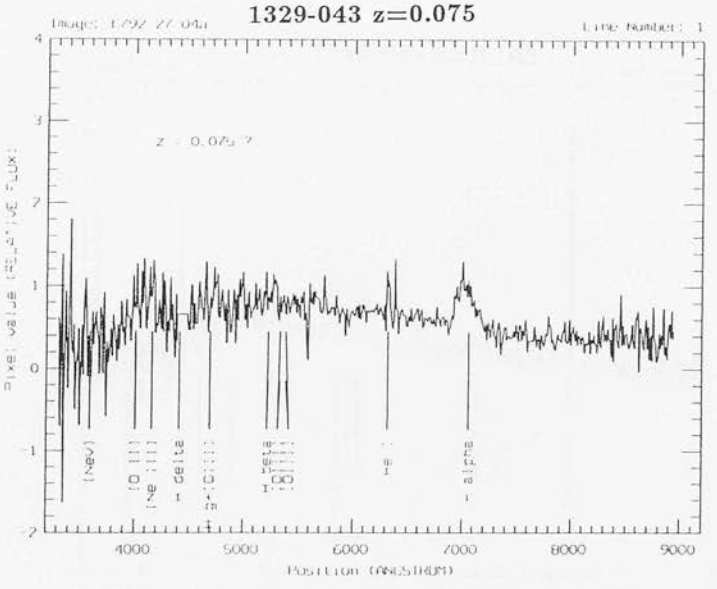

Figure 3.14: Extra-galactic objects observed during the 1991 ESO run.

1333-070 z=0.328

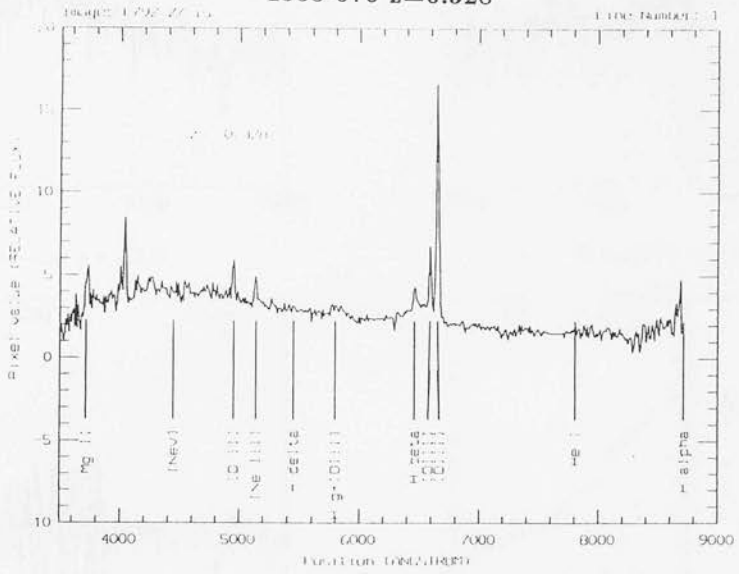

1336-033 z=0.155

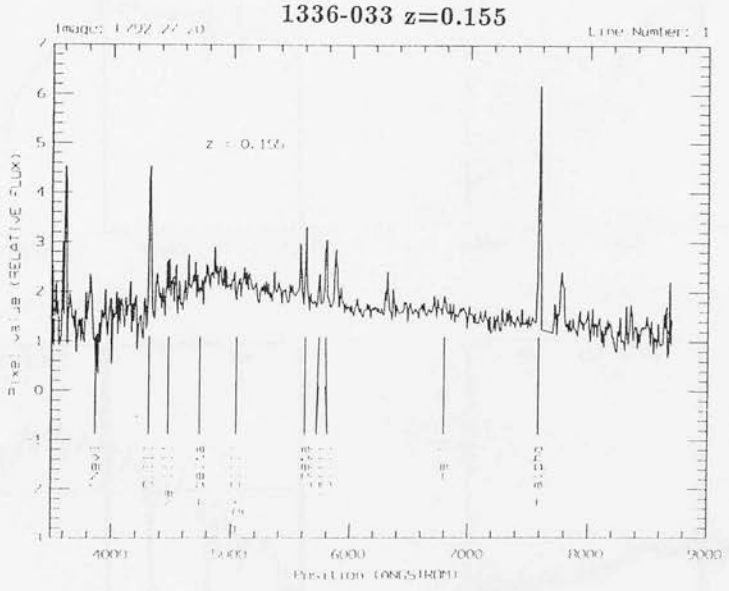

Extra-galactic objects observed during the 1991 ESO run.

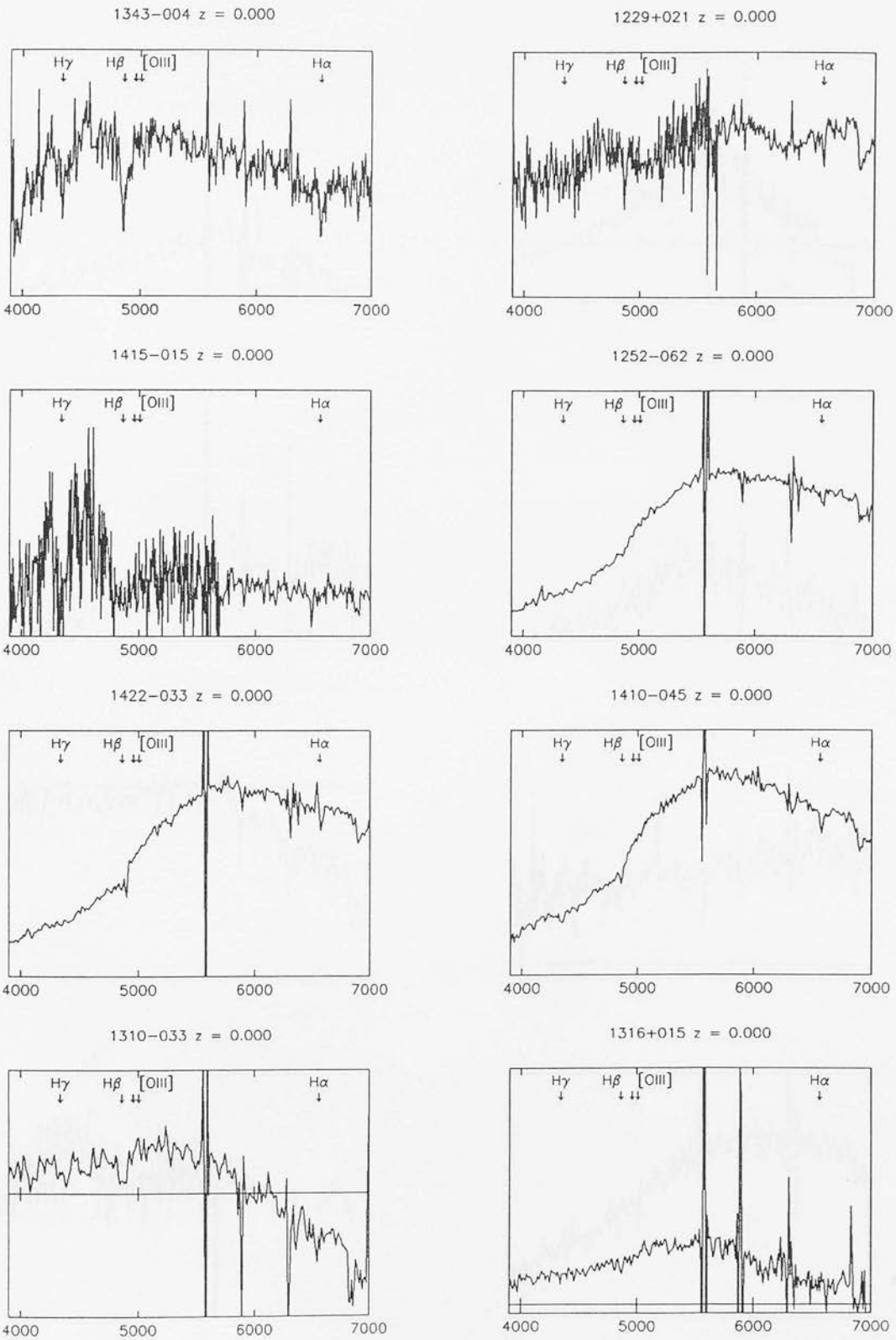

Figure 3.15: Spectra of typical stars found during observing runs.

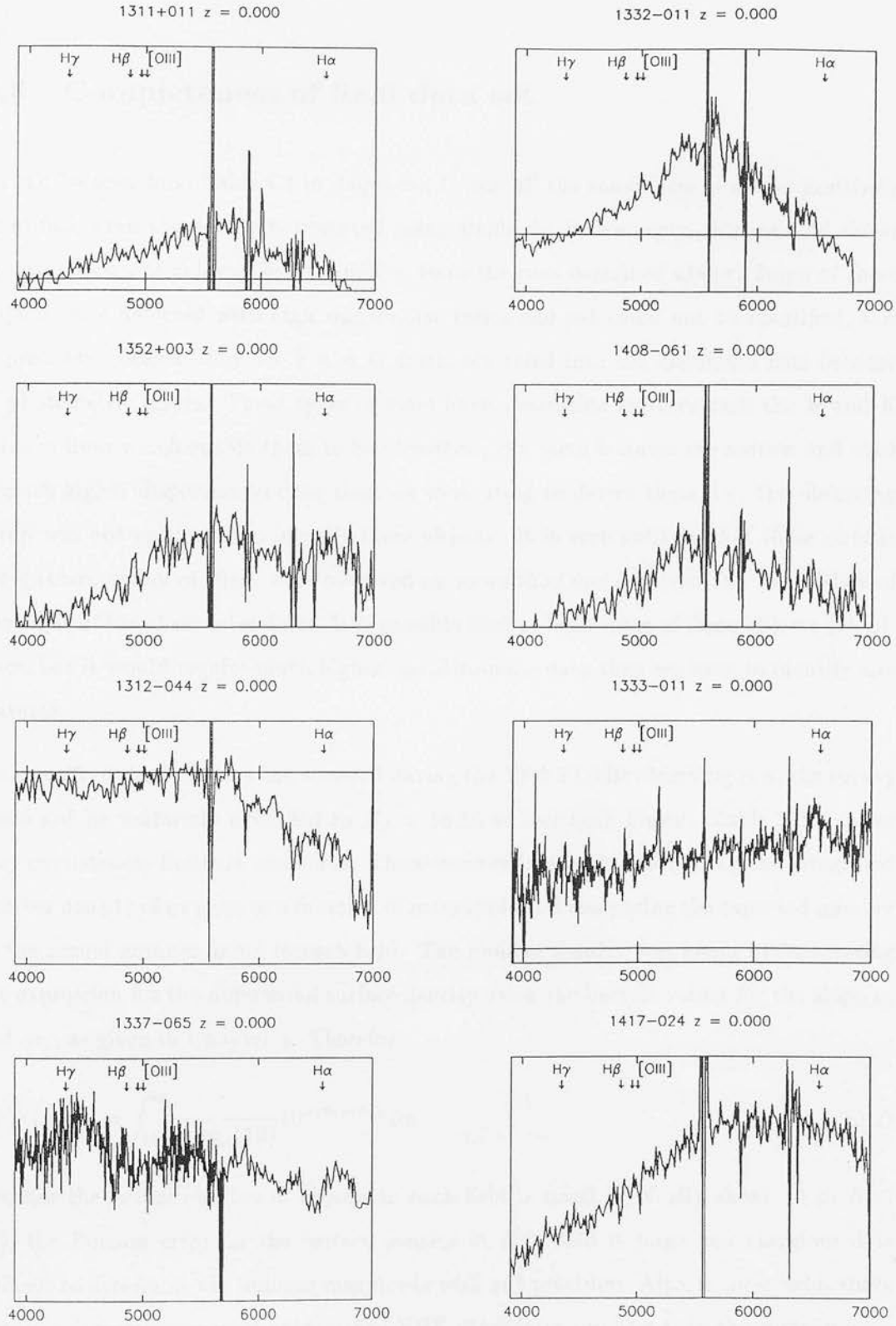

Figure 3.16: Typical unidentified candidates found during observing runs.

3.5 Completeness of final data set

As can be seen from Table C1 in Appendix C, not all the candidates could be positively identified, even those objects observed using single-slit instruments. Figure 3.16 shows typical spectra of unidentified candidates from the runs described above. Some of these objects were detected with high signal-noise ratios and yet could not be identified; this is probably because they are F and G stars, scattered into the candidate lists because of photometric errors. These types of stars have absorption features such the H and K calcium lines which enable them to be identified, but these features are narrow and need a much higher dispersion grating than we were using to detect them, i.e. the observing setup was not optimised to identify these objects. It is very unlikely that these objects are quasars, many of them were observed on more than one occasion and never showed any signs of broad emission lines. It is possible that at least some of these objects are BL Lacs, but it would require much higher signal-to-noise data than we have to identify any features.

As a result of the problems encountered during the 1992 FLAIR observing run, the survey could not be uniformly extended to $B_J = 18.50$ as had been hoped. Table 3.2.1 shows the completeness limits in each field. These were estimated by calculating the integrated number density of quasars as a function of magnitude and comparing the expected number to the actual number found in each field. The number density was found by integrating the expression for the differential surface density using the best-fit values for the slope α, and m_*, as given in Chapter 4. Therefore

$$N(<m) = \int_{15}^{m} \frac{2}{\alpha \log_e(10)} 10^{\alpha(m-m_*)} dm \tag{3.2}$$

Because the actual number of objects in each field is small (typically about 10 to $B \leq 18$), the Poisson error on the surface density in each field is large and therefore it is difficult to determine the limiting magnitude with any precision. Also, in most fields there remain a few unobserved or unidentified UVX candidates brighter than the completeness limits. This means that no field can be considered to be 100% complete. Therefore the effective areas searched have been adjusted accordingly to take into account the fraction of candidates remaining in each field. This was done by taking the number of unidentified

candidates and assuming that half were quasars (using the fact that roughly half the positively identified candidates were quasars) to estimate the total number of quasars in each field. Then the fraction of identified quasars to total number of quasars gives the fractional completeness, and the area in each field was multiplied by this fraction to give the effective area. For instance, if in one field, there were 18 known quasars, and 4 UVX candidates, then this gives a fractional completeness of 90%, and the area of the field is reduced by 10%. Typically the correction applied was not large; of the order of $\sim 5-10\%$, apart from field 794 which is incomplete within any magnitude limits.

It should be noted that the analysis in chapters 4 & 5 is not sensitive to this adjustment of the effective areas due to incompleteness. If one assumes that the fields are 100% complete, this has the effect of reducing the surface density, and hence the space density, of quasars found by this survey but does not change the conclusion that the space density of luminous quasars is higher than was previously thought.

Table 3.2 shows the effective areas in each field. Note that field 794 has a smaller effective area compared to the rest of the survey. This is because it is obviously considerably incomplete when the surface density of quasars found in that field is compared to that found in the rest of the survey. This is probably due to the fact that this field has only ever been observed using FLAIR and with bad seeing.

We can also judge the completeness by looking at the number-redshift histogram. If we look at figure 3.17 we can see that the relation is smooth, apart from an obvious deficiency in objects at redshift $\sim 0.8-0.9$. This is a slightly higher redshift than the classical "hole" at $0.6 \leq z \leq 0.9$ caused by the $U-B$ colours becoming red due to no emission lines in the U band, and MgII in the B band (Wampler & Ponz 1985). Therefore, it is more probable that quasars in this redshift range are being *selected* as candidates, but not being positively *identified* as quasars from their spectra. This could be because at these redshifts MgII is at ~ 5300 Å, i.e. near the sky lines. Also there are no other emission lines in the optical window in this redshift range. The combination of these effects means that even if MgII is present it may well not be identified, and the object not noted as a quasar. The gap in the number-redshift distribution occurs in a relatively narrow redshift range, and probably results in the loss of ~ 8 quasars.

Field	Eff. area (degs^2)
789	22.7
790	23.5
791	23.9
792	23.6
793	23.7
794	4.8
861	23.9
862	23.4
863	23.2
864	22.3
865	24.7
866	23.7
867	23.8

Table 3.2: This table shows the effective areas in each field, after taking into account morphological selection, and unidentified candidates in each field.

Chapter 4 describes the comparison of the quasars found by this survey and by the LBQS (Hewett et al. 1991) in four fields common to both surveys.

Table 3.5 shows all the extra-galactic objects discovered by the observing runs described above, and gives their B_J magnitudes and $U - B_J$ colours. The following two chapters describe the analysis of this data set combined with the UVX quasars discovered by PSM. Table B1 in appendix B shows all the extra-galactic objects found during all the observing runs, including the ones described by PSM, and also an additional run at the INT carried out by Dr. L. Miller in 1989. The key to the notes for tables 3.5, B1 and C1 are the same and are as follows;

a refers to objects which were observed as part of the Edinburgh survey but for which the data were not good enough to allow postive identifications. These objects were also observed as part of the LBQS and the redshifts come from Hewett et al. (1991).

b refers to objects identified by PSM.

c refers to objects identified by Dr. L. Miller from his 1989 observing run.

d refers to objects with positive identifications both in the Edinburgh survey and in the LBQS.

e refers to objects identified from data obtained during the observing runs described in this chapter.

f refers to the quasar found by Palomar-Green; 1352+011.

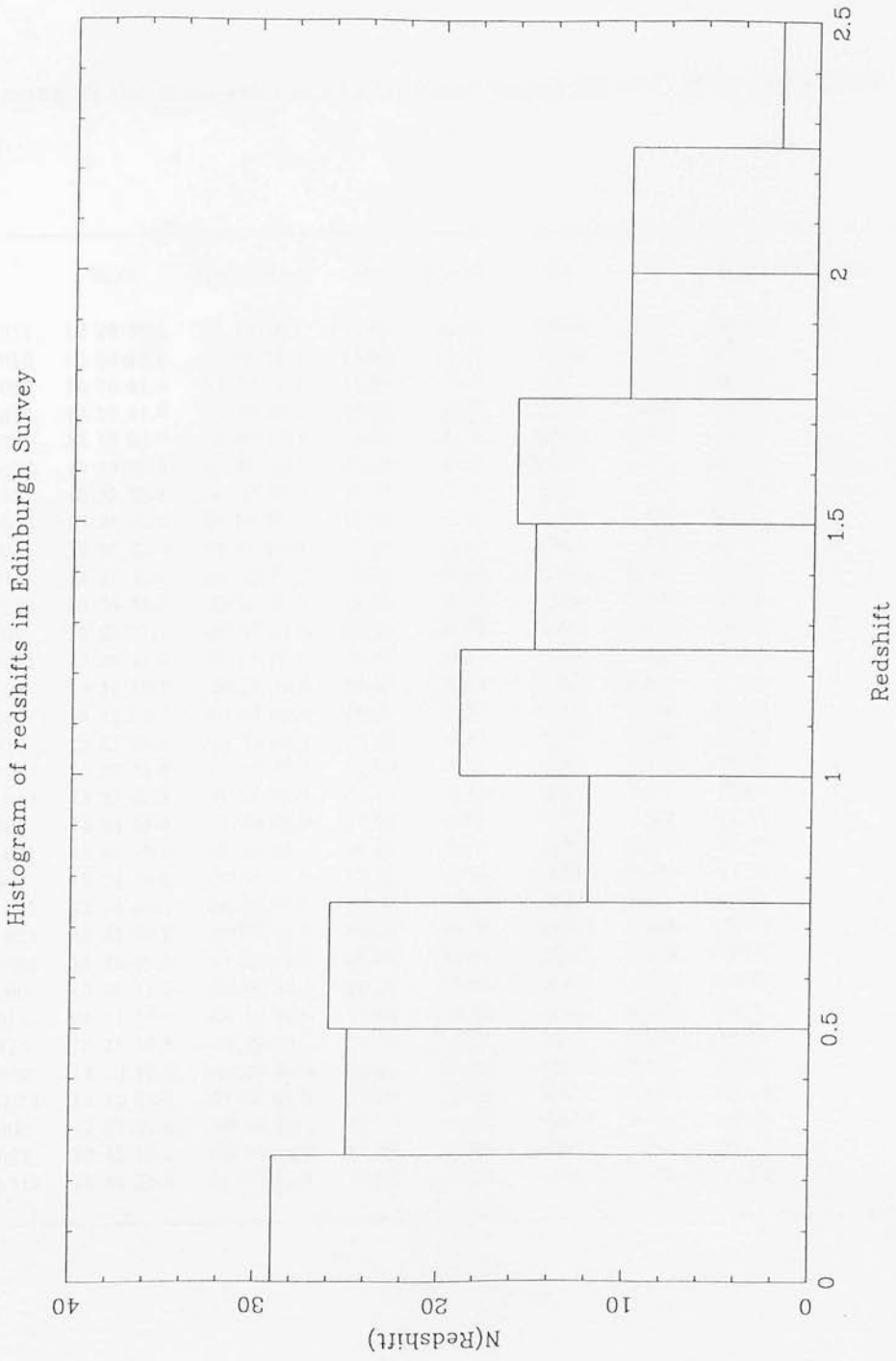

Figure 3.17: The number-redshift relation for all the quasars in the sample in bins of $\Delta z = 0.25$

Table 3.5, showing all the extra-galactic objects found during the INT, ESO and FLAIR observing runs.

Name	R.A.	Declination	B_J	$U-B_J$	ID	z	M_B	Quality	Notes
1228+011	12 28 08.5	01 14 48.7	17.63	-0.04	QSO	1.409	-26.89	2	e
1305+010	13 05 20.8	01 00 21.5	17.89	-0.27	QSO	0.763	-25.33	1	e
1308+010	13 08 47.7	01 09 15.4	17.90	-0.32	QSO	1.074	-26.05		a
1315+014	13 15 41.9	01 40 36.5	18.07	-0.72	QSO	0.689	-24.93	1	e,d
1317-003	13 17 04.7	-00 33 56.1	18.57	-0.75	QSO	0.890	-24.98	1	e,d
1319+014	13 19 39.0	01 46 15.3	17.52	-0.58	NELG	0.183	-22.62	1	e
1323-013	13 23 59.1	-01 38 59.0	18.35	-0.86	QSO	1.142	-25.73	1	e,d
1324+012	13 24 50.9	01 26 55.2	18.49	-0.84	QSO	0.864	-25.00	1	e,d
1325+001	13 25 23.8	00 19 47.0	17.58	-0.27	QSO	0.375	-24.11	3	e
1325-011	13 25 59.8	-01 13 47.3	16.71	-0.30	QSO	0.150	-23.00	1	e,d
1328+020	13 28 58.7	02 05 12.0	18.25	-0.36	QSO	0.692	-24.76		a
1329-000	13 29 57.1	-00 07 54.5	18.39	-0.68	QSO	0.962	-25.33	1	e,d
1330+011	13 30 48.6	01 13 46.9	18.15	-0.67	QSO	1.506	-26.51	1	e,d
1331-001	13 31 10.3	-00 18 16.6	18.31	-0.98	QSO	0.859	-25.16	3	e
1331-010	13 31 53.7	-01 08 29.0	18.01	-0.25	QSO	1.883	-27.12		a
1331-012	13 31 58.8	-01 23 05.7	18.23	-0.41	QSO	0.289	-22.90		a
1332-004	13 32 51.8	-00 45 09.6	17.53	-0.37	QSO	0.675	-25.43	1	e,d
1333+013	13 33 01.7	01 33 24.0	18.15	-0.18	QSO	1.577	-26.61	1	e,d
1334-003	13 34 13.0	-00 33 40.9	17.59	-0.22	QSO	2.806	-28.36	1	e,d
1334+021	13 34 13.8	02 12 58.7	18.10	-0.18	QSO	2.384	-27.52		a
1334-000	13 34 15.2	-00 05 41.0	17.84	-0.64	QSO	0.298	-23.36		a
1334+005	13 34 49.2	00 53 27.0	18.41	-0.45	QSO	0.647	-24.46		a
1335+022	13 35 06.9	02 22 12.8	18.16	-0.58	QSO	1.354	-26.68		a
1335+003	13 35 49.5	00 31 25.5	18.48	-0.56	QSO	2.169	-26.94	1	e
1336-000	13 36 11.0	-00 06 34.5	18.26	-0.65	QSO	1.771	-26.74	1	e
1337-014	13 37 17.0	-01 46 07.9	18.06	-0.45	QSO	1.010	-25.76	1	e,d
1338-015	13 38 46.6	-01 53 48.6	17.60	-0.62	QSO	2.094	-27.75	1	e
1340-002	13 40 12.2	-00 20 38.4	18.27	-0.60	QSO	0.792	-25.03	1	e,d
1340+010	13 40 25.8	01 07 02.8	17.99	-0.67	QSO	1.067	-25.95		a
1342-000	13 42 25.6	-00 00 58.4	17.75	-0.57	QSO	0.245	-23.02	1	e,d
1343-022	13 43 13.1	-02 21 54.8	18.32	-0.32	QSO	0.509	-24.03		a
1344+013	13 44 03.6	01 37 11.5	17.46	-0.67	QSO	1.915	-27.70		a

Table 3.5 continued.

Name	R.A.	Declination	B_J	$U - B_J$	ID	z	M_B	Quality	Notes
1344-022	13 44 38.1	-02 27 36.4	18.28	-0.36	QSO	0.511	-24.08		a
1344-010	13 44 58.0	-01 05 07.8	18.11	-0.74	QSO	1.714	-26.82	1	e,d
1345-013	13 45 14.5	-01 37 28.5	18.49	-0.57	QSO	1.929	-26.69		a
1345-000	13 45 17.8	-00 00 23.0	18.11	-0.44	QSO	0.552	-24.42		a
1346+012	13 46 01.8	01 21 19.9	18.52	-0.67	QSO	1.930	-26.66		a
1346+000	13 46 48.3	00 07 54.5	18.36	-0.19	QSO	1.127	-25.69		a
1347-002	13 47 00.2	-00 26 10.8	17.77	-0.40	QSO	0.515	-24.61	1	e,d
1347-023	13 47 47.7	-02 37 07.7	17.34	-0.35	NELG	0.139	-22.20	1	e
1348-005	13 48 10.3	-00 54 09.5	18.21	-0.36	QSO	1.474	-26.41		a
1354+011	13 54 17.2	01 17 21.6	17.97	-0.77	QSO	1.210	-26.23	1	e
1357-001	13 57 09.1	-00 19 53.2	17.43	-0.57	QSO	0.164	-22.47	1	e
1402-011	14 02 11.2	-01 16 02.0	18.32	-0.43	QSO	2.520	-27.41	2	e
1404-010	14 04 20.7	-01 02 54.2	18.49	-0.64	QSO	0.911	-25.11	1	e
1407-003	14 07 38.0	-00 38 17.3	18.30	-0.57	QSO	0.025	-17.53	1	e
1408+005	14 08 34.5	00 50 11.7	18.09	-0.69	QSO	1.712	-26.84	1	e
1408+005	14 08 50.3	00 56 56.8	18.44	-0.31	QSO	2.260	-27.07	1	e
1424+011	14 24 41.6	01 12 50.7	16.38	-0.35	NELG	0.052	-21.03	1	e
1429-010	14 29 07.3	-01 00 17.4	17.49	-0.68	QSO	0.661	-25.42	1	e,d
1429-003	14 29 09.4	-00 36 57.7	18.47	-0.74	QSO	1.179	-25.68		a
1433-001	14 33 50.7	-00 16 3.9	18.07	-0.56	QSO	0.324	-23.31	1	e,d
1437-014	14 37 46.8	-01 43 37.0	18.41	-0.60	QSO	0.718	-24.68	1	e,d
1250-070	12 50 46.1	-07 00 37.5	16.43	-0.67	QSO	0.097	-22.33	2	e
1251-073	12 51 59.7	-07 37 32.1	18.02	-1.12	QSO	1.476	-26.60	3	e
1252-065	12 52 51.3	-06 59 06.7	18.00	-1.25	QSO	0.250	-22.82	1	e
1253-032	12 53 30.4	-03 29 36.9	17.49	-1.20	QSO	2.238	-28.00	2	e
1254-073	12 54 39.8	-07 36 42.2	18.00	-1.28	QSO	0.175	-22.04	1	e
1255-043	12 55 55.8	-04 37 37.7	16.64	-1.04	QSO	0.173	-23.38	1	e
1256-045	12 56 49.0	-04 58 39.3	17.10	-1.34	QSO	0.126	-22.23	1	e
1300-065	13 00 10.7	-06 57 48.8	16.80	-1.01	QSO	0.183	-23.34	1	e
1304-061	13 04 31.0	-06 15 58.5	17.88	-1.27	QSO	1.441	-26.69	2	e
1308-060	13 08 11.6	-06 07 35.8	18.46	-0.93	QSO	0.173	-21.56	2	e
1316-042	13 16 03.6	-04 24 22.6	18.10	-0.42	NELG	0.018	-17.01	1	e
1316-073	13 16 48.4	-07 34 43.2	16.49	-0.74	QSO	0.538	-25.98	1	e
1319-025	13 19 26.1	-02 59 03.0	18.34	-0.29	QSO	0.074	-19.84	2	e
1322-064	13 22 07.9	-06 41 50.2	17.99	-0.43	QSO	0.147	-21.68	1	e

Table 3.5 continued.

Name	R.A.	Declination	B_J	$U-B_J$	ID	z	M_B	Quality	Notes
1326-051	13 26 52.5	-05 16 06.6	15.47	-0.45	QSO	0.580	-27.16	1	e
1329-061	13 29 09.4	-06 15 20.6	17.57	-0.46	QSO	0.714	-25.51	1	e
1329-043	13 29 23.9	-04 31 10.7	16.58	-0.23	QSO	0.075	-21.63	2	e
1332-065	13 32 50.0	-06 59 45.9	18.29	-0.26	QSO	2.621	-27.52	1	e
1333-070	13 33 41.5	-07 07 35.4	18.04	-0.88	NELG	0.328	-23.36	1	e
1335-024	13 35 01.6	-02 41 53.6	18.15	-0.52	QSO	0.610	-24.59	1	e,d
1335-042	13 35 20.2	-04 22 36.0	18.35	-0.36	QSO	0.272	-22.65	3	e
1336-033	13 36 00.3	-03 34 09.4	17.90	-0.59	NELG	0.155	-21.88	1	e
1336-042	13 36 09.4	-04 23 40.9	17.10	-0.68	QSO	0.163	-22.79	1	e
1339-045	13 39 39.3	-04 59 49.2	18.25	-0.77	QSO	0.884	-25.29	2	e
1339-052	13 39 41.4	-05 26 12.4	18.11	-0.47	QSO	1.252	-26.16	2	e
1339-064	13 39 49.7	-06 48 04.6	18.34	-0.88	QSO	1.220	-25.88	2	e
1340-054	13 40 52.8	-05 45 26.8	17.94	-0.77	QSO	0.319	-23.40	1	e
1346-025	13 46 53.5	-02 51 55.8	18.21	-0.88	QSO	1.721	-26.73	1	e,d
1351-064	13 51 11.9	-06 41 02.7	17.95	-1.08	QSO	0.334	-23.49	2	e
1354-044	13 54 03.9	-04 49 53.0	17.70	-0.81	QSO	1.423	-26.84	2	e
1354-024	13 54 15.5	-02 40 30.2	16.97	-0.48	QSO	0.026	-18.94	1	e
1356-060	13 56 44.9	-06 07 43.8	16.17	-0.66	NELG	0.072	-21.95	1	e
1358-044	13 58 41.6	-04 41 20.6	18.04	-0.84	QSO	0.200	-22.29	2	e
1358-041	13 58 48.7	-04 12 42.3	17.37	-0.76	QSO	1.354	-27.07	2	e
1359-055	13 59 03.8	-05 53 56.1	17.72	-0.94	QSO	1.990	-27.52	1	e
1403-030	14 03 35.2	-03 04 56.4	17.01	-0.80	QSO	0.860	-26.47	2	e
1404-045	14 04 53.9	-04 55 56.0	15.79	-0.62	QSO	0.031	-20.57	1	e
1407-072	14 07 52.8	-07 22 31.7	17.97	-0.85	QSO	0.900	-25.60	2	e
1408-051	14 08 01.9	-05 11 35.3	17.65	-0.54	QSO	0.154	-22.12	1	e
1408-065	14 08 28.1	-06 51 10.6	17.80	-0.88	QSO	1.770	-27.20	2	e
1411-033	14 11 41.4	-03 33 46.5	17.91	-0.78	QSO	0.860	-25.57	2	e
1414-033	14 14 30.3	-03 31 16.0	17.66	-0.63	QSO	0.780	-25.61	3	e
1416-051	14 16 33.6	-05 18 59.7	18.50	-0.72	QSO	0.96	-25.21	2	e
1416-032	14 16 50.1	-03 24 51.0	18.10	-0.71	QSO	0.73	-25.03	3	e
1421-073	14 21 08.6	-07 30 05.0	17.77	-0.37	NELG	0.301	-23.44	1	e
1422-044	14 22 41.1	-04 44 51.3	18.23	-0.33	QSO	1.730	-26.72	2	e
1422-032	14 22 48.9	-03 23 50.9	18.08	-0.46	QSO	0.205	-22.31	2	e
1423-053	14 23 04.7	-05 34 46.8	17.42	-0.74	QSO	0.291	-23.73	1	e
1423-071	14 23 22.2	-07 18 00.3	18.46	-1.03	QSO	0.040	-18.38	3	e
1423-043	14 23 55.1	-04 34 01.1	17.91	-0.60	NELG	0.124	-21.32	1	e

Chapter 4

The Surface Density of Bright Quasars

4.1 Introduction

In this chapter I calculate the surface density of quasars in the Edinburgh survey as a function of magnitude; the differential log(number)-magnitude relation, and compare it with that of other surveys, principally the Palomar-Green survey (Schmidt & Green, 1983) and the Large Bright Quasar Survey (Morris *et al.* 1991, and references therein). The main aims are to see how complete this survey is with respect to other surveys and to see whether the surface density of bright quasars is significantly different from previous measurements. I then discuss the implications of this result. Part of this work was originally published as a paper in *Monthly Notices of the Royal Astronomical Society* (Goldschmidt, Miller, La Franca & Cristiani, 1992).

The initial evidence for cosmological evolution of quasars came from the steep cumulative number-magnitude relation. Braccesi *et al.* (1980) calculated the gradient from the AB survey and found that $d\log_{10}(n < m)/dm = 0.86$ for bright quasars with $z \leq 2.2$, significantly steeper than 0.6; the value for a non-evolving population in a Euclidean universe. Schmidt & Green (1983, hereafter SG) used the Palomar Bright Quasar sample

(consisting of 93 quasars with $M_B \leq -23$ selected from the Palomar-Green survey (Green, Schmidt & Liebert, 1986)) with the AB survey to calculate the gradient of the cumulative relation and obtained a value of $0.90 + / - 0.05$. They also used the $< V/V_{max} >$ test (Schmidt, 1968) as a function of absolute magnitude for quasars in the PG survey and found $< V/V_{max} >= 0.613 + / - 0.030$ again showing significant evolution. However, Wampler & Ponz (1985) have argued that much of the evidence for evolution in optically selected samples can come from biases such as the observed anti-correlation between the equivalent width of Ly-α, C IV and total luminosity (the Baldwin effect, Baldwin 1977) which can lead to the luminosities of quasars with $z \sim 2$ (the redshift at which Lyα and C IV are detected in the optical) being overestimated, leading to overestimates in the rate of evolution. Also if the photometric errors are large and increase as a function of magnitude then Malmquist bias can be important. This is because the bias will lead to objects fainter than the survey flux limit being scattered brighter and therefore being included in the survey. Because these objects are faint, they are more likely to be at large distances and hence high redshifts, again leading to an overestimate in the space density of high redshift objects and a corresponding overestimate in the rate of evolution needed to account for the observed space density. Wampler & Ponz ran simulations upon model distributions with no evolution and discovered that by adding in photometric errors of $\sim$ 0.3m, values of $< V/V_{max} >= 0.67$ can be obtained, leading one to doubt the measured values from optical surveys. But these biases cannot explain the evolution measured for *radio* selected samples, and so Wampler & Ponz conclude that at least some of the detected evolution must be genuine.

The Palomar BQS is the largest complete sample of very bright quasars, and so is ideal for use with fainter samples to constrain the form of quasar evolution. SG found that the best fit model was luminosity-dependent density evolution, in which the most luminous quasars evolved faster than fainter ones. In contrast, Boyle *et al.* (1988) used this sample with the fainter larger AAT sample and found that Pure Luminosity Evolution (PLE) in which all quasars evolve at the same rate in terms of luminosity, regardless of their initial luminosity, was the best fit model.

However, it has been suggested that the PG survey is far more incomplete than SG calculated, and thus the space density of bright quasars is underestimated. Wampler &

Ponz note the paucity of quasars in the PG survey with $0.45 \leq z \leq 0.95$, presumably due to the effect of MgII ($\lambda = 2798$ Å) on the measured flux in the B band, rendering these objects less UVX. This implies that the observational UVX limits that SG set are too blue and thus they miss quasars. However this incompleteness in the PG survey has been difficult to quantify, because of the lack of other surveys in the same magnitude range. Section 4.3 compares the surface density of quasars in the PG and the Edinburgh surveys to see if the PG survey is indeed incomplete.

4.2 The differential number-magnitude relation.

The surface density of quasars in the Edinburgh survey was compared with that in other surveys, specifically the Palomar-Green survey (SG), the MBQS (Mitchell *et al.*, 1984), the AAT survey (Boyle *et al.*, 1990), the SA94 survey (La Franca et al., 1992) and the LBQS (Morris *et al.* 1991, and references therein). In order to carry out a direct comparison between surveys, photographic magnitudes in the B_J system in the Edinburgh survey were converted to the standard $B_{JOHNSON}$ system, using the colour equations for stars of Blair & Gilmore (1982);

$$B_{JOHNSON} = B_J + 0.28(B_{JOHNSON} - V) \tag{4.1}$$

and

$$V = v + 0.10(B_{JOHNSON} - V) \tag{4.2}$$

where B_J and v are the photographic magnitudes, and $B_{JOHNSON}$ and V are the standard photoelectric magnitudes. Equations 4.1 and 4.2 can be re-arranged to give

$$B_{JOHNSON} = B_J + 0.34(B_J - v) \tag{4.3}$$

The mean $B_J - v$ colour of 0.18, computed from all the quasars in the survey, was used, and so the B_J magnitudes were transformed onto the $B_{JOHNSON}$ system by adding a constant offset of $0.06m$. In the PG survey, the magnitudes of individual objects are

B_J lim	Eff. Area (degs^2)
17.5	244
17.7	223
18.0	201
18.1	97
18.2	41
18.3	20

Table 4.1: This table shows the effective area searched to find quasars as a function of limiting magnitude, taking into account incompleteness due to morphological selection and uncertain IDs.

in the $B_{JOHNSON}$ system, but the limiting magnitudes are not, so these too had to be converted so that the effective area at each magnitude could be calculated accurately. The effective areas as a function of magnitude in the Edinburgh survey were calculated from the effective areas in each field as discussed in Chapter 3. Table 4.1 shows the effective areas searched in the Edinburgh survey as a function of limiting magnitude. Table B1 in Appendix B shows all the quasars in the Edinburgh Survey.

Fig. 4.1 shows the differential log(number)-magnitude relation for the surveys. The errors on the points are Poissonian with 68% confidence limits. Only quasars in the range $0.3 \leq z \leq 2.2$ have been included because the morphological criteria that most workers use will discriminate against quasars at lower redshifts. (See Chapter 3 for a more extensive discussion of this point.)

It can be seen that the surface density of quasars in this survey agrees well with the MBQS survey. Indeed, the brightest point in the MBQS survey, which used to appear anomalous compared to other data, agrees well with the Edinburgh data. It can also be seen that the data from this survey lie above that from the PG survey, implying the latter survey is incomplete. The surface density as determined from the Edinburgh survey agrees well with that from the LBQS.

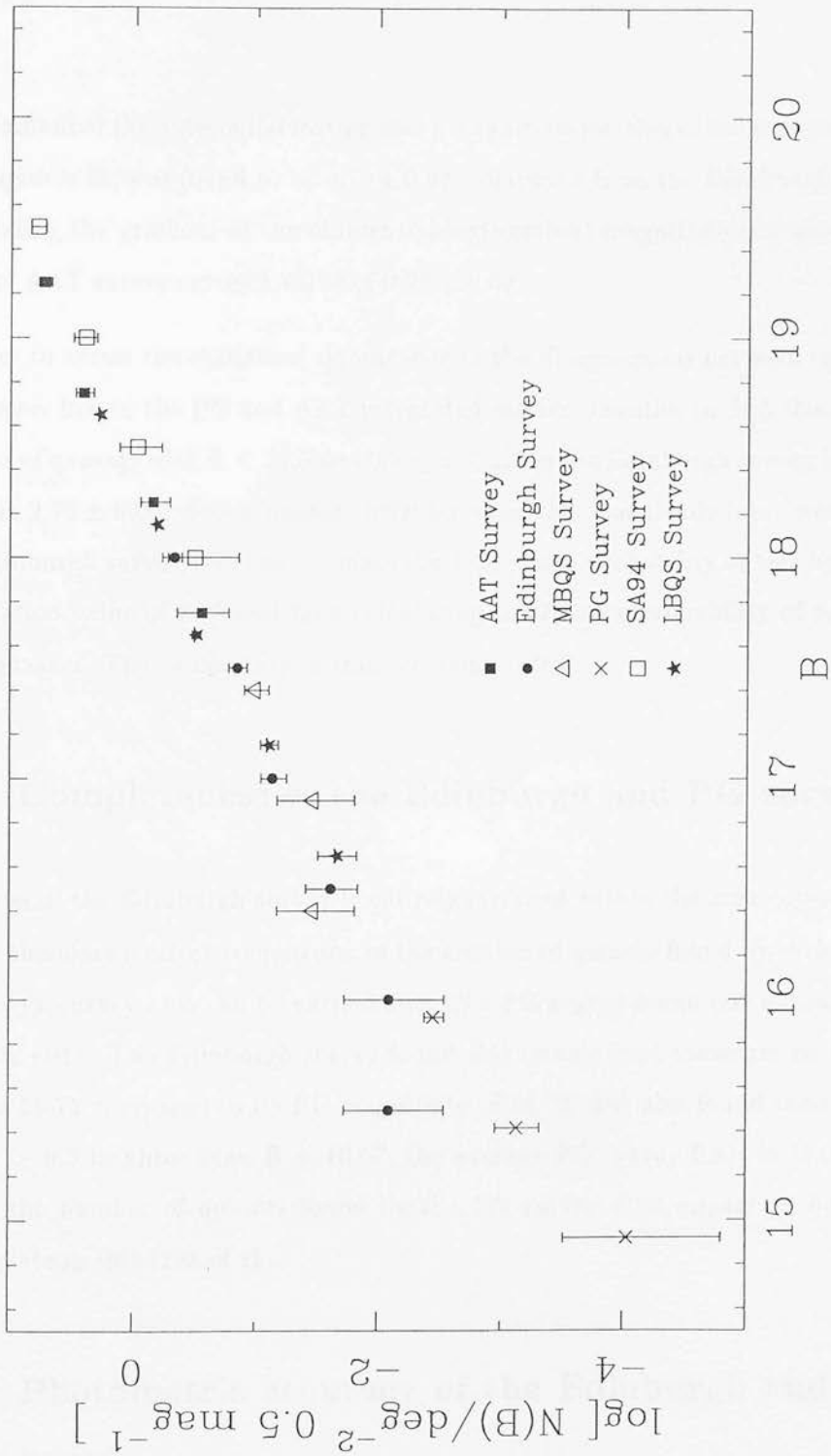

Figure 4.1: The differential log(number)–magnitude relation for the Edinburgh, AAT, MBQS, SA94 and LBQS surveys.

The gradient of the differential log(number)-magnitude relation calculated from a weighted least-squares fit, was found to be 0.79 ± 0.07, computed from the Edinburgh survey alone. Calculating the gradient of the differential log(number)-magnitude relation from the PG and the AAT surveys gives a value of 0.98 ± 0.02.

In order to assess the statistical significance of the disagreement between the surveys, we fit a power law to the PG and AAT integrated surface densities to find that the expected number of quasars with $B < 16.5$ and $0.3 \leq z \leq 2.2$ in the Edinburgh survey in this redshift range is 2.75 ± 0.06. Seven quasars brighter than this magnitude limit were detected in the Edinburgh survey. We can estimate the Poissonian probability of this by assuming an expectation value of 2.75 and then calculating the Poisson probability of measuring 7 or more quasars. The probability of this occurring is 2%.

4.3 Completeness of the Edinburgh and PG surveys

The area of the Edinburgh survey is entirely included within the area covered by the PG survey therefore a direct comparison of the number of quasars found by each survey in the Edinburgh survey area can be carried out. The PG survey found one quasar in this area, PG 1352+011. The Edinburgh survey found this quasar (and measures its magnitude to be $B = 16.71$ compared to its PG magnitude of 16.02) but also found three new quasars with $z \geq 0.3$ brighter than $B = 16.07$, the average PG survey limit in this area (GSL). Hence the number of quasars found by the PG survey does appear to be significantly incomplete in this area of sky.

4.4 Photometric accuracy of the Edinburgh and PG surveys

One possible explanation for the apparent incompleteness of the PG survey is that there exists a systematic difference in the calibration of the two surveys. This can be tested by making a direct comparison of measured magnitudes of other UVX objects found in common. Most of the objects found in the PG survey are hot stars, and GSL provide a list

of these with their photographic B_{PG} magnitudes and, in a few cases, photoelectric U, B_{pe} and V magnitudes. In this section, all photometry in the B_J system from the Edinburgh survey will be referred to as B_{Edin}. There are 24 stars in common with both surveys in the range $15 < B_{Edin} < 17$. The quasar PG 1352+011 is excluded since its magnitude could have varied between measurements. The mean offset between the measured photographic magnitudes is $B_{Edin} - B_{PG} = +0.34$. The photographic magnitudes are plotted as open circles in Fig. 4.2 which shows that this difference exists throughout the magnitude range, and is most likely due to a systematic zero-point error in the PG survey in this region of sky. This offset is significantly larger than the colour term applied to the Edinburgh magnitude system in order to make it consistent with that of the PG system, so it is unlikely that it is due to any residual difference between the two photometry systems. In contrast, if we only consider the seven objects which have photoelectric photometry in the PG survey we find an average offset of $B_{Edin} - B_{pe} = 0.06$ (filled circles in Fig.4.2), so the Edinburgh photometry agrees with GSL's photoelectric photometry.

The quoted random error in B_{PG} is 0.29, so that with the average value of $d\log(n)/dm = 0.32$ for the UVX objects, we expect a Malmquist bias (see section below) of 0.03 magnitudes (GSL), which is not a significant contribution to the observed offset in photographic magnitudes. Malmquist bias cannot explain the observed deficit in the PG survey, as its effect is always to scatter brighter objects fainter than the flux limit and increase the observed surface density *above* the true value. The same is true of the offset between the two surveys, whatever its origin, since the magnitudes of the PG survey are measured as being too bright, so the objects in the survey are fainter than measured. The effect should be to increase the surface density, not decrease it and hence the observed *deficit* in numbers of PG quasars cannot be explained by this offset between the two surveys.

We should note that the systematic difference between the Edinburgh and PG surveys may well not extend to all regions of the PG survey. However there is insufficient information currently available to determine the cause of the incompleteness in the PG survey.

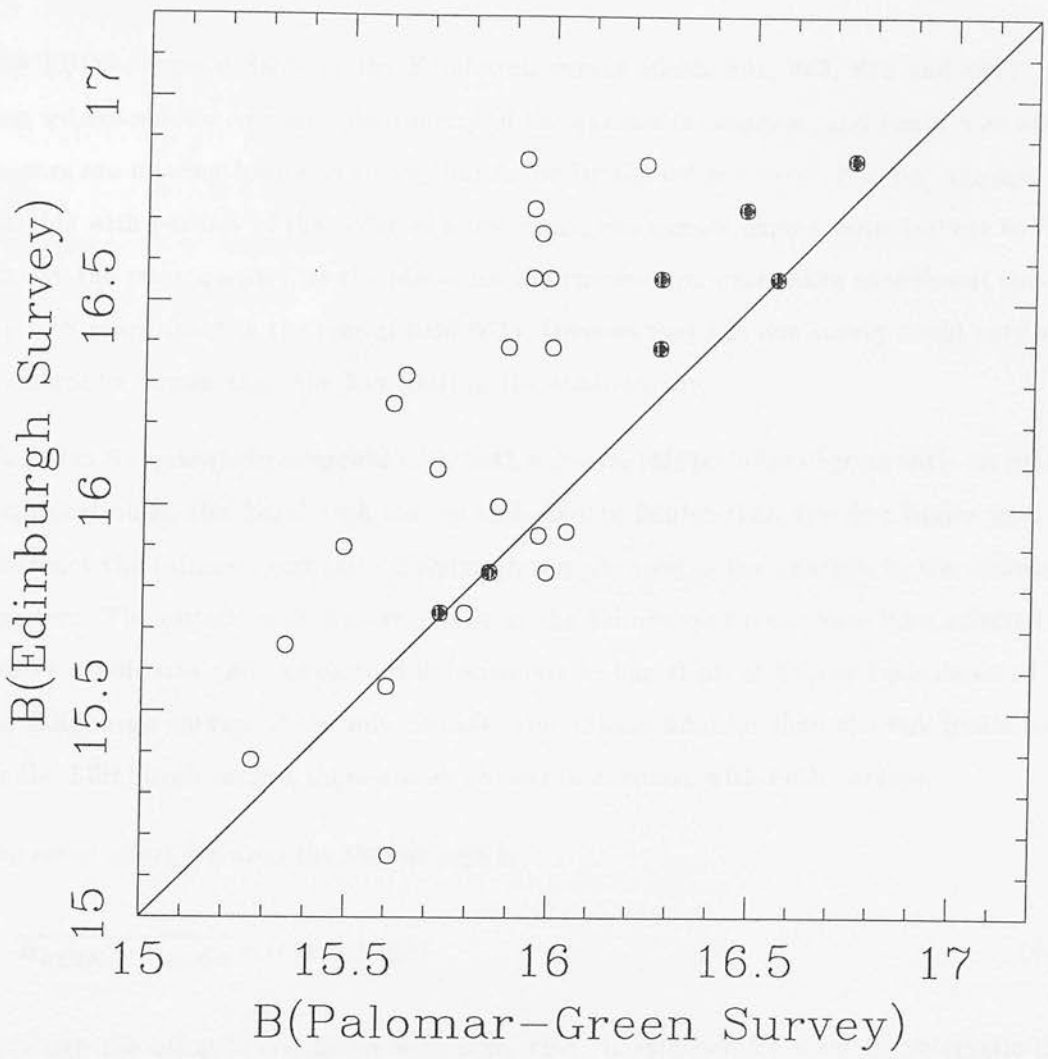

Figure 4.2: Photographic and photoelectric magnitudes for UVX stars in common with both the Edinburgh and the PG surveys. Filled circles are stars with photoelectric data in the PG survey, empty circles are stars with photographic data in both surveys.

4.5 Comparing the Edinburgh survey with the LBQS

The LBQS covers 4 fields in the Edinburgh survey (fields 861, 863, 864 and 867), and thus we are able to compare photometry of the quasars in common, and count how many quasars are missing from one survey but found by the other survey. Because quasars are variable with periods of the order of a few years, one cannot expect both surveys to find exactly the same quasars, as the plates for the two surveys were taken at different epochs (up to 6 years apart in the case of field 861). Quasars found in one survey could vary and therefore be fainter than the flux limit in the other survey.

There are 84 quasars in common with both surveys, this includes objects with uncertain identification in the Edinburgh survey and objects fainter than the flux limits used to construct the (almost) complete Edinburgh sample used in the analysis in the following chapters. The objects with uncertain IDs in the Edinburgh survey have been selected as quasar candidates and therefore it is legitimate to flag them as having been detected by the Edinburgh survey. If we only consider the objects brighter than the flux limits used for the Edinburgh survey, there are 38 objects in common with both surveys.

The mean offset between the two surveys is

$$\overline{B_{EDIN} - B_{LBQS}} = 0.15m \pm 0.21 \tag{4.4}$$

Although the offset is consistent with zero, there is evidence for a small systematic difference in the photometry of the two surveys. When the offset was calculated for each of the four fields, it was found to be positive in all four fields.

The LBQS found 9 quasars in the area in common that were missed by the Edinburgh survey, and the Edinburgh survey found 8 quasars that were missed by the LBQS. Five quasars missed by the Edinburgh survey and detected by the LBQS are in field 861. As mentioned above, this field has the longest baseline between plates taken for each of the two surveys. Half the quasars missing from the Edinburgh survey in field 861 have magnitudes in the LBQS with $B_{LBQS} \geq B_{Ed.lim} - 0.1$, i.e. within $0.1m$ of the Edinburgh flux limit, suggesting that variability is the partial cause of the non-detections. The remaining three fields have a total of four quasars flagged as detected by the LBQS

and not by the Edinburgh survey. This implies that these fields are not significantly incomplete. Some incompleteness is allowed for in the calculation of the effective areas due to the morphological criteria applied.

The LBQS appears to be missing eight quasars in the four fields. Two of these quasars have quality flags of 3 and therefore if they have not been detected by the LBQS are quite likely not to be quasars at all. This apparent incompleteness is most likely taken care of in the calculation of the effective area of the LBQS, allowing for spectra being obscured on the objective prism plates. Again, variability could also be important, although 5 quasars flagged as missing from the LBQS have $B_{EDIN} \leq B_{LBQSlim} - 1$, i.e. they are at least a magnitude brighter than the flux limit in the LBQS, implying that variability cannot be wholly responsible.

No quasar survey can claim to be 100% complete, and apart from field 861 in the Edinburgh survey, both surveys show a high fractional completeness with respect to each other. This is borne out by the differential number-magnitude diagram (Figure 4.1) showing the good agreement between the surface density of quasars measured by each survey.

4.6 Malmquist bias in the Edinburgh survey

Malmquist bias occurs because a) all measurements have a finite rms error and b) the slope of the differential log(n)–m relation is greater than zero. This means that when a flux limit is imposed on a sample of objects, objects fainter than that limit will be measured as being brighter and will hence be erroneously included in the sample, and objects brighter than the flux limit will be scattered out of the sample. This will result in a net increase in the number of observed objects, over and above the true number. The objects scattered into the sample at the faint flux limit are, obviously, fainter than the rest of the sample and therefore will have a different redshift distribution. This will lead to errors in the measured number-redshift distribution for the sample.

For instance, in the case of quasar surveys this could lead to overestimates in the rate of evolution, as empirically the faint objects will be found at higher redshifts than the rest of the sample so the space density of high redshift objects will be overestimated, and the

bright objects scattered out will be at lower redshifts, leading to an underestimate in the number of low redshift objects.

The effect of Malmquist bias on this sample is quantified by convolving the error distribution with the differential log(n)-m relation to calculate the net number of objects scattered into the survey at the flux limit. Assuming a power law distribution for the log(n)-m relation gives

$$N = 2 \times 10^{-0.4\alpha(m-m_*)} \tag{4.5}$$

where $\alpha = 2.175$, $m_* = 18.37$ (calculated from the AAT, and Edinburgh surveys in the magnitude range $17.5 \leq m \leq 18.5$) and N is the number of objects per square degree per magnitude. Convolving this with the normal error distribution

$$f(\delta S) = \frac{1}{\sqrt{(2\pi\sigma^2)}} \exp(\frac{\delta S^2}{2\sigma^2}) \tag{4.6}$$

where σ is the 1 σ error on the measured magnitudes (in this case, $\approx 0.1m$, see Chapter 3) and S is the measured flux (i.e. $m = -2.5\log(S)$) gives

$$\Delta(\ln N) = \frac{\Delta(N)}{N} \approx \frac{\alpha^2\sigma^2}{2S^2} \tag{4.7}$$

σ/S is the fractional error in the measured fluxes and for an error of $0.1m$ is equal to 0.08. Therefore the above equation gives a fractional error in the measured number of objects of

$$\frac{\Delta(N)}{N} = \frac{(-2.175)^2}{2} \times (0.08)^2 = 0.02 \tag{4.8}$$

This shows that the malmquist effect is about 2% and is therefore considerably smaller than the Poisson error and cannot have a large effect on the measured rate of evolution.

4.7 Conclusions

The gradient of the differential log(number)-magnitude relation is 0.79 for quasars brighter than $B = 18$ (significantly lower than was previously thought), and the surface density of

quasars brighter than $B \leq 18$ has been measured with greater accuracy than previously. The shallower gradient implies that these quasars now evolve slower than was previously thought, and so it is not clear whether the luminosity function will still have a "break" in it at all redshifts and whether PLE is still the best fit model.

A comparison of the Edinburgh survey photometry with that of the Palomar-Green survey shows a systematic offset between the photographic photometry of both surveys in that the photographic magnitudes in the PG survey are brighter than those in the Edinburgh survey, although the photoelectric photometry of the PG survey agrees well with the photographic photometry in the Edinburgh survey. The PG survey has been shown to be incomplete by a factor of 3.0 compared to the Edinburgh survey. The cause of the incompleteness is not known.

It has also been shown that Malmquist bias does not have a significant effect on the measured surface density of quasars in the Edinburgh survey.

The next step is to compute the luminosity function in redshift bins for the Edinburgh survey, and see if Pure Luminosity Evolution is still a good description of the data.

Chapter 5

The Cosmological Evolution of Luminous Quasars

5.1 Introduction

In this chapter I use the complete sample of bright quasars from the Edinburgh Survey to construct the luminosity function in redshift shells. By comparing the observed differential luminosity function and the observed cumulative absolute magnitude distribution with that predicted by the Pure Luminosity Evolution model of Boyle *et al.* (1988, 1990, 1991) I show that the model does not describe the data well. I then discuss the implications in terms of various models of quasar evolution.

5.2 Calculating the Luminosity Function

The cosmological evolution of a population of objects can be quantified by calculating the comoving space density binned as a function of redshift; the luminosity function (LF). The simplest method of calculating the LF, if the survey samples a wide range of fluxes and hence a wide range of luminosities at each redshift, is the method of summing inverse accessed volumes (Schmidt 1968) in which nothing has to be assumed about the shape or

the evolution of the luminosity function.

5.2.1 The Differential Luminosity Function

The differential luminosity function is calculated in the following way; the quasar sample is divided up into narrow redshift slices and it is assumed that the quasars do not evolve significantly within each slice. The LF is the weighted addition of objects as a function of luminosity and redshift, where the weighting is inversely proportional to the volume in the universe searched to find that object, given its flux and redshift, and the flux limit of the survey.

$$\Phi(M,z) = \sum_{i=1}^{N} \frac{1}{V_a(M,z)} \tag{5.1}$$

Note that the accessible volume V_a is nearly always larger than the actual volume of the universe enclosed by the redshift of the object. This is because, given that the object's flux is higher than the flux limit of the survey the object could in fact be moved to a higher redshift and become fainter, and still be detected by the survey. If the LF is being calculated from more than one survey (as will be the case here) then in order to extract the maximum information using the measured flux and redshift of each object, and the flux limits of all the surveys considered, the total accessible volume for each object is the sum of the accessible volumes for that object as calculated for *each* survey. This is because, although the object was only actually detected by one survey, given its flux and the flux limits of each survey, it could in principle have been detected *a priori* by all the surveys (Avni & Bahcall, 1980).

The accessible volume V_a searched to find an object is found from the comoving distance d_c corresponding to the minimum and maximum redshifts that the object could have and still be included within the survey;

$$d_c = \left(\frac{c}{H_0}\right) \frac{q_0 z + (q_0 - 1)[(2q_0 z + 1)^{1/2} - 1]}{(1+z)q_0^2} \tag{5.2}$$

where q_0 is the dimensionless deceleration parameter ($q_0 = \Omega_0/2$) and H_0 is the Hubble constant (see Chapter 1). If $q_0 = 0.5$ then the above simplifies to;

$$d_c = \left(\frac{2c}{H_0}\right)\left[1-(1+z)^{-1/2}\right] \tag{5.3}$$

The volume out to a distance d_c, subtended by a solid angle Ω (in steradians) on the sky is

$$V = \frac{\Omega}{4\pi}\frac{4\pi}{3}d_c^3 \tag{5.4}$$

Therefore the *accessible* volume is the difference between the volumes enclosed by the minimum and maximum comoving distances;

$$V_a = \frac{\Omega}{3}(d_{max}^3 - d_{min}^3) \tag{5.5}$$

where d_{max} and d_{min} are the maximum and minimum comoving distances the object could have and still be included within the sample.

5.2.2 The Cumulative Luminosity Function

The unbinned cumulative LF will also be used in this chapter to see if the model sufficiently describes the data. It has been argued (*e.g.* Hewett *et al.* 1993) that this form of the LF is preferable to the differential form as there is no need for binning (and hence smoothing) the data into wide bins of absolute magnitude, and one can see the contribution that each quasar makes to the function. Also, binning the differential LF into bins of absolute magnitude is not trivial, as one is faced with the problem of converting the flux limits into luminosity limits over the wide range of redshifts that each redshift bin covers.

One advantage of using the cumulative LF is that the one-sample Kolmogorov-Smirnoff (KS) test can then be used to assess the goodness-of-fit of any model (*e.g.* Conover, 1980). This non-parametric test calculates the maximum discrepancy (*i.e.* vertical distance) between the normalised observed and model distribution functions. The distribution of the distances is known and so can be used to calculate the probability that the data are drawn from the model distribution.

5.2.3 Calculating the luminosities of the quasars

In order to calculate the LF, the luminosities of the quasars in a particular rest-frame band must be calculated. However the *observed* fluxes are all measured at the same band in the observer's frame. Because all the quasars are at different redshifts, this observed band translates to a different band centred on a different wavelength for each quasar.

If we consider the *bolometric* luminosity of the quasar; L_{bol}, and the measured bolometric flux; S_{bol} then

$$S_{bol} = \frac{L_{bol}}{4\pi d_c^2 (1+z)^2} \tag{5.6}$$

The measured flux is reduced by more than the factor $4\pi d_c^2$ because of a) the rate of arrival of the photons is reduced due to the expansion of the universe, and b) the energy of each photon is reduced, because of the redshift. If we define Luminosity Distance d_L to be

$$d_L = d_c(1+z) = \frac{2c}{H_0}\left(1+z-\sqrt{1+z}\right) \tag{5.7}$$

then the above equation looks like the inverse square law;

$$S_{bol} = \frac{L_{bol}}{4\pi d_L^2} \tag{5.8}$$

If we now consider measurements made in a fixed band centred on a fixed frequency we have to consider two more effects due to the expansion of the universe. It is these effects that are contained in the K-correction. These extra effects are a) the rest band expands as the universe expands, and b) the central wavelength of the band is redshifted. This K-correction must assume something about the shape of the spectral energy distribution over a wide range of wavelengths, to extrapolate from the observed luminosity to the intrinsic luminosity. Following the brief discussion in the introduction to Chapter 2, we assume a power-law distribution with a spectral index of $\alpha = -0.5$, ignoring any contribution to the measured flux from emission lines. This assumption is also used by Schmidt & Green (1983) and by BSP (1988), so that our results will be directly comparable to

theirs. This is a realistic assumption for quasars with $z \leq 2.2$, as has been shown by Cristiani & Vio (1990). They calculated empirically the K-correction at different redshifts using observations of quasars with a wide range of luminosities and redshifts. Their determination of the K-correction does not deviate significantly from that calculated by assuming a power-law spectrum for quasars with $z \leq 2.2$.

In practice, the absolute magnitude of the quasar is used instead of its luminosity. This is calculated from

$$M_B = B_{JOHNSON} - 5\log_{10}\left(\frac{d_L}{10}\right) + 2.5(1+\alpha)\log_{10}(1+z) \tag{5.9}$$

where $B_{JOHNSON}$ is the apparent magnitude transformed to the Johnson system (as discussed in Chapter 4), d_L is the luminosity distance in parsecs, and the final term is the K-correction, as discussed above. For $q_0 = 0.5$, $H_0 = 50\text{kms}^{-1}\text{Mpc}^{-1}$ and $\alpha = -0.5$ this reduces to

$$M_B = B_{JOHNSON} - 5\log_{10}(1+z-\sqrt{1+z}) - 45.396 + 1.25\log_{10}(1+z) \tag{5.10}$$

5.3 The Observed Luminosity Functions

The above method was used to construct the differential luminosity function for the Edinburgh and AAT surveys (see Figure 5.1). The samples used were the Edinburgh sample as discussed in Chapter 4, and the AAT survey from Boyle et al (1990) which comprises 420 quasars. The AAT survey was constructed in a non-standard photometric system, whereby the data are in the B_J system but zero-pointed to the $B_{JOHNSON}$ system using calibrating stars with an average colour of $B_{JOHNSON} - V = 0.9$; this non-standard magnitude system of the AAT data is referred to as b hereafter. This method of calibration implies that there is an offset between b and $B_{JOHNSON}$ where the offset is determined by the colour of the calibrating stars. Using the colour relations in Blair & Gilmore (1982) gives the following transformation for the AAT survey;

$$B_{JOHNSON} = b + 0.28(B_{JOHNSON} - V - 0.9) \tag{5.11}$$

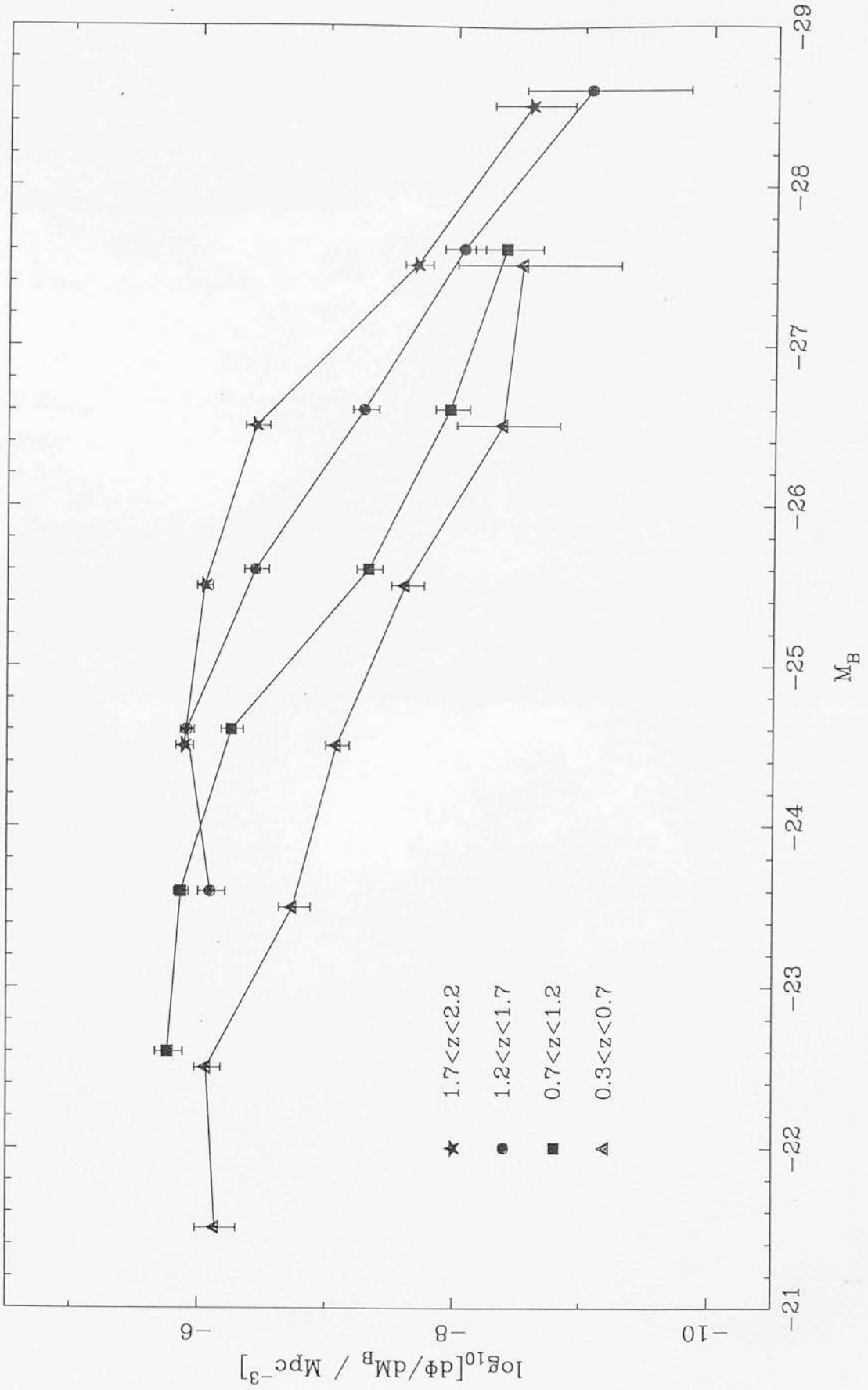

Figure 5.1: The differential luminosity function calculated for the Edinburgh and the AAT surveys in four redshift bins spanning a redshift range $0.3 \leq z \leq 2.2$, and in bins of unit absolute magnitude.

which, for a mean quasar colour of $B_{JOHNSON} - V = 0.3$ gives

$$B_{JOHNSON} = b - 0.168 \tag{5.12}$$

In BSP the apparent magnitudes for the objects in this survey were transformed onto the $B_{JOHNSON}$ system using the transformation empirically determined by Boyle et al (1990);

$$B_{JOHNSON} = b - 0.10 \pm 0.05 \tag{5.13}$$

This does not agree with the Blair & Gilmore transformation, although the difference is much smaller than the random errors on the magnitudes of quasars in the AAT survey. It was decided to use equation 5.13, as this is what was used in the analysis of the AAT survey (Boyle et al. 1988). It was also deemed preferable to use equation 5.13 as this was directly determined from quasars measured in the b and the $B_{JOHNSON}$ systems. Using the Blair & Gilmore transformation for this survey relies on knowing accurately the colour of the calibrating stars in the AAT survey, and while the mean colour is given in the 1990 paper, there is no discussion of how accurately this has been determined and what the intrinsic spread in the colours is. It is unfortunate that both the Edinburgh and the AAT surveys have to be transformed to another magnitude system with correspondingly increased uncertainties in the magnitudes. However it should be stressed that the size of the transformations is smaller than, or comparable to, the random errors in the magnitudes in both surveys. The results obtained can be compared directly with the Pure Luminosity Function models Boyle et al (1988) derived from the analysis of the AAT survey.

The redshift bins were chosen to be the same as those used in BSP. The effective areas for the Edinburgh survey in Chapter 4 were used to calculate Ω in equation 5.5. The first impression when looking at Figure 5.1 is that the luminosity function changes shape as a function of redshift, and that the space density of low-redshift luminous quasars is higher than that predicted by the PLE model.

5.3.1 Using the KS test to compare the models with the data

We would like to test formally the hypothesis that the LF changes shape as a function of redshift. One way of doing this is to compare the observed distribution of objects to the model distribution by using the KS test. Because we only wish to compare the shapes and *not* the rates of evolution of the observed and model distributions, we use the one-dimensional version of the test in each redshift bin.

The test was performed by calculating the cumulative distribution of absolute magnitudes in each redshift bin. This was done using three different datasets.

a) The whole of the Edinburgh and the AAT surveys were used.

b) The data from both surveys was used up to the absolute magnitude corresponding to the "break" in each redshift bin. This absolute magnitude was calculated from the PLE model;

$$M_B(z) = M_0 - 2.5k\log_{10}(1+z) \tag{5.14}$$

as discussed in Chapter 1. Here we take z to be the upper redshift limit in each redshift bin, and the parameters k and M_0 from the 1988 and 1991 versions of the PLE model. Under the null hypothesis, using this method should mean that the data used has the same shape distribution, regardless of redshift, if PLE holds.

c) The whole of the Edinburgh survey was used alone.

The model distribution was calculated by using the model LFs and using the effective areas searched as a function of absolute magnitude and redshift to convert this into a cumulative distribution of absolute magnitudes;

$$N(<M_n) = \int_{z_1}^{z_2}\int_{M_{bright}(z)}^{M_n} \Phi(M,z)\Omega(M,z)\frac{dV}{dz}dMdz \tag{5.15}$$

where $M_{bright}(z)$ is the absolute magnitude corresponding to the bright flux limit at each redshift z, and M_n is the absolute magnitude of each object being used to calculate the distribution. This integral is calculated for each M_n, so that for each object both the observed and the model distributions are known. It was necessary to calculate the

cumulative distribution in absolute magnitude, and *not* the cumulative LF, as the standard KS test requires all the data to be weighted equally, *i.e.* the steps between adjacent points in the cumulative distribution need to be of equal size. For the LF this is not so, as discussed above, each object is weighted according to the inverse of the volume searched to find it.

Two variations of the PLE model were used. The first is from the BSP (1988) paper; this paper only uses samples of quasars with $z \leq 2.2$ to compute the best-fit model. The second is from Boyle (1991) and includes samples which are complete out to $z = 2.9$. In order to model the slowing down in the rate of evolution for quasars with $z \geq 2$ the 1991 model has an upper redshift limit of $z = 1.9$ beyond which the "break" magnitude and hence the space density do not evolve. For quasars with $z \leq 1.9$ the 1991 model has a higher rate of evolution (which at a given redshift translates into a higher space density) than the 1988 model.

Figures 5.2, 5.3 and 5.4 show the observed and model distributions for the three cases a, b and c outlined above. Table 5.1 shows the results of the KS test in each redshift bin. It shows the probability that the observed cumulative distribution is drawn from the model distribution. We can see that in the lowest redshift bin, as we include proportionately more data from the Edinburgh survey (*i.e.* as we go from case a) to case c)) the data and the models disagree at increasingly significant levels. This is partly due to the KS test being insensitive to the extreme tails of distributions, which is what we are testing here. As the overall number of objects used for the test decreases, the fractional contribution from any one object to the overall distribution increases. Only the lowest redshift bin shows any significant disagreement with the models, again this could be due to the fraction of Edinburgh data to AAT data in each redshift bin. As we go to higher redshift bins, the fraction of AAT data increases, and because these were the data used to fit the models by BSP and Boyle (1991), it is perhaps not surprising that they agree with the data. The results from the KS test are interesting, but not in themselves conclusive evidence for or against PLE. The next section describes what happens when we assume a simple parameterisation of the data.

Dataset(s) used	Redshift bin	1988 model	1991 model
Case a	$0.3 \leq z < 0.7$	7.6%	10.1%
	$0.7 \leq z < 1.2$	85.0%	78.2%
	$1.2 \leq z < 1.7$	32.8%	94.7%
	$1.7 \leq z < 2.2$	85.9%	37.6%
Case b	$0.3 \leq z < 0.7$	0.5%	0.1%
	$0.7 \leq z < 1.2$	26.3%	17.0%
	$1.2 \leq z < 1.7$	71.3%	42.1%
	$1.7 \leq z < 2.2$	30.7%	65.4%
Case c	$0.3 \leq z < 0.7$	0.1%	0.1%
	$0.7 \leq z < 1.2$	21.8%	20.5%
	$1.2 \leq z < 1.7$	29.2%	27.3%
	$1.7 \leq z < 2.2$	88.9%	79.7%

Table 5.1: This table shows the probabilities of various datasets agreeing with the Pure Luminosity Evolution model.

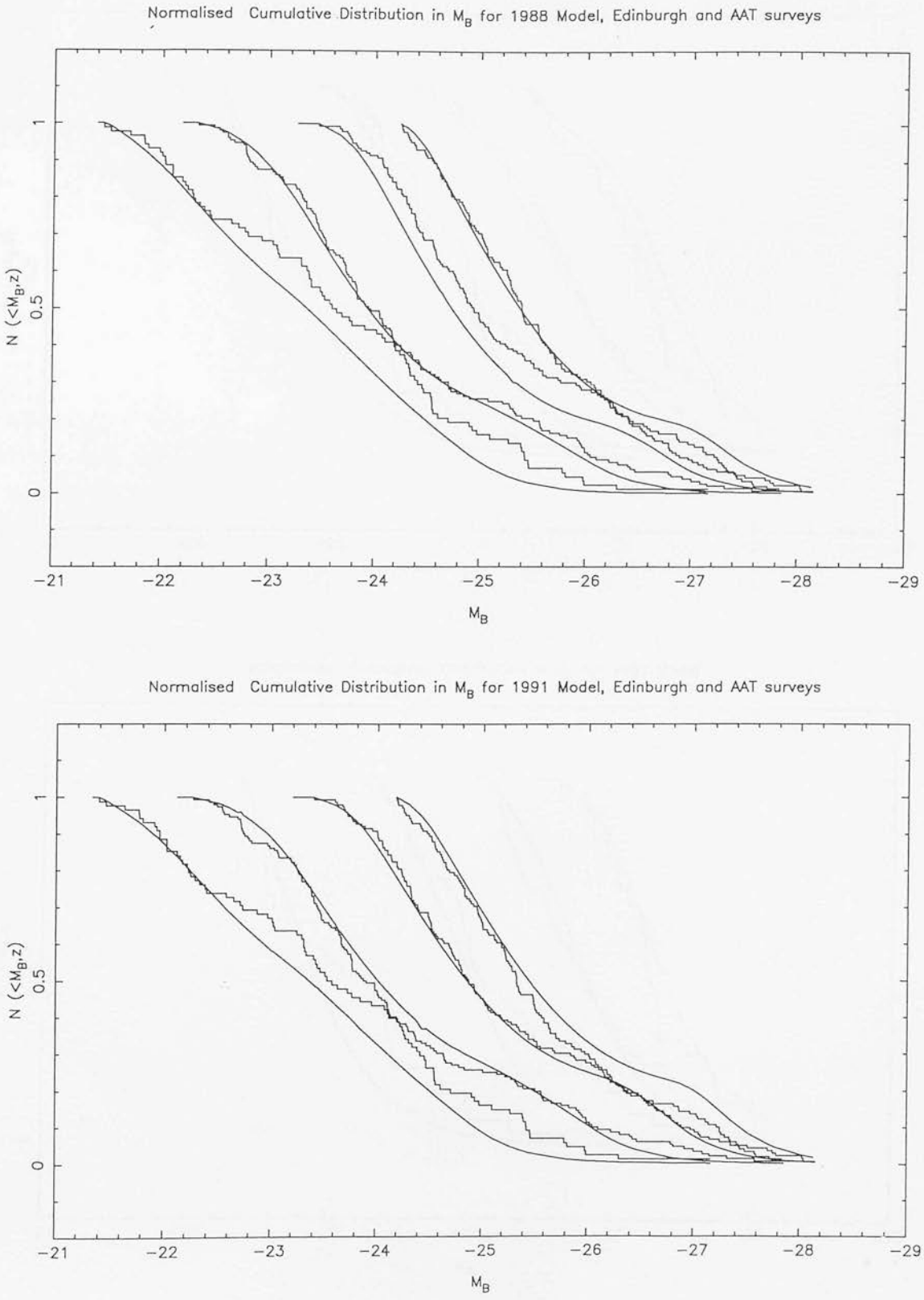

Figure 5.2: The normalised cumulative distributions in absolute magnitude for the whole of the Edinburgh and the AAT surveys, for the 1988 (top) and the 1991 (bottom) PLE models.

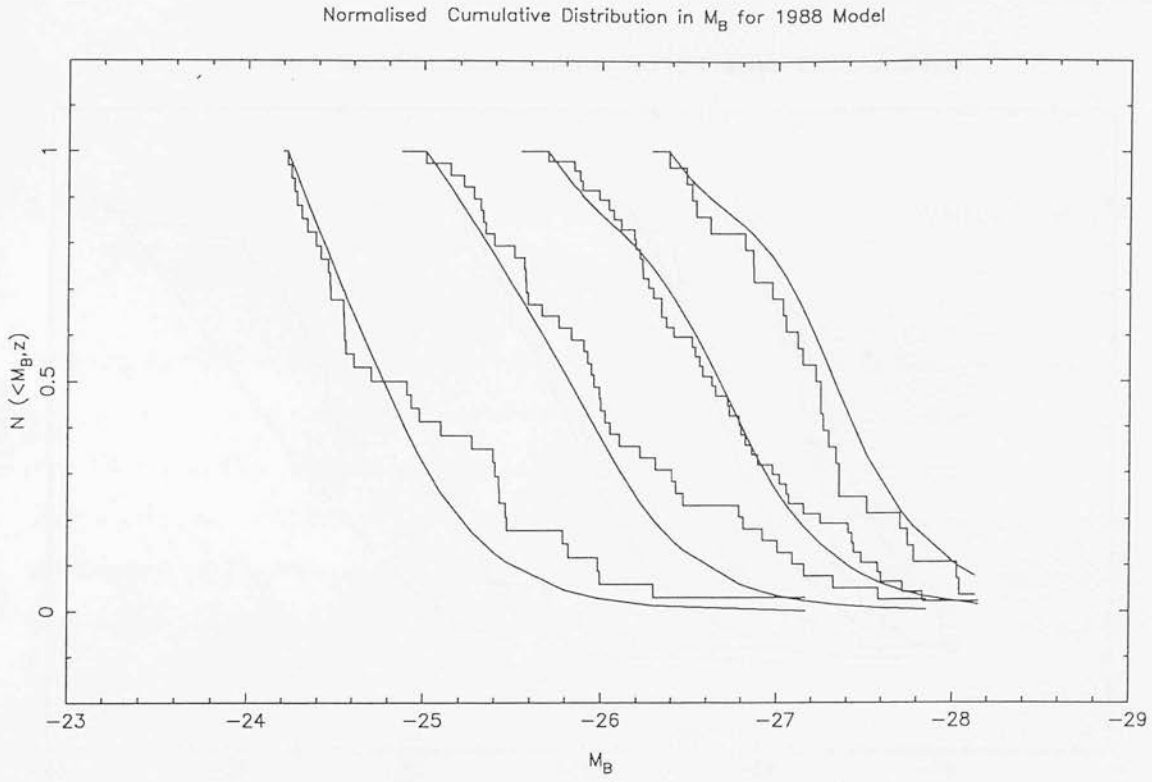

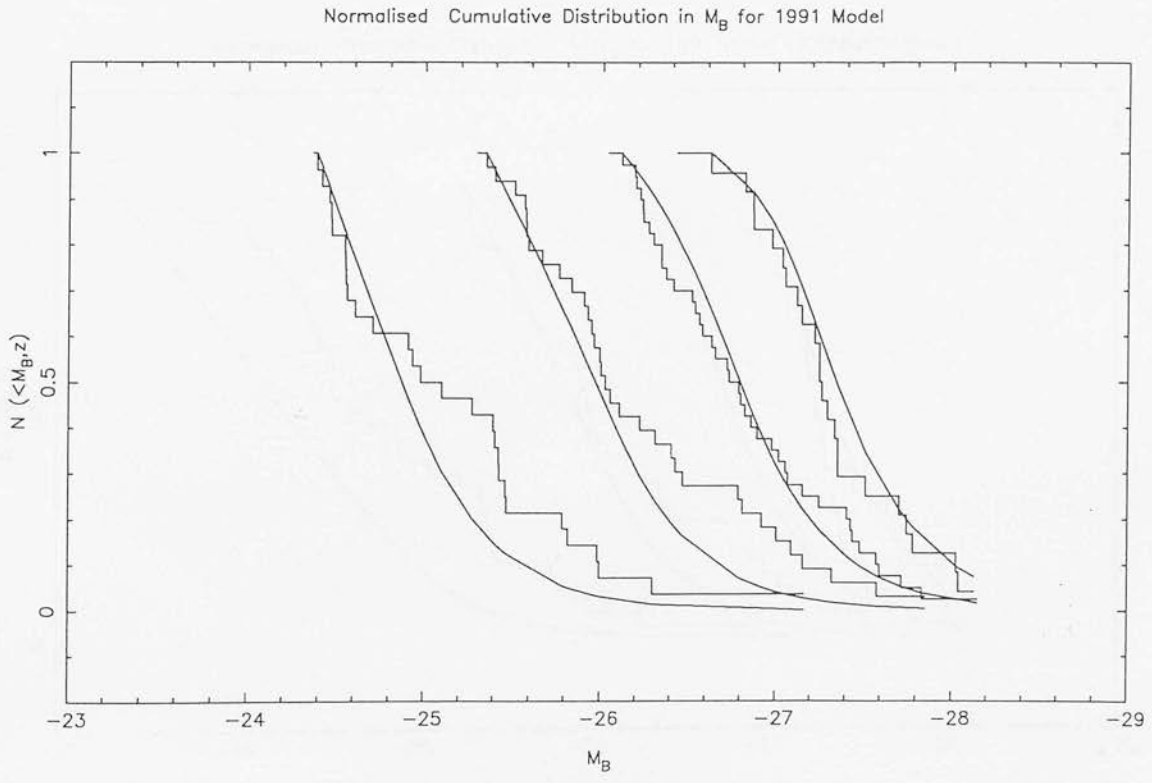

Figure 5.3: The normalised cumulative distributions in absolute magnitude for the Edinburgh and the AAT surveys up to the "break", for the 1988 (top) and the 1991 (bottom) PLE models.

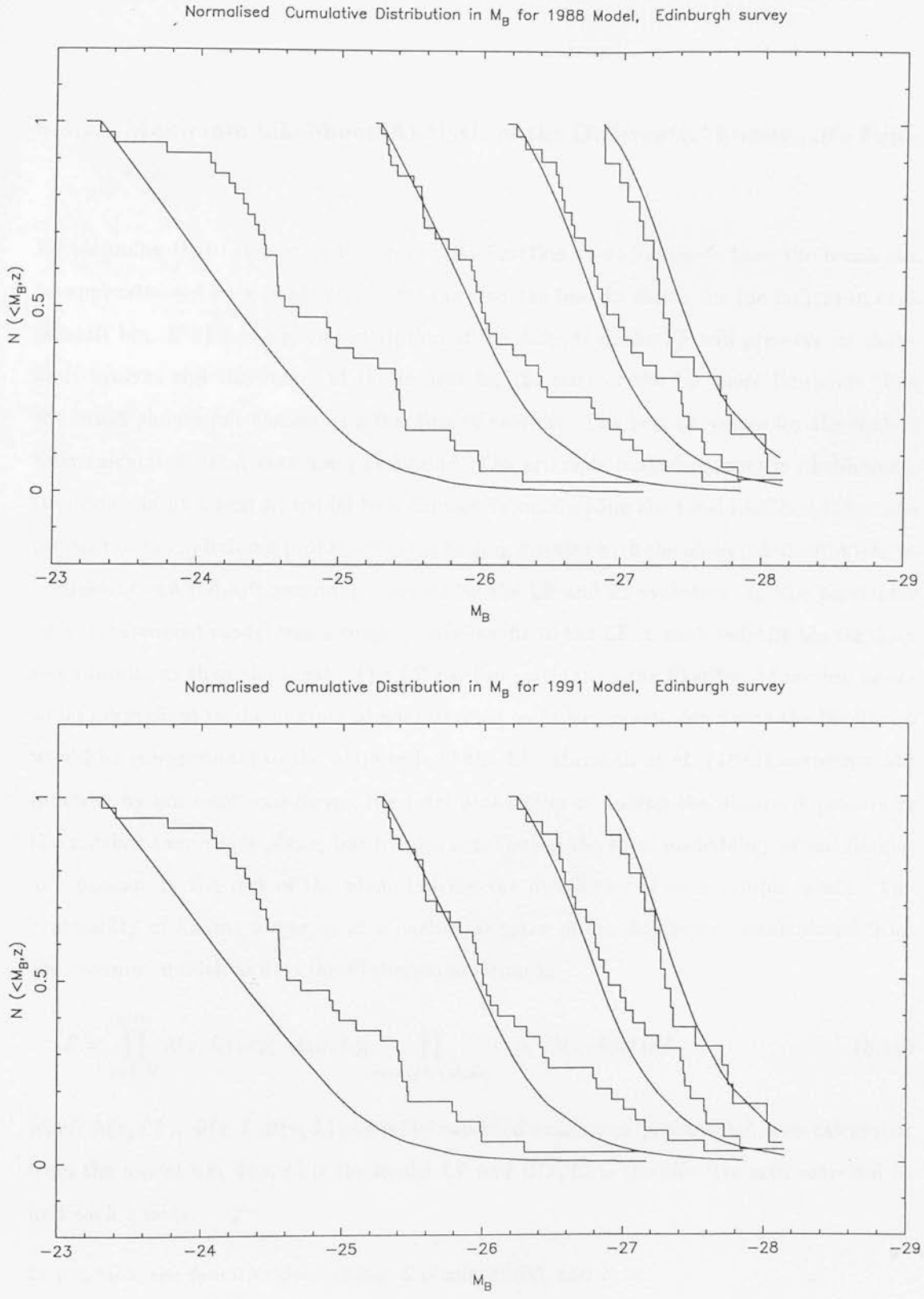

Figure 5.4: The normalised cumulative distributions in absolute magnitude for the Edinburgh survey, for the 1988 (top) and the 1991 (bottom) PLE models.

5.3.2 Maximum Likelihood Analysis of the Differential Luminosity Function

By assuming that the part of the luminosity function more luminous than the break can be approximated by a single power, we can find the best-fit values for the indices in each redshift bin. If PLE is a good description of the data, then the LF will preserve its shape as it evolves and the values of the indices for the part of the LF more luminous than the break should not change as a function of redshift. The best-fit values for the indices were calculated using maximum likelihood. The principle behind maximum likelihood is that one can fit a best-fit model to a dataset by maximising the total likelihood (*i.e.* the product of the individual probabilities) of finding quasars with the observed distribution in luminosity and redshift assuming a model for the LF and its evolution. In this particular case the assumed model was a single power-law fit to the LF in each redshift bin for data more luminous than the break. The LF used in calculating the likelihood function needs to be normalised to the number of quasars used to fit the model, otherwise the likelihood would be proportional to the amplitude of the LF. Marshall *et al.* (1983) normalise the function by not only considering the total probability of finding the observed quasars in the redshift-luminosity plane, but by also considering the total probability of *not* finding any quasars in the rest of the plane (within the flux limits of each sample used). The probability of finding a quasar at a particular place in the L, z plane is calculated from the assumed model; and so the likelihood function is

$$\mathcal{L} = \prod_{i=1,N}^{qsos} \lambda(z,L)\exp[-\lambda(z,L)] \prod_{rest of L,z plane} \exp[-\lambda(z,L)]dzdL \tag{5.16}$$

where $\lambda(z,L) = \Phi(z,L)\Omega(z,L)$ and is the expected number of quasars at L, z as calculated from the model LF, $\Phi(z,L)$ is the model LF and $\Omega(z,L)$ is the effective area searched to find each quasar.

In practice, the function $\mathcal{S} = -2\log_e \mathcal{L}$ is minimised, and $\mathcal{S}$ is

$$\mathcal{S} = -2\sum_{i=1,N}^{qsos} \log_e(\Phi(z_i,L_i)) + 2\int\int \Phi(z,L)\Omega(z,L)\frac{dV}{dz}dzdL \tag{5.17}$$

where

$$\frac{dV}{dz} = \left(\frac{2c}{H_0}\right) d_c^2 (1+z)^{-1.5} \tag{5.18}$$

is the volume element. The first part of the RHS is calculated using the actual L, z distribution of the quasar samples, the second part is integrated over the area in the L, z parameter space covered by each sample, given their flux limits.

The best fit parameters of the model were found by minimising $\mathcal{S}$ iteratively. The confidence region of one parameter is found by incrementing $\mathcal{S}$ and assuming a χ^2 distribution with 1 degree of freedom (*e.g.* Lampton *et al.* 1976) for the distribution of $\mathcal{S}$–$\mathcal{S}_{max}$.

The model fitted in this way was a single power law fit to the quasars more luminous than the "break" in each redshift bin, and the model was fitted independently in each bin, *i.e.* no attempt was made to model the evolution;

$$\Phi(M_B) = \Phi^* 10^{0.4(\alpha+1)M_B} \tag{5.19}$$

where Φ^* is the normalization and α is the index of the power law.

The faintest absolute magnitude in each redshift bin used to fit the model to the data was calculated by using the model to calculate the absolute magnitude of the "break" at the far redshift limit in each redshift slice. Only data more luminous than this limit were used to fit the model. The 1988 PLE model was used for this.

Goodness-of-fit of the model

The goodness-of-fit of this model was tested in each redshift bin by using the best-fit model to construct the cumulative distribution in absolute magnitude and comparing this to the observed distribution by using the Kolmogorov-Smirnoff test. Figure 5.6 shows the cumulative distributions of the Edinburgh data and this model with changing power-law index.

If the model is an acceptable fit to the data then this is reflected in the probability that the observed distribution is drawn from the model distribution. As can be seen from table 5.2 the probability is never less than 24% and thus we can conclude that the model is

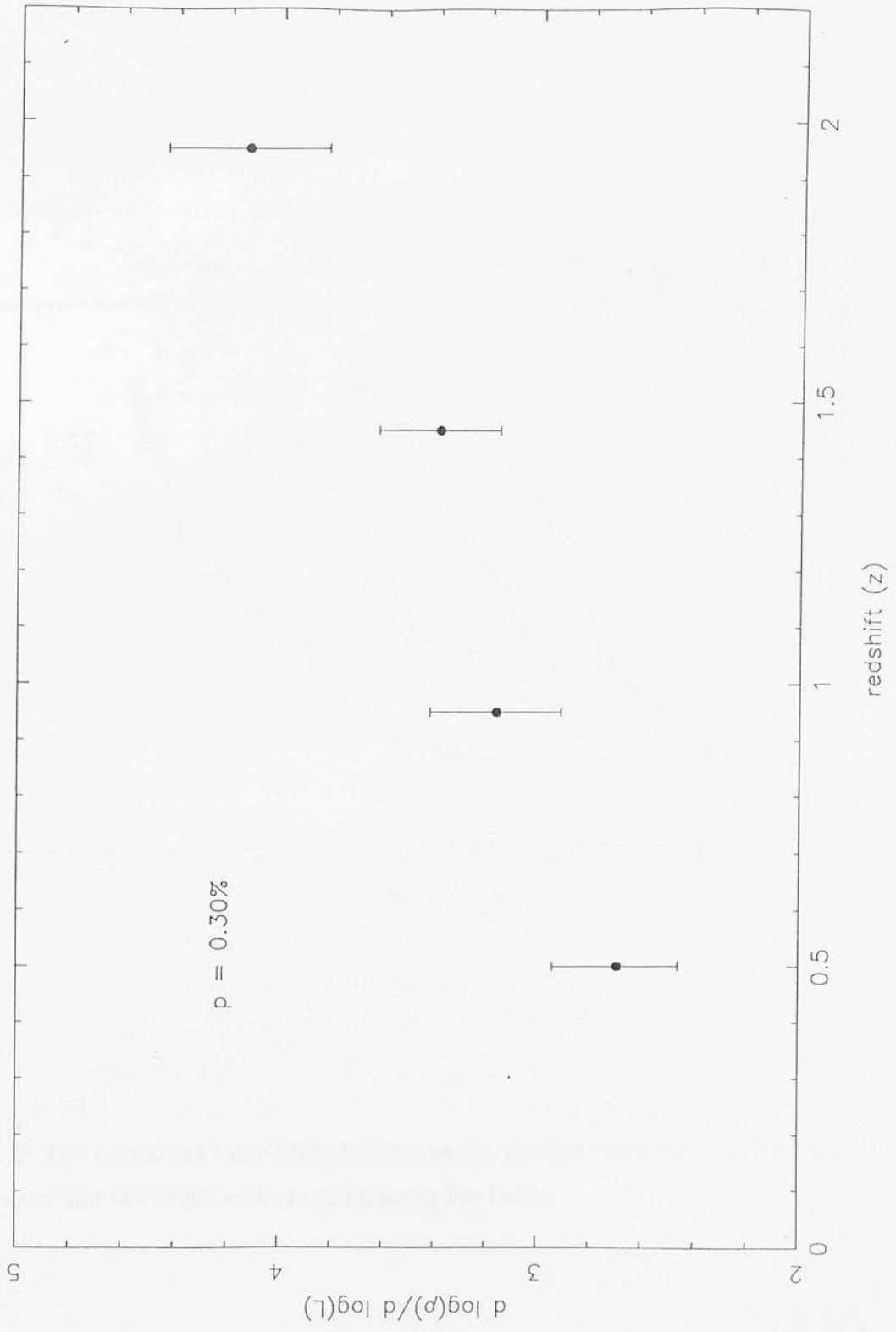

Figure 5.5: The best-fit values to α; the index of the luminous part of the LF in each redshift bin for the four redshift bins. Errors shown are 1 sigma deviations.

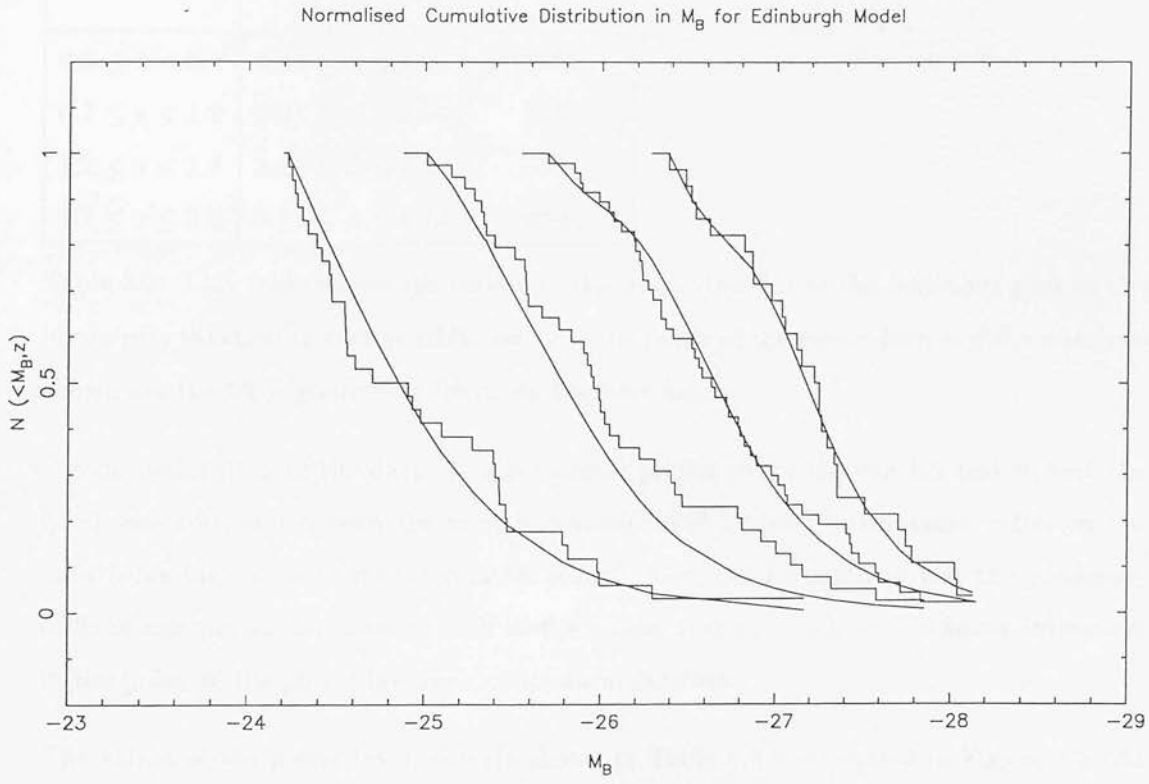

Figure 5.6: The normalised cumulative distributions in absolute magnitude for the Edinburgh survey and the model with changing power-law index.

Redshift bin	α	Probability
$0.3 \leq z < 0.7$	$2.50 \leq \alpha \leq 2.97$	56%
$0.7 \leq z < 1.2$	$2.91 \leq \alpha \leq 3.40$	24%
$1.2 \leq z < 1.7$	$3.15 \leq \alpha \leq 3.61$	94%
$1.7 \leq z \leq 2.2$	$3.81 \leq \alpha \leq 4.43$	99%

Table 5.2: This table shows the results to the power-law fits to the luminous part of the luminosity function in each redshift bin. α is the index of the power-law, and the numbers shown are the 68 % confidence limits on the best fits.

a good description of the data. It was deemed preferable to use the KS test to test the goodness-of-fit, rather than the more commonly used χ^2 test, as the latter relies on the data being binned and thus information is lost. Also, the KS test can test the goodness-of-fit of one parameter models, such as the model here in which we are solely interested in the index of the power-law and not its normalisation.

The values of the power-law index are shown in Table 5.2 and plotted in Figure 5.5. As can be seen, the values for α steadily increase from 2.7 in the lowest redshift bin to 4.1 in the highest bin. To see whether these values were consistent with a single underlying value for α, both the χ^2 test and maximum likelihood were used to calculate the weighted mean of the slopes and the goodness-of-fit of this mean, given the distribution in α. Both tests gave almost identical results; a mean value of $\overline{\alpha} = 3.20$ with an associated probability of 0.3%. Therefore the null hypothesis is ruled out at this significance level. Not only does this rule out the 1988 PLE model (which has $\alpha = -3.79$), but this *also* rules out all luminosity evolution models which require uniform evolution.

It should be noted that the above analysis relies on using the 1988 PLE model to calculate the absolute magnitude limits, fainter than which no data are used to fit the model. If the 1991 model is used instead, the increased rate of evolution in that model corresponds to a more luminous absolute magnitude limit in each redshift bin. Therefore fewer data are used to fit the model. This results in a decreased level of significance, the null hypothesis is ruled out at a significance level of 1.4%.

5.3.3 Effect of errors upon the analysis

As discussed and quantified in Chapter 2, the final dataset from which the quasar candidates were selected suffers from both systematic and random errors on the measured magnitudes. Also, a few quasars have doubtful redshifts. In this section I quantify the combined effect of these errors and uncertainties on the results discussed earlier. As can be seen from figures 5.2, 5.3 and 5.4 our result relies upon finding an excess of bright quasars compared to the model predictions. If this excess is due to a systematic error in the calibration then we can estimate the size of the error needed to produce this result by looking at the cumulative distributions and estimating by how much the objects' magnitudes would have to be fainter in order to shift the observed distribution onto the model distribution. In the lowest redshift bin the objects would, on average, have to be 0.5 magnitudes fainter in order to agree with the model distribution. There is no evidence for any systematic error this large in the measured magnitudes and therefore we can conclude that the observed excess of bright quasars is a real effect and not an artifact of the errors in the dataset. This is also supported by the log(n)-m relation shown in Chapter 4, which shows the surface density of the quasars in this sample agreeing with that measured by other surveys apart from the Palomar-Green. Any systematic difference in the calibration of this survey would show up clearly in this diagram. We have already shown that the calibration of the Edinburgh survey and the LBQS agree to better than 0.2 magnitudes.

Random errors in the measured magnitudes could only cause a systematic excess in the measured number of quasars if malmquist bias were important. As has already been shown in Chapter 4, malmquist bias cannot have an important effect on this sample.

The effect of the objects with doubtful identifications (i.e. with quality flags of 3) has been quantified by excluding them from the dataset and redoing the analysis. This has little effect upon the results; in the lowest redshift bin the probability of the data agreeing with the 1988 and the 1991 PLE models is now 0.12%. When doing the maximum likelihood analysis the probability that the values for α are drawn from a constant value is 0.34%. The model that we have fitted with a different value for α in each redshift bin is still a good fit.

5.4 Discussion

We have shown that the LF changes shape significantly as a function of redshift and this means that PLE, and any other form of uniform evolution, is no longer a good description of quasar evolution. Overall the rates of evolution for all luminous quasars are lower than previously thought because the space density of low-redshift quasars is now much higher. In the lowest redshift bin, the slope of the luminous part of the LF is now so flat that the *whole* LF in this bin appears to be a featureless power-law, with no break at all. We have shown that this result cannot be due to the systematic errors in the measured magnitudes, or to the inclusion of objects with doubtful redshifts.

If we consider the most luminous quasars with $M_b \approx -28$ then the space density is consistent with no evolution at all over the entire redshift range. Indeed, if we also consider the space density of quasars of the same luminosity at $z \approx 3.5$ as measured from the Edinburgh survey by Mitchell *et al.* (1990) then the space density of these objects is consistent with no evolution for $\sim 90\%$ of the age of the universe.

5.4.1 Using Galaxy Formation Models to Predict the Quasar LF

Although it seems counterintuitive that the most luminous quasars should evolve less than fainter quasars, perhaps it is understandable if we consider standard hierarchical galaxy formation formalisms, *e.g.* Press-Schechter (Press & Schechter, 1974). Efstathiou & Rees (1988) used this formalism to see how the comoving number density of different size groups varies with redshift in the Cold Dark Matter scenario, *i.e.* given the initial distribution of density perturbations and $\Omega = 1$. Figure 5.7 is taken from their paper and shows that whilst the most massive groups are much rarer at $z \sim 2$ than less massive groups, their space density increases much faster as redshift decreases. This is because massive groups can only form at high peaks in the underlying density field. High peaks are rare in the early universe and then become more common as redshift decreases and matter flows into overdense regions.

Carlberg (1990) used the Press-Schechter formalism to see if it could explain the observed quasar LF. At that time, the accepted model for quasar evolution was PLE, and Carlberg

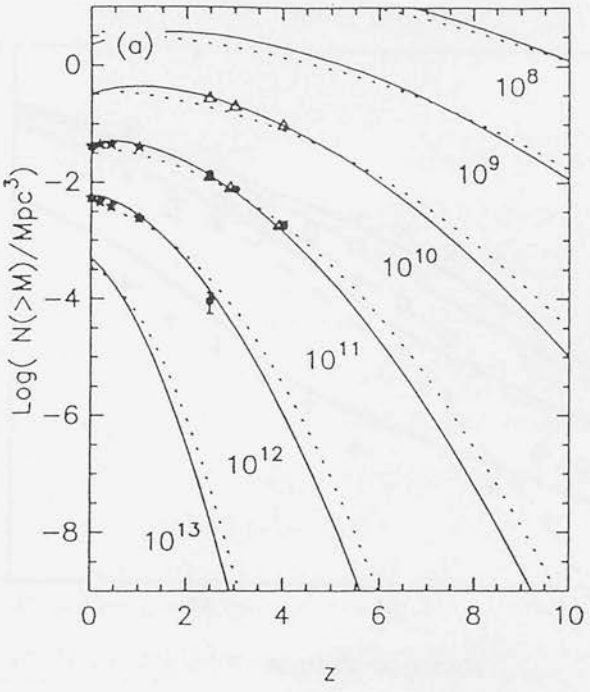

Figure 5.7: The comoving number of groups with mass > M versus redshift, calculated using the Press-Schechter formalism (solid lines) from Efstathiou & Rees (1988). It can be seen that the most massive groups with $M > 10^{12}$ evolve much faster than less massive groups, in the sense that their space density increases rapidly as redshift decreases.

concluded that given the large number of uncertainties in his modelling, the model LFs were a reasonable fit to the data, although they predicted a slower rate of evolution than was observed. However, if we look at Carlberg's model LFs (see Figure5.8) we can see that they show a rate of evolution dependent on quasar luminosity, with the highest luminosity objects evolving slowest, in agreement with what we have found. This model predicts less evolution at faint luminosities compared to what is observed, implying that the evolution of the least luminous objects does not just depend on the dynamics of galaxy formation, but also on other factors.

It should be remembered that the above argument is based on many assumptions about how matter clumps on different sizes in the universe. It also relies on the assumption that quasar luminosity is directly related to the total halo mass of the galaxy. Observational evidence that quasar luminosity is related to the *luminous* mass in the galaxy comes from Dunlop *et al.* (1993). Their study of the infrared properties of the host galaxies of low-redshift quasars shows that the host galaxy luminosities all come from the most luminous part of the luminosity function. Even though there appears to be a link between quasar luminosity and host galaxy luminosity, as Carlberg (1990) acknowledges, extrapolating

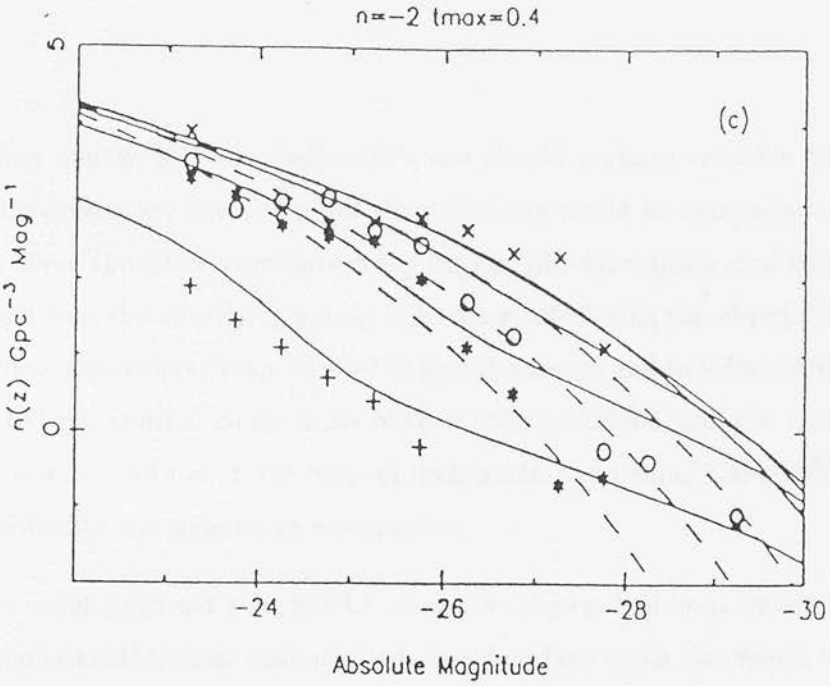

Figure 5.8: Model quasar luminosity functions calculated assuming a hierarchical merging model from Carlberg (1990). The solid lines represent luminosity functions up to $z = 2$ and the dotted lines represent luminosity functions in the range $2 < z < 4$. The various symbols represent the data that Carlberg used to compare with his models.

from the measured luminosity of a galaxy to the total mass of the surrounding halo involves many assumptions.

5.4.2 Comparison with the Seyfert LF and Quasar Lifetimes

The PLE model was *consistent* with (although offered no new evidence for) a single epoch of quasar formation and very long-lived objects. This point of view was also supported by the shape and normalisation of the Seyfert LF agreeing with that of the quasar LF (Marshall 1986, Weedman 1986) suggesting that quasars evolve into Seyferts at low redshifts. However it is not straightforward to compare directly quasar and Seyfert luminosity functions. Marshall and Weedman both assumed that Seyfert 1s alone were the low-luminosity counterparts to quasars, and ignored any contribution to the LF from Seyfert 2 galaxies. However, in some versions of unified schemes (*e.g.* Lawrence & Elvis, 1982) which relate the properties of various different classes of AGNs, Sey 2s can be explained as being obscured (by dust) Sey 1s. This scheme is backed up by spectral observations in the infra-red of Sey 2s (*e.g.* Blanco, 1991) showing broad wings to narrow emission lines. Therefore

in comparing quasar LFs and Seyfert LFs one should perhaps consider both types of Seyferts. However, even then, it is not clear that one would be comparing similar sorts of objects. Even though workers presenting Seyfert LFs have taken care to separate the nuclear light from the underlying galaxy light when calculating the objects' luminosities, many of these objects have been selected in galaxy surveys and in infra-red surveys. The objects have been selected on the basis of their stellar emission, and the amount of dust that they contain, and *not* on the basis of their nuclear emission. The resulting LFs are therefore probably incomplete and meaningless.

Even if one could construct a Seyfert LF where the objects had been chosen on the basis of their (unobscured) nuclear emission, it is not clear how much this would tell us about quasar lifetimes. Seyferts could either represent the endpoint of a single generation of longlived quasars, or they could be the latest in a succession of generations of quasars. In either scenario, one would expect the Seyfert LF to agree with the quasar LF. The latter would imply that there may be many remnant black holes in ordinary galaxies at low redshift due to previous quasar activity. The degree of agreement between Seyfert and quasar LFs could tell us what fraction of Seyferts are obscured quasars, and what fraction are powered by other means, such as starbursts. The similarities between Sey 2s and starburst galaxies, in particular the equivalent widths of low-excitation emission lines, have been pointed out by many authors (*e.g.* Terlevich & Melnick, 1985).

Because the PLE model was consistent with the idea of a single generation of longlived objects, and the alternative viewpoint of a succession of shortlived objects seemed contrived given the lack of a need for any density evolution, workers became accustomed to the idea that the LF and its evolution was giving them a direct insight into the physics of quasar evolution. However it is clear that this is no longer the case, if it ever were. This is because the observed LF as presented in this chapter could be equally well described by either a model combining luminosity and density evolution (LDE) or a luminosity-dependent luminosity evolution model (LDLE), *i.e.* we have no idea how the different LFs in the different redshift slices map onto each other. LDE implies a continuous rate of quasar formation and short lifetimes, whereas LDLE is similar to PLE in that it is consistent with no density evolution, one epoch of quasar formation and long lifetimes. We need extra information, such as constraints on the masses of black holes in low redshift

quasars, to tell us something about the lifetimes of quasars, so that we can deconvolve the LF and find out how the birthrate of objects varies with epoch.

5.4.3 Comparison with the Radio Properties of Quasars

An alternative explanation of the observed LF is that there are two populations of quasars, each evolving uniformly but at different rates. Miller *et al.* (1990) showed that the distribution of radio properties of a sample of optically selected quasars was bimodal and suggested that the changing rate of radio detections of optically selected quasars as a function of redshift could be due to the two populations of quasars, each having optical luminosity functions (OLFs) with different slopes but evolving at the same rate. This is supported by Wills & Lynds' (1978) calculation of the OLF for a combined sample of radio-selected quasars at $z \approx 1$ showing that the OLF has a much shallower slope than optically selected samples and evolves at a slower rate. If the overall OLF changes shape then this requires that the two populations evolve at different rates.

5.5 Summary of Results

We have used a sample of bright quasars to calculate the luminosity function and show that the Pure Luminosity Evolution model is not a good description of the data. The overall rate of evolution for luminous quasars is less than was previously thought, and now seems to depend on luminosity, in that the most luminous quasars evolve least. This can be qualitatively explained by hierarchical galaxy formation models, *provided* that quasar luminosities are related to the total halo mass of the host galaxy.

Because PLE is no longer a good fit, we cannot infer anything about quasar lifetimes from the LF. It is expected that the observed LF could be equally well fitted by a luminosity-dependent density evolution model, implying short lifetimes and no one epoch of quasar formation, or by a luminosity-dependent luminosity evolution model, implying long lifetimes and one epoch of formation. Future work will probably involve assessing the prevalence of low-level nuclear activity in "normal" galaxies, as well as Seyferts, in order to distinguish between the two models and to put constraints on quasar lifetimes.

Appendix A

COSMOS data versus Calibration data

The following pages show diagrams of COSMOS data versus photoelectric and CCD sequences used to calibrate each field. They show the efficacy of the field-to-field corrections as discussed in Chapter 2.

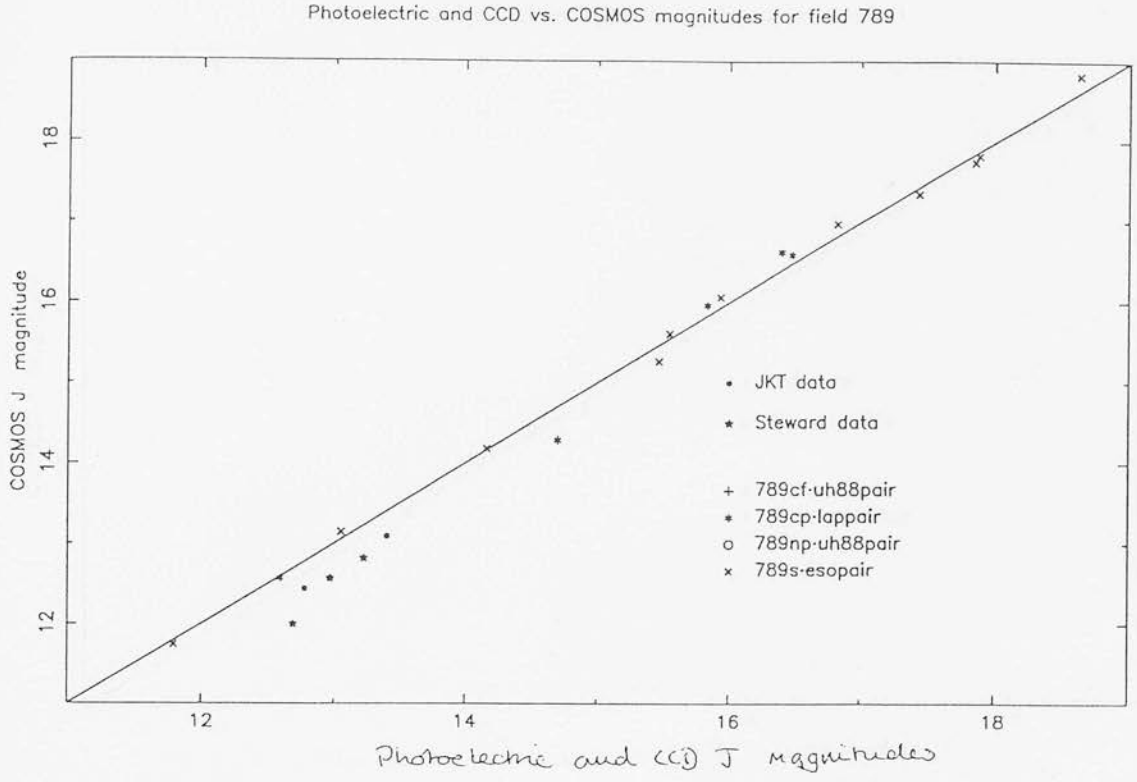

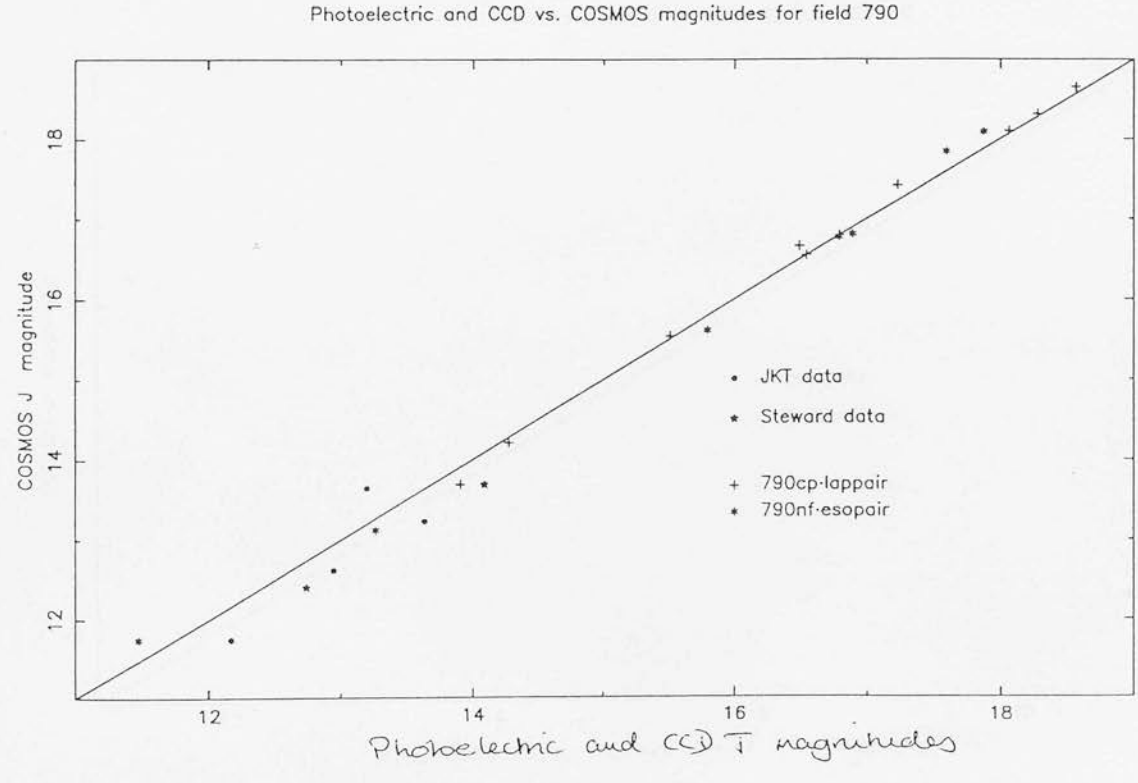

COSMOS data vs. calibration data for fields 789 (top) and 790 (bottom).

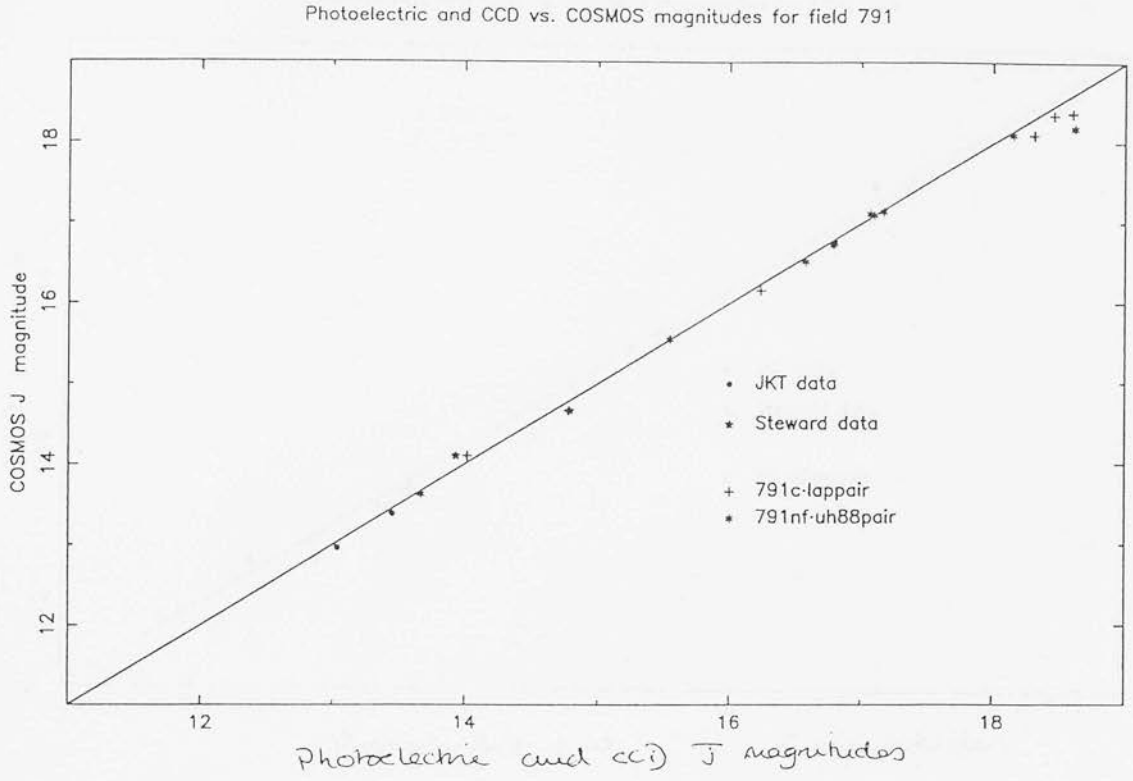

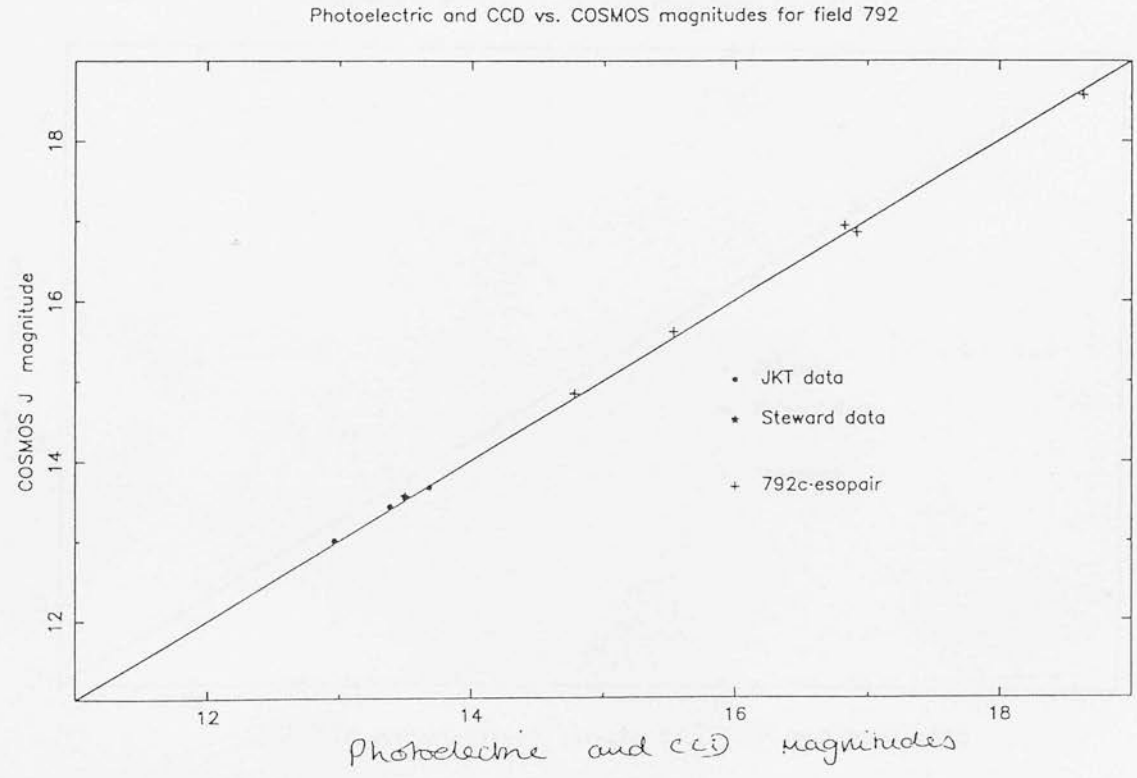

COSMOS data vs. calibration data for fields 791 (top) and 792 (bottom).

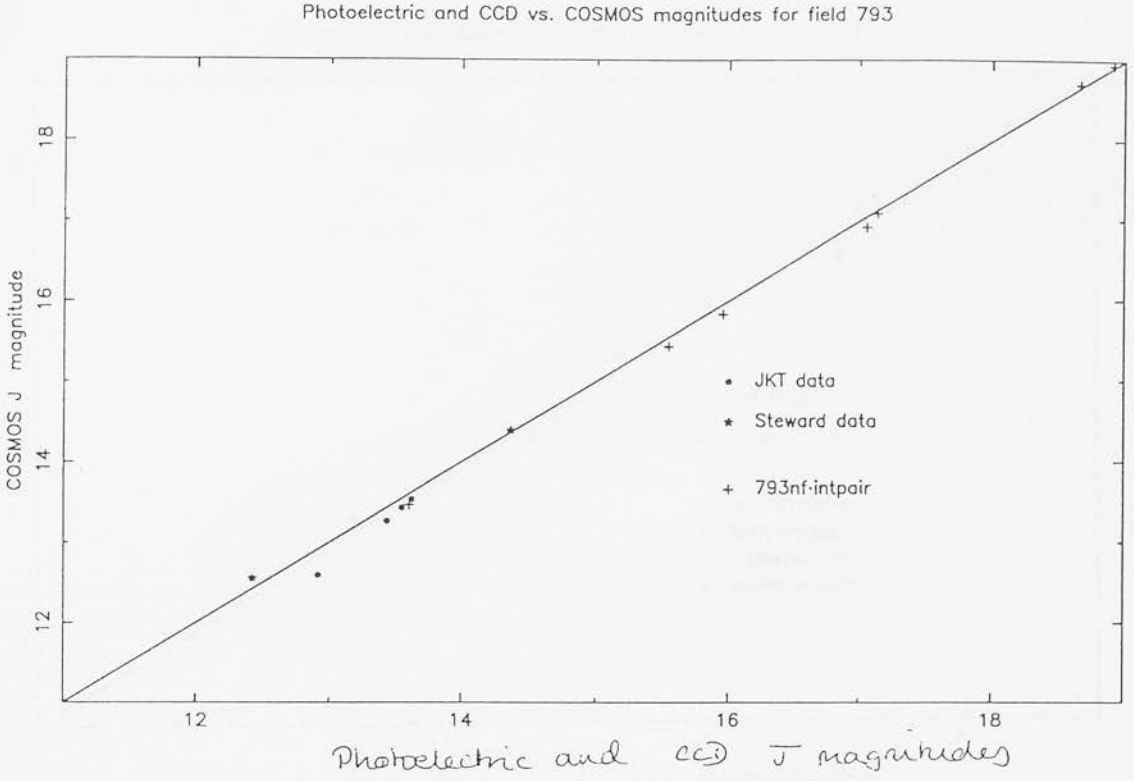

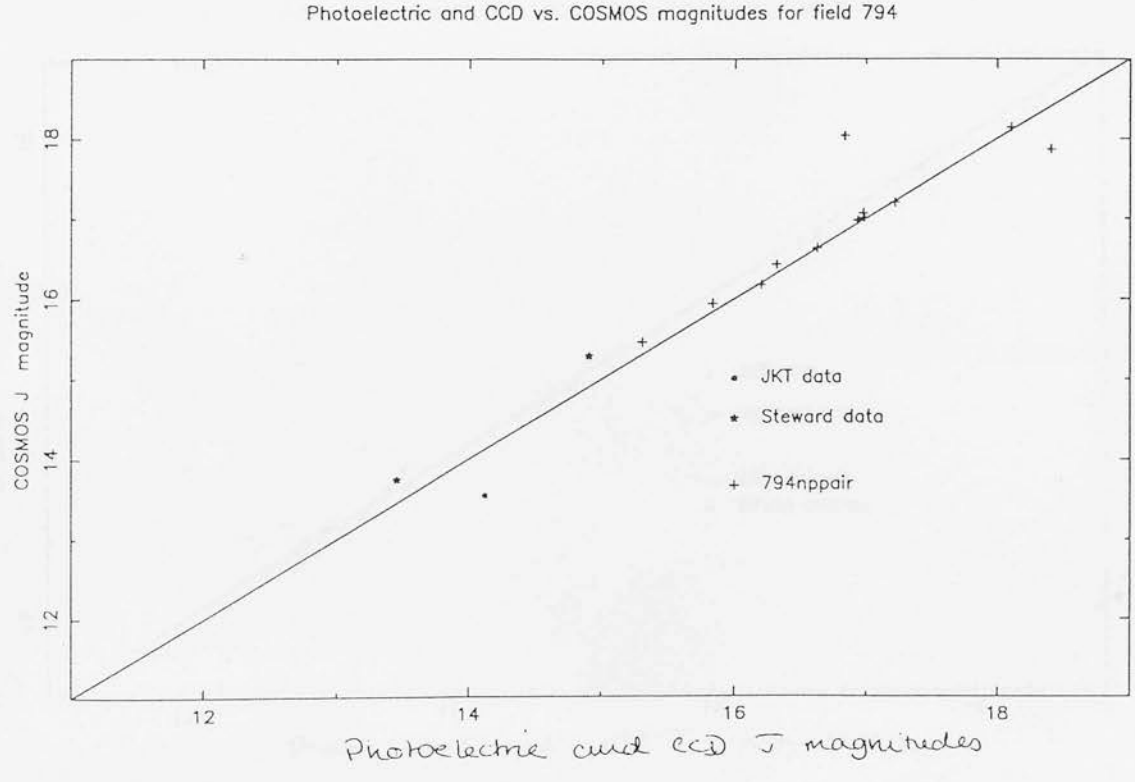

COSMOS data vs. calibration data for fields 793 (top) and 794 (bottom).

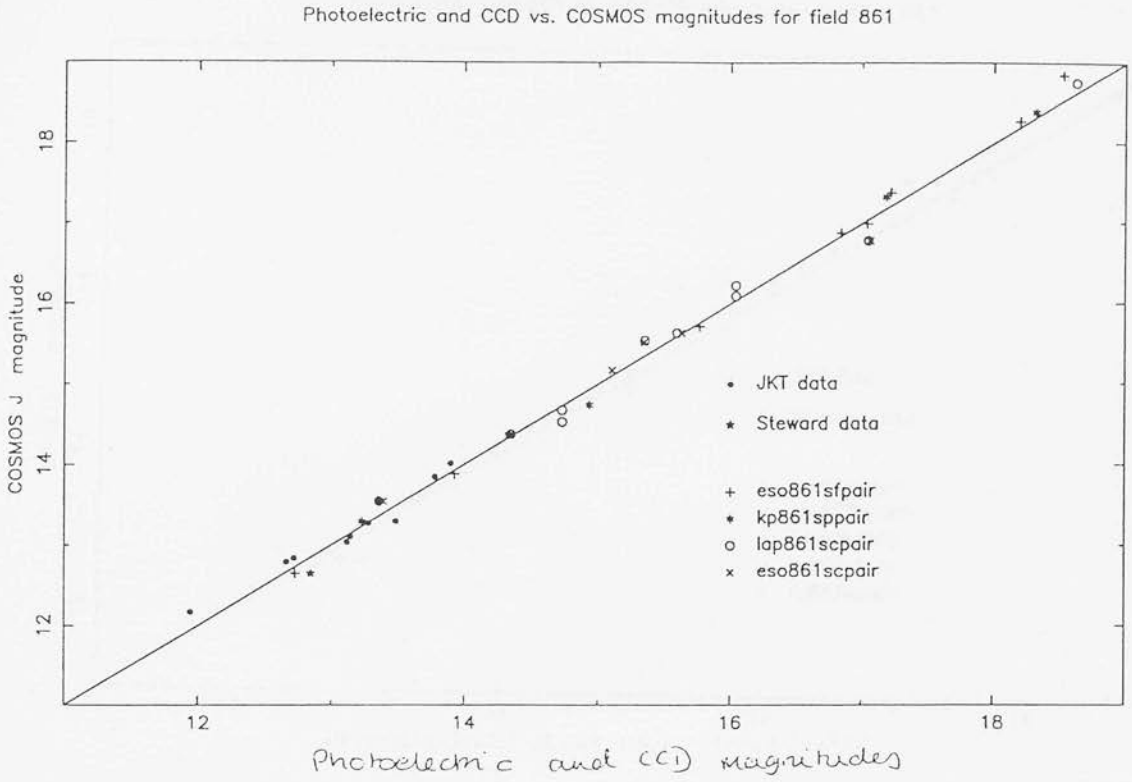

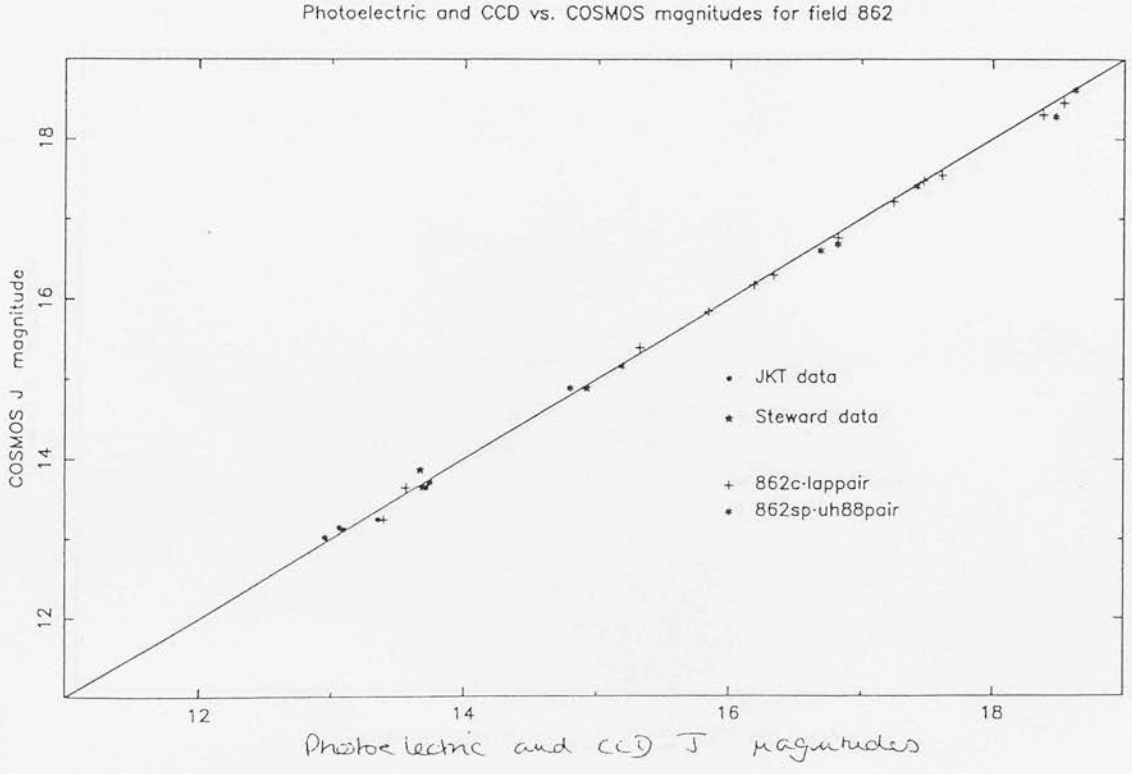

COSMOS data vs. calibration data for fields 861 (top) and 862 (bottom).

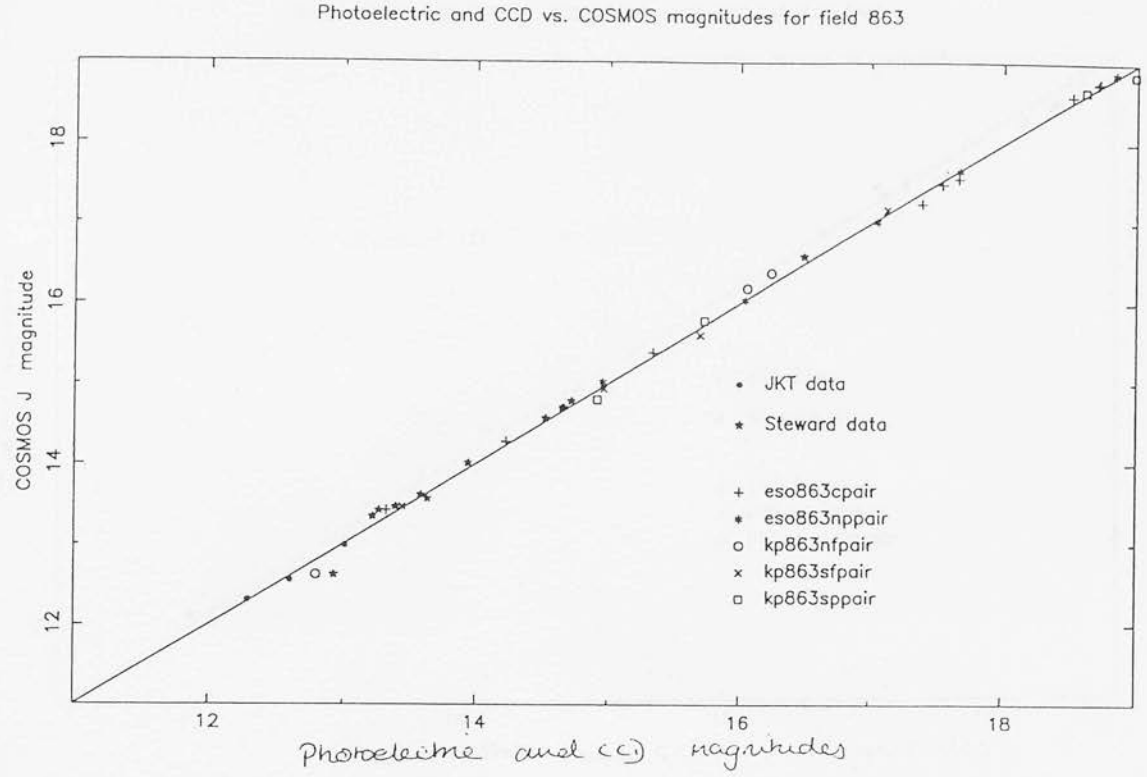

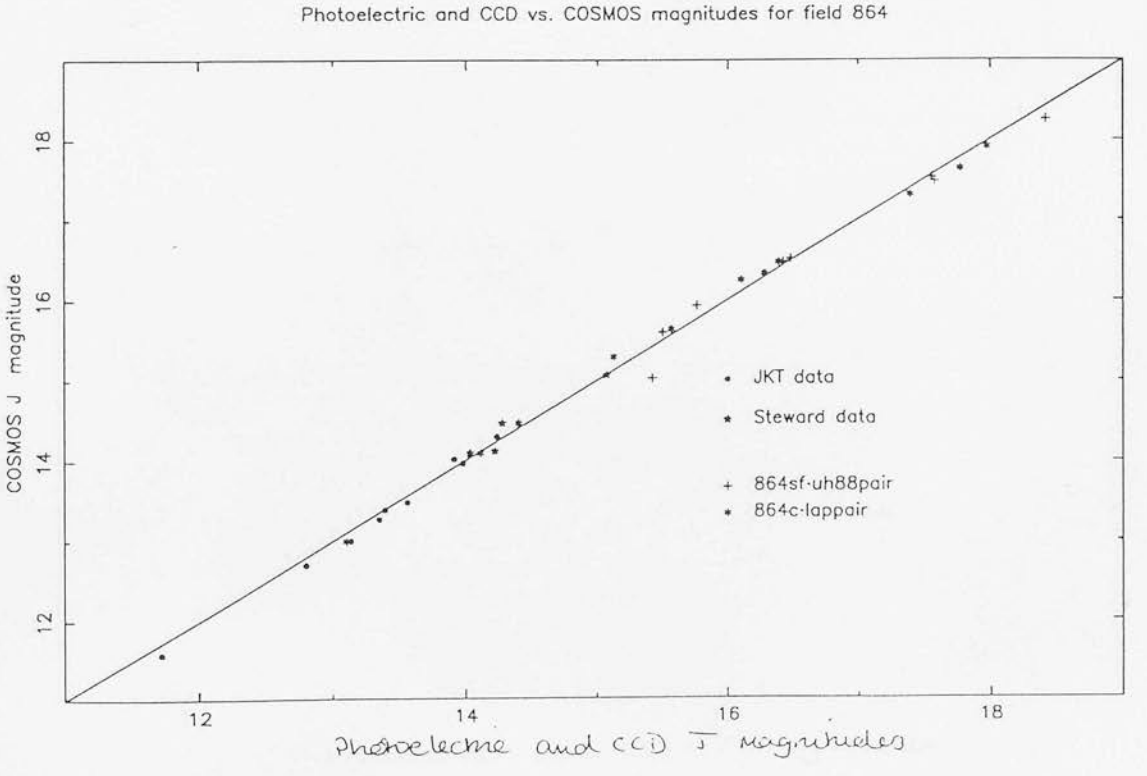

COSMOS data vs. calibration data for fields 863 (top) and 864 (bottom).

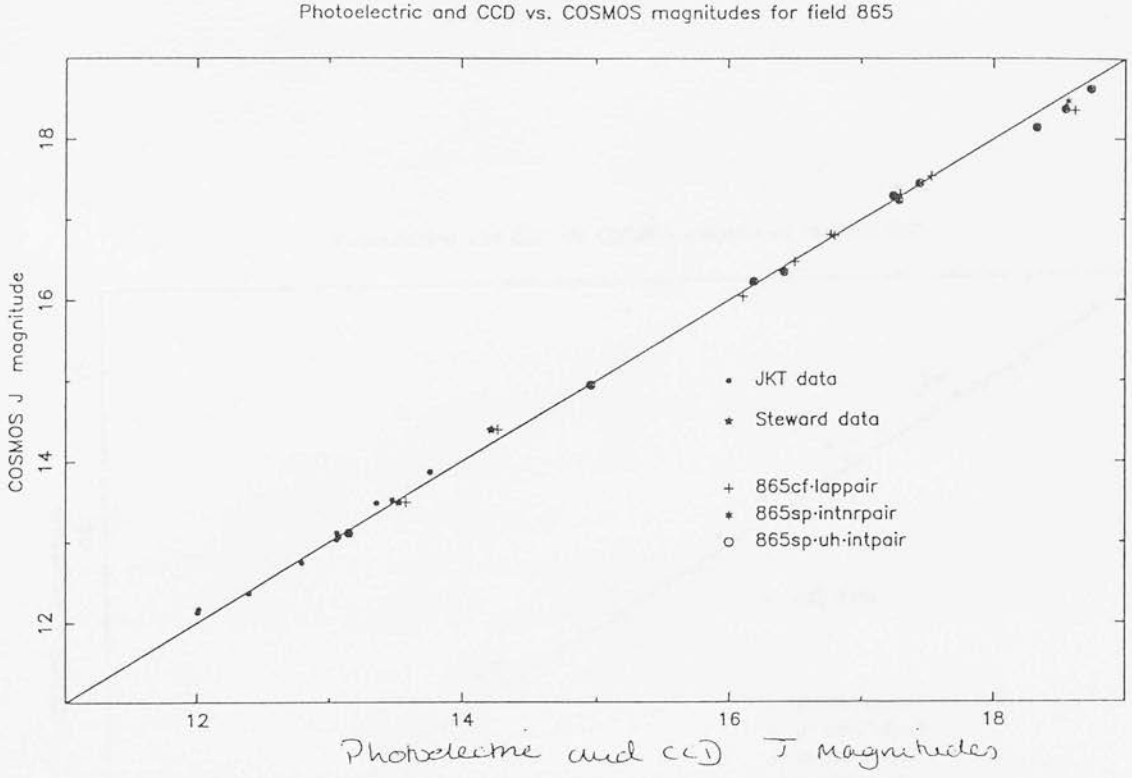

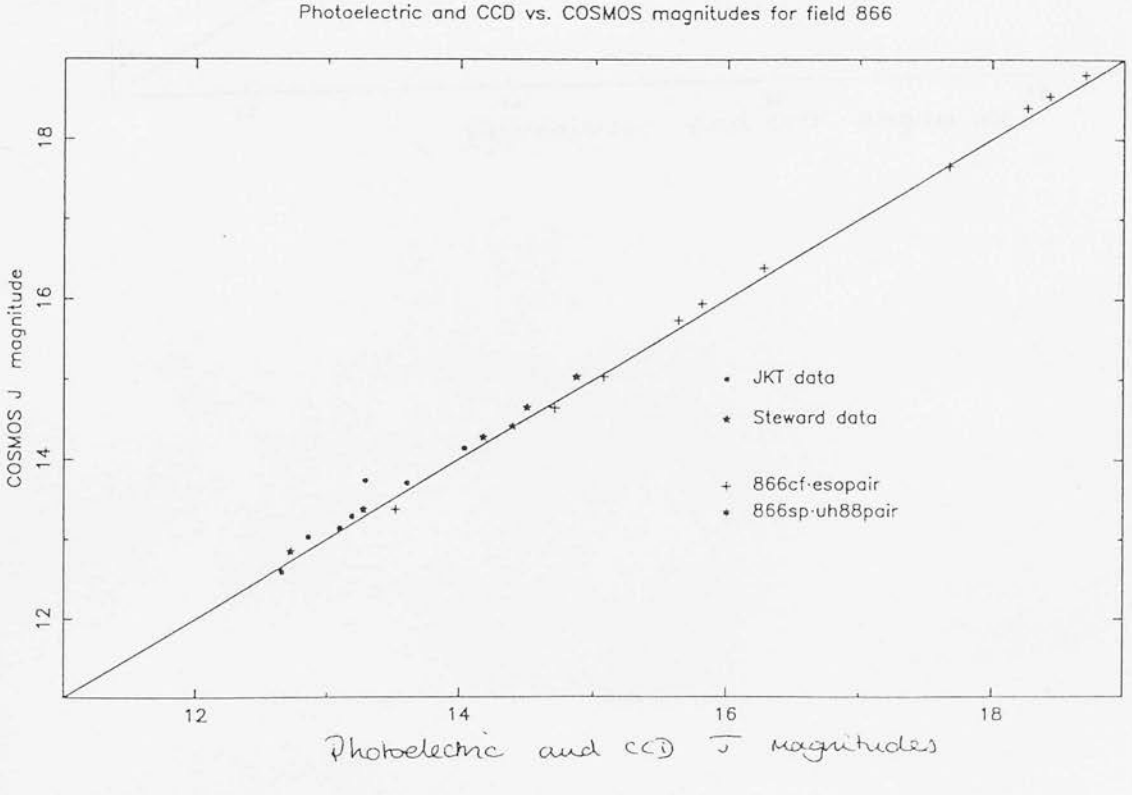

COSMOS data vs. calibration data for fields 865 (top) and 866 (bottom).

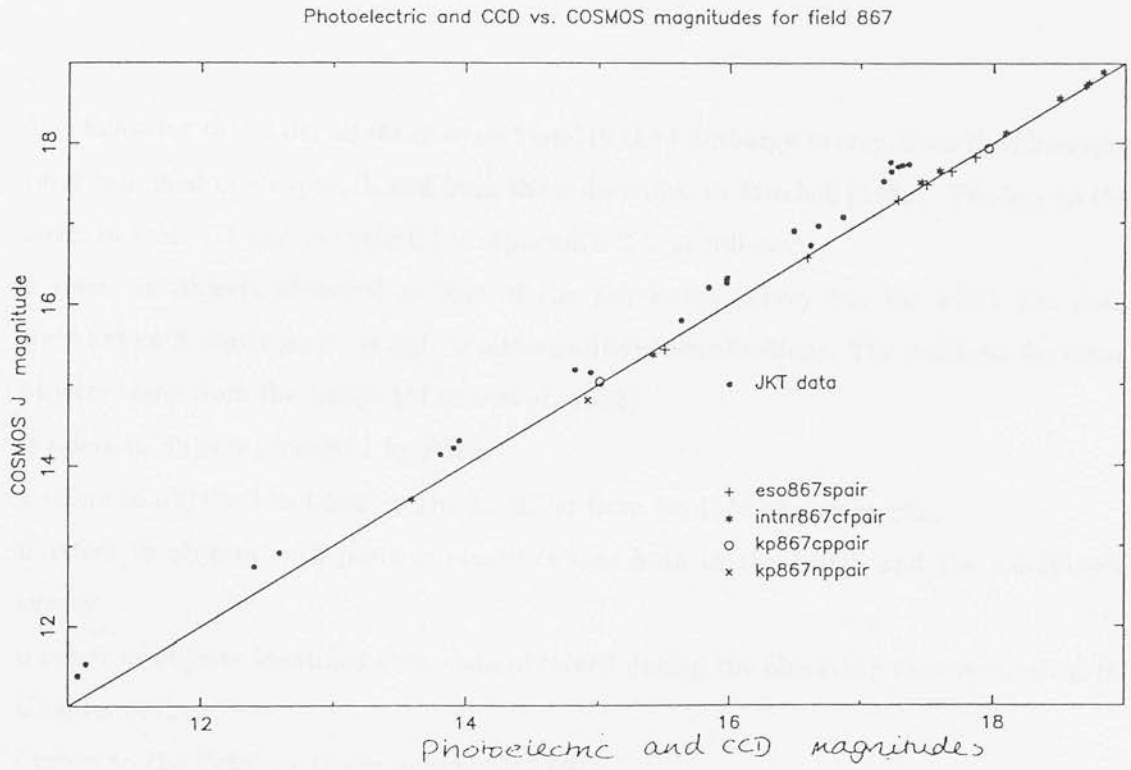

COSMOS data vs. calibration data for field 867.

Appendix B

Quasars found in the Edinburgh Survey

The following tables list all the quasars found in the Edinburgh survey, from the observing runs described in Chapter 3, and from those described in Mitchell (1989). The key to the notes in table B1 and in table C1 in Appendix C is as follows;

a refers to objects observed as part of the Edinburgh survey but for which the data were not sufficiently good enough to allow positive identifications. The redshifts for these objects come from the LBQS (Morris et al. 1992).

b refers to objects identified by PSM.

c refers to objects identified by Dr. L. Miller from his 1989 observing run.

d refers to objects with positive identifications both in the LBQS and the Edinburgh survey.

e refers to objects identified from data obtained during the observing runs desccribed in Chapter 3.

f refers to the Palomar-Green quasar 1352+011.

Table B1: Quasars in the Edinburgh Survey.

Extra-galactic objects found in field 861

Name	R.A.	Declination	B_J	$U-B_J$	ID	z	M_B	Quality	Notes
1228+011	12 28 08.5	01 14 48.7	17.63	-0.04	QSO	1.409	-26.89	2	e
1228-013	12 28 17.1	-01 30 30.8	17.71	-1.15	QSO	0.706	-25.35		a
1229-020	12 29 26.0	-02 07 33.2	17.70	-0.92	QSO	1.06	-26.22	1	b,d
1230-001	12 30 30.2	-00 15 05.0	17.71	-1.04	QSO	0.470	-24.47		a
1234-020	12 34 14.3	-02 09 36.0	17.94	-0.42	QSO	1.606	-26.86		a
1234+012	12 34 51.0	01 22 45.0	18.01	-0.68	QSO	2.02	-27.27	1	c,d
1235+021	12 35 39.7	02 16 47.6	18.17	-0.42	QSO	0.672	-24.78		a
1236+012	12 36 38.0	01 28 42.4	17.99	-1.16	QSO	1.258	-26.29	1	b,d
1237+020	12 37 58.4	02 04 44.0	17.58	-0.52	QSO	0.56	-24.98	1	c,d
1239-023	12 39 23.1	-02 31 05.6	17.61	-0.63	QSO	1.233	-26.63	1	b,d
1240+022	12 40 13.9	02 24 43.3	17.72	-0.69	QSO	0.79	-25.58	1	c,d
1242-012	12 42 22.1	-01 23 09.8	17.85	-0.68	QSO	0.489	-24.42	2	b,d
1242-000	12 42 50.8	00 06 45.6	17.92	-0.74	QSO	2.02	-27.36	1	c,d
1243-002	12 43 39.2	-00 26 10.1	17.06	-0.98	QSO	0.650	-25.82		c
1246-021	12 46 50.5	-02 17 19.2	18.06	-0.71	QSO	2.10	-27.30	1	c,d
1247-021	12 47 13.2	-02 13 09.2	18.48	-0.95	QSO	1.312	-25.89		a
1247+003	12 47 56.8	00 36 18.6	17.92	-0.54	QSO	0.214	-22.56		c

Table B1: (continued)

Extra-galactic objects found in field 862

Name	R.A.	Declination	B_J	$U-B_J$	ID	z	M_B	Quality	Notes
1249-020	12 49 17.1	-02 07 17.8	17.00	-0.55	QSO	1.184	-27.16	1	b
1251-014	12 51 00.6	-01 42 23.0	17.18	-0.78	QSO	1.688	-27.72		c
1252+020	12 52 46.4	02 00 26.5	15.52	-1.39	QSO	0.345	-25.99	1	b
1253-000	12 53 16.4	-00 02 17.4	17.82	-0.57	QSO	0.721	-25.28	2	b
1253+004	12 53 54.5	00 48 12.4	17.73	-0.64	QSO	0.833	-25.68	3	b
1254+004	12 54 29.5	00 40 48.0	17.74	-0.68	QSO	1.267	-26.56	1	b
1254+020	12 54 33.3	02 06 51.7	17.39	-0.61	QSO	0.421	-24.55		c
1254+010	12 54 46.0	01 06 31.0	17.69	-0.44	QSO	1.510	-26.98	1	b
1255-014	12 55 40.9	-01 43 07.9	17.78	-0.52	QSO	0.410	-24.11	1	b
1256-003	12 56 38.8	-00 37 03.7	17.83	-0.79	QSO	1.333	-26.58		c
1257-014	12 57 18.2	-01 40 57.9	17.77	-0.58	QSO	0.448	-24.31	1	b
1259+001	12 59 02.4	00 18 05.6	17.85	-0.28	QSO	1.767	-27.15		c
1259+015	12 59 57.4	01 53 12.3	17.62	-0.66	QSO	1.251	-26.65		c
1301+022	13 01 44.0	02 21 41.5	17.36	-0.71	QSO	0.229	-23.27		c
1303+020	13 03 21.0	02 05 32.0	17.22	-0.64	QSO	0.736	-25.92	2	b
1305+010	13 05 20.8	01 00 21.5	17.89	-0.27	QSO	0.763	-25.33	1	e
1305+023	13 05 42.5	02 30 10.2	17.29	-0.36	QSO	0.773	-25.96	2	b
1306-021	13 06 32.4	-02 13 17.5	17.75	-0.50	QSO	0.835	-25.66	1	b
1307+001	13 07 58.2	00 18 08.4	17.93	-0.13	QSO	0.178	-22.15		c
1308+001	13 08 01.0	00 19 50.8	17.64	-0.38	QSO	1.311	-26.73	1	b
1308+010	13 08 47.7	01 09 15.4	17.90	-0.32	QSO	1.074	-26.05		a

Table B1: (continued)

Extra-galactic objects found in field 863

Name	R.A.	Declination	B_J	$U-B_J$	ID	z	M_B	Quality	Notes
1311+021	13 11 53.6	02 17 06.9	17.05	-1.02	QSO	0.306	-24.20	1	b,d
1313-013	13 13 35.4	-01 38 15.2	17.79	-0.67	QSO	0.406	-24.08	1	b,d
1313+010	13 13 57.0	01 07 13.8	18.21	-0.54	QSO	2.398	-27.42	1	b,d
1315+000	13 15 11.1	00 02 55.9	18.04	-0.69	QSO	0.917	-25.57	1	c,d
1315+012	13 15 37.5	01 27 26.9	18.03	-0.64	QSO	1.630	-26.80	1	b,d
1315+014	13 15 41.9	01 40 36.5	18.07	-0.72	QSO	0.689	-24.93	1	e,d
1316+002	13 16 06.5	00 23 20.6	17.93	-0.65	QSO	0.490	-24.34	1	b,d
1317-003	13 17 04.7	-00 33 56.1	18.57	-0.75	QSO	0.890	-24.98	1	e,d
1317-014	13 17 15.9	-01 42 20.3	17.39	-0.68	QSO	0.225	-23.20	1	b,d
1317-001	13 17 46.3	-00 18 45.5	17.78	-0.84	QSO	0.350	-23.76	1	b,d
1319+003	13 19 06.0	00 39 38.4	18.02	-0.66	QSO	1.614	-26.79	1	c,d
1319+003	13 19 32.6	00 33 39.9	18.07	-0.65	QSO	0.535	-24.39	1	c,d
1319+014	13 19 39.0	01 46 15.3	17.52	-0.58	NELG	0.183	-22.62	1	e
1320-000	13 20 49.9	-00 06 17.1	18.56	-0.51	QSO	1.388	-25.93		a
1320+010	13 20 59.6	01 03 28.0	18.04	-0.90	QSO	1.780	-26.97	1	c,d
1323-013	13 23 59.1	-01 38 59.0	18.35	-0.86	QSO	1.142	-25.73	1	e,d
1324+012	13 24 50.9	01 26 55.2	18.49	-0.84	QSO	0.864	-25.00	1	e,d
1325+001	13 25 23.8	00 19 47.0	17.58	-0.27	QSO	0.375	-24.11	3	e
1325-011	13 25 59.8	-01 13 47.3	16.71	-0.30	QSO	0.150	-23.00	1	e,d
1326+020	13 26 10.6	02 06 47.6	17.40	-0.98	QSO	1.430	-27.15	1	b,d
1328-023	13 28 38.5	-02 31 46.4	18.57	-0.70	QSO	1.240	-25.68		c

Table B1: (continued)

Extra-galactic objects found in field 864

Name	R.A.	Declination	B_J	$U-B_J$	ID	z	M_B	Quality	Notes
1328+020	13 28 58.7	02 05 12.0	18.25	-0.36	QSO	0.692	-24.76		a
1329-000	13 29 57.1	-00 07 54.5	18.39	-0.68	QSO	0.962	-25.33	1	e,d
1330+011	13 30 48.6	01 13 46.9	18.15	-0.67	QSO	1.506	-26.51	1	e,d
1331-001	13 31 10.3	-00 18 16.6	18.31	-0.98	QSO	0.859	-25.16	3	e
1331-010	13 31 53.7	-01 08 29.0	18.01	-0.25	QSO	1.883	-27.12		a
1331-012	13 31 58.8	-01 23 05.7	18.23	-0.41	QSO	0.289	-22.90		a
1332-004	13 32 51.8	-00 45 09.6	17.53	-0.37	QSO	0.675	-25.43	1	e,d
1333+013	13 33 01.7	01 33 24.0	18.15	-0.18	QSO	1.577	-26.61	1	e,d
1334-003	13 34 13.0	-00 33 40.9	17.59	-0.22	QSO	2.806	-28.36	1	e,d
1334+021	13 34 13.8	02 12 58.7	18.10	-0.18	QSO	2.384	-27.52		a
1334-000	13 34 15.2	-00 05 41.0	17.84	-0.64	QSO	0.298	-23.36		a
1334+005	13 34 49.2	00 53 27.0	18.41	-0.45	QSO	0.647	-24.46		a
1335+022	13 35 06.9	02 22 12.8	18.16	-0.58	QSO	1.354	-26.68		a
1335+003	13 35 49.5	00 31 25.5	18.48	-0.56	QSO	2.169	-26.94	1	e
1336-000	13 36 11.0	-00 06 34.5	18.26	-0.65	QSO	1.771	-26.74	1	e
1337-014	13 37 17.0	-01 46 07.9	18.06	-0.45	QSO	1.010	-25.76	1	e,d
1338-003	13 38 10.4	-00 30 07.3	17.22	-0.57	QSO	0.389	-24.55	1	c,d
1338-003	13 38 39.7	-00 38 06.5	18.18	-0.70	QSO	0.238	-22.53	1	c,d
1338-015	13 38 46.6	-01 53 48.6	17.60	-0.62	QSO	2.094	-27.75	1	e
1340-002	13 40 12.2	-00 20 38.4	18.27	-0.60	QSO	0.792	-25.03	1	e,d
1340+010	13 40 25.8	01 07 02.8	17.99	-0.67	QSO	1.067	-25.95		a
1342-000	13 42 25.6	-00 00 58.4	17.75	-0.57	QSO	0.245	-23.02	1	e,d
1343-022	13 43 13.1	-02 21 54.8	18.32	-0.32	QSO	0.509	-24.03		a
1344+013	13 44 03.6	01 37 11.5	17.46	-0.67	QSO	1.915	-27.70		a
1344-022	13 44 38.1	-02 27 36.4	18.28	-0.36	QSO	0.511	-24.08		a
1344-010	13 44 58.0	-01 05 07.8	18.11	-0.74	QSO	1.714	-26.82	1	e,d
1345-013	13 45 14.5	-01 37 28.5	18.49	-0.57	QSO	1.929	-26.69		a
1345-000	13 45 17.8	-00 00 23.0	18.11	-0.44	QSO	0.552	-24.42		a
1346+012	13 46 01.8	01 21 19.9	18.52	-0.67	QSO	1.930	-26.66		a
1346+000	13 46 48.3	00 07 54.5	18.36	-0.19	QSO	1.127	-25.69		a
1347-002	13 47 00.2	-00 26 10.8	17.77	-0.40	QSO	0.515	-24.61	1	e,d
1347-005	13 47 14.1	-00 51 30.1	16.29	-0.41	QSO	0.600	-24.62		c
1347-023	13 47 47.7	-02 37 07.7	17.34	-0.35	NELG	0.139	-22.20	1	e
1348-005	13 48 10.3	-00 54 09.5	18.21	-0.36	QSO	1.474	-26.41		a

Table B1: (continued)

Extra-galactic objects found in field 865

Name	R.A.	Declination	B_J	$U-B_J$	ID	z	M_B	Quality	Notes
1348+011	13 48 55.1	01 18 27.5	17.68	-0.74	QSO	1.094	-26.31	1	b,d
1349+000	13 49 16.6	00 07 08.8	17.12	-0.75	QSO	1.435	-27.44	1	b
1349+005	13 49 59.2	00 57 39.1	18.07	-0.77	QSO	1.151	-26.03	1	c,d
1351+000	13 51 51.3	00 00 44.4	17.06	-0.67	QSO	1.501	-27.60	1	b
1352+010	13 52 25.4	01 06 52.7	16.71	-0.68	QSO	1.117	-27.32	1	c,f
1352-004	13 52 51.4	-00 43 00.3	18.40	-0.80	QSO	0.900	-25.17		c
1354+011	13 54 17.2	01 17 21.6	17.97	-0.77	QSO	1.210	-26.23	1	e
1354-023	13 54 53.8	-02 33 02.6	17.16	-0.55	QSO	0.559	-25.39	2	b
1355+022	13 55 51.6	02 28 18.0	16.61	-0.61	QSO	0.955	-27.09	1	b
1357-001	13 57 09.1	-00 19 53.2	17.43	-0.57	QSO	0.164	-22.47	1	e
1357-022	13 57 31.4	-02 27 01.8	17.68	-0.70	QSO	0.418	-24.25		c
1358+005	13 58 31.6	00 58 00.9	17.52	-0.58	QSO	0.664	-25.40		c
1358+000	13 58 36.9	00 01 24.3	17.06	-0.57	QSO	1.845	-28.03	1	b
1402-011	14 02 11.2	-01 16 02.0	18.32	-0.43	QSO	2.520	-27.41	2	e
1404-010	14 04 20.7	-01 02 54.2	18.49	-0.64	QSO	0.911	-25.11	1	e
1406-014	14 06 54.2	-01 43 08.1	17.76	-0.67	QSO	0.644	-25.10		c
1407-003	14 07 38.0	-00 38 17.3	18.30	-0.57	QSO	0.025	-17.53	1	e
1407-023	14 07 20.9	-02 31 55.0	17.88	-0.74	QSO	1.263	-26.41	2	b
1408+005	14 08 34.5	00 50 11.7	18.09	-0.69	QSO	1.712	-26.84	1	e

Table B1: (continued)

Extra-galactic objects found in field 866

Name	R.A.	Declination	B_J	$U-B_J$	ID	z	M_B	Quality	Notes
1408+005	14 08 50.3	00 56 56.8	18.44	-0.31	QSO	2.260	-27.07	1	e
1409+010	14 09 48.5	01 01 21.4	17.00	-0.43	QSO	1.635	-27.84	1	b,d
1411-001	14 11 53.7	-00 14 11.1	17.98	-0.49	QSO	0.026	-17.93		c
1412-001	14 12 54.8	-00 12 38.4	17.28	-0.67	QSO	1.148	-26.81	1	b
1413+010	14 13 16.6	01 07 50.8	17.46	-0.55	QSO	1.042	-26.43	2	b
1413+013	14 13 18.3	01 36 36.8	17.73	-0.74	QSO	1.246	-26.53	2	b
1419-010	14 19 39.3	-01 07 08.0	18.13	-0.88	QSO	1.915	-27.03		c
1420-005	14 20 05.9	-00 53 08.5	17.77	-0.45	QSO	0.717	-25.32		c
1421-001	14 21 29.8	-00 13 23.9	16.33	-0.53	QSO	0.151	-23.39		c
1421+010	14 21 57.3	01 08 32.2	18.09	-0.68	QSO	1.060	-25.83	2	b
1423-001	14 23 26.2	-00 13 31.1	17.96	-0.63	QSO	1.078	-26.00	2	b
1423+005	14 23 41.6	00 55 27.8	17.93	-0.63	QSO	0.890	-25.62	3	b
1424-007	14 24 24.6	-00 07 29.6	16.52	-0.53	QSO	0.632	-26.30	2	b
1424+011	14 24 41.6	01 12 50.7	16.38	-0.35	NELG	0.052	-21.03	1	e
1425+000	14 25 00.0	00 02 43.4	17.90	-0.68	QSO	1.548	-26.82	2	b
1428+020	14 28 08.5	02 02 55.9	18.14	-0.70	QSO	2.107	-27.22	1	b,d

Table B1: (continued)

Table 7: Extra-galactic objects found in field 867

Name	R.A.	Declination	B_J	$U - B_J$	ID	z	M_B	Quality	Notes
1429-010	14 29 07.3	-01 00 17.4	17.49	-0.68	QSO	0.661	-25.42	1	e,d
1429-003	14 29 09.4	-00 36 57.7	18.47	-0.74	QSO	1.179	-25.68		a
1429-005	14 29 54.7	-00 53 04.6	18.08	-0.86	QSO	2.075	-27.25	1	b,d
1429+013	14 29 57.9	01 37 47.8	18.18	-0.62	QSO	1.530	-26.52	1	b,d
1430-004	14 30 10.0	-00 46 04.3	17.85	-0.83	QSO	1.020	-25.99	1	b,d
1430-004	14 30 47.0	-00 41 36.1	16.17	-0.87	QSO	1.112	-27.85	1	b,d
1433+022	14 33 07.6	02 23 48.8	18.38	-0.61	QSO	2.130	-27.01	1	b,d
1433-001	14 33 50.7	-00 16 03.9	18.07	-0.56	QSO	0.324	-23.31	1	e,d
1435-013	14 35 13.3	-01 34 13.8	16.22	-1.13	QSO	1.310	-28.15	1	b,d
1437-014	14 37 46.8	-01 43 37.0	18.41	-0.60	QSO	0.718	-24.68	1	e,d
1440+014	14 40 18.0	01 49 37.9	18.32	-0.83	QSO	1.170	-25.81	1	b,d
1440-002	14 40 25.7	-00 24 42.0	18.19	-1.02	QSO	1.820	-26.87	1	b,d
1440-023	14 40 38.4	-02 34 40.4	17.49	-0.65	QSO	0.675	-25.47	1	b,d
1441+014	14 41 27.2	01 42 36.9	17.92	-0.65	QSO	0.296	-23.26	1	b,d
1445-023	14 45 08.8	-02 31 38.2	18.09	-0.80	QSO	1.730	-26.86	1	b,d
1446+021	14 46 05.7	02 18 54.2	18.23	-0.49	QSO	0.668	-24.71	1	b,d
1447+002	14 47 29.0	00 28 51.8	18.38	-0.78	QSO	0.946	-25.30	3	b

Table 8: Extra-galactic objects found in field 789

Name	R.A.	Declination	B_J	$U - B_J$	ID	z	M_B	Quality	Notes
1228-041	12 28 28.5	-04 12 02.2	17.44	-0.49	QSO	0.658	-25.46		c
1229-050	12 29 36.1	-05 01 53.9	17.17	-0.77	QSO	1.078	-26.79	2	b
1235-034	12 35 30.5	-03 40 39.4	17.23	-0.82	QSO	1.489	-27.41		c
1237-035	12 37 05.7	-03 59 22.1	17.21	-0.64	QSO	0.371	-24.46		c
1237-043	12 37 41.7	-04 35 03.2	17.76	-0.65	QSO	0.810	-25.59		c
1239-071	12 39 05.0	-07 16 40.3	17.21	-0.63	QSO	1.170	-26.92		c
1239-072	12 39 10.1	-07 26 28.5	17.15	-0.87	QSO	1.184	-27.01	1	b
1245-033	12 45 00.4	-03 33 47.4	15.93	-0.89	QSO	0.379	-25.79	1	b
1246-043	12 46 17.0	-04 30 3.2	17.17	-0.92	QSO	0.531	-25.27		c
1248-044	12 48 44.3	-04 48 44.5	17.04	-0.64	QSO	1.410	-27.48	1	b

Table 9: Extra-galactic objects found in field 790

Name	R.A.	Declination	B_J	$U - B_J$	ID	z	M_B	Quality	Notes
1249-064	12 49 20.9	-06 48 44.1	16.58	-1.36	QSO	1.187	-27.58		c
1250-070	12 50 46.1	-07 00 37.5	16.43	-0.67	QSO	0.097	-22.33	2	e
1251-073	12 51 59.7	-07 37 32.1	18.02	-1.12	QSO	1.476	-26.60	3	e
1252-065	12 52 51.3	-06 59 06.7	18.00	-1.25	QSO	0.250	-22.82	1	e
1253-032	12 53 30.4	-03 29 36.9	17.49	-1.20	QSO	2.238	-28.00	2	e
1253-060	12 53 35.4	-06 03 15.3	17.38	-1.17	QSO	0.175	-22.66		c
1254-073	12 54 39.8	-07 36 42.2	18.00	-1.28	QSO	0.175	-22.04	1	e
1255-043	12 55 55.8	-04 37 37.7	16.64	-1.04	QSO	0.173	-23.38	1	e
1256-045	12 56 49.0	-04 58 39.3	17.10	-1.34	QSO	0.126	-22.23	1	e
1258-041	12 58 16.0	-04 15 50.6	18.06	-1.17	QSO	1.738	-26.90	1	b
1300-065	13 00 10.7	-06 57 48.8	16.80	-1.01	QSO	0.183	-23.34	1	e
1300-033	13 00 56.8	-03 38 43.0	18.07	-1.22	QSO	0.390	-23.71	1	b
1304-061	13 04 18.8	-06 14 02.2	17.49	-1.06	QSO	1.563	-27.25	1	b
1304-061	13 04 31.0	-06 15 58.5	17.88	-1.27	QSO	1.441	-26.69	2	e
1306-035	13 06 28.8	-03 50 14.1	17.97	-1.08	QSO	0.399	-23.86	2	b
1308-060	13 08 11.6	-06 07 35.8	18.46	-0.93	QSO	0.173	-21.56	2	e

Table 10: Extra-galactic objects found in field 791

Name	R.A.	Declination	B_J	$U - B_J$	ID	z	M_B	Quality	Notes
1315-041	13 15 14.0	-04 10 14.0	17.63	-0.67	QSO	0.469	-24.55	1	b
1316-042	13 16 03.6	-04 24 22.6	18.10	-0.42	NELG	0.018	-17.01	1	e
1316-073	13 16 48.4	-07 34 43.2	16.49	-0.74	QSO	0.538	-25.98	1	e
1318-065	13 18 06.9	-06 59 58.5	17.22	-0.98	NELG	0.104	-21.70		c
1319-025	13 19 26.1	-02 59 03.0	18.34	-0.29	QSO	0.074	-19.84	2	e
1320-063	13 20 12.9	-06 35 28.2	17.31	-0.67	QSO	1.678	-27.58		c
1321-054	13 21 38.6	-05 49 00.8	16.73	-0.57	QSO	0.732	-26.40	2	b
1322-064	13 22 07.9	-06 41 50.2	17.99	-0.43	QSO	0.147	-21.68	1	e
1323-024	13 23 40.2	-02 48 24.1	17.25	-0.54	QSO	2.125	-28.13	1	b,d
1326-065	13 26 14.0	-06 57 52.2	17.26	-0.67	NELG	0.078	-21.03		c
1326-051	13 26 52.5	-05 16 06.6	15.47	-0.45	QSO	0.580	-27.16	1	e

Table B1: (continued)

Table 11: Extra-galactic objects found in field 792

Name	R.A.	Declination	B_J	$U - B_J$	ID	z	M_B	Quality	Notes
1329-061	13 29 09.4	-06 15 20.6	17.57	-0.46	QSO	0.714	-25.51	1	e
1329-043	13 29 23.9	-04 31 10.7	16.58	-0.23	QSO	0.075	-21.63	2	e
1329-042	13 29 58.7	-04 20 30.8	17.33	-0.92	QSO	1.295	-27.02		c
1332-065	13 32 50.0	-06 59 45.9	18.29	-0.26	QSO	2.621	-27.52	1	e
1333-032	13 33 35.4	-03 26 26.9	18.25	-0.75	NELG	0.006	-14.47		c
1333-070	13 33 41.5	-07 07 35.4	18.04	-0.88	NELG	0.328	-23.36	1	e
1334-023	13 34 37.9	-02 32 37.2	17.71	-0.77	QSO	0.723	-25.40		a
1335-024	13 35 01.6	-02 41 53.6	18.15	-0.52	QSO	0.610	-24.59	1	e,d
1335-042	13 35 20.2	-04 22 36.0	18.35	-0.36	QSO	0.272	-22.65	3	e
1335-061	13 35 31.1	-06 11 57.6	17.87	-0.42	QSO	0.620	-24.91		c
1336-033	13 36 00.3	-03 34 09.4	17.90	-0.59	NELG	0.155	-21.88	1	e
1336-042	13 36 09.4	-04 23 40.9	17.10	-0.68	QSO	0.163	-22.79	1	e
1338-072	13 38 26.0	-07 24 40.5	17.40	-0.37	QSO	2.353	-28.19		c
1339-045	13 39 39.3	-04 59 49.2	18.25	-0.77	QSO	0.884	-25.29	2	e
1339-052	13 39 41.4	-05 26 12.4	18.11	-0.47	QSO	1.252	-26.16	2	e
1339-064	13 39 49.7	-06 48 04.6	18.34	-0.88	QSO	1.220	-25.88	2	e
1340-054	13 40 52.8	-05 45 26.8	17.94	-0.77	QSO	0.319	-23.40	1	e
1341-035	13 41 34.4	-03 57 46.9	17.39	-0.75	QSO	0.835	-26.02		c
1343-053	13 43 14.4	-05 38 21.8	17.52	-0.85	QSO	2.047	-27.78	1	b
1343-060	13 43 23.7	-06 07 44.0	17.72	-0.73	QSO	1.012	-26.10		c
1344-041	13 44 23.1	-04 19 26.1	17.13	-0.94	QSO	1.922	-28.04	1	b
1344-062	13 44 59.7	-06 23 13.4	17.78	-0.55	QSO	0.118	-21.41		c
1345-051	13 45 47.7	-05 10 19.0	17.06	-0.77	QSO	1.386	-27.43	1	b
1345-031	13 45 55.0	-03 17 27.7	17.86	-1.00	QSO	1.947	-27.34	1	b
1346-030	13 46 19.9	-03 06 48.6	17.83	-0.82	QSO	2.090	-27.52	1	b
1346-025	13 46 53.5	-02 51 55.8	18.21	-0.88	QSO	1.721	-26.73	1	e,d

Table 12: Extra-galactic objects found in field 793

Name	R.A.	Declination	B_J	$U - B_J$	ID	z	M_B	Quality	Notes
1351-064	13 51 11.9	-06 41 02.7	17.95	-1.08	QSO	0.334	-23.49	2	e
1354-044	13 54 03.9	-04 49 53.0	17.70	-0.81	QSO	1.423	-26.84	2	e
1354-024	13 54 15.5	-02 40 30.2	16.97	-0.48	NELG	0.026	-18.94	1	e
1356-060	13 56 44.9	-06 07 43.8	16.17	-0.66	NELG	0.072	-21.95	1	e
1358-044	13 58 41.6	-04 41 20.6	18.04	-0.84	QSO	0.200	-22.29	2	e
1358-041	13 58 48.7	-04 12 42.3	17.37	-0.76	QSO	1.354	-27.07	2	e
1359-055	13 59 03.8	-05 53 56.1	17.72	-0.94	QSO	1.990	-27.52	1	e
1403-030	14 03 35.2	-03 04 56.4	17.01	-0.80	QSO	0.860	-26.47	2	e
1404-045	14 04 53.9	-04 55 56.0	15.79	-0.62	QSO	0.031	-20.57	1	e
1407-072	14 07 52.8	-07 22 31.7	17.97	-0.85	QSO	0.900	-25.60	2	e
1408-051	14 08 01.9	-05 11 35.3	17.65	-0.54	QSO	0.154	-22.12	1	e
1408-065	14 08 28.1	-06 51 10.6	17.80	-0.88	QSO	1.770	-27.20	2	e

Table 13: Extra-galactic objects found in field 794

Name	R.A.	Declination	B_J	$U - B_J$	ID	z	M_B	Quality	Notes
1411-033	14 11 41.4	-03 33 46.5	17.91	-0.78	QSO	0.860	-25.57	2	e
1414-033	14 14 30.3	-03 31 16.0	17.66	-0.63	QSO	0.780	-25.61	3	e
1414-054	14 14 30.8	-05 44 46.2	17.37	-0.60	QSO	0.419	-24.56		c
1415-064	14 15 02.9	-06 48 23.3	18.08	-0.69	QSO	0.234	-22.59		c
1416-051	14 16 33.6	-05 18 59.7	18.50	-0.72	QSO	0.96	-25.21	2	e
1416-032	14 16 50.1	-03 24 51.0	18.10	-0.71	QSO	0.73	-25.03	3	e
1421-073	14 21 08.6	-07 30 05.0	17.77	-0.37	NELG	0.301	-23.44	1	e
1421-040	14 21 33.4	-04 07 42.2	18.05	-0.43	QSO	0.650	-24.83		c
1422-044	14 22 41.1	-04 44 51.3	18.23	-0.33	QSO	1.730	-26.72	2	e
1422-032	14 22 48.9	-03 23 50.9	18.08	-0.46	QSO	0.205	-22.31	2	e
1423-053	14 23 04.7	-05 34 46.8	17.42	-0.74	QSO	0.291	-23.73	1	e
1423-071	14 23 22.2	-07 18 00.3	18.46	-1.03	QSO	0.040	-18.38	3	e
1423-043	14 23 55.1	-04 34 01.1	17.91	-0.60	NELG	0.124	-21.32	1	e

Appendix C

UVX Candidate lists

The following tables list all the candidates observed during the INT runs (1990, 1991), the FLAIR runs at the UKST (1991, 1992) and the ESO run (1991).

Table C1: UVX Candidates observed.

Table 1: UVX candidates and their IDs in field 861

R.A. (1950)	Declination	B_J	$U - B_J$	ID	z	Quality	Notes
12 28 08.5	01 14 48.7	17.63	-0.04	QSO	1.409	2	e
12 28 17.1	-01 30 30.8	17.71	-1.15	QSO	0.706		a
12 28 19.6	00 59 10.4	17.40	0.11	star			
12 28 25.2	02 19 06.0	15.66	-0.51	star			
12 28 36.2	00 57 16.1	17.81	0.02	star			
12 28 42.6	01 15 13.2	17.55	-0.12	star			
12 29 26.0	-02 07 33.2	17.70	-0.92	QSO	1.06	1	b,d
12 29 46.7	02 12 31.7	17.33	-0.31	star			
12 30 30.2	-00 15 05.0	17.71	-1.04	QSO	0.470		a
12 31 35.8	-00 11 35.0	18.12	-0.57	?			
12 31 36.3	-02 11 32.0	18.13	-0.62	star			
12 34 14.3	-02 09 36.0	17.94	-0.42	QSO	1.606		a
12 34 51.0	01 22 45.0	18.01	-0.68	QSO	2.02	1	c,d
12 35 39.7	02 16 47.6	18.17	-0.42	QSO	0.672		a
12 36 38.0	01 28 42.4	17.99	-1.16	QSO	1.258	1	b,d
12 37 58.4	02 04 44.0	17.58	-0.52	QSO	0.56	1	c,d
12 38 04.8	-02 35 54.6	15.60	-0.26	star			
12 38 47.1	00 41 14.0	18.20	-0.26	?			
12 39 23.1	-02 31 05.6	17.61	-0.63	QSO	1.233	1	b,d
12 40 13.9	02 24 43.3	17.72	-0.69	QSO	0.79	1	c,d
12 41 27.4	02 24 49.0	18.32	-0.36	?			
12 42 22.1	-01 23 9.8	17.85	-0.68	QSO	0.489	2	b,d
12 42 50.8	00 6 45.6	17.92	-0.74	QSO	2.02	1	c,d
12 43 39.2	-00 26 10.1	17.06	-0.98	QSO	0.650		c
12 44 58.7	01 32 24.6	16.07	-0.45	star			
12 46 50.5	-02 17 19.2	18.06	-0.71	QSO	2.10	1	c,d
12 47 13.2	-02 13 09.2	18.48	-0.95	QSO	1.312		a
12 47 24.8	00 05 36.4	17.51	-0.15	star			
12 47 53.6	00 36 09.0	18.01	-0.38	?			
12 47 56.8	00 36 18.6	17.92	-0.54	QSO	0.214		c
12 48 05.2	-00 06 44.0	18.12	-0.08	?			
12 48 21.9	00 06 54.3	17.24	-0.15	star			
12 48 29.2	00 11 46.6	18.20	-0.19	star			

Table C1: (continued)

Table 2: UVX candidates and their IDs in field 862

R.A. (1950)	Declination	B_J	$U - B_J$	ID	z	Quality	Notes
12 48 40.1	00 09 43.3	17.36	0.26	star			
12 49 17.1	-02 7 17.8	17.00	-0.55	QSO	1.184	1	b
12 49 55.6	00 04 54.3	15.91	-0.10	?			
12 51 00.6	-01 42 23.0	17.18	-0.78	QSO	1.688		c
12 52 25.7	-02 35 54.4	16.09	-0.10	?			
12 52 46.4	02 00 26.5	15.52	-1.39	QSO	0.345	1	b
12 53 16.4	-00 2 17.4	17.82	-0.57	QSO	0.721	2	b
12 53 51.7	00 25 15.6	16.85	-0.23	star			
12 53 54.5	00 48 12.4	17.73	-0.64	QSO	0.833	3	b
12 54 29.5	00 40 48.0	17.74	-0.68	QSO	1.267	1	b
12 54 33.3	02 6 51.7	17.39	-0.61	QSO	0.421		c
12 54 46.0	01 6 31.0	17.69	-0.44	QSO	1.510	1	b
12 55 40.9	-01 43 07.9	17.78	-0.52	QSO	0.410	1	b
12 56 38.8	-00 37 03.7	17.83	-0.79	QSO	1.333		c
12 57 18.2	-01 40 57.9	17.77	-0.58	QSO	0.448	1	b
12 57 52.0	01 01 39.3	15.65	-1.04	?			
12 57 56.7	-02 11 23.0	15.58	-0.35	star			
12 59 02.4	00 18 05.6	17.85	-0.28	QSO	1.767		c
12 59 41.0	-02 29 10.8	18.04	-0.30	?			
12 59 57.4	01 53 12.3	17.62	-0.66	QSO	1.251		c
13 01 44.0	02 21 41.5	17.36	-0.71	QSO	0.229		c
13 03 21.0	02 5 32.0	17.22	-0.64	QSO	0.736	2	b
13 03 34.7	-01 27 30.6	16.39	-0.09	star			
13 05 15.8	01 43 06.6	17.68	-0.09	?			
13 05 20.8	01 00 21.5	18.00	-0.47	QSO	0.763	1	e
13 05 42.5	02 30 10.2	17.29	-0.36	QSO	0.773	2	b
13 06 32.4	-02 13 17.5	17.75	-0.50	QSO	0.835	1	b
13 07 07.5	-00 59 08.4	15.72	-0.96	star			
13 07 58.2	00 18 8.4	17.93	-0.23	QSO	0.178		c
13 08 01.0	00 19 50.8	17.64	-0.48	QSO	1.311	1	b
13 08 05.4	-02 22 37.2	16.00	-0.32	?			
13 08 19.6	-02 25 39.5	17.99	0.22	?			
13 08 29.5	-00 18 52.3	17.91	0.17	star			
13 08 47.3	-01 59 21.3	17.31	0.10	?			
13 08 47.7	01 09 15.4	17.90	-0.32	QSO	1.074		a

Table C1: (continued)

Table 3: UVX candidates and their IDs in field 863

R.A. (1950)	Declination	B_J	$U-B_J$	ID	z	Quality	Notes
13 08 59.1	-00 39 55.8	17.30	-0.25	star			
13 09 03.0	-02 06 15.8	18.30	-0.27	?			
13 09 17.1	00 45 14.1	18.41	-0.34	?			
13 10 27.2	00 02 19.3	17.39	-0.33	star			
13 10 44.6	-02 32 45.2	17.96	-0.28	star			
13 11 07.0	-01 36 49.7	18.27	-0.27	?			
13 11 22.4	00 46 04.6	17.49	-0.27	star			
13 11 49.4	01 13 15.2	18.19	-0.79	?			
13 11 52.1	01 27 44.7	15.72	-0.66	?			
13 11 53.6	02 17 6.9	17.05	-1.02	QSO	0.306	1	b,d
13 12 06.2	02 26 54.5	17.49	-0.28	star			
13 12 30.6	-02 29 24.6	15.26	-0.58	star			
13 12 34.2	-01 34 11.7	15.71	-0.38	star			
13 12 44.1	02 12 37.2	18.12	-0.20	star			
13 12 52.0	00 50 32.3	17.32	-0.34	star			
13 13 35.4	-01 38 15.2	17.79	-0.67	QSO	0.406	1	b,d
13 13 57.0	01 7 13.8	18.21	-0.54	QSO	2.398	1	b,d
13 14 02.2	00 04 23.4	17.76	-0.24	?			
13 14 06.7	-01 12 23.9	15.80	-0.38	star			
13 14 51.4	00 54 24.9	18.14	-0.26	?			
13 15 01.3	01 02 38.2	18.08	-0.32	star			
13 15 11.1	00 2 55.9	18.04	-0.69	QSO	0.917	1	c,d
13 15 37.5	01 27 26.9	18.03	-0.64	QSO	1.630	1	b,d
13 15 41.9	01 40 36.5	18.07	-0.72	QSO	0.689	1	e,d
13 15 56.1	-02 28 20.8	17.51	-0.32	?			
13 16 06.5	00 23 20.6	17.93	-0.65	QSO	0.490	1	b,d
13 16 03.1	-00 16 22.7	17.43	-0.29	?			
13 16 23.2	01 51 46.0	17.42	-0.31	star			
13 16 25.4	00 51 15.4	18.34	-0.90	?			
13 16 41.9	-00 58 20.1	16.31	-0.65	star			
13 17 04.7	-00 33 56.1	18.57	-0.75	QSO	0.890	1	e,d
13 17 07.9	02 03 52.7	17.61	-0.95	?			
13 17 15.9	-01 42 20.3	17.39	-0.68	QSO	0.225	1	b,d
13 17 20.7	-02 27 21.2	18.19	-0.30	?			
13 17 21.2	01 50 02.0	17.68	-0.37	star			
13 17 46.3	-00 18 45.5	17.78	-0.84	QSO	0.350	1	b,d
13 19 06.0	00 39 38.4	18.02	-0.66	QSO	1.614	1	c,d
13 19 06.4	-02 22 09.1	17.81	-0.23	?			
13 19 32.6	00 33 39.9	18.07	-0.65	QSO	0.535	1	c,d
13 19 39.0	01 46 15.3	17.52	-0.58	NELG	0.183	1	e
13 20 08.9	-01 43 28.6	15.31	-0.52	star			
13 20 45.0	02 17 27.5	18.37	-0.10	?			
13 20 49.9	-00 06 17.1	18.56	-0.51	QSO	1.388		a
13 20 59.6	01 03 28.0	18.04	-0.90	QSO	1.780	1	c,d
13 21 28.4	01 03 21.7	18.30	-0.95	?			
13 21 55.2	-01 51 33.6	17.86	-0.24	?			

Table C1: (continued)

Table 4: UVX candidates and their IDs in field 863 (cont.)

R.A. (1950)	Declination	B_J	$U - B_J$	ID	z	Quality	Notes
13 22 19.2	-00 25 25.2	15.51	-0.41	star			
13 22 19.8	-02 27 44.6	18.20	-0.30	?			
13 22 20.4	00 09 09.4	18.47	-0.12	star			
13 22 50.7	-02 09 33.0	17.38	-0.29	star			
13 22 56.6	-00 11 14.9	17.26	-0.41	?			
13 23 36.9	-00 03 01.8	18.32	-0.82	?			
13 23 40.4	01 02 14.7	18.54	-0.14	?			
13 23 53.3	01 25 48.7	17.80	-0.28	star			
13 23 59.1	-01 38 59.0	18.35	-0.86	QSO	1.142	1	e,d
13 24 50.9	01 26 55.2	18.49	-0.84	QSO	0.864	1	e,d
13 25 23.8	00 19 47.0	17.58	-0.27	QSO	0.375	3	e
13 25 45.4	-01 29 58.2	18.42	-0.28	star			
13 25 58.1	-01 10 59.4	17.27	-0.34	?			
13 25 59.8	-01 13 47.3	16.72	-0.30	QSO	0.150	1	e,d
13 26 10.6	02 6 47.6	17.40	-0.98	QSO	1.430	1	b,d
13 26 20.1	02 08 18.0	17.59	-0.23	?			
13 26 27.5	-01 39 50.6	18.07	-0.27	?			
13 26 31.8	-00 10 09.7	16.66	-0.37	?			
13 26 41.2	-01 36 11.4	16.84	-0.41	star			
13 26 50.5	-00 41 14.6	16.47	-0.98	star			
13 26 54.2	00 51 41.1	17.68	-0.23	star			
13 27 28.6	-01 52 46.2	17.83	-0.26	?			
13 27 41.5	00 18 56.7	18.38	-0.63	?			
13 28 20.9	-00 17 00.6	17.37	-0.29	?			
13 28 21.9	-02 03 54.3	18.19	-0.28	?			
13 28 37.0	-00 50 11.0	17.71	-0.30	?			
13 28 38.5	-02 31 46.4	18.57	-0.70	QSO	1.240		c
13 28 47.1	00 02 22.1	16.09	-0.53	star			

Table 5: UVX candidates and their IDs in field 864

R.A. (1950)	Declination	B_J	$U - B_J$	ID	z	Quality	Notes
13 28 58.7	02 05 12.0	18.25	-0.36	QSO	0.692		a
13 29 03.6	-00 46 29.9	16.07	-0.18	star			
13 29 06.5	-01 36 48.4	18.18	-0.51	?			
13 29 20.7	00 56 44.6	17.77	-1.08	star			
13 29 44.4	-01 16 51.7	16.77	-0.17	star			
13 29 57.1	-00 07 54.5	18.39	-0.68	QSO	0.962	1	e,d
13 30 17.6	01 32 33.9	17.32	-0.26	star			
13 30 21.2	-01 22 52.5	18.46	-0.41	?			
13 30 48.6	01 13 46.9	18.15	-0.67	QSO	1.506	1	e,d
13 30 53.4	-02 17 57.7	17.41	-0.13	star			
13 31 10.3	-00 18 16.6	18.31	-0.98	QSO	0.859	3	e
13 31 22.4	00 27 50.6	17.78	-0.34	star			
13 31 41.4	-01 50 03.5	18.46	-0.48	?			
13 31 43.9	-00 19 44.7	16.38	-0.42	star			
13 31 46.3	-00 52 24.4	18.12	-0.26	?			
13 31 53.7	-01 08 29.0	18.01	-0.25	QSO	1.883		a
13 31 58.8	-01 23 05.7	18.23	-0.41	QSO	0.289		a
13 32 03.0	-01 17 49.3	17.68	-0.23	?			
13 32 17.2	01 17 38.8	18.43	-0.23	?			
13 32 51.8	-00 45 09.6	17.53	-0.37	QSO	0.675	1	e,d
13 33 01.7	01 33 24.0	18.15	-0.18	QSO	1.577	1	a
13 33 42.7	00 32 51.8	17.56	-0.24	star			
13 33 58.8	-01 15 59.9	17.34	-0.88	?			
13 34 13.0	-00 33 40.9	17.59	-0.22	QSO	2.806	1	e,d
13 34 13.8	02 12 58.7	18.10	-0.18	QSO	2.384		a
13 34 15.2	-00 05 41.0	17.84	-0.64	QSO	0.298		a
13 34 18.4	-01 13 45.8	18.44	-0.87	star			
13 34 49.2	00 53 27.0	18.41	-0.45	QSO	0.647		a
13 35 06.9	02 22 12.8	18.16	-0.58	QSO	1.354		a
13 35 23.2	-00 41 33.0	17.71	-0.15	star			
13 35 28.2	02 12 47.8	18.32	-0.80	?			
13 35 49.5	00 31 25.5	18.48	-0.56	QSO	2.169	1	e
13 35 50.6	-01 15 02.7	17.93	-0.55	?			
13 35 57.8	-00 08 14.3	17.19	-0.34	star			
13 36 11.0	-00 06 34.5	18.26	-0.65	QSO	1.771	1	e
13 36 30.8	00 37 34.1	18.17	-0.42	star			
13 37 01.2	-01 21 15.3	18.40	-0.62	?			
13 37 13.8	-00 04 52.4	18.17	-0.25	star			
13 37 17.0	-01 46 07.9	18.06	-0.45	QSO	1.010	1	e,d
13 37 40.1	-00 49 33.1	18.29	-0.20	star			
13 38 10.4	-00 30 07.3	17.22	-0.57	QSO	0.389	1	c,d
13 38 21.1	-02 19 40.4	16.48	-0.17	star			
13 38 39.7	-00 38 06.5	18.18	-0.70	QSO	0.238	1	c,d
13 38 46.6	-01 53 48.6	17.60	-0.62	QSO	2.094	1	e
13 39 42.2	01 25 31.8	18.26	-0.12	star			
13 39 55.0	01 49 10.4	16.83	-0.10	star			

Table 6: UVX candidates and their IDs in field 864 (cont.)

R.A. (1950)	Declination	B_J	$U - B_J$	ID	z	Quality	Notes
13 40 04.3	00 55 54.6	17.67	-0.24	star			
13 40 12.2	-00 20 38.4	18.27	-0.60	QSO	0.792	1	e,d
13 40 25.8	01 07 02.8	17.99	-0.67	QSO	1.067		a
13 41 19.6	01 15 12.7	18.37	-0.39	?			
13 41 45.2	01 44 48.7	18.37	-0.45	star			
13 42 25.6	-00 00 58.4	17.75	-0.57	QSO	0.245	1	e,d
13 42 35.3	-00 42 30.4	17.58	-0.96	?			
13 43 11.4	00 08 18.1	17.64	-0.84	star			
13 43 13.0	00 02 59.3	17.98	-0.15	star			
13 43 13.1	-02 21 54.8	18.32	-0.32	QSO	0.509		a
13 43 16.8	-00 40 36.8	16.92	-0.52	star			
13 43 45.9	-00 39 10.3	18.22	-0.39	?			
13 43 47.8	02 11 46.2	17.96	-0.18	?			
13 43 53.0	-02 04 42.0	18.09	-0.15	?			
13 44 03.6	01 37 11.5	17.46	-0.67	QSO	1.915		a
13 44 23.4	-01 06 21.9	18.45	-0.48	?			
13 44 38.1	-02 27 36.4	18.28	-0.36	QSO	0.511		a
13 44 58.0	-01 05 07.8	18.11	-0.74	QSO	1.714	1	e,d
13 45 00.7	-00 37 30.6	17.43	-0.78	?			
13 45 14.5	-01 37 28.5	18.49	-0.57	QSO	1.929		a
13 45 17.8	-00 00 23.0	18.11	-0.44	QSO	0.552		a
13 45 29.7	02 26 17.0	16.76	-0.23	star			
13 45 46.0	-00 57 30.2	18.32	-0.89	?			
13 46 01.8	01 21 19.9	18.52	-0.67	QSO	1.930		a
13 46 36.7	02 13 58.4	15.01	-0.23	star			
13 46 48.3	00 07 54.5	18.36	-0.19	QSO	1.127		a
13 46 48.6	-00 20 10.0	16.90	-0.37	star			
13 47 00.2	-00 26 10.8	17.77	-0.40	QSO	0.515	1	e,d
13 47 13.2	-02 31 48.5	17.75	-0.11	star			
13 47 14.1	-00 51 30.1	16.29	-0.41	QSO	0.600		c
13 47 21.2	00 14 23.0	15.90	-0.29	star			
13 47 41.5	02 22 11.6	15.19	-0.31	?			
13 47 47.7	-02 37 07.7	17.34	-0.35	NELG	0.139	1	e
13 48 10.3	-00 54 09.5	18.21	-0.36	QSO	1.474		a
13 48 16.4	-01 03 30.3	18.21	-0.37	star			

Table C1: (continued)

Table 7: UVX candidates and their IDs in field 865

R.A. (1950)	Declination	B_J	$U - B_J$	ID	z	Quality	Notes
13 48 37.0	00 36 35.2	18.14	-0.34	?			
13 48 55.1	01 18 27.5	17.68	-0.74	QSO	1.094	1	b,d
13 49 16.6	00 7 8.8	17.12	-0.75	QSO	1.435	1	b
13 49 26.9	01 48 49.4	17.51	-0.24	?			
13 49 27.7	-00 39 31.2	18.05	-0.69	star			
13 49 52.1	-00 26 29.0	17.63	-0.27	?			
13 49 59.2	00 57 39.1	18.07	-0.77	QSO	1.151	1	c,d
13 49 59.8	00 03 41.4	17.82	-0.29	star			
13 50 14.2	-02 32 33.0	18.21	-0.23	star			
13 50 33.4	00 08 07.9	18.42	-0.38	star			
13 51 03.5	02 08 01.5	17.90	-0.36	?			
13 51 37.0	-02 18 40.9	18.23	-0.34	star			
13 51 51.3	00 0 44.4	17.06	-0.67	QSO	1.501	1	b
13 52 12.1	00 35 32.0	18.25	-0.48	?			
13 52 25.4	01 6 52.7	16.71	-0.68	QSO	1.117	1	c,f
13 52 26.9	01 23 00.9	16.67	-0.30	star			
13 52 34.0	-02 29 49.8	17.76	-0.30	star			
13 52 48.5	01 20 20.8	17.75	-0.28	star			
13 52 51.4	-00 43 00.3	18.40	-0.80	QSO	0.900		c
13 53 48.1	-00 19 06.9	18.09	-0.70	star			
13 54 06.9	00 52 50.5	17.81	-0.29	star			
13 54 14.9	01 59 26.0	18.08	-0.66	star			
13 54 17.2	01 17 21.6	17.97	-0.77	QSO	1.210	1	e
13 54 23.8	-02 24 48.0	18.27	-0.36	?			
13 54 53.8	-02 33 2.6	17.16	-0.55	QSO	0.559	2	b
13 55 05.8	01 42 49.4	17.77	-0.62	?			
13 55 51.2	-00 41 46.9	17.79	-0.29	star			
13 55 51.6	02 28 18.0	16.61	-0.61	QSO	0.955	1	b
13 56 03.5	-01 49 50.9	17.98	-0.91	?			
13 56 09.0	02 04 03.7	18.33	-0.39	star			
13 56 47.9	-00 12 10.4	18.04	-0.80	?			
13 56 58.2	-02 02 43.9	17.94	-1.04	?			
13 57 09.1	-00 19 53.2	17.43	-0.57	QSO	0.164	1	e
13 57 26.5	-01 18 20.8	17.51	-0.26	star			
13 57 31.4	-02 27 1.8	17.68	-0.70	QSO	0.418		c
13 57 41.9	02 25 26.5	17.58	-0.39	star			
13 58 04.6	-01 35 05.1	17.75	-0.39	star			
13 58 18.3	01 40 23.1	18.32	-0.38	?			
13 58 29.1	-00 36 02.6	18.36	-0.78	?			
13 58 31.6	00 58 0.9	17.52	-0.58	QSO	0.664		c
13 58 36.5	02 06 48.4	18.40	-0.62	?			
13 58 36.9	00 1 24.3	17.06	-0.57	QSO	1.845	1	b
13 58 44.2	-01 05 57.2	17.14	-1.13	star			
13 59 21.1	-02 04 38.0	18.38	-0.73	star			
13 59 59.1	00 20 20.7	16.64	-1.09	?			
14 02 11.2	-01 16 02.0	18.32	-0.43	QSO	2.520	2	e
14 04 20.7	-01 02 54.2	18.49	-0.67	QSO	0.911	1	e
14 06 54.2	-01 43 8.1	17.76	-0.67	QSO	0.644		c
14 07 20.9	-02 31 55.0	17.88	-0.74	QSO	1.263	2	b
14 07 38.0	-00 38 17.3	18.30	-0.57	QSO	0.025	1	e
14 08 34.5	00 50 11.7	18.09	-0.69	QSO	1.712	1	e

Table C1: (continued)

Table 8: UVX candidates and their IDs in field 866

R.A. (1950)	Declination	B_J	$U - B_J$	ID	z	Quality	Notes
14 08 50.3	00 56 56.8	18.44	-0.31	QSO	2.260	1	e
14 09 03.4	01 51 02.3	18.43	-0.46	?			
14 09 48.5	01 01 21.4	17.00	-0.43	QSO	1.635	1	b,d
14 11 53.7	-00 14 11.1	17.98	-0.49	QSO	0.026		c
14 12 51.2	00 29 56.7	17.51	-0.54	star			
14 12 54.8	-00 12 38.4	17.28	-0.67	QSO	1.148	1	b
14 13 16.6	01 7 50.8	17.46	-0.55	QSO	1.042	2	b
14 13 18.3	01 36 36.8	17.73	-0.74	QSO	1.246	2	b
14 13 32.4	-02 29 31.3	15.48	-0.45	star			
14 15 41.6	-01 54 27.9	17.68	-0.71	star			
14 16 34.4	01 19 08.2	17.82	-0.27	star			
14 16 39.7	-02 30 44.8	18.03	0.30	?			
14 19 39.3	-01 7 8.0	18.13	-0.88	QSO	1.915		c
14 20 05.9	-00 53 8.5	17.77	-0.45	QSO	0.717		c
14 21 29.8	-00 13 23.9	16.33	-0.53	QSO	0.151		c
14 21 57.3	01 8 32.2	18.09	-0.68	QSO	1.060	2	b
14 23 26.2	-00 13 31.1	17.96	-0.63	QSO	1.078	2	b
14 23 41.6	00 55 27.8	17.93	-0.63	QSO	0.890	3	b
14 24 24.6	-00 7 29.6	16.52	-0.53	QSO	0.632	2	b
14 24 41.6	01 12 50.7	16.38	-0.35	NELG	0.052	1	e
14 25 00.0	00 2 43.4	17.90	-0.68	QSO	1.548	2	b
14 27 38.2	01 46 40.0	16.85	-0.44	star			
14 28 08.5	02 2 55.9	18.14	-0.70	QSO	2.107	1	b,d

Table C1: (continued)

Table : UVX candidates and their IDs in field 867

R.A. (1950)	Declination	B_J	$U - B_J$	ID	z	Quality	Notes
14 28 58.4	-03 36 48.7	15.15	-0.67	star			
14 29 07.3	-01 0 17.4	17.49	-0.68	QSO	0.661	1	e,d
14 29 03.0	01 45 25.5	16.15	-0.47	?			
14 29 09.4	-00 36 57.7	18.47	-0.74	QSO	1.179		a
14 29 26.0	00 15 29.8	18.20	-0.66	star			
14 29 54.7	-00 53 4.6	18.08	-0.86	QSO	2.075	1	b,d
14 29 57.9	01 37 47.8	18.18	-0.62	QSO	1.530	1	b,d
14 30 10.0	-00 46 4.3	17.85	-0.83	QSO	1.020	1	b,d
14 30 47.0	-00 41 36.1	16.17	-0.87	QSO	1.112	1	b,d
14 31 22.8	-00 29 33.0	17.94	-0.39	?			
14 33 07.6	02 23 48.8	18.38	-0.61	QSO	2.130	1	b,d
14 33 50.7	-00 16 3.9	18.07	-0.56	QSO	0.324	1	e,d
14 35 13.3	-01 34 13.8	16.22	-1.13	QSO	1.310	1	b,d
14 36 49.4	01 53 56.2	17.67	-0.77	?			
14 37 46.8	-01 43 37.0	18.41	-0.60	QSO	0.718	1	e,d
14 38 07.2	02 12 56.2	15.62	-0.70	star			
14 40 18.0	01 49 37.9	18.32	-0.83	QSO	1.170	1	b,d
14 40 25.7	-00 24 42.0	18.19	-1.02	QSO	1.820	1	b,d
14 40 38.4	-02 34 40.4	17.49	-0.65	QSO	0.675	1	b,d
14 40 59.4	-02 31 11.4	16.68	-0.32	star			
14 41 27.2	01 42 36.9	17.92	-0.65	QSO	0.296	1	b,d
14 43 33.5	02 03 20.2	16.09	-0.67	star			
14 43 49.7	00 44 14.9	17.82	-0.45	?			
14 45 08.8	-02 31 38.2	18.09	-0.80	QSO	1.730	1	b,d
14 46 05.7	02 18 54.2	18.23	-0.49	QSO	0.668	1	b,d
14 47 29.0	00 28 51.8	18.38	-0.78	QSO	0.946	3	b

Table : UVX candidates and their IDs in field 789

R.A. (1950)	Declination	B_J	$U-B_J$	ID	z	Quality	Notes
12 28 28.5	-04 12 02.2	17.44	-0.49	QSO	0.658		c
12 28 40.7	-06 01 18.6	16.54	-0.44	star			
12 29 36.1	-05 01 53.9	17.17	-0.77	QSO	1.078	2	b
12 35 30.5	-03 40 39.4	17.23	-0.82	QSO	1.489		c
12 37 05.7	-03 59 22.1	17.21	-0.64	QSO	0.371		c
12 37 41.7	-04 35 03.2	17.76	-0.65	QSO	0.810		c
12 38 56.9	-02 51 02.2	16.31	-0.31	star			
12 39 03.7	-05 33 56.4	18.00	-1.03	star			
12 39 05.0	-07 16 40.3	17.21	-0.63	QSO	1.170		c
12 39 10.1	-07 26 28.5	17.15	-0.87	QSO	1.184	1	b
12 39 23.0	-02 44 15.9	17.51	-0.19	star			
12 39 43.5	-02 41 50.5	16.07	-0.24	star			
12 41 23.0	-02 38 12.0	16.21	-0.34	star			
12 43 33.1	-05 00 50.0	15.76	-0.45	star			
12 45 00.4	-03 33 47.4	15.93	-0.89	QSO	0.379	1	b
12 46 17.0	-04 30 3.2	17.17	-0.92	QSO	0.531		c
12 48 17.2	-02 41 58.5	17.02	-0.18	star			
12 48 37.4	-07 36 32.3	17.61	-0.34	star			
12 48 39.6	-04 46 40.3	18.00	-0.51	star			
12 48 44.3	-04 48 44.5	17.04	-0.64	QSO	1.410	1	b
12 49 12.3	-04 14 35.9	16.53	-0.60	star			

Table 11: UVX candidates and their IDs in field 790

R.A. (1950)	Declination	B_J	$U-B_J$	ID	z	Quality	Notes
12 49 12.3	-04 14 35.9	16.31	-0.64	star			
12 49 20.9	-06 48 44.1	16.58	-1.36	QSO	1.187		c
12 50 46.1	-07 00 37.5	16.43	-0.67	QSO	0.097	2	e
12 51 26.0	-07 15 06.9	17.03	-0.74	star			
12 51 59.7	-07 37 32.1	18.02	-1.12	QSO	1.476	3	e
12 52 06.2	-06 24 58.2	15.66	-0.53	star			
12 52 51.3	-06 59 06.7	18.00	-1.25	QSO	0.250	1	e
12 53 30.4	-03 29 36.9	17.49	-1.20	QSO	2.238	2	e
12 53 35.4	-06 03 15.3	17.38	-1.17	QSO	0.175		c
12 54 39.8	-07 36 42.2	18.00	-1.28	QSO	0.175	1	e
12 55 55.8	-04 37 37.7	16.64	-1.04	QSO	0.173	1	e
12 55 59.0	-06 10 16.3	16.10	-0.60	star			
12 56 49.0	-04 58 39.3	17.10	-1.34	QSO	0.126	1	e
12 57 06.9	-06 12 42.3	16.02	-0.58	star			
12 57 42.4	-03 34 42.7	16.69	-0.63	star			
12 58 16.0	-04 15 50.6	18.06	-1.17	QSO	1.738	1	b
12 58 37.9	-07 11 19.6	16.66	-0.62	star			
13 00 10.7	-06 57 48.8	16.80	-1.01	QSO	0.183	1	e
13 00 32.2	-05 14 38.2	16.22	-0.86	star			
13 00 38.2	-03 07 16.4	17.24	-0.78	star			
13 00 56.8	-03 38 43.0	18.07	-1.22	QSO	0.390	1	b
13 04 18.8	-06 14 2.2	17.49	-1.06	QSO	1.563	1	b
13 04 26.3	-04 18 49.6	18.09	-1.31	star			
13 04 31.0	-06 15 58.5	17.88	-1.27	QSO	1.441	2	e
13 04 37.5	-03 24 14.3	15.17	-0.53	star			
13 04 40.9	-04 11 39.0	16.65	-0.66	star			
13 04 53.5	-05 31 25.8	17.48	-1.64	star			
13 06 28.8	-03 50 14.1	17.97	-1.08	QSO	0.399	2	b
13 07 09.6	-05 14 38.2	16.49	-0.62	star			
13 07 13.5	-05 18 01.6	16.51	-1.05	star			
13 07 45.4	-05 22 24.1	15.18	-0.66	star			
13 08 06.3	-03 39 17.9	18.11	-1.08	star			
13 08 11.6	-06 07 35.8	18.46	-0.93	NELG	0.173	2	e
13 08 14.0	-04 41 04.9	18.01	-0.95	star			
13 08 36.4	-05 45 07.7	15.33	-0.24	?			
13 08 43.3	-05 35 20.5	18.47	-0.96	?			

Table 12: UVX candidates and their IDs in field 791

R.A. (1950)	Declination	B_J	$U - B_J$	ID	z	Quality	Notes
13 08 36.4	-05 45 07.7	15.47	-0.20	?			
13 08 43.3	-05 35 20.5	18.25	-0.60	?			
13 08 54.5	-03 53 42.9	18.26	-0.71	?			
13 09 00.7	-05 36 43.7	17.68	-0.25	star			
13 09 26.1	-04 42 16.7	17.32	-0.85	star			
13 09 37.7	-05 45 50.3	16.75	-0.34	?			
13 09 56.2	-04 31 22.7	18.03	-0.68	?			
13 10 24.5	-04 44 09.5	18.15	-0.64	star			
13 10 53.2	-03 37 26.5	16.41	-0.96	star			
13 11 24.2	-03 08 52.7	18.30	-0.43	?			
13 12 00.5	-03 14 44.7	18.39	-0.83	?			
13 12 16.0	-04 40 29.9	18.04	-0.68	?			
13 12 18.8	-05 19 22.7	18.26	-0.81	?			
13 13 15.2	-03 26 04.3	18.11	-0.36	star			
13 13 16.5	-04 20 26.0	18.44	-0.31	star			
13 13 33.0	-03 58 00.0	17.68	-0.50	?			
13 13 41.7	-03 33 14.2	16.39	-0.45	?			
13 14 06.9	-03 46 24.2	17.79	-0.35	star			
13 14 42.1	-06 43 39.6	16.03	-0.83	star			
13 15 02.4	-04 29 44.9	16.95	-0.73	star			
13 15 14.0	-04 10 14.0	17.63	-0.67	QSO	0.469	1	b
13 15 38.8	-05 36 06.7	18.41	-0.63	?			
13 15 57.5	-06 11 01.3	15.15	-0.34	star			
13 16 03.6	-04 24 22.6	18.10	-0.42	NELG	0.018	1	e
13 16 09.1	-03 36 08.7	18.08	-0.55	?			
13 16 26.9	-05 41 44.8	17.51	-0.84	?			
13 16 47.2	-05 44 42.1	18.24	-0.63	?			
13 16 48.4	-07 34 43.2	16.49	-0.74	QSO	0.538	1	e
13 17 17.3	-04 36 15.6	15.38	-0.33	?			
13 17 24.8	-07 31 19.9	18.25	-0.75	?			
13 17 28.5	-07 40 36.0	17.97	-0.56	?			
13 17 33.2	-07 05 08.3	17.79	-0.84	star			
13 17 35.4	-04 29 46.9	18.37	-0.34	star			
13 17 52.3	-04 34 35.2	18.29	-1.02	star			
13 18 06.9	-06 59 58.5	17.22	-0.98	NELG	0.104		c
13 18 32.7	-04 21 41.5	18.20	-0.40	?			

Table 13: UVX candidates and their IDs in field 791 (cont.)

R.A. (1950)	Declination	B_J	$U - B_J$	ID	z	Quality	Notes
13 18 38.5	-06 07 23.8	18.11	-0.90	?			
13 18 47.9	-03 41 06.3	17.98	-0.55	?			
13 18 53.6	-06 37 37.6	18.01	-0.43	?			
13 19 01.4	-04 53 32.2	18.29	-0.72	?			
13 19 26.1	-02 59 03.0	18.34	-0.29	QSO	0.074	2	e
13 20 10.6	-05 58 25.2	15.41	-0.68	star			
13 20 12.9	-06 35 28.2	17.31	-0.67	QSO	1.678		c
13 20 37.8	-02 39 17.0	17.98	-0.39	star			
13 20 47.1	-06 30 01.2	18.14	-0.70	star			
13 20 55.4	-03 56 29.7	18.41	-0.73	?			
13 21 02.3	-04 02 12.6	18.02	-0.48	?			
13 21 09.5	-05 37 51.7	17.96	-0.48	?			
13 21 38.6	-05 49 00.8	16.73	-0.57	QSO	0.732	2	b
13 22 04.7	-03 03 47.1	18.19	-0.58	?			
13 22 07.9	-06 41 50.2	17.99	-0.43	QSO	0.147	1	e
13 22 11.3	-05 42 53.6	18.06	-0.97	star			
13 22 17.1	-03 32 59.0	18.07	-0.51	?			
13 22 31.2	-03 06 50.9	18.39	-0.67	?			
13 22 31.3	-05 32 30.4	18.38	-0.62	?			
13 22 45.0	-04 54 12.7	18.25	-0.61	?			
13 22 50.7	-02 09 33.0	17.64	-0.45	star			
13 23 23.7	-03 15 16.0	18.20	-0.40	?			
13 23 40.2	-02 48 24.1	17.25	-0.54	QSO	2.125	1	b,d
13 23 40.9	-07 39 38.0	16.05	-0.31	?			
13 23 42.9	-03 27 37.6	15.19	-0.44	star			
13 23 45.4	-06 19 55.4	18.37	-0.82	?			
13 24 06.5	-03 37 20.0	15.21	-0.32	star			
13 24 23.9	-03 55 21.7	18.32	-0.88	?			
13 24 37.3	-06 25 54.8	18.26	-0.55	star			
13 24 50.7	-03 15 54.9	18.00	-0.68	?			
13 26 14.0	-06 57 52.2	17.26	-0.67	NELG	0.078		c
13 26 14.7	-03 37 29.4	18.01	-0.66	?			
13 26 52.5	-05 16 06.6	15.47	-0.45	QSO	0.580	1	e
13 27 02.2	-02 42 35.0	18.17	-0.50	?			
13 27 56.7	-05 02 35.7	18.38	-0.77	?			
13 28 05.5	-03 02 43.7	18.41	-0.66	?			
13 28 12.8	-06 07 19.2	18.32	-0.62	?			
13 28 23.6	-06 50 11.5	18.48	-0.45	?			
13 28 44.3	-05 59 36.8	17.20	-0.22	star			
13 28 49.2	-04 23 35.4	17.59	-0.05	?			

Table C1: (continued)

Table 14: UVX candidates and their IDs in field 792

R.A. (1950)	Declination	B_J	$U - B_J$	ID	z	Quality	Notes
13 28 23.6	-06 50 11.5	18.42	-0.77	?			
13 29 00.7	-05 28 52.6	17.32	-0.28	star			
13 29 02.2	-04 11 28.7	18.44	-1.01	?			
13 29 09.4	-06 15 18.4	17.57	-0.46	QSO	0.714	1	e
13 29 11.9	-04 21 43.4	17.24	-0.36	star			
13 29 17.8	-05 32 47.3	18.31	-0.86	?			
13 29 23.9	-04 31 10.7	16.58	-0.23	QSO	0.075	2	e
13 29 32.8	-06 01 28.7	15.78	-0.73	star			
13 29 35.9	-04 10 26.2	15.67	-0.32	star			
13 29 38.8	-07 00 52.5	17.96	-0.26	?			
13 29 40.8	-04 39 43.4	17.14	-0.30	star			
13 29 49.8	-06 37 11.1	17.81	-0.29	?			
13 29 52.8	-06 43 19.5	17.80	-0.26	star			
13 29 54.5	-04 09 41.5	16.50	-0.46	star			
13 29 58.7	-04 20 30.8	17.33	-0.92	QSO	1.295		c
13 30 25.5	-04 22 50.2	17.82	-0.88	star			
13 30 34.9	-02 50 33.2	16.50	-0.31	star			
13 30 35.1	-03 54 42.9	15.39	-0.37	star			
13 30 39.5	-07 26 16.9	15.10	-0.68	star			
13 31 51.2	-07 37 14.3	16.34	-0.45	star			
13 32 12.7	-06 15 25.3	18.13	-0.70	?			
13 32 15.0	-03 19 23.0	17.65	-0.37	star			
13 32 22.1	-03 11 15.3	18.05	-0.26	?			
13 32 36.8	-07 06 16.2	18.34	-0.44	?			
13 32 37.9	-03 28 51.9	17.82	-0.32	star			
13 32 45.7	-05 06 25.5	18.22	-0.26	star			
13 32 50.0	-06 59 45.9	18.29	-0.26	QSO	2.621	1	e
13 32 54.3	-04 19 02.8	18.00	-0.50	?			
13 32 56.0	-07 27 05.6	16.83	-0.72	star			
13 33 01.2	-05 40 43.3	18.39	-0.48	?			
13 33 27.6	-03 47 41.0	18.06	-0.58	?			
13 33 35.4	-03 26 26.9	18.25	-0.75	NELG	0.006		c
13 33 41.5	-07 07 35.4	18.04	-0.88	NELG	0.328	1	e
13 33 42.8	-06 22 42.1	16.17	-1.00	star			
13 33 43.4	-07 38 13.2	17.65	-0.48	star			
13 33 44.7	-02 39 28.4	18.08	-0.46	star			
13 33 47.5	-06 22 07.2	18.34	-0.32	?			
13 34 26.3	-03 02 16.6	18.32	-0.45	star			
13 34 37.9	-02 32 37.2	17.71	-0.77	QSO	0.723		a
13 34 39.5	-05 18 22.6	17.98	-0.26	?			
13 35 01.6	-02 41 53.6	18.15	-0.52	QSO	0.610	1	e,d
13 35 20.2	-04 22 36.0	18.35	-0.36	QSO	0.272	3	e
13 35 31.1	-06 11 57.6	17.87	-0.42	QSO	0.620		c
13 35 47.2	-03 32 06.3	16.57	-0.95	star			
13 36 00.3	-03 34 09.4	17.90	-0.59	NELG	0.155	1	e
13 36 07.3	-04 10 04.8	18.38	-0.69	?			
13 36 09.4	-04 23 40.9	17.10	-0.68	QSO	0.163	1	e
13 36 36.4	-05 28 53.1	17.80	-0.27	star			
13 36 57.9	-05 49 14.7	16.76	-0.29	star			

Table C1: (continued)

Table 15: UVX candidates and their IDs in field 792 (cont.)

R.A. (1950)	Declination	B_J	$U - B_J$	ID	z	Quality	Notes
13 37 02.6	-07 35 11.9	17.81	-0.26	star			
13 37 02.7	-06 58 05.1	16.41	-0.77	?			
13 37 05.7	-03 51 10.0	17.82	-0.29	star			
13 37 13.5	-02 34 48.0	16.41	-0.28	star			
13 37 35.6	-04 36 24.7	18.23	-0.28	?			
13 38 06.0	-04 05 13.4	17.76	-0.24	star			
13 38 06.6	-05 36 31.6	17.56	-0.69	star			
13 38 26.0	-07 24 40.5	17.40	-0.37	QSO	2.353		c
13 38 52.6	-05 30 18.8	18.16	-0.55	star			
13 39 06.8	-03 57 10.9	18.25	-0.31	star			
13 39 39.3	-04 59 49.2	18.25	-0.77	QSO	0.884	2	e
13 39 41.4	-05 26 12.4	18.11	-0.47	QSO	1.252	2	e
13 39 49.7	-06 48 04.6	18.34	-0.88	QSO	1.220	2	e
13 39 58.5	-05 49 43.0	17.55	-0.31	star			
13 40 07.5	-06 56 29.5	17.52	-0.83	star			
13 40 22.5	-05 15 31.0	18.00	-0.57	star			
13 40 52.8	-05 45 26.8	17.94	-0.77	QSO	0.319	1	e
13 40 57.1	-04 59 47.6	18.01	-0.45	star			
13 41 07.4	-07 08 37.3	18.35	-0.51	?			
13 41 10.9	-03 55 37.3	17.70	-0.25	?			
13 41 34.4	-03 57 46.9	17.39	-0.75	QSO	0.835		c
13 41 49.2	-03 31 51.2	15.31	-0.39	star			
13 41 50.2	-07 10 16.6	18.39	-0.68	?			
13 42 18.1	-06 11 16.6	18.16	-0.95	?			
13 43 14.4	-05 38 21.8	17.52	-0.85	QSO	2.047	1	b
13 43 23.7	-06 7 44.0	17.72	-0.73	QSO	1.012		c
13 44 23.1	-04 19 26.1	17.13	-0.94	QSO	1.922	1	b
13 44 45.7	-06 53 53.9	18.35	-0.51	?			
13 44 59.7	-06 23 13.4	17.78	-0.55	QSO	0.118		c
13 45 01.3	-04 44 17.2	18.25	-0.98	?			
13 45 10.5	-05 54 24.7	18.09	-0.43	star			
13 45 15.2	-05 31 56.1	18.24	-0.45	star			
13 45 18.3	-03 56 28.9	18.10	-0.63	star			
13 45 21.6	-06 37 45.5	17.68	-0.25	star			
13 45 47.7	-05 10 19.0	17.06	-0.77	QSO	1.386	1	b
13 45 55.0	-03 17 27.7	17.86	-1.00	QSO	1.947	1	b
13 46 01.4	-04 25 05.3	18.01	-0.48	?			
13 46 11.0	-06 32 26.6	16.43	-0.88	star			
13 46 18.8	-05 26 51.9	18.22	-0.44	?			
13 46 19.9	-03 6 48.6	17.83	-0.82	QSO	2.090	1	b
13 46 24.5	-05 15 41.7	18.39	-0.59	?			
13 46 43.8	-04 13 22.9	17.69	-0.69	star			
13 46 45.6	-02 47 17.5	18.38	-0.70	?			
13 46 45.9	-06 20 04.0	17.66	-0.80	star			
13 46 47.4	-07 06 28.4	17.91	-0.34	star			
13 46 53.5	-02 51 55.8	18.21	-0.88	QSO	1.721	1	e,d
13 48 05.1	-02 57 42.4	18.37	-0.73	?			
13 48 09.5	-05 43 41.0	15.92	-0.75	star			
13 48 30.4	-04 39 22.8	18.42	-0.49	?			
13 48 32.5	-05 25 48.9	18.05	-0.26	star			
13 48 39.5	-06 56 17.5	18.36	-0.86	?			

Table 16: UVX candidates and their IDs in field 793

R.A. (1950)	Declination	B_J	$U - B_J$	ID	z	Quality	Notes
13 49 10.9	-06 15 35.8	15.38	-0.37	?			
13 49 21.9	-04 21 25.1	16.91	-0.48	?			
13 50 05.1	-06 58 30.9	16.54	-0.83	?			
13 51 11.9	-06 41 02.7	17.95	-1.08	QSO	0.334	2	e
13 52 47.0	-03 50 02.1	18.07	-0.57	?			
13 53 01.0	-04 26 20.1	16.77	-0.73	?			
13 53 01.7	-03 58 00.9	18.15	-0.63	star			
13 53 03.8	-07 20 58.2	15.09	-0.52	star			
13 53 10.7	-07 32 46.6	15.30	-0.36	?			
13 54 03.9	-04 49 53.0	17.70	-0.81	QSO	1.423	2	e
13 54 15.5	-02 40 30.2	16.97	-0.48	NELG	0.026	1	e
13 54 32.0	-05 13 25.5	18.17	-0.91	star			
13 56 29.3	-03 44 15.3	17.79	-0.89	?			
13 56 44.9	-06 07 43.8	16.17	-0.66	NELG	0.072	1	e
13 58 41.6	-04 41 20.6	18.04	-0.84	QSO	0.200	2	e
13 58 48.7	-04 12 42.3	17.37	-0.76	QSO	1.354	2	e
13 59 03.8	-05 53 56.1	17.72	-0.94	QSO	1.990	1	e
13 59 33.7	-03 39 55.8	18.17	-0.69	?			
13 59 40.5	-06 27 56.1	18.00	-0.85	star			
13 59 47.5	-04 27 54.8	18.06	-0.60	?			
13 59 56.2	-07 22 25.1	16.84	-0.63	star			
13 59 58.2	-04 40 38.6	16.83	-0.49	star			
14 00 17.4	-03 13 36.6	18.00	-0.52	?			
14 01 23.5	-03 42 20.3	17.96	-0.84	?			
14 01 58.3	-06 38 05.8	17.95	-0.84	?			
14 03 35.2	-03 04 56.4	17.01	-0.80	QSO	0.860	2	e
14 03 47.2	-03 03 28.1	17.82	-0.95	?			
14 04 19.5	-05 58 11.4	16.56	-0.47	star			
14 04 53.9	-04 55 56.0	15.79	-0.62	QSO	0.031	1	e
14 05 13.4	-02 37 14.0	18.10	-0.46	?			
14 06 10.0	-04 10 18.8	17.90	-0.96	?			
14 06 32.0	-05 09 28.5	17.19	-0.92	?			
14 06 41.5	-03 24 28.3	18.08	-0.61	?			
14 07 00.2	-07 23 30.2	17.45	-0.68	?			
14 07 52.8	-07 22 31.7	17.97	-0.85	QSO	0.900	2	e
14 08 01.9	-05 11 35.3	17.65	-0.54	QSO	0.154	1	e
14 08 16.8	-06 20 36.6	17.75	-0.75	?			
14 08 28.1	-06 51 10.6	17.80	-0.88	QSO	1.770	2	e
14 08 51.8	-06 14 18.6	17.93	-0.72	?			

Table C1: (continued)

Table 17: UVX candidates and their IDs in field 794

R.A. (1950)	Declination	B_J	$U - B_J$	ID	z	Quality	Notes
14 08 51.8	-06 14 18.6	17.92	-0.55	?			
14 09 54.5	-05 35 42.8	18.43	-0.44	?			
14 10 03.1	-04 55 12.3	16.07	-0.36	star			
14 10 13.1	-07 41 05.3	16.69	-0.96	star			
14 10 37.0	-04 24 49.5	16.22	-0.37	star			
14 10 37.6	-04 24 23.9	18.31	-0.36	?			
14 10 39.6	-07 44 02.7	17.96	-0.27	star			
14 10 47.8	-03 26 56.0	18.35	-0.50	?			
14 11 05.1	-07 25 35.7	18.30	-0.22	star			
14 11 10.9	-05 15 51.1	17.64	-0.25	?			
14 11 28.8	-04 41 16.4	18.11	-0.85	?			
14 11 31.8	-05 19 10.4	16.86	-0.37	star			
14 11 41.4	-03 33 46.5	17.91	-0.78	QSO	0.860	2	e
14 11 50.7	-04 03 07.5	18.42	-0.65	?			
14 11 50.7	-05 21 42.2	17.57	-1.04	star			
14 12 32.5	-02 40 32.3	16.95	-1.02	star			
14 12 46.2	-05 59 28.7	15.45	-0.33	star			
14 12 51.6	-07 14 31.8	16.34	-0.34	star			
14 12 52.0	-04 02 18.6	18.10	-0.65	?			
14 13 00.8	-05 41 07.8	16.56	-0.41	star			
14 13 16.8	-06 51 35.7	17.59	-0.84	?			
14 13 44.3	-06 42 32.1	17.82	-0.23	?			
14 13 52.9	-07 27 13.6	16.17	-0.34	star			
14 14 24.4	-06 51 08.7	18.39	-0.47	star			
14 14 30.3	-03 31 16.0	17.66	-0.63	QSO	0.780	3	e
14 14 30.8	-05 44 46.2	17.37	-0.60	QSO	0.419		c
14 14 51.7	-05 20 14.8	18.20	-0.45	?			
14 15 01.6	-02 41 36.0	17.72	-0.25	star			
14 15 02.9	-06 48 23.3	18.08	-0.69	QSO	0.234		c
14 15 05.6	-07 30 13.5	16.49	-0.42	star			
14 15 21.7	-06 26 13.2	16.35	-1.11	?			
14 15 24.2	-06 43 29.8	18.32	-0.38	?			
14 15 45.0	-03 09 05.4	16.61	-1.15	star			
14 15 45.2	-06 10 43.6	18.47	-0.87	star			
14 15 55.7	-06 01 31.9	17.75	-0.27	star			
14 16 08.5	-07 25 29.3	18.45	-0.76	?			
14 16 09.5	-06 43 07.7	16.71	-0.58	star			
14 16 12.7	-05 27 16.5	15.40	-0.33	star			
14 16 17.2	-05 39 32.1	17.83	-0.63	?			
14 16 21.7	-07 13 12.9	18.26	-0.22	?			
14 16 33.6	-05 18 59.7	18.50	-0.72	QSO	0.96	2	e
14 16 50.1	-03 24 51.0	18.10	-0.71	QSO	0.73	3	e
14 17 16.5	-06 10 10.0	18.41	-0.44	?			
14 17 27.5	-02 42 42.0	17.71	-0.28	?			
14 18 04.5	-04 48 47.4	18.15	-0.27	?			
14 18 23.0	-07 40 34.0	15.89	-0.31	star			
14 18 31.2	-06 55 39.0	18.42	-0.67	?			
14 18 39.4	-05 03 39.3	15.68	-0.32	star			
14 18 48.4	-07 22 29.1	18.22	-0.80	?			
14 19 48.6	-04 13 25.9	18.08	-0.35	?			

Table C1: (continued)

Table 18: UVX candidates and their IDs in field 794 (cont.)

R.A. (1950)	Declination	B_J	$U - B_J$	ID	z	Quality	Notes
14 19 52.0	-04 19 15.3	18.15	-0.56	?			
14 20 11.5	-04 02 54.5	18.19	-0.57	star			
14 21 08.6	-07 30 05.0	17.77	-0.37	NELG	0.301	1	e
14 21 14.2	-03 21 31.8	18.36	-0.60	?			
14 21 22.3	-07 18 57.1	18.41	-0.44	?			
14 21 33.4	-04 07 42.2	18.05	-0.43	QSO	0.650		c
14 22 12.7	-03 35 41.0	16.80	-0.31	star			
14 22 41.1	-04 44 51.3	18.23	-0.33	QSO	1.730	2	e
14 22 43.4	-02 46 41.4	17.35	-0.16	?			
14 22 43.6	-05 06 29.8	18.41	-0.89	?			
14 22 48.9	-03 23 50.9	18.08	-0.46	QSO	0.205	2	e
14 22 57.3	-06 52 27.5	17.72	-0.99	?			
14 22 59.8	-07 05 52.9	18.41	-0.37	?			
14 23 04.7	-05 34 46.8	17.42	-0.74	QSO	0.291	1	e
14 23 05.9	-05 09 11.1	18.01	-0.23	?			
14 23 10.4	-03 45 48.2	16.58	-0.54	?			
14 23 17.5	-06 16 31.1	18.43	-0.19	star			
14 23 22.2	-07 18 00.3	18.46	-1.03	QSO	0.040	3	e
14 23 55.1	-04 34 01.1	17.91	-0.60	NELG	0.124	1	e
14 23 56.4	-03 56 28.5	17.92	-0.22	?			
14 24 16.3	-04 39 53.3	17.97	-0.28	?			
14 24 34.6	-05 34 47.3	17.07	-1.10	star			
14 24 50.8	-04 31 42.6	15.67	-0.34	star			
14 24 52.0	-04 50 53.5	18.40	-0.22	?			
14 24 56.9	-06 37 41.2	18.17	-0.36	?			
14 25 15.5	-03 06 10.1	17.96	-0.50	?			
14 26 18.2	-07 02 59.2	18.00	-0.25	star			
14 26 31.0	-03 34 57.4	18.45	-0.48	?			
14 26 47.8	-03 45 28.6	17.94	-0.36	?			
14 26 52.5	-06 11 14.6	18.25	-0.55	?			
14 27 02.9	-06 37 12.8	18.25	-0.81	?			
14 27 33.1	-07 12 13.5	18.19	-0.77	?			
14 27 57.6	-04 06 17.7	17.71	-0.64	star			
14 28 58.4	-03 36 48.7	15.35	-0.30	star			

References

Avni,Y. & Bahcall,J.N., 1980, *ApJ*, **235**, 694.

Bahcall,J.N. & Soneira,R.M., 1980, *ApJS* **44**, 73.

Baldwin,J., 1977, *ApJ* **214**, 679.

Blair,M. & Gilmore,G., 1982, *PASP* **94**, 742.

Blanco, P.R., 1991, *Ph.D. thesis*, University of Edinburgh.

Boyle,B.J., Fong,R., Shanks,T. & Clowes,R.G., 1985, *MNRAS*, **216**, 623.

Boyle,B.J., Shanks,T. & Peterson,B.A., 1988, *MNRAS* **235**, 935. (BSP)

Boyle,B.J., Fong,R., Shanks,T. & Peterson,B.A., 1990, *MNRAS*, **243**, 1.

Boyle,B.J., 1991, *in Proc Texas/ESO/CERN ed. J.D. Barrow et al.*, 14.

Boyle,B.J., Jones,L.R. & Shanks,T., 1991, *MNRAS* **251**, 482.

Braccesi,A., Formiggini,L. & Gandolfi,E., 1970, *A & A* **5**, 264.

Braccesi,A., Zitelli,V., Bonoli,F. & Formiggini,L., 1980, *A & A* **85**, 80.

Burstein,D. & Heiles,C., 1982, *AJ* **87**, 1165.

Carlberg,R.G., 1990, *ApJ* **350**, 505.

Clowes,R.G., 1986, *MNRAS* **218**, 139.

Conover,W.A., 1980, *Practical Nonparametric Statistics*, Wiley, New York.

Cristiani,S. & Vio,R., 1990, *A & A* **227**, 385.

Cristiani,S., Vio,R. & Andreani,P., 1990, *AJ* **100**, 56.

Dawe,J.A., Coyte,E. & Metcalfe,N., 1984, *Astronomical Photography, eds Sim, M.E. & Ishida, K., Occ. Rep. R. Obs. Edin.* **14**, 59.

Dicke,R.H., Peebles,P.J.E., Roll,P.G. & Wilkinson,D.T., 1965, *ApJ* **142**, 414.

Dunlop,J.S., Taylor,G.L., Hughes,D.H. & Robson, E.I., 1993, *preprint*

Efstathiou,G. & Rees,M.J., 1988, *MNRAS* **230** 5P.

Field, Arp,H. & Bahcall,J.N., 1973, *"The Redshift Controversy"* W.A. Benjamin Inc.

Gamow,G., 1946, *Phys Rev* **70**, 527.

Goldschmidt,P., Miller,L., La Franca,F.L. & Cristiani,S., 1992, *MNRAS*, **256**, 65p.

Green,R.F., Schmidt,M. & Liebert,J., 1986, *ApJ Suppl* **61**, 305.

Hale-Sutton,D., Shanks,T. & Fong,R., 1991, *in "Digitised Optical Sky Surveys" eds. H.T. MacGillivray & E.B. Thomson* Kluwer-Dordrecht.

Hawkins,M.R.S. & Veron, P., 1993, *MNRAS* **260**, 202.

Hawkins,M.R.S., 1986, *MNRAS* **219**, 417.

Hazard,C., Mackay,M.B. & Shimmins,A.J., 1963, *Nature* **197**, 1037.

Hazard,C. & McMahon,R.G., 1985, *Nature* **314**, 238.

Hazard,C., McMahon,R.G. & Sargent,W.L.W., 1986, *Nature* **322**, 39.

Hewett,P.C., Foltz,C.B. & Chaffee,F.H., 1993, *AJ* **406**, L43.

Hubble,E., 1929, *Proc. NAS* **15**, 168.

Irwin,M., McMahon,R.G. & Hazard,C., 1991, *in The Space Distribution of Quasars ed. D. Crampton, ASPCS* **21**, 117.

Kolb,E.W. & Turner,M.S., 1990 *The Early Universe*, Addison Wesley

Koo,D.C. & Kron,R.G., 1982, *A & A* **105**, 107.

La Franca,F., Cristiani,S. & Barbieri,C., 1992, *AJ* **102**, 1062.

Lampton,M., Margon,B. & Bowyer,S., 1976, *ApJ* **208**, 177.

Lawrence,A., 1987, *P.A.S.P.* **99**, 309.

Lawrence,A. & Elvis,M., 1982, *ApJ* **256**, 410.

Longair,M.S. & Scheuer,P.A.G., 1970, *M.N.R.A.S* **151**, 45.

MacGillivray,H.T. & Stobie,R.S., 1984, *Vistas Astr.* **27**, 433.

Maddox,S.J., Sutherland,W.J., Efstathiou,G. & Loveday,J., 1990, *MNRAS* **243**, 692.

Malkan,M.A. & Sargent,W.L.W., 1982, *Ap.J.* **254**, 22.

Marshall,H.L., Avni,Y., Tananbaum,H. & Zamorani,G., 1983, *ApJ* **269**, 35.

Marshall,H.L., Avni,Y., Braccesi,A., Tananbaum,H., Zamorani,G. & Zitelli, V., 1984, *ApJ* **283**, 50.

Marshall,H.L., 1986, *in The Structure and Evolution of Active Galactic Nuclei, eds Mardirossian et al.* , 627.

Mathez,G., 1976, *A & A* **68**, 17.

Miller,L., Peacock,J.A. & Mead,A.R.G., 1990, *MNRAS*, **244**, 207.

Mitchell,K., Warnock,A.III & Usher,P.D., 1984, *ApJ* **287**, L3.

Mitchell,P.S., 1989, *Ph.D. thesis*, University of Edinburgh. (PSM)

Mitchell,P.S., Miller,L. & Boyle,B.J., 1990, *MNRAS* **244** 1.

Morris,S.L., Weymann,R.J., Anderson,S.F., Hewett,P.C., Foltz,C.B., Chaffee,F.H., Francis,P.J. & MacAlpine,G.M., 1991, *AJ* **102**, 1627.

Osmer,P.S., 1982, *ApJ* **253**, 28.

Osmer,P.S. & Smith,M.G., 1977, *ApJ* **217**, L73.

Penzias,A.A. & Wilson,R.W., 1965, *ApJ* **142**, 419.

Press,W.H. & Schechter,P., 1974, *ApJ* **187**, 425.

Rowan-Robinson,M., 1986, *The Cosmological Distance Ladder*, Freeman.

Sandage, A. & Veron, P., 1965, *ApJ* **142**, 412.

Schmidt,M., 1963, *Nature* **197**, 1040.

Schmidt,M., 1968, *ApJ* **151**, 393.

Schmidt,M. & Green,R.F., 1983, *ApJ* **269**, 352.

Schmidt,M., Schneider,D.P. & Gunn,J.E., 1991, *in The Space Distribution of Quasars ed. D. Crampton ASPCS* **21**, 109.

Shanks,T, Fong,R. & Boyle,B.J., 1983, *Nature* **303**, 156.

Smithsonian Astrophysical Observatory (S.A.O.) Star Catalog, *ed. F.L. Whipple Smithsonian publication 4652.*

Smoot,G. *et al.*, 1992, *ApJL* **396**, L1.

Terlevich,R.J. & Melnick,J., 1985, *MNRAS* **213**, 841.

Veron,P., 1983, *Quasars & Gravitational Lenses, 24th Liege Astrophysical Symposium*, 210.

Wagoner,R., 1973, *ApJ* **179**, 343.

Wallace,P.T. & Tritton,K.P., 1979, *MNRAS* **189**, 115.

Wampler,E.J. & Ponz,D., 1985, *ApJ* **298**, 448.

Warren,S.J., Hewett,P.C. & Osmer,P.S., 1989, *in The Epoch of Galaxy Formation, eds. C.S. Frenk et al.*, 135.

Webster,A., 1976, *MNRAS* **175**, 71.

Weedman,D.W., 1986, *in The Structure and Evolution of Active Galactic Nuclei, eds Mardirossian et al.*, 215.

Weinberg,S., 1972, *Gravitation & Cosmology*, Wiley, New York.

Wills, B. & Lynds, J., 1978, *ApJS* **36**, 31.

Wyse,R. & Gilmore, G., 1992, *MNRAS* **257**, 1.

Zitelli,V., Mignoli,M., Zamorani,G., Marano,B. & Boyle,B.J., 1992, *MNRAS* **256**, 349.

Mon. Not. R. astr. Soc. (1992) **256,** *Short Communication,* 65P–68P

The high surface density of bright ultraviolet-excess quasars

Pippa Goldschmidt,[1] Lance Miller,[2] Fabio La Franca[3] and Stefano Cristiani[3]
[1]*Department of Astronomy, University of Edinburgh, Blackford Hill, Edinburgh EH9 3HJ*
[2]*Royal Observatory, Blackford Hill, Edinburgh EH9 3HJ*
[3]*Dipartimento di astronomia, Università di Padova, vicolo dell'Osservatorio 5, 35122 Padova, Italy*

Accepted 1992 April 13. Received 1992 April 8; in original form 1992 March 22

SUMMARY

We have measured the surface density of bright ($B \leq 16.5$) UVX quasars in the recently completed Edinburgh quasar survey, and have found a higher density, by a factor of 3.4, than has previously been measured. The surface density of quasars brighter than $B = 16.50$ is 0.024 deg^{-2} in this survey, and the gradient of the differential log(number)–magnitude relation for quasars brighter than $B = 17.7$ has decreased from 0.98 to 0.78. Future work is expected to show that new models of the optical luminosity function for luminous quasars will need a smaller amount of cosmological evolution, more comparable to that seen at radio wavelengths.

Key words: quasars: general – cosmology: observations.

1 INTRODUCTION

Samples of ultraviolet-excess (UVX) quasars have a very steep number–magnitude relation, which is important evidence for cosmological evolution of the quasar population. The main evidence for the steep relation comes from the Anglo–Australian Telescope (AAT) survey of Boyle *et al.* (1990) at $B > 18.0$ and the low surface density of quasars in the Palomar–Green (hereafter PG) quasar survey (Schmidt & Green 1983; Green, Schmidt & Liebert 1986, hereafter GSL) at $B < 16.17$. The PG survey has been the most important source of bright, optically selected quasars for almost a decade, and has been vitally important in quantifying the luminosity function and evolution of quasars.

However, it has long been suspected that the PG quasar survey may be incomplete because of large errors in the measured magnitudes and colours of the objects (Wampler & Ponz 1985). Until now, this incompleteness has been difficult to quantify due to a lack of other complete samples in this magnitude range. This paper reports on the first results based on a UVX sample generated from the Edinburgh multicolour survey, which has previously been used to select luminous quasars at high redshifts (Mitchell, Miller & Boyle 1990). Full details of the construction and calibration of the survey and selection of the UVX candidates, with a list of the complete catalogue and identification of the objects selected, will be published in the near future. A brief summary is given by Goldschmidt *et al.* (1991). In this paper we present details of the bright quasars found and discuss their surface density.

2 THE EDINBURGH QUASAR SURVEY

The survey is based on 130 UK Schmidt telescope (UKST) plates taken in 13 contiguous fields at high Galactic latitude covering 330 deg^2. The plates' field centres are 5° apart and correspond to standard UKST fields. The coordinates of the field centres range from 12^h40^m to 14^h20^m (equinox 1950) in RA at Dec. −5° (fields 789 to 794) and from 12^h40^m to 14^h40^m at Dec. 0° (fields 861 to 867). Two plates were taken in each field in each of the photographic wavebands corresponding to U (IIIa-J emulsion and UG1 filter), B (IIIa-J and GG395), commonly known as B(J), V (IIaD and GG495), R (IIIaF and OG590) and I (IV-N and RG715). These photographic bands will be referred to as u, b, v, r and i hereafter. The photographic b magnitudes in this quasar sample have been converted to the B system for the purposes of comparing the quasars in this survey to those in other surveys, by adding a constant offset of 0.05 [derived assuming a mean quasar colour of $b - v = 0.18$ with the colour equation for stars of Blair & Gilmore (1982)]. The plates in each field were taken close together in time so that incompleteness and contamination due to variability should be insignificant. The plates were scanned and measured on the COSMOS machine (MacGillivray & Stobie 1984) and the resulting catalogue of objects was calibrated with photoelectric and CCD sequences in every waveband in every UKST field (Mitchell 1989), obtained at the ESO–Danish 1.5-m, University of Hawaii 88-inch, Steward Observatory 60- and 90-inch and Jacobus Kapteyn (JKT) 1-m telescopes. The

error in the mean measured magnitude was determined from a comparison of the two plates in each waveband, and is <0.05.

The prime selection criterion for the UVX quasar sample was $u-b$ colour, requiring quasar candidates to have $u-b<-0.30$. A further criterion of $b-r\geq 0$ was imposed to eliminate hot blue stars. The other wavebands were not used in generating the UVX sample. A morphological criterion was also imposed to exclude any candidates which appeared extended on the UKST U plates. Spectroscopic confirmation of all the candidates with $b<17.5$ has been carried out at the Isaac Newton (INT) 2.5-m, the ESO 1.5- and 2.2-m telescopes and the UKST, the latter using the FLAIR multi-object spectrograph, and spectroscopic confirmation is also complete to $b\leq 17.7$ in seven fields and to $b\leq 18$ in four fields. We expect the resulting quasar sample to be complete in the ranges $15\leq b\leq 18$ and $0.3\leq z\leq 2.2$. The lower redshift limit arises because low-redshift quasars may have host galaxies that are visible and hence appear extended, or they may have redder colours due to the underlying host galaxy. The PG quasar survey contains large numbers of low-redshift Seyfert galaxies, in contrast to the Edinburgh survey, because of the different morphological constraints imposed. The completeness of the Edinburgh survey compared with the PG survey is discussed below.

In this paper we shall discuss primarily quasars with $b<16.5$. Twelve such quasars have been found (Table 1), of which eight have $B<16.5$ and $0.3\leq z\leq 2.2$.

3 THE NUMBER–MAGNITUDE RELATION

Fig. 1 shows the differential log(number)–magnitude relation for this survey and compares it with other surveys. The errors on the points are Poissonian with 68 per cent confidence limits. We only include quasars in the redshift range $0.3\leq z\leq 2.2$.

It can be seen that the surface density of quasars in this survey agrees well with the MBQS survey of Mitchell, Warnock & Usher (1984). Indeed, the brightest point in the MBQS survey, which used to appear anomalous compared to other data, agrees well with the Edinburgh data. It can also be seen that the data from this survey lie above those from the PG survey, implying that the latter survey is incomplete. The gradient of the differential log(number)–magnitude relation for quasars with $B\leq 17.67$ is 0.78 ± 0.12, computed from the Edinburgh survey alone. Calculating the gradient of the differential log(number)–magnitude relation from the PG and the AAT surveys gives a value of 0.98 ± 0.02. This value is different from Braccesi *et al.*'s (1980) canonical value of 0.86 because we exclude from our analysis quasars with $z<0.3$ (see also Boyle, Shanks & Peterson 1988). The integrated surface density of quasars with $B\leq 16.17$ (the nominal limit for the PG survey) in the Edinburgh survey is 0.018 ± 0.009 deg^{-2}.

In order to assess the statistical significance of the disagreement between the surveys, we fitted a power law to the PG and AAT integrated surface densities to find that the expected number of quasars with $B<16.5$ in the Edinburgh survey in this redshift range is 2.75 ± 0.06. Eight quasars brighter than this magnitude limit were detected in the Edinburgh survey; the Poissonian probability of this is 0.73 per cent, implying a significant statistical difference between the surface densities found by the two surveys.

Table 1. Quasars in the Edinburgh survey with $b\leq 16.50$.

R.A. (1950)	Decl.	b	Redshift
12 45 00.4	-03 33 47	16.07	0.379
12 50 46.1	-07 00 38	16.43	0.097
12 52 46.4	02 00 27	15.48	0.345
13 16 48.4	-07 34 43	16.49	0.538
13 26 52.5	-05 16 07	15.59	0.580
13 47 14.1	-00 51 30	16.29	0.600
13 56 44.9	-06 07 44	16.17	0.072
14 04 53.9	-04 55 56	15.79	0.380
14 21 29.8	-00 13 24	16.02	0.151
14 24 24.6	-00 07 30	16.31	0.632
14 30 47.0	-00 41 36	16.17	1.112
14 35 13.1	-01 34 14	15.97	1.310

4 COMPLETENESS OF THE SURVEYS

Where does this discrepancy between the two surveys arise? The Edinburgh survey is entirely included within the area of the PG survey, and hence we can make a direct comparison of the number of quasars found by the two surveys. The PG survey found one quasar in the area, PG 1352+011. The Edinburgh survey finds this quasar (and measures its magnitude to be $B=16.75$ compared to its PG magnitude of 16.02) but also finds five *new* quasars brighter than $B=16.07$, the PG survey limit in this area (GSL). Hence the number of quasars found by the PG survey does appear to be significantly incomplete in this area of sky.

5 PHOTOMETRIC ACCURACY OF THE SURVEYS

One possible explanation for the apparent incompleteness is that there exists a systematic difference in the calibration of the two surveys. This can be tested by making a direct

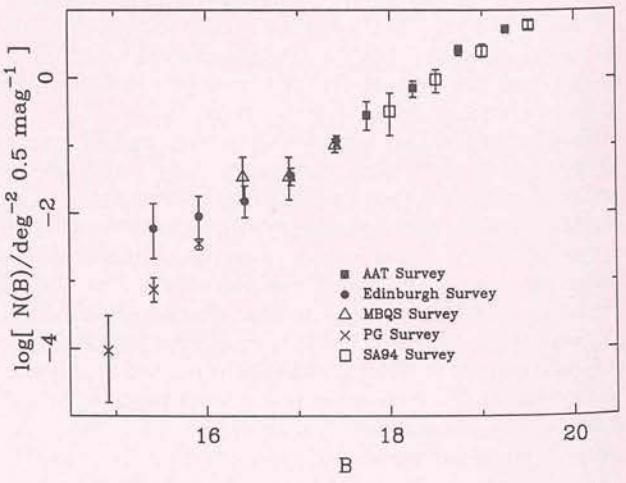

Figure 1. The differential number–magnitude diagram comparing the surface densities found in the Edinburgh survey to those in other surveys in the redshift range $0.3<z<2.2$.

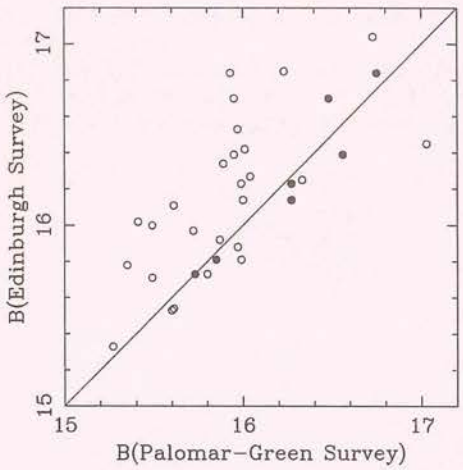

Figure 2. Photometry in the Edinburgh survey plotted against photometry in the Palomar–Green survey for UVX objects found in common with both surveys. The line plotted is the line of perfect agreement. The open circles represent Palomar–Green survey photographic measurements and the filled circles represent Palomar–Green survey photoelectric measurements.

comparison of measured magnitudes of other UVX objects found in common. Most of the objects found in the complete PG survey are hot stars, and GSL provide a list of these with their photographic B_{PG} magnitudes and, in a few cases, photoelectric U, B_{pe} and V magnitudes. In this section, photometry from the Edinburgh survey will be referred to as B_{Edin}. There are 25 stars in common with both surveys in the range $15 < B_{Edin} < 17$. We exclude the quasar, since its magnitude could have varied between measurements. The average offset between the measured photographic magnitudes is $B_{Edin} - B_{PG} = +0.28$. The photographic magnitudes are plotted as open circles in Fig. 2, which shows that this difference exists throughout the magnitude range, and is most likely due to a systematic zero-point error in the PG survey in this region of sky. In contrast, if we only consider the seven objects which have photoelectric photometry in the PG survey, we find an average offset of $B_{Edin} - B_{pe} = -0.01$ (filled circles in Fig. 2), so the Edinburgh photometry agrees well with GSL's photoelectric photometry. The quoted random error in B_{PG} is 0.29, so that with the average value of $d\log(n)/dm = 0.32$ for the UVX objects, we expect a Malmquist bias of 0.03 mag (GSL), which is not a significant contribution to the observed offset in photographic magnitudes. Regardless of the origin of the photographic magnitude offset, the effect should be to *increase* the numbers of objects in the PG survey, and hence the observed *deficit* in numbers of PG quasars cannot be explained by this offset between the two surveys.

This comparison appears to agree with the conclusion of Wampler & Ponz (1985) who carried out photometry of the quasars in the PG survey and also found that the PG photographic magnitudes are systematically too bright, but we should note that the systematic difference between the Edinburgh and PG surveys may not extend to all regions of the PG survey. There is insufficient information currently available to determine the cause of the incompleteness in the PG survey.

6 CONCLUSIONS

The surface density of bright ($B \leq 16.5$) UVX quasars measured by this survey is 0.024 deg^{-2}, higher than that measured previously. For quasars with $16.5 < B < 17.7$, the surface densities in this survey agree well with those measured by other surveys and are defined with greater accuracy than before. The gradient of the differential log(number)–magnitude relation has changed from 0.98 to 0.78 for UVX quasars with $B \leq 17.7$. The ratio of bright quasars at low redshifts to fainter quasars of the same luminosity at high redshifts has increased, and so the amount of cosmological evolution will decrease from that deduced by Boyle *et al.* (1990) and possibly become more comparable to that measured at radio wavelengths (see e.g. Peacock 1985). There is still a need for a much larger complete sample of bright quasars in order to model the evolution of luminous quasars more accurately since, in order to do this, one needs to model the dependence of the luminosity function on redshift. This requires a significant number of luminous quasars in each narrow redshift bin. It remains to be seen if the 'break' in the luminosity function will still be seen at all redshifts, and if pure luminosity evolution (Boyle *et al.* 1988) is still the best-fitting model to the evolution of the luminosity function.

ACKNOWLEDGMENTS

We acknowledge the UK Schmidt telescope unit of the Royal Observatory, Edinburgh for obtaining the plate material and the COSMOS unit for the measurements on which the survey is based. We also acknowledge allocations at the ESO–Danish 1.5-m telescope of the European Southern Observatory, La Silla, Chile, the 60- and 90-inch telescopes of the Steward Observatory of the University of Arizona, the 88-inch telescope of the University of Hawaii and the JKT 1 m, for photometric calibration, and the INT, the ESO 2.2- and 1.5-m telescopes and the UK Schmidt telescope at the Anglo–Australian Observatory for spectroscopic observations. The JKT and the INT are operated by the Royal Greenwich Observatory in the Spanish Observatorio del Roque de los Muchachos of the Instituto de Astrofísica de Canarias. Data reduction was carried out on STARLINK. PG acknowledges receipt of an SERC studentship. FLF acknowledges financial support from a research fellowship of the Fondazione Ing. Aldo Gini.

REFERENCES

Blair, M. & Gilmore, G., 1982. *Publs astr. Soc. Pacif.*, **94**, 742.

Boyle, B. J., Shanks, T. & Peterson, B. A., 1988. *Mon. Not. R. astr. Soc.*, **235**, 935.

Boyle, B. J., Fong, R., Shanks, T. & Peterson, B. A., 1990. *Mon. Not. R. astr. Soc.*, **243**, 1.

Braccesi, A., Zitelli, V., Bonoli, F. & Formiggini, L., 1980. *Astr. Astrophys.*, **85**, 80.

Goldschmidt, P., Miller, L., Mitchell, P. S., Boyle, B. J., Cannon, R. D., Griffiths, W. K., Lilly, S. J., Prestage, R. M. & Stobie, R. S., 1991. In: *The Space Distribution of Quasars, Astr. Soc. Pacif. Conf. Ser.*, Vol. 21, p. 93, ed. Crampton, D., Astr. Soc. Pacif., San Francisco.

Green, R. F., Schmidt, M. & Liebert, J., 1986. *Astrophys. J. Suppl.*, **61**, 305 (GSL).

La Franca, F., Cristiani, S. & Barbieri, C., 1992. *Astr. J.*, **103,** 1062.
MacGillivray, H. T. & Stobie, R. S., 1984. *Vistas Astr.*, **27,** 433.
Mitchell, K., Warnock, A., III & Usher, P. D., 1984. *Astrophys. J. Lett.*, **287,** L3.
Mitchell, P. S., 1989. *PhD thesis,* University of Edinburgh.
Mitchell, P. S., Miller, L. & Boyle, B. J., 1990. *Mon. Not. R. astr. Soc.*, **244,** 1.
Peacock, J. A., 1985. *Mon. Not. R. astr. Soc.*, **217,** 601.
Schmidt, M. & Green, R. F., 1983. *Astrophys. J.*, **269,** 352.
Wampler, E. J. & Ponz, D., 1985. *Astrophys. J.*, **298,** 448.